Magnetoelectric Effect in Lead-Free Multiferroic Composites and Thin Films

A dissertation submitted to
The Faculty of Engineering,
University of Duisburg-Essen
as a partial fulfillment of requirements
for the academic degree of
Doctor of Natural Sciences
Doctor rerum naturalium (Dr. rer. nat.)

by

Muhammad Naveed-Ul-Haq
M. Phil. Physics, QAU Islamabad
Born on 9 December, 1985
Citizen of Pakistan

Essen, October 2017

1st Examiner: Prof. Dr. rer. nat. Doru C. Lupascu
2nd Examiner: Prof. Dr. rer. nat. Heiko Wende
Date of Oral Examination: 02.02.2018

To the loving memory of my maternal grandparents
Mrs. Channan Bi and Mr. Muhammad Zaman

Declaration

I affirm that the contents of this dissertation are original except when a particular reference is made to the work of others. This work has not been submitted entirely or partially for any other degree or qualification in this, or any other University. This dissertation is the outcome of my original work and the work done in collaboration has been duly acknowledged.

Muhammad Naveed-Ul-Haq
Essen, October 2017.

Acknowledgments

During my PhD, I got a lot of help and encouragement from many people. I would be happy to express my appreciation and acknowledgment during this exciting journey.

First and foremost, I would like to thank Prof. Dr. Doru C. Lupascu, my advisor, for providing me with the funding to complete my Ph.D. His kind guidance during my PhD. study, his passionate, diligent, critical thinking inspires my research tremendously. I owe a lot to him for most of the things I learned in the lab.

The person whom I like to admire very highly is Vladimir Shvartsman who introduced me in UDE-Mat. Afterward, his constant support and encouragement have been with me. He mentored me very well. I can hardly describe his skills as a colleague, as a scientist, and as an excellent team player.

I would like to express my gratitude for Prof. Heiko Wende who provided me with the lab facilities and guided me. Also, I would like to acknowledge the support from the Wende's team, especially Soma Salamon who helped me in most of the magnetic and magnetoelectric characterizations. We also had some really fruitful discussions over our topic. I acknowledge the support I received during my collaboration with M.Sc. Samira Webers. We were trying hard to make better PLD thin films. I would also like to thank Joachim Landers for support in measurement and interpretation of Mössbauer data.

I acknowledge the support from Prof. Nikolai Sobolev and Joáo Vidal in the measurement of direct ME measurements during my stay at University of Aveiro. I acknowledge the financial support from TUMOCS Rise program for my stay.

Harsh Trivedi, I thank you for your all-round support and especially, the generous help in proof-reading my thesis with patience. Then comes my UDE-MAT family. Dr. Hans-Joachim Keck has been a staunch support and a motivating person during my stay in Essen. I will cherish the happy moments with my buddies Danka, Nazrabi, and Constantinescu. My daily coffee group most of the time consisted only of Kevin. I gratefully mention my good friend Mehmet Sanlialp. I highly acknowledge the support in official matters which I got from Frau Sabine Kriegel. I also thank the technical support from Patrick Dubray and Karl-Heinz Menze. I would like to thank Frau Vadala, Maryam, Christian Fettkenhauer, Christian Hübner, Martina Pantaler, Irina Anusca, Tommy Mielke, Frau Escobar, Alfred Gäbel, and Morad Etier for their company and support.

The financial support from DAAD program (57052629) (NUH) and Deutsche Forschungsgemeinschaft via Forschergruppe 1509 Ferroic Functional Materials during the PhD duration is highly acknowledged.

At last, I highly admire how my family tolerated me. My mother and aunt (khala) who have always been affectionate, supportive and tolerant. My uncle Muhammad Luqman who stood by me in most of my hard times. My sister who tried to support me even in her busiest times. I also acknowledge the support from my other uncle Javed Ahmed and Aunt Azra Begum for their generous support and love. I mention Hassan and Farrukh here for their moral support. I also appreciate the support from uncles Muhammad Farooq and Abdul Jabbar. My friend list is a bit long. I highly admire Usman bhai for his long lasting support. Other praiseworthy people include Tayyab Razzaq, Osama Rana, Shahzad Chughtai, Muhammad Tariq, and Qurban Syed. Last but not the least, I mention my wife who remained in regular contact with me during all times. Her support and patience is highly commendable.

Abstract

The functional behavior of two-phase composites consisting of piezoelectric and magnetostrictive components is a manifestation of the coupled nature of their constituent phases, known as magnetoelectric (ME) effect. It has a promise in it to a progress in the modern electronic industry by not only improving the existing properties but also reducing the size of microelectronic components. However, the demand for miniaturization has not seized because it is now accompanied by the demand of environment-friendly materials. Therefore, the primary aims of this dissertation are to develop new lead-free multiferroic materials and to study the relationship between the intrinsic properties of piezoelectric and magnetostrictive components and the resulting ME coupling between them. The ferroelectric component with excellent piezoelectric properties combined with the component with excellent magnetostrictive properties would lead to enhanced ME coupling and value-added understanding of the science behind it.

At first, a piezoelectric composition in the system of (1-x)(Ba,Ca)TiO_3 -xBa(Zr,Ti)O_3 with $x = 0.5$ was identified (BCT50-BZT) with piezoelectric coefficient of value greater than 500 pC/N in order to utilize it as the piezoelectric phase. The converse ME coefficient of 0.5(Ba,Ca)TiO_3 - 0.5Ba(Zr,Ti)O_3-15% $CoFe_2O_4$ was found to be around 6 ps/m. It was discovered that the constituent electromechanical coupling factor and magnetomechanical coupling factor might play a role on the ME response. To understand the role of magnetostrictive phase, it was modified with a non-magnetic Al^{3+} ion. The composite of 0.5(Ba,Ca)TiO_3 - 0.5Ba(Zr,Ti)O_3 - 50% Co($Fe_{1.5}Al_{0.5}O_4$ was found to possess 3-times larger converse ME coefficient compared to its unmodified counterpart. This enhancement was attributed to the improved effective piezomagnetic coefficient $d\lambda/dH$ and increased initial permeability of the Al^{3+} modified CFO.

Secondly, using the knowledge from the BCZT-CFO composites, $NiFe_2O_4$ (NFO) was introduced as the magnetostrictive phase which has initial magnetic permeability of 39 that is much larger than that of CFO. This provided an enhancement of around 400 % in the ME coupling in BCZT-30%NFO (converse ME coefficient of 45 ps/m) sample as compared with that of BCZT-50%CFO(Al) (11 ps/m). Hence it gave a substantial evidence that the most important properties to be considered to improve the ME response of two-phase composites are the initial magnetic permeability of the ferrite phase and the maximal elastic compliance of the piezoelectric phase. This discovery has a potential to open new horizons for tailoring of new ME materials.

Thirdly, a two-phase system consisting of relaxor ferroelectric Ba(Ti, Sn)O_3 combined with CFO was studied. This system is a unique example of two-phase systems in which the dielectric properties were almost entirely retained even in the composite, which is in contrast to the case in other non-relaxor-magnetostrictive composites reported here.

The ME coupling of the composite consisting of $Ba(Ti_{0.7}Sn_{0.3})O_3$-20%CFO was much better than the normal ferroelectric-magnetostrictive composites studied for their magnetodielectric properties, previously. The correlation of the maximum of elastic compliance versus temperature and the induced ME versus temperature curves was highlighted, providing another evidence of the vital role electromechanical softness of the ferroelectric material on the stress/strain mediated ME coupling.

Lastly, when the connectivity was changed from (0-3) to (2-2) which is a bilayer geometry, improved local direct ME coupling was observed, due to the better interface between the magnetostrictive phase and the ferroelectric phase. Bilayered thin films of CFO and $BaTiO_3$ (BTO) were synthesized with pulsed laser deposition on two differently oriented substrates. TEM analyses revealed that the CFO layer had a better interface when it was grown on (111) oriented substrate in comparison to that of (100) oriented substrate. This is a discovery as there are no reports in literature on the growth bilayered thin films on (111) oriented substrate. Direct ME coupling studied with PFM under an applied *dc* magnetic field. The bilayered thin film on (111) oriented substrate has an improved ME coupling in comparison to that of bilayered thin film grown on the (100) oriented substrate.

Kurzfassung

Die funktionellen Eigenschaften eines Zweiphasen-Komposits sind das Resultat der Wechselwirkung ihrer piezoelektrischen und magnetostriktiven Komponenten. Diese Wechselwirkung-magnetoelektrische (ME) Kopplung genannt wird hat den schnellen Fortschritt der modernen Elektronikindustrie durch Verbesserung der Materialeigenschaften sowie der Miniaturisierung der Bauteile ermöglicht. Neben der Skalierbarkeit der Bauteile ist heutzutage aber auch die Umweltvertraeglichkeit des Materials ein wichtiger Faktor. Daher ist das Hauptanliegen dieser Dissertation die Herstellung von neuartigen und umweltschonenden multiferroischen Werkstoffen sowie deren Untersuchung hinsichtlich der intrinsischen Eigenschaften der piezoelektrischen und magnetostriktiven Phasen und dem Einfluss der Grenzflaechen. Es soll die magnetoelektrische Kopplung verbessert und die zugrundeliegende Physik dahinter besser verstanden werden.

Zuerst wird das piezoelektrische System (1-x)(Ba,Ca)TiO_3-xBa(Zr,Ti)O_3 (kurz: BCZT) mit x = 0,5 und einem piezoelektrischen Koeffizienten > 500 pC/N betrachtet. Es soll als Matrix für die piezoelektrische-magnetostriktive Phase CFO dienen. Der s.g. konverse ME Koeffizient von BCZT-15% CFO beträgt rund 6 ps/m. Es zeigte sich, dass die entsprechende elektromechanik kopplung faktor und die magnetomechanik kopplung factor der entscheidende Faktor für die ME Eigenschaften ist. Um den Einfluss der magnetostriktiven Phase zu verstehen, wurde diese mit nicht-magnetischen Al^{3+}-Ionen modifiziert. Das Komposit bestehend aus BCZT-50% CFO(Al) zeigte einen um drei fache höheren ME Koeffizienten im Vergleich zu seinem nicht-modifizierten Gegenstück. Diese Verbesserung ist vermutlich auf die Erhöhung der magnetostriktiven Dehnung des Ferrits in Magnetfeld zurückzuführen. Man nimmt an, dass die Modifizierung von CFO mit Al^{3+} zu einer Verbesserung von $d\lambda/dH$ führt, die proportional zum Stress-Sensitivität und der magnetischen Permeabilität ist.

Als Zweites wird das Wissen über BCZT-CFO Komposite genutzt, um $NiFe_2O_4$ (NFO) als magnetostriktive Phase mit einer magnetischen Permeabilität von 39 einzubauen, was ein deutlich höherer Wert ist als der von CFO (1-2). Dies führte zu einer rund 400% igen Erhöhung der ME Kopplung in BCZT-30%NFO (konverser ME Koeffizient von 45 ps/m) verglichen mit BCZT-50%CFO(Al) mit 11 ps/m und einer allgemeinen Verbesserung der BCZT-NFO-Proben. Dies ist ein deutliches Zeichen dafür, dass die wichtigste Eigenschaft zur Erhöhung der konversen ME Kopplung eines Zweiphasen-Komposits die ursprüngliche magnetische Permeabilität der ferritischen Phase sowie das Maximum der Auftragung der elastische Komplianz über der Temperatur der piezoelektrischen Phase. Diese Entdeckung bietet neue Möglichkeiten für die Herstellung besserer ME Materialien.

Als Drittes wurde das Zweiphasen-System aus dem ferroelektrischen Relaxor Ba(Ti,Sn)O_3 und CFO untersucht. Dies ist ein einzigartiges Beispiel eines Zweiphasen-

Systems, bei dem die Dielektrische-Eigenschaften im Komposit beinahe komplett erhalten bleiben - im Gegensatz zu den anderen hier dargestellten magnetostriktiven Nicht-Relaxor-Kompositen. Das Komposit $Ba(Ti_{0,7}Sn_{0,3})O_3$-20%CFO wurde aufgrund seine ME Kopplung untersucht, die auch bei Raumtemperatur auftritt. Diese Kopplung war deutlich besser als bei gewöhnlichen ferroelektrisch-magnetostriktiven Kompositen, die zuvor wegen ihrer magnetodielektischen Eigenschaften betrachtet wurden. Zudem konnte die Übereinstimmung der Maxima der Kurven der elastische Komplianz und des induzierten ME über die Temperatur gezeigt werden, die ein weiterer Beweis für die Wichtigkeit der elektromechanischen Nachgiebigkeit von ferroelektrischen Werkstoffen.

Als Letzes wurde die Konnektivität von (0-3) zu (2-2) geändert, was einer Zweischicht-Geometrie entspricht. Hierdurch kann die lokal direkte ME Kopplung durch bessere Grenzflächen zwischen magnetostriktiver und ferroelektrischer Phase verbessert werden. Zweischicht-Filme aus CFO und $BaTiO_3$ (BTO) wurden mit Hilfe gepulster Laser auf zwei unterschiedlich orientierte Substrate abgeschieden. TEM-Messungen haben gezeigt, dass die CFO-Schichten bessere Grenzflächen aufweisen, wenn sie auf einem in (111)-Richtung orientierten Substrat wachsen anstatt auf einem in (100)-Richtung. Mittels PFM wurde die direkte ME Kopplung bei im Magnetfeld untersucht. Dadurch konnte gezeigt werden, dass ein Zweischicht-Film auf einem (111)-Substrat eine größere direkte ME Kopplung aufweisen, als auf einem (100)-Substrat.

Contents

List of Symbols

$\vec{p}$	dipole moment vector
β_{ij}	polarizability tensor
D_i	electric flux density tensor
E_i	Electric field intensity tensor
χ_{ij}	magnetic susceptibility tensor
ϵ_{ij}	electric permittivity tensor
$\vec{P_s}$	spontaneous polarization vector
ε_{ij}	relative electric permittivity tensor
g	Gibbs free energy density
U	internal energy
H_i	magnetic field tensor
B_i	magnetic induction tensor
σ_{ij}	stress tensor
e_{ij}	strain tensor
α_{ij}^{E}	converse ME tensor
α_{ij}^{M}	direct ME tensor
α_c	converse ME coefficient
α_d	direct ME coefficient
d_{ijk}	piezoelectric tensor
μ_{ij}	magnetic permeability tensor
q_{ijk}	piezomagnetic tensor
s_{ijkl}	elastic compliance tensor
M_{ME}	magnetoelectric magnetization
M	magnetization

$\vec{S}$	total spin angular momentum
$\vec{L}$	total orbital angular momentum
λ_{100}	saturation longitudinal magnetostriction along [100]
λ_{111}	saturation longitudinal magnetostriction along [111]
μ_0	permeability of vacuum $\mu_0 = 4\pi \times 10^{-7} Hm^{-1}$
μ_B	Bohr magneton $\mu_B = 9.27400949 \times 10^{-24} JT^{-1}$
λ_s	isotropic saturation magnetostriction

List of Abbreviations

ME	magnetoelectric
BTO	$BaTiO_3$
CFO	$CoFe_2O_4$
NFO	$NiFe_2O_4$
PNRs	polar nanoregions
BLF100	bilayered thin film STO(100)//CFO//BTO
BLF111	bilayered thin film STO(111)//CFO/BTO
PFM	piezoresponse force microscopy
MFM	magnetic force microscopy
SSPFM	Switching Spectroscopy Piezoresponse Force Microscopy

Chapter 1

Fundamentals of the Magnetoelectric Effect

1.1 Introduction

Historically, humanity made use of materials which were readily available to it. However, in the past two centuries or so the requirements for new materials have become complex and ever-demanding. Extraordinary progress has been made in developing materials based on empirical knowledge of their properties and behavior related to their source and subsequent treatment. Consider the field of solid-state electronics, which acts as a backbone for every other field, cannot fulfill its demands from currently existing materials which have led researchers to become interested in the discovery and development of completely new electronic materials.

Ferroics are a class of materials that show long-range order concerning at least one macroscopic property, and they give rise to domains that can be altered by an associated field.[1] Sometimes, the term primary ferroic is used to indicate ferromagnetic, ferroelectric, ferroelastic and ferrotoroidic order.[2] The word *multiferroics* refers to materials with a coexistence of two or more primary ferroic orders in the same phase. Its present-day use is diverse; it designates a coexistence of ferroelectric and ferro-, ferri- or antiferromagnetic order in single- or even multiphase materials. Note that the term multiferroic was first used by Hans Schmid in 1994,[3] whereas terms like ferroelectromagnetic were in use before. Multiferroics with both magnetic and electric orders do not necessarily display the linear magnetoelectric effect (for example, hexagonal $YMnO_3$), and not all materials displaying the linear magnetoelectric effect are multiferroic (for example, Cr_2O_3). In this day and age, the term magnetoelectric usually refers comprehensively to any coupling between magnetic and electric properties. The versatility of multiferroic materials allows the design of novel electronic devices for diverse functions like sensing, transduction, and memory. The magnetoelectric feature plays a vital role in the modern electronics industry. Multiferroic magnetoelectric materials have a potential to become an integral component of memory technology[4,5] sensing devices,[6,7] energy harvesting devices,[8] electric field tunable devices,[9] and voltage/current converters.[10]

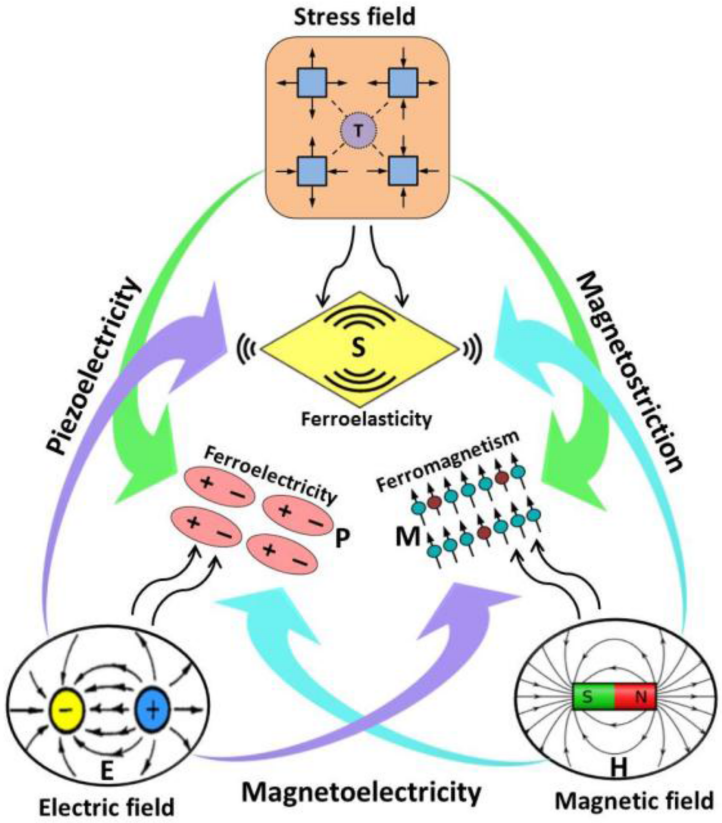

Figure 1.1: Schematic diagram showing different forms of couplings that exist in ferroic materials. H, E and T stand for magnetic field, electric field, and stress field, respectively.[11]

Magnetoelectrics, a term which will frequently be used in this dissertation, is a class of functional materials. First, it is necessary to describe what is meant by a functional material. From an application perspective, a material which has one or more properties which are sensitive to environmental/external variables such as pressure, temperature, electric, and magnetic fields. These external variables are used to utilize the intrinsic properties of materials to achieve intelligent action. For example, if pressure is used to generate an electric voltage across a piece of material, the intelligent action is termed as the piezoelectric effect. Another such intelligent action is the magnetoelectric (ME) effect, that is the ability to control electric polarization with the magnetic field, and controlling magnetization with an electric field. The well-known Heckman diagram for multiferroics is Fig.1.1 which connects different intesive and extensive variables.

Discovery of ME effect can be traced back to 1888 when Röntgen discovered that a moving dielectric became magnetized when placed in electric field.[12] Seventeen years later, the discovery of polarization in a magnetic field was made.[13] Curie in 1894 pointed out the possibility of ME effect in crystals. Later Dzyaloshinskii provided the theoretical background of ME effect in Cr_2O_3.[14] First experimental confirmation about ME coupling came in 1960 when Astrov demonstrated electric field induced magnetism in Cr_2O_3.[15] In 1961, Folen *et al.* confirmed the converse magnetoelectric effect in the same.[16]

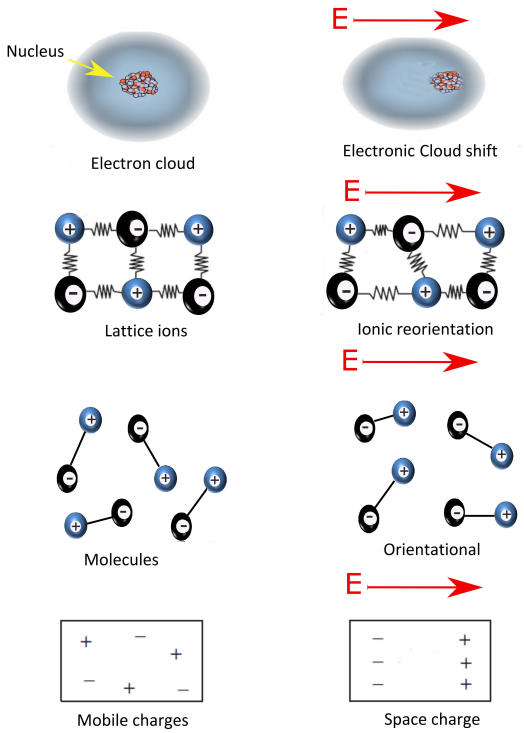

Figure 1.2: How different polarziation entities transform themselves under an applied electric field, diagram adapted from Ref.[25]

1.2 Piezoelectricty and Ferroelectricity

In this section basic concepts about ferroics are introduced.[1]

1.2.1 Polarization

Let's consider a charge $+q$ at position $\vec{r_1}$ and another charge $-q$ at $\vec{r_2}$, the dipole moment of this pair is given by

$$\vec{p} = q\vec{r_1} + (-q)\vec{r_2}; \tag{1.1}$$

and it is directed from negative toward positive charge. This can be generalized for i number of charges with vectors $\vec{r_i}$ to get net dipole moment as:

$$\vec{p} = \sum_i q_i \vec{r_i} \tag{1.2}$$

Thus spontaneous polarization $\vec{P}$ will be defined as:

$$\vec{P_s} = \vec{p}/V \tag{1.3}$$

[1]Most of the content of this section comes from the books of Kittel,[17] Jaffe,[18] Wadhawan,[1] Rabe,[19] Strukov,[20] Lines and Glass,[21] Kao,[22] Waser[23] and Cardarelli[24] unless stated otherwise.

where V is the volume occupied by the charge distribution. Under the action of an applied electric field can induce such a dipole moment. Such an induced dipole moment can be given by:

$$p_{Ei} = \beta_{ij} E_j \tag{1.4}$$

where β_{ij} is known as polarizability tensor. Polarization term is used both for the spontaneous as well as induced polarization.

$$P_i = P_{Ei} + P_{si} \tag{1.5}$$

1.2.2 Dielectric constant and Loss

The electric flux density is defined as:

$$D_i = \varepsilon_0 E_i + P_i \tag{1.6}$$

where $\vec{E}$ is electric field intensity. If $\vec{E}$ is not too strong, the following relationship holds for induced polarization:

$$P_{Ei} = \varepsilon_0 \chi_{ij} E_j \tag{1.7}$$

where χ_{ij} is electric susceptibility tensor. From Eq.1.6 we have:

$$D_i = \varepsilon_0(\delta_{ij} + \chi_{ij})E_j + P_{si} \equiv \epsilon_{ij} E_j + P_{si} \tag{1.8}$$

where ϵ_{ij} is the electric permittivity tensor of the medium. To make ε_{ij} dimensionless it is divided by ε_0 to get:

$$\varepsilon_{ij} = \epsilon_{ij}/\varepsilon_0 \tag{1.9}$$

where ε_{ij} is known as the relative electric permittivity. In practice, it is usually defined as a ratio between a charge stored on a set of electrodes separated by a dielectric slab due to a voltage applied to it and the charge stored on a set of identical electrodes separated by vacuum.

A time-varying electric field $\vec{E(t)}$ applied to a dielectric gives rise to a time-delayed process due to inertial response of the charged species. Under the assumption that the linear response theory is applicable, the time dependent polarization can be written as:

$$P(t) = \varepsilon_0 \int_{-\infty}^{t} \chi(t') E(t - t') dt' \tag{1.10}$$

And electric field itself can be written as:

$$E(t) = \frac{1}{2\pi} \int_{-\infty}^{\infty} E(\omega) e^{i\omega t} d\omega \tag{1.11}$$

where $\omega = 2\pi f$ is the angular frequency. Eq.1.11 can be Fourier-inverted to get:

$$E(\omega) = \int_{-\infty}^{\infty} E(t)e^{-i\omega t}dt \tag{1.12}$$

Similar relationships hold for $P(t)$ and $P(\omega)$ i.e.,

$$P(t) = \frac{1}{2\pi}\int_{-\infty}^{\infty} P(\omega)e^{i\omega t}d\omega \tag{1.13}$$

and

$$P(\omega) = \int_{-\infty}^{\infty} P(t)e^{-i\omega t}dt \tag{1.14}$$

Substituting Eq.1.10 into Eq.1.14, one gets:

$$P(\omega) = \varepsilon_0\chi(\omega)E(\omega) \tag{1.15}$$

Where $\chi(\omega)$ is frequency-dependent susceptibility and is a Fourier transform of response function $\chi(t)$:

$$\chi_(\omega) = \int_0^{\infty} \chi(t)e^{i\omega t}dt \equiv \chi' + i\chi''(\omega) \tag{1.16}$$

Thus real and imaginary parts of dielectric susceptibility are defined as:

$$\chi'(\omega) = \int_0^{\infty} \chi(t)cos\omega t dt \tag{1.17}$$

$$\chi''(\omega) = \int_0^{\infty} \chi(t)sin\omega t dt \tag{1.18}$$

If the electric displacement is shifted with respect to applied electric field by a phase angle δ it would be given by:

$$\vec{D} = \vec{D}e^{i(\omega t+\delta)} \tag{1.19}$$

Fourier inversion of Eq.1.8 gives:

$$D(\omega) = \varepsilon_0(1 + \chi'(\omega) + i\chi''(\omega)) = \varepsilon(\omega)E(\omega) \tag{1.20}$$

Where

$$\varepsilon = \varepsilon'(\omega) + i\varepsilon''(\omega) \tag{1.21}$$

and

$$\varepsilon'(\omega) = \varepsilon_0\Big(1 + \sum_m \chi'(\omega)\Big) \tag{1.22}$$

$$\varepsilon''(\omega) = \varepsilon_0\Big(\sum_m \chi''(\omega)\Big) \tag{1.23}$$

where m stands for various polarization processes involved.

1.2.3 Mechanisms of Polarization

Generally there are 5 mechanisms of polarization,[17] 4 out of those are illustrated in Fig. 1.2. A short description of each is given below:

- **Electronic:** It exists in all dielectrics and originates from the displacement of the negatively charged electron shell against the positively charged core under an applied electric field. It is temperature-independent, and large atoms have a large electronic polarizability.
- **Ionic:** It is observed in ionic crystals and describes the displacement of the positive and negative sublattices under the application of an applied electric field.
- **Orientation:** It exists in materials with permanent dipoles. At ambient conditions, the direction distribution of all the dipoles is statistical due to thermal fluctuations and can only be made unidirectional by applying a substantially high electric field.
- **Space charge:** Dielectrics with spatial inhomogeneities of charge carriers have this kind of polarization. One popular term for such polarization is *Maxwell-Wagner polarization* which occurs in ceramics with electrically conducting grains and insulating grain boundaries.
- **Domain wall:** The mechanism responsible for such polarization is the motion of a domain wall (a small area that separates regions of differently oriented polarizations), which takes place by a mechanism that favors oriented domains with respect to the applied field which tend to grow.

The net polarization of dielectric material results from all the contributions discussed above, which are subdivided into intrinsic (from the lattice) and extrinsic (all other) contributions.

$$\epsilon = \underbrace{\epsilon_{elec} + \epsilon_{ion}}_{intrinsic} + \underbrace{\epsilon_{or} + \epsilon_{sc} + \epsilon_{dw}}_{extrinsic} \tag{1.24}$$

Each contribution has its origin in a short-range movement so each has a different response time when subjected to a time-varying electric field. This means that each of them manifests itself in a certain specific frequency regime. For the oscillating entities experiencing a restoring force, a relaxation behavior is evidenced. For the ionic and electronic polarization, resonance effects are observed. The resultant dispersion function is depicted in Fig. 1.3.

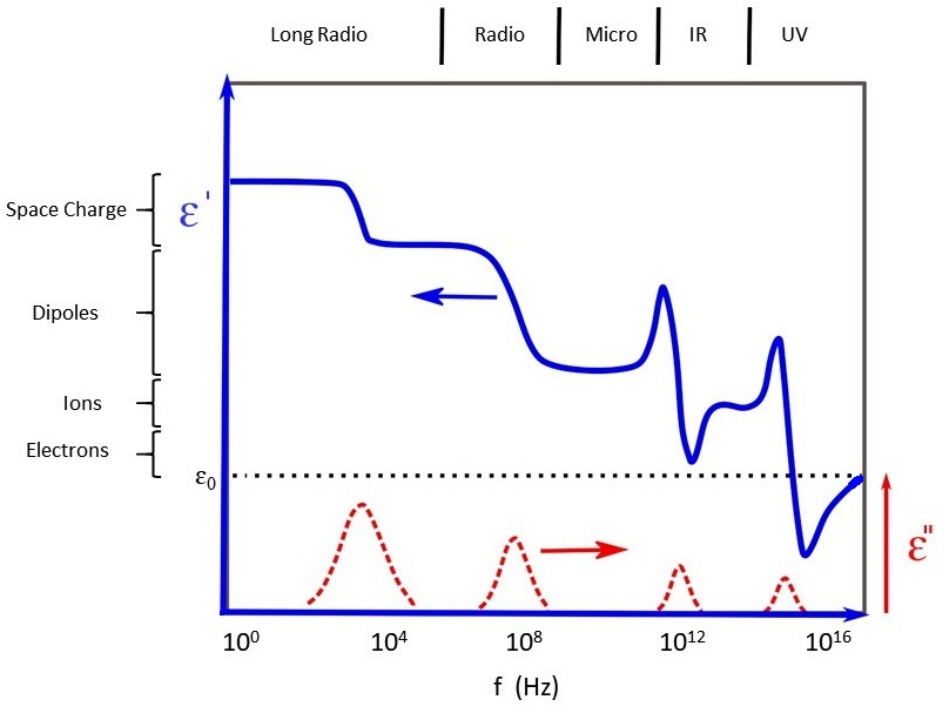

Figure 1.3: Real and imaginary parts of dielectric dispersion function belonging to different polarization species.

1.2.4 Ferroics

Continuing from the brief definition of ferroics in the introduction, formally the ferroic materials are characterized according to the following peculiarities[2]:

1. *Long-range ordering of some at least one macroscopic tensor property*, for example spontaneous polarization or magnetization.

2. *Occurrence of a domain structure (domains and domain boundaries) in the ferroics phase, and possibility of its modification by a field conjugate to the order parameter.*

3. *Large and nonlinearly varying response functions corresponding to certain properties particularly in the vicinity of the transition temperature.*

4. *The possibility of field-induced phase transitions.*

1.2.4.1 Ferroic Phase Transitions

These are divided into two types:

- **Ferroelastic transitions** which involve a distortion of crystal lattice involving a change of crystal family accompanying a transition. Typical example is cubic ($Pm\bar{3}m$) to teragonal (P4/mmm) phase transition of $BaTiO_3$.

[2]taken from Wadhawan[1]

- **Non-ferroelastic transition** in which crystal lattice is not distorted. Typical example is the phase transition of triglycine sulphate.

1.2.4.2 Thermodynamic classification of ferroic materials:

For a ferroic crystal under the action of external electric field (E_i), a magnetic field (H_i), and a uniaxial stress ((σ_{ij})($i, j = 1, 2, 3$)), its generalized Gibbs free energy density can be written as:

$$g = U - TS - E_i D_i - H_i B_i - \sigma_{ij} e_{ij} \tag{1.25}$$

Where U is the internal energy density, S is entropy density, D_i is dielectric displacement, B_i is magnetic induction, and e_{ij} is the strain. According to the first law of thermodynamics $dU = dW + dQ = dW + TdS$ where dU is the increase in the internal energy of the crystal, dW is a small amount of work, and $dQ = TdS$ is a small amount of heat that flows into the system (reversible process). The work done per unit volume is given by:

$$dW = E_i dD_i + H_i dB_i + \sigma_{ij} de_{ij} \tag{1.26}$$

Differentiating Eq.1.25 and substituting for dU and dW, one gets:

$$dg = -SdT - D_i dE_i + B_i dH_i + e_{ij} d\sigma_{ij} \tag{1.27}$$

Considering T, E_i, H_i, and σ_{ij} as independent variables gives

$$dg = \Big(\frac{\partial g}{\partial T}\Big)_{E,H,\sigma} dT + \Big(\frac{\partial g}{\partial E_i}\Big)_{T,H,\sigma,P_j \neq i} dE_i + \Big(\frac{\partial g}{\partial H_i}\Big)_{E,T,\sigma,H_j \neq i} dH_i + \Big(\frac{\partial g}{\partial \sigma_{ij}}\Big)_{E,H,T} d\sigma_{ij} \tag{1.28}$$

Comparing equations 1.27 and 1.28

$$D_i = -\Big(\frac{\partial g}{\partial E_i}\Big) = D_{(s)i} + \varepsilon_{ij} E_j + \alpha_{ij}^M H_j + d_{ijk} \sigma_{jk} + \cdots \tag{1.29}$$

where ε_{ij}, α_{ij}, and d_{ijk} are the elements of the electric permittivity tensor, the magnetoelectric tensor, and the piezoelectric tensor, respectively. Eq.1.29 represents the electric displacement as a sum of a *spontaneous* and the *induced* parts that may arise due to the external fields. Similarly for total magnetic induction tensor

$$B_i = -\Big(\frac{\partial g}{\partial H_i}\Big) = B_{(s)i} + \mu_{ij} H_j + \alpha_{ij}^E E_j + q_{ijk} \sigma_{jk} + \cdots \tag{1.30}$$

where μ_{ij} is magnetic permeability and q_{ijk} are the elements of the piezomagnetic tensor. For the strain tensor

$$e_{ij} = -\Big(\frac{\partial g}{\partial \sigma_{ij}}\Big) = e_{(s)ij} + s_{ijkl} \sigma_{kl} + d_{kij} E_k + q_{kij} H_k + \cdots \tag{1.31}$$

Here s_{ijkl} are the coefficients of the elastic compliance tensor and $e_{(s)ij}$ is the spontaneous strain. q_{kij} are the elements of converse piezomagnetic tensor and

$$q_{ijk} = q_{kij} \tag{1.32}$$

1.2.5 Piezoelectrics

Some special types of crystals polarize under applied stress or can change dimensions upon application of an electric field. Thus the piezoelectric effect involves a linear coupling between electrical and mechanical energies which can either be given by:

$$D_i = d_{ijk}\sigma_{jk} \tag{1.33}$$

or

$$e_{ij} = d_{kij}E_k \tag{1.34}$$

where d_{ijk} and d_{kij} are the elements of piezoelectric tensor and inverse piezoelectric tensor, respectively. The piezoelectric coefficients are third rank tensors, therefore the piezoelectric response is anisotropic. A two subscript matrix notation is also commonly used. The number of non-zero coefficients depends on crystal symmetry. Piezoelectric coefficients are temperature dependent quantities and, usually, the piezoelectric response of a ferroelectric material increases as the transition temperature is approached from below.[23]
All crystalline systems can be described by 32 crystallographic point groups, 11 of them are centrosymmetric (i.e. possess an inversion center) and hence are nonpolar. Among the other 21 systems, 20 do not have an inversion center and can show piezoelectricity. Among these 20, there are 10 polar groups with a unique polar axis and may show a spontaneous polarization parallel to the polar axis. Barium titanate $BaTiO_3$ (BTO) in its tetragonal phase is a typical example in this case, however, in the cubic perovskite phase (cubic structure), the central titanium ion serves as an inversion center and spontaneous polarization is not possible. The cubic to tetragonal phase transformation, where the positively charged barium and titanium ions are displaced with respect to the six negatively charged oxygen ions, a polar axis is developed in the direction of the tetragonal transformation, which also becomes the direction of the spontaneous polarization 1.4.[23] This spontaneous polarization is connected with surface charges $P_s = \sigma$ following Maxwell's equations, and in general, are compensated by charged defects.

1.2.6 Ferroelectrics

The subgroup of ferroic materials in which it is possible to reorient the spontaneous polarization between crystallographically equivalent orientations by an external electric field are known as ferroelectrics. This gives a definition of ferroelectrics in which not only

the spontaneous polarization is present but also the switchability of this polarization is possible by an external electric field. An ideal ferroelectric shows a polarization versus electric field $P(E)$ hysteresis behavior as is shown in Fig.1.5. The division of ferroelectrics is also consistent with the definition of ferroic phase transitions (1.2.4.1). Ferroelectrics often display large electric permittivities (of the order some thousands) and piezoelectric coefficients (of the order some hundreds of pC/N).

1.2.6.1 Classification of Ferroelectrics

The dielectric constant κ of a ferroelectric approaches its highest value near the paraelectric-ferroelectric transition. Above the transition, in the paraelectric state, the decrease in κ can be described by the Curie-Weiss Law:

$$\kappa - \kappa_0 = \frac{C}{T - T_{CW}} \tag{1.35}$$

Where κ_0 is the temperature independent parameter, and C and T_{CW} are empirical parameters. It has been shown that[26] that the value of C gives an indication of the type of ferroelectric. Thus these are divided as follows:

1. **Displacive** for which the value is of the order of 10^5 and have *active* ions (for example Ti^{4+}, Nb^{5+}, W^{6+}) having a strong tendency to promote distortions. $BaTiO_3$ is the best example of this group. Its various phase transitions are shown in Fig.1.4.

2. **Order-disorder** where C is of the order of 10^3. Almost all the water-soluble ferroelectrics are the examples of this class. Rotatable permanent dipoles order at the transition temperature.

3. **Improper** ferroelectrics with values of C close to unity. Ferroelectricity in them originates from piezoelectric coupling to an elastic instability, an example of this class is the ferroelastic $Gd_3(MoO_4)_2$.

1.2.7 Ginzburg-Landau-Devonshire Theory of Ferroelectric Phase Transition

According to the classification of phase transitions by Paul Ehrenfest,[27] these are based on the behavior of the thermodynamic free energy as a function of other thermodynamic variables. It is the lowest derivative of free energy that determines the type of transition involved. The first-order phase transitions show a discontinuity in the first derivative of the free energy with respect to some thermodynamic variable. This involves transfer of heat to or from the system. On the other hand, the second-order phase transitions are continuous in the first derivative of free energy but exhibit discontinuity in a second derivative. The second-order phase transitions do not involve any latent heat.

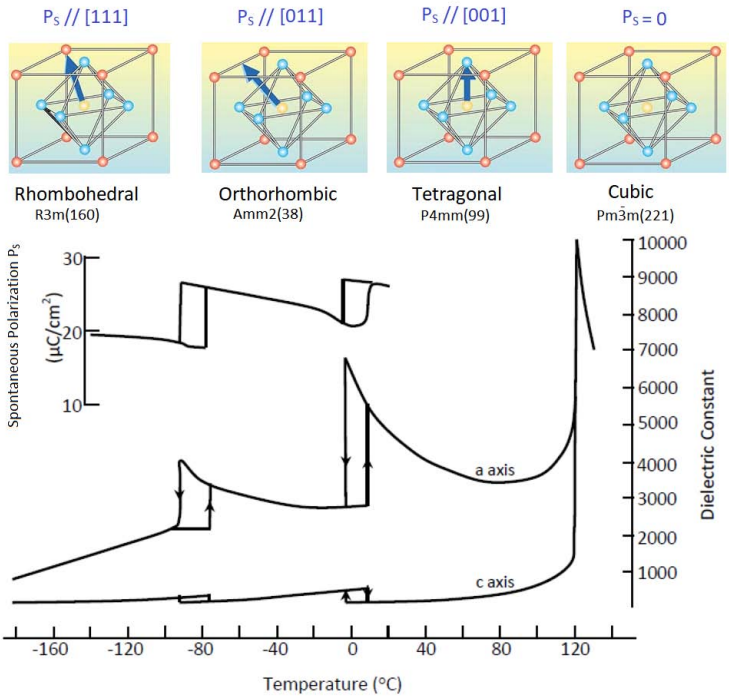

Figure 1.4: Electric permittivity and spontaneous polarization of barium-titanate as a function of temperature, different unit cells belonging to different phases are depicted in the top panel along with their displacive polarization direction for clarity, adapted from Kittel.[17]

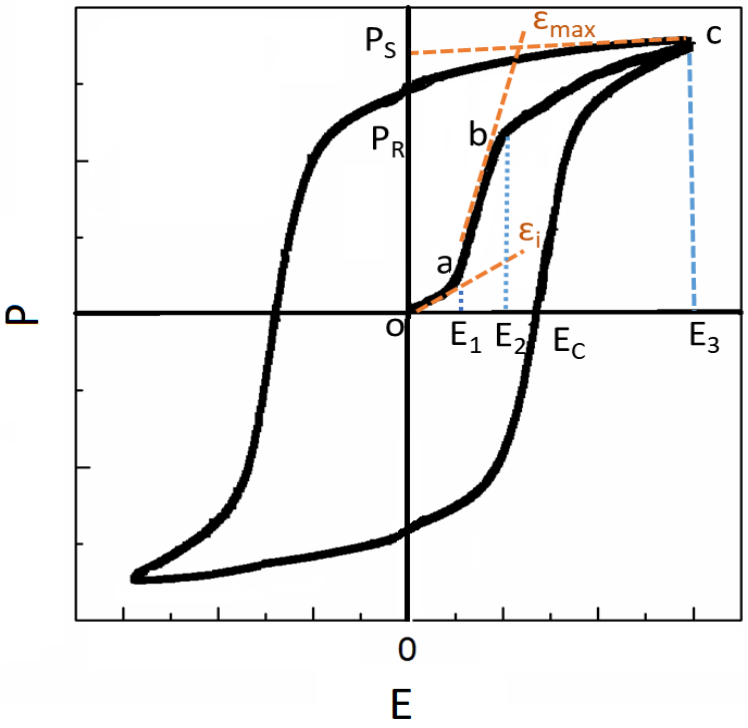

Figure 1.5: A typical polarization hysteresis, adapted from Wadhawan.[1] The curve *oabc* is for a virgin specimen consisting of randomly oriented domains. The slope of line *oa* gives the initial electric permittivity ε_i, while slope of the line *ab* gives the maximum electric permittivity ε_{max}.

The Ginzburg-Landau theory is a kind of mean field theory that is based on the thermodynamics of dipoles in the mean/averaged field of the others. It is assumed that the mode of interaction of a particular dipole is through this mean field and not on the individual basis. Close to the phase transition temperature T_C, the free energy of the system can be written as an expansion of powers of an order parameter P[17]

$$F(P,T,E) = \frac{1}{2}g_2P^2 + \frac{1}{4}g_4P^4 + \frac{1}{6}g_6P^6 - EP \tag{1.36}$$

For the equilibrium configuration,

$$\frac{\partial F}{\partial P} = 0 \tag{1.37}$$

one gets an expression for electric field E as a function of polarization:

$$E = g_2P + g_4P^3 + g_6P^4 \tag{1.38}$$

Differentiating Eq.1.38 with respect to P and then setting $P = 0$ gives us:

$$\chi = \frac{1}{g_2} \tag{1.39}$$

where χ is dielectric susceptibility. In Ginzburg-Landau-Devonshire theory, it is assumed that around the Curie point Θ, g_2 can be expanded as:

$$g_2 = g_0(T - \Theta) \tag{1.40}$$

and all the other expansion coefficients are temperature independent. Combing the two equations from above, one gets:

$$\frac{1}{\chi} = g_0(T - \Theta) \tag{1.41}$$

which is the famous Curie-Weiss behavior in ferroelectrics. Here it is important to mention that the Curie point Θ is not the same as the Curie temperature T_C, although they lie close to each other. Combining Eq.1.36 with 1.40, we have:

$$F(P,T,E)) = \frac{1}{2}g_0(T - \Theta)P^2 + \frac{1}{4}g_4P^4 + \frac{1}{6}g_6P^6 - EP \tag{1.42}$$

where g_0 and g_6 are both positive for all ferroelectrics.[21]

1.2.7.1 First Order Phase Transition

Considering the case for $g_4 < 0$ while $g_6 > 0$ in Eq.1.42 implies that F might have sub-minima at non-zero P values. This is depicted in Fig.1.6 (a). As g_2 is reduced (which signifies decrease in temperature), this minimum will drop in energy below that of the

unpolarized state, and so it will be a thermodynamically favored configuration. The temperature at which this transformation occurs, by definition, is the Curie temperature T_C, and $T_C \geq \Theta$.[19] Electric polarization (which is the first derivative of the free energy F) jumps discontinuously to zero at T_C, thus the transition is known as discontinuous or first order phase transition. We note from Fig.1.6 (a) that at $T = T_C$ the three minima are energetically degenerate/equivalent. Consequently, the system's behavior at $T = T_C$ will depend on whether it is approaching T_C from lower or higher temperatures, and thus thermal hysteresis. This is evident in a number of first order ferroelectrics including barium titanate.[19]

1.2.7.2 Second-Order Phase Transition

Also known as continuous phase transition, it occurs at $T = \Theta$ for the case in which $g_4 \leq 0$. The free energy evolves continuously as temperature is decreased, from a state with one minimum ($P = 0$) to a state with two minima ($P = \pm P_0$). Setting $E = 0$ in Eq.1.38, spontaneous polarization is obtained because all coefficients are positive. One also notes that if we determine the dielectric susceptibility or dielectric stiffness κ) below the transition ($T < \Theta$), one gets:

$$\kappa = \frac{1}{\chi} = 2g_2(\Theta - T) \tag{1.43}$$

Comparing this to Eq.1.41, these two equations suggest that κ approaches zero at $T = \Theta$ and thus χ diverges. In reality, χ achieves large but finite values. Another discontinuous parameter that is worth mentioning here is the heat capacity which is basically a second derivative of the free energy F with respect to electric field.

Schematics of second-order phase transition are depicted in Fig. 1.6 (d-f).

1.2.8 Doping of Barium Titanate and Tolerance factor

The tolerance factor (TF) for ferroelectric materials with perovskite structure ABO_3 is defined as:

$$TF = \frac{R_{A-O}}{\sqrt{2}R_{B-O}} \tag{1.44}$$

Where $R_{A\text{-}O}(R_{B\text{-}O})$ is the bond length between $O^{2\text{-}}$ and the A-site (B-site) ions. The tolerance factor represents the close-packing property of crystals. Normal closed-pack structures like $BaTiO_3$ have two closed-packing directions available: First along the face diagonal (Ba-O-Ba), and the other passing through the center (O-Ti-O).[28] Tolerance factor also reflects the stacking mode of the crystal. When TF > 1, <110> are the close packing directions which means that there exists sufficient space between oxygen octahedron and the B-site ions, permitting ion displacements, e.g., in $BaTiO_3$. However, in

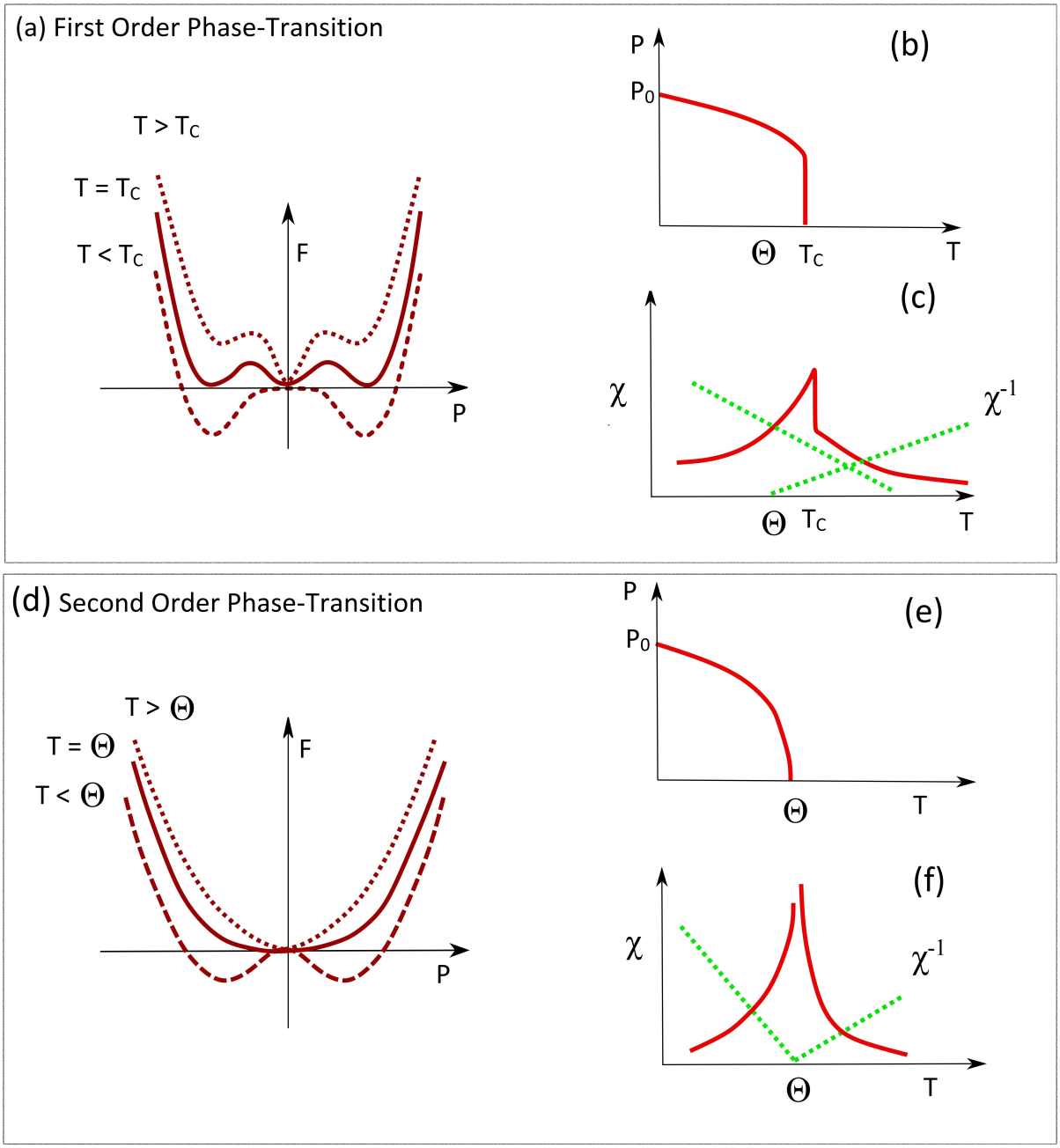

Figure 1.6: (a) First-order and (b) Second-order phase transition in terms of variation with temperature of their free-energy, spontaneous polarization and susceptibility.

case of TF < 1, the close-packing occurs in <100> directions, leaving small displacement margin for B-site cations displacement, e.g., in the case of $GdScO_3$.

The TF also hints toward the crystal structure of a closed-pack structure. Ions with the same type of charge on them must be separated to avoid electric repulsion. Here two things are needed to be noticed: the ratio of positive to negative ionic radii, and the coordination number. According to Pauling rules, when the ionic ratio is close to unity, the typical coordination number is 12. The radius of Ba^{2+} is 137 pm which equals that of O^{2-} (140 pm), making their ionic ratio of almost 1. Thus a coordination number of Ba^{2+} is 12. However, for smaller cations, the ionic ratios with O^{2-} are much smaller than 1, the coordination number must also decrease to decrease repulsion between oxygen ions, and to make the structure stable. The coordination environment is this case is optimized by the rotation of the oxygen octahedron. Benedict *et al.*[29] studied the relationship between octahedral tilt and coordination number. They pointed out that perovskites with low ionic ratios (between the cations and the oxygen anions) and small tolerance factors can only exist in (O) orthorhombic phases (Pnma and Pnm2 space groups) and rhombohedral (R) phases with low coordination number.

The value of TF is also expected to increase in another case scenario. A small-sized B-site cation would have more space for displacement, and thus would be subjected to a weaker repulsion from the oxygen octahedron. Thus the discussion about ion replacement can be summarized with a statement that A-site elements with large ionic radii and B-site elements with smaller ionic radii are more appropriate for ferroelectrics to enhance their ferroelectric as well as piezoelectric properties. A size chart of certain well-known ions is given in Table 1.1.

Table 1.1: Ionic radii of some interesting cations which can be substituted for either Ba^{2+} or Ti^{4+} in barium-titanate.

Ions	Ti^{4+}	Zr^{4+}	Hf^{4+}	Sn^{4+}	Nb^{5+}	Ta^{5+}	Mg^{2+}	Zn^{2+}	Fe^{3+}
Radii/pm	60.5	72	71	69	64	64	72	74	55
Ions	Sc^{3+}	Mn^{3+}	Ba^{2+}	Pb^{2+}	Sr^{2+}	Ca^{2+}	Bi^{3+}	La^{3+}	Gd^{3+}
Radii/pm	74.5	58	135	119	118	100	103	103	93.8
Ions	K^{+}	Na^{+}	Li^{+}						O^{2-}
Radii/pm	138	102	76						140

1.2.9 Barium calcium zirconate titanate (Ba,Ca)(Ti,Zr)O_3 (BCZT) system

In connection with the discussion in the very previous section, $BaTiO_3$ can be doped at both A and B sites which results in an interesting phase diagram of the resultant material, (Ba,X)(Ti,Y)O_3, similar to the one depicted in Fig.1.7. On such a phase di-

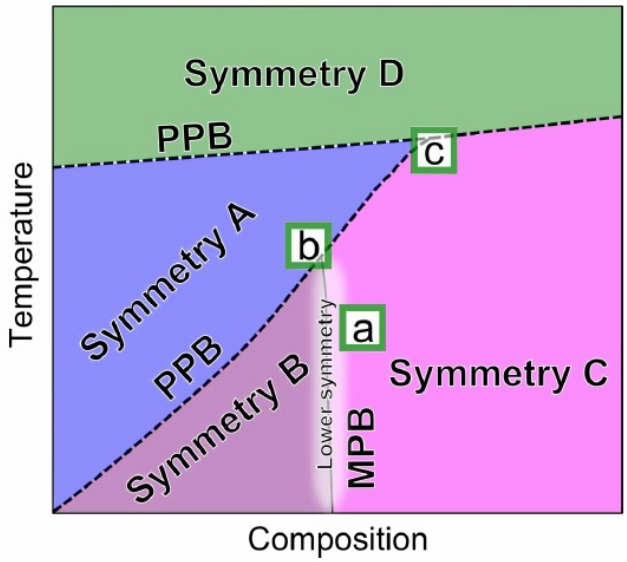

Figure 1.7: Types of different phase boundaries that might exist in s system, e.g., polymorphic phase boundary (PPB) and morphotropic phase boundary (MPB).

agram, interesting features like polymorphic phase boundaries and morphotropic phase boundaries develop. The role of such boundaries is discussed as follows:

1.2.9.1 The Role of Polymorphism and Morphotropic Phase Boundaries

It is a fact that electromechanical and dielectric properties are enriched around phase instabilities.[18] Polymorphism is present in a material if it has a phase instability. This phase instability is manifested as the presence of two or more crystal structures depending on either the variation of composition or thermodynamic variables. The composition driven phase boundary is known as a morphotropic phase boundary (MPB), while a thermodynamic variables driven phase boundary is known as polymorphic phase boundary.[30] The origin of enhanced properties at phase boundaries of different ferroelectric phases have been attributed to a transverse instability in saturation polarization P_S^i. This instability which results in the convenient reorientation of polarization states due to increased degeneracy reduction in free anisotropy energy, and softening of the crystal lattice.[18,31–35] Fig.1.7 depicts a schematic of a composition-temperature phase diagram illustrating MPBs and PBBs.

It has been pointed out by some authors that quantum criticality is the fundamental reason behind the enhanced properties.[20,36,37] Thermodynamically, a critical point is defined as a point in a phase diagram where a first order phase transition becomes a second order phase transition at thermal equilibrium, as marked by the point b in Fig.1.7. Near these critical points, the phase transition energy barrier is even reduced further from its value for first-order phase transitions, which results in a pronounced enhancement of

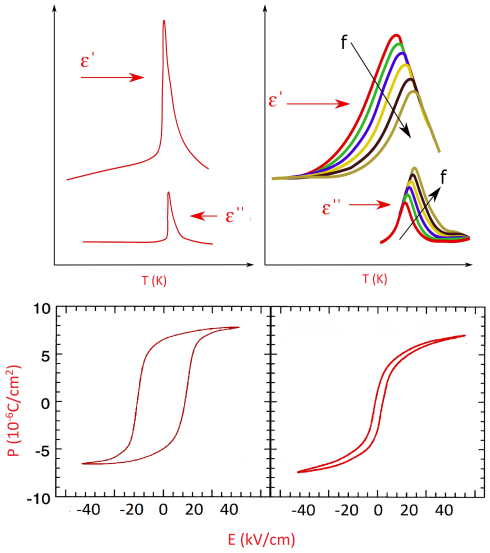

Figure 1.8: Difference between a normal ferroelectric and a relaxor ferroelectric system explained regarding polarisation hysteresis, spontaneous polarisation versus temperature curve, and electric permittivity versus temperature curve.[23]

electromechanical properties due to the decrease in free energy anisotropy. In Fig.1.7, we see another point marked as c, which also represents a vertex of three different phase boundaries. However c is different from b in the sense that it represents a point where two first-order phase transitions lead to a phase transition with increasing temperature that is also a first-order one, and therefore, criticality is missing. Point c is termed as just a *triple point*. On the other hand b has features of both a triple point as well as a critical point.

1.2.10 Relaxors

Relaxor ferroelectrics (RFEs) are classified as a subgroup of ferroelectrics whose physical properties are not so adequately described by the Ginzburg-Landau-Devonshire theory of ferroelectrics. The main features which make RFEs are the following:

- A pronounced frequency dependence of electric permittivity,
- An absence of spontaneous polarization,
- Phase transition-like electric permittivity behavior but without structural macroscopic symmetry breaking.
- A response similar to ferroelectrics when field-cooled to low temperature.

Fig.1.8 illustrates the difference between a normal and relaxor ferroelectrics. To imagine relaxor ferroelectrics in a physical sense, let us consider a mixture of two or more ABO_3 perovskites which contain dipolar species due to chemical substitution and lattice defects.

At very high temperatures, there exists no net dipole moment, because all of the dipoles are affected by thermal fluctuations. On cooling, the dipoles start to show their character, here onward called polar nanoregions. Below a certain characteristic temperature T_d, known as Burn's temperature, their role is significant. These polar nanoregions grow in size with decreasing temperature, as their correlation length r_c increases and give rise to two alternative possibilities:

- The sample may undergo a cooperative ferroelectric phase transition if polar nanoregions percolate to the extent of the whole sample dimensions.
- If the growth of polar nanoregions is not complete with decreasing temperature and no percolation is possible, then there is a dynamic slowing down of the thermal fluctuations at $T \leq T_m$ leading to a state of randomly oriented polar nanoregions.

It is well-accepted that the specific properties of the relaxors originate from the compositional/charge disorder, i.e., equivalent crystallographic sites are occupied by different types of ions.[38] This gives rise to a peculiar polar structure consisting of short-range ordered regions of nanometric scale, known in the literature as polar nanoregions (PNRs). The charge disorder gives rise to quenched electric random fields, which prevent the formation of the long-range ordered ferroic state in these perovskites.[39] At high temperatures, these polar nanoregions are considered dynamic enough, with the interaction between them very weak, thus with the result that they quickly go back to their equilibrium state after the applied excitation is removed (short relaxation time).[40] This state of the system is called *ergodic relaxor*. On decreasing temperature, not only the number of PNRs grow, but also the size of each PNR increases. This promotes strong interaction between these which eventually transform the system either to a non-ergodic (short range glass like interactions) or ferroelectric state.

1.2.10.1 Barium Tin Titanate Ba(Ti,Sn)O_3, (BSnT) System

Barium titanate-based ferroelectric and relaxor systems have gained considerable attention due to their environment-friendly nature. Barium tin titanate $Ba(Ti_{1-x}Sn_x)O_3$ is basically a solid solution of $BaTiO_3$ and $BaSnO_3$. The first $Ba(Ti_{1-x}Sn_x)O_3$ system was reported by Smolenskii and Isupov.[41] For the concentration range (8-20%), the electric permittivity exhibits a maximum much broader than that in $BaTiO_3$, without the typical frequency dispersion of relaxors. This behavior of the phase transition is known as a diffuse phase transition (DPT). However, the compositions $> 20\%$ exhibit relaxor behavior.[42] It has been observed that for these compositions, the frequency dispersion of T_m (the temperature corresponding to ε_{max}) follows an empirical Vogel-Fulcher law:

$$f(T_m) = f_0 exp\Big[-\frac{E_a}{\kappa_B(T_m - T_{VF})}\Big] \tag{1.45}$$

where E_a is activation energy and T_{VF} is the Vogel-Fulcher temperature corresponding to the dynamic slowing down and freezing of PNR dynamics.

1.3 Magnetism

An atom is magnetic if it carries a permanent magnetic moment. Every material is formed from an assembly of atoms which can be either magnetic or non-magnetic. However, magnetic materials are classified according to their respective response to the magnetic field. : *dia-, para-, antiferro-, ferro-, and ferrimagnetic materials*. However, here only paramagnetic, ferromagnetic, antiferromagnetic, and ferrimagnetic materials are described in brief.

1.3.1 Paramagnetism

Most of the times, the magnetism of paramagnetic substances originates from the permanent magnetic moments of some or all of the constituent atoms or ions. If these moments interact negligibly with each other, then they can orient themselves freely in any direction, this is called paramagnetism of free atoms. When a magnetic field is applied, the average direction of the moments is changed, and a magnetization parallel to the field is induced. However, such a magnetization is temperature dependent and decreases by increasing the temperature due to thermal agitation. In the ideal case, the magnetic susceptibility is positive, and the reciprocal susceptibility varies linearly with temperature: famously known as *Curie's law of magnetism*. Paramagnetism is depicted schematically in Fig. 1.9(a).

1.3.2 Antiferromagnetism

Antiferromagnetism is similar to paramagnetism: with a weak and positive susceptibility as depicted in Fig. 1.9(b). However, the reciprocal susceptibility exhibits a minimum for antiferromagnetic materials, at a certain temperature known as *Neel's temperature* T_N. This minimum in the inverse susceptibility originates from the appearance of an antiparallel arrangement of the magnetic moments below T_N. In the most simple case, the magnetic moments are distributed into two sublattices so that their magnetizations are equal but opposite. In the absence of magnetic field, the resulting magnetization is zero. Above T_N, the inverse susceptibility behaves similarly to that of paramagnets but increases below it, because of the decrease in the thermal agitation which works against the antiferromagnetic ordering. The antiferromagnetic interaction is also termed as a negative exchange interaction.

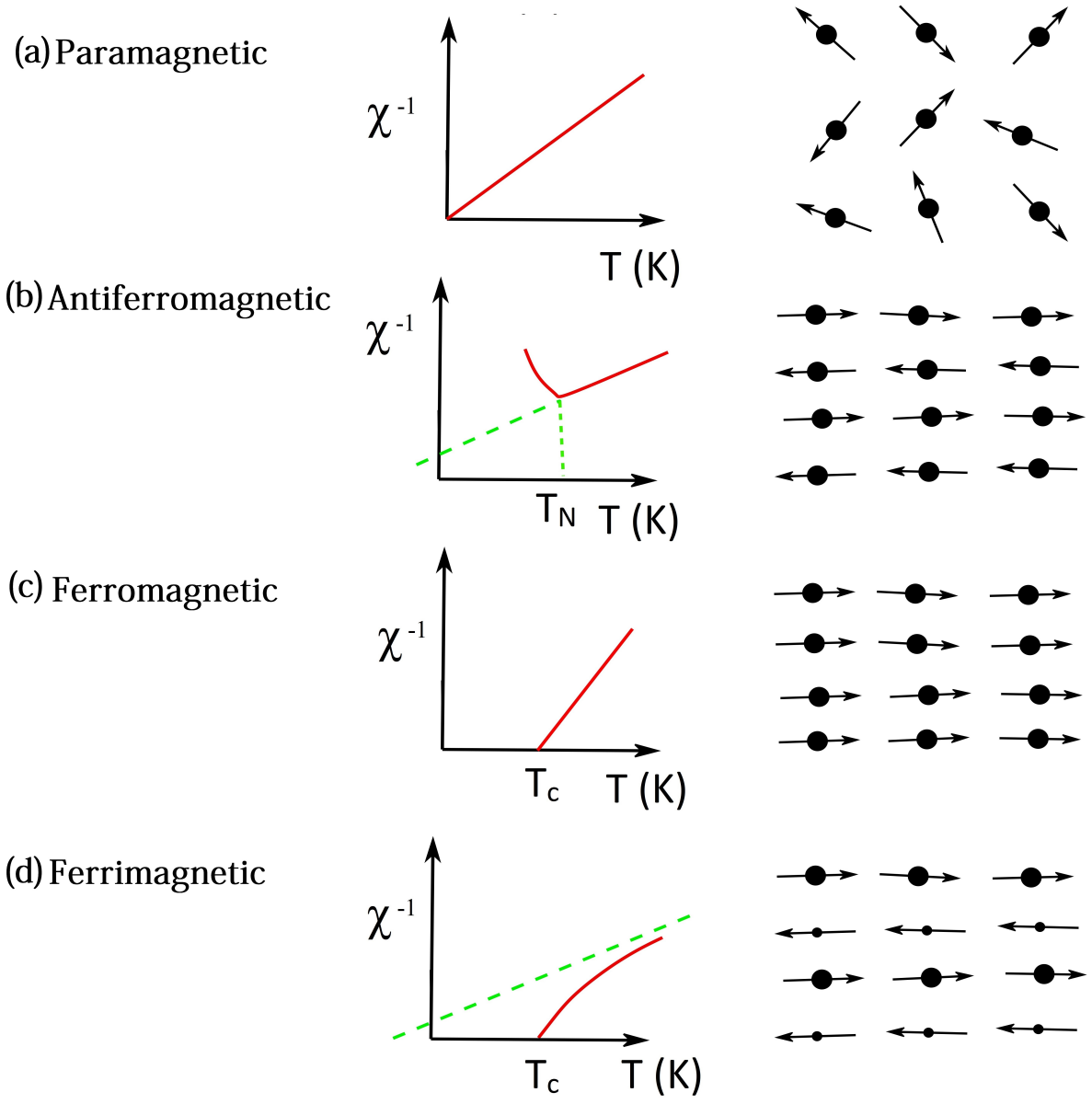

Figure 1.9: Different kinds of magnetic materials distincted by their behavior in an externally applied magnetic field, and behavior of susceptibility with temperature correspondingly.[43]

1.3.3 Ferromagnetism

Ferromagnetism is a parallel arrangement of magnetic moments of neighboring atoms, which is favored by *positive exchange interactions*. The effect is the same as if some fictitious field is acting on all the moments. At high enough temperature, thermal agitation leads to a susceptibility behavior similar to that in paramagnets. The inverse susceptibility becomes zero at a characteristic temperature T_C (for each material) owing to the strong magnetic interactions. Below T_C, interactions overcome thermal agitation and a spontaneous magnetization (M_S) appears in the absence of a magnetic field. This spontaneous magnetization reaches a maximum at 0 K corresponding to the parallel configuration of all the individual moments, as shown schematically in Fig. 1.9(c).
The existence of M_S does not guarantee that overall piece of a material will be spontaneously magnetized below T_C. Such a material is said to be demagnetized. This effect is due to the existence of magnetic domains inside such materials, each domain possessing its own spontaneous magnetization orientation, however, the distribution of domain orientations is such that the resulting magnetic moment of the whole sample is zero. However, when a magnetic field is applied, this orientation distribution of magnetic domains is modified (most of them pointing in the direction of the field). This gives rise to a solid curve shown in Fig.1.10. Thus, a ferromagnetic material has a strong magnetic field induced magnetization. In the presence of large magnetic fields, the magnetization saturates, and if the field is swept between two extreme values in either direction, the behavior of magnetization is irreversible, represented by the dashed line in Fig. 1.10, also known as *hysteresis loop*. It is worth mentioning that this hysteresis loop is of extreme importance for technological applications.

1.3.4 Ferrimagnetism

Intuitively, ferrimagnetism is similar to antiferromagnetism, consisting of two sublattices with opposite magnetization orientations. However, the difference from antiferromagnetism lies in the fact that the magnetizations of the sublattices are not the same. Thus, compensation does not occur. Consequently, a spontaneous magnetic moment appears in such a material below T_C, thus making ferrimagnet behave like a ferromagnet below this temperature. At temperatures much higher than T_C it also behaves as a paramagnet. This magnetic behavior is illustrated in Fig.1.9(d).

1.4 Ferrimagnetic Spinel Ferrites

In this dissertation, it is endeavored to show that $CoFe_2O_4$ and $NiFe_2O_4$ have been chosen due to their extremely good magnetostrictive coefficients and magnetomechanical coupling factors amongst metal oxides. This choice is of great interest as the magnetoe-

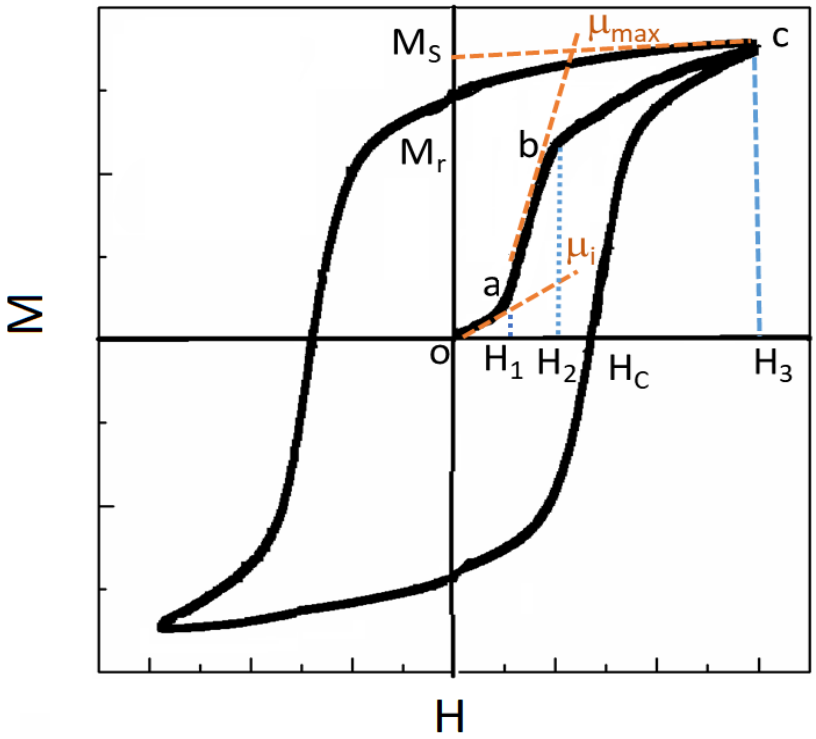

Figure 1.10: A typical hysteresis loops ($M(H)$) of a magnetic material. The important quantity is initial permeability μ_i defined by the slope of curve *oa*.

lastic interaction plays a key role in magnetoelectric composites via interface coupling. Spinels [AB_2O_4] can be classified into main three categories:[44]

- **Normal spinel** has only divalent cations residing on the eight A sites with trivalent ions filling the sixteen available B sites. An example of a normal ferrite is the Zn spinel ferrite $[Zn^{II}][Fe^{III}]_2O_4$, where divalent Zn^{2+} fills A sites and Fe^{3+} the B sites, a schematic inverse-spinel is shown in Fig. 1.11.

- **Inverse spinel** when divalent ions fill 8 of the 16 B sites while trivalent ions occupy the remaining A and B sites, a typical example being nickel ferrite $[Fe][Ni_{0.5}Fe_{0.5}]_2O_4$. The typical inverse spinel structure is illustrated in Fig.1.11.

- **Mixed spinel** has valence ions occupying both A and B sublattices. Each ionic species has thermodynamically preferred lattice positions, mainly due to the cation ionic radius, electrostatic energy, and electronic configuration. This type of ferrites mostly results from nonequilibrium processing such as pulsed-laser deposition (PLD), sputter deposition, and high kinetic energy transfer, for example, ball milling, etc.

1.4.1 Magnetic Anisotropy

An important characteristic of a magnetic crystal is the dependence of magnetic properties on the direction of the applied magnetic field and on the direction in which they are

measured, known as magnetic anisotropy. There are several kinds of anisotropies which are categorized as:

- Crystal/Magnetocrystalline anisotropy
- Shape anisotropy
- Stress anisotropy
- Anisotropy induced by
  a. Magnetic annealing
  b. Plastic deformation
  c. Irradiation
- Exchange anisotropy

Among these, only magnetocrystalline anisotropy is intrinsic, and all others are induced anisotropies. Only magnetocrystalline anisotropy will be further discussed here due to its relevance to magnetostriction of ferrites.

1.4.1.1 Magnetocrystalline Anisotropy in Cubic Crystals

In anisotropic solids certain crystallographic axes are favored by the magnetic moments which will prefer to lie along these directions leading to a lower energy. These preferred orientations are known as magnetic easy-axes which also means that the applied field must do work against the anisotropy force to turn the magnetization vector away from an easy direction. Therefore, storing energy in the crystal, thus for crystals where magnetization points to a non-easy or hard direction, the stored energy in a cubic crystal is given by:[45]

$$E_a = K_0 + K_1(\alpha_1^2\alpha_2^2 + \alpha_2^2\alpha_3^2 + \alpha_3^2\alpha_1^2) + K_2(\alpha_1^2\alpha_2^2\alpha_3^2) + \cdots \tag{1.46}$$

where α_1, α_2, and α_3 are the directional cosines of the magnetization vectors with the crystal axes a, b and c, respectively. K_0, K_1, and K_2 are material constants. The first term is neglected as it is angle independent and K_2 is also neglected, so anisotropy energy has the form:

$$E_a = K_1(\alpha_1^2\alpha_2^2 + \alpha_2^2\alpha_3^2 + \alpha_3^2\alpha_1^2) \tag{1.47}$$

The relative signs of K_1 and K_2 are used for the determination of the easy axis of cubic crystals. When K_2 is zero, the direction of the easy axis is determined by the sign of K_1 only. If K_1 is positive, <100> is the easy direction, <111> is the hard direction and the order of energies is $E_{100} < E_{110} < E_{111}$. The examples of positive K_1 materials include

iron and cubic ferrites that contain cobalt. On the other hand if K_2 is negative, the order of energies is $E_{111} < E_{110} < E_{100}$ with <111> be the easy axis. Typical examples include nickel and cubic ferrites with little or no cobalt.

The physical origin of magnetocrystalline anisotropy mainly lies in spin-orbit coupling i.e., the interaction between the spin and the orbital motion of each electron. When an external field tries to reorient the spin of an electron, the orbit of that electron also has a tendency to be reoriented. But the orbit is strongly coupled to the lattice and therefore repels the attempt to rotate the spin axis. The anisotropy energy, therefore, is the energy required to overcome the spin-orbit coupling.

1.4.2 Cobalt Ferrite $CoFe_2O_4$ (CFO)

1.4.2.1 Structure

Cobalt ferrite has an inverse spinel structure with eight formula units per unit cell. Its crystallographic structure corresponds to the $Fd\bar{3}m$, which is cubic with a lattice parameter of 8.392 Å. The spinel structure can be divided into eight face-centered cubes of oxygen, and each cube has eight tetrahedral (A) and four octahedral (B) sites in the AB_2O_4 unit cell, all of which can be occupied by metallic cations. Fe^{3+} occupies all of the tetrahedral sites with 1/8 contribution for the each site $(8 \times 1/8 = 1)$. The octahedral sites are equally divided between Co^{2+} and the remaining Fe^{3+} sites, also with 1/8 contribution from each. Thus the formula unit for an ideal inverse spinel can be described as follows:

$$(Fe^{3+})_A(Co^{2+}, Fe^{3+})_BO_4$$

1.4.2.2 Magnetism in CFO

Bulk polycrystalline CFO has a saturation magnetization, M_s, of 398 $kA.m^{-1}$ or 80 $emu.g^{-1}$ according to the literaure.[43] The magnetic properties of CFO arise from several exchange coupling mechanisms between the different cations, the predominant of these are *superexchange* interactions in which Fe^{3+} and Co^{2+} couple via an overlap of $3d$ orbitals with the $2p$ orbitals of an intermediate oxygen anion. Another ferromagnetic interaction, called *double-exchange*, occurs by the direct transfer of the electron from Co^{2+} ($3d^7$) towards the empty d-levels in Fe^{3+} ($3d^5$), however, this interaction is rather weak and is over-shadowed by the super-exchange interaction. The main exchange interactions of CFO along with their strengths in units of κ_B are summarized after Kim *et al.*:[47]

1. **First antiferromagnetic super-exchange A-O-B** involving the overlap of ${Fe^{3+}}_A$ with ${Fe^{3+}}_B$ or ${Co^{2+}}_B$ across the $2p$ orbitals of an intermediate O^{2-}. This is the strongest interaction with an energy of $J_{AF} = -24\kappa_B$.

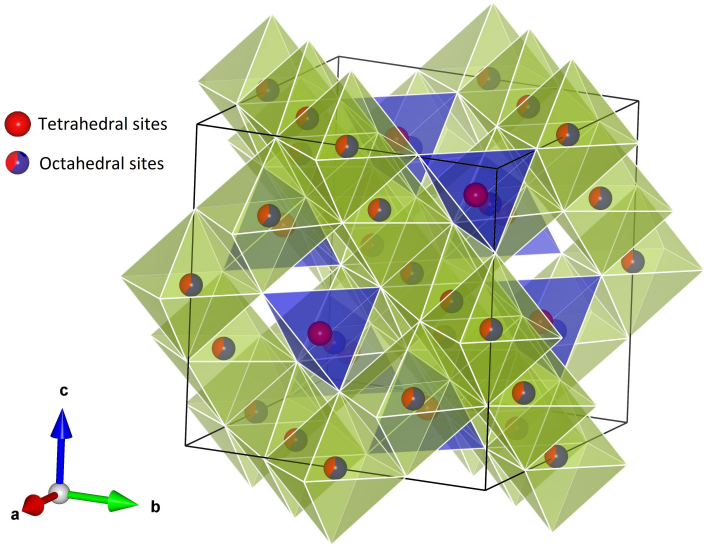

Figure 1.11: Inverse spinel unit cell, differentiated by tetrahedral and octahedral sites. In an inverse spinel structure, tetrahedral sites are occupied by cations with 3+ charge, while the octahedral sites might be occupied by equal number of cations of 2+ and 3+ charge states, figure was drawn using freeware Vesta.[46]

2. **Second antiferromagnetic super-exchange A-O-A** involving only $Fe^{3+}{}_A$, again via O^{2-} with a strength of $J_{AF} = -19\kappa_B$.

3. **A ferromagnetic super-exchange B-O-B** coupling $Fe^{3+}{}_B$ to $Co^{2+}{}_B$, its energy being low at a value of $J_F = 4\kappa_B$.

4. **A direct ferromagnetic double-exchange B-B** involving the same ions, $Fe^{3+}{}_B$ and $Co^{2+}{}_B$, however, strongly masked by the super-exchange interaction.

To calculate the net magnetic moment of CFO, it is important to know that $Fe^{3+}{}_A$ and $Fe^{3+}{}_B$ provide 5 μ_B/formula unit of magnetic moment each. However, this is canceled by the A-O-B antiferromagnetic interactions as discussed above. On the other hand $Co^{2+}{}_B$ provides 3 μ_B/formula unit, thus the overall magnetic moment of CFO is provided by $Co^{2+}{}_B$ only in the *ideal* inverse spinel. It is worth mentioning that inverse spinels are seldom ideal and migration of X^{2+} occurs readily in XFe_2O_4 leading to a mixed spinel structure whose total magnetic moment would vary greatly from the ideal one.[48]

1.4.2.3 Spin-Orbit Coupling in CFO

As discussed earlier, for ideal inverse spinel structure consisting of a close-packed oxygen framework with face-centered cubic structure, metal ions occupy the tetrahedral sites and octahedral sites in a ratio of 1:2. These are the Co^{2+} ions in the octahedral site which are expected to produce a large anisotropy. So here the spin-orbit coupling in Co^{2+} will be discussed:

In the free ion state, energy levels of d-electrons of an ion degenerate, however, they split into doubly degenerate d_γ and triply degenerate d_ϵ levels once the ion is placed at an octahedral site as shown in Fig.1.12(b). This happens because the d_γ wave function stretches along a cubic axis on which the nearest neighbor O^{2-} ion is located. This causes high Coulomb interaction between the negatively charged electron and the O^{2-} ion, thus raising the energy level of d_γ; while the d_ϵ wave function stretches between two cubic axes, thereby avoiding the O^{2-} ions, so that the Coulomb repulsion is relatively small and the d_ϵ level is lowered. Additionally, the second nearest neighbor ions which are arranged symmetrically about the trigonal axis produce a *trigonal* field and thus attempt to attract electrons along the trigonal axis. This causes further splitting of triply degenerate d_ϵ levels into an isolated lower energy level(corresponding to wave-function stretching along the trigonal axis) and doubly degenerate higher levels (which correspond to levels perpendicular to the trigonal axis) (Fig.1.12(c)).
Five out of seven electrons in the valence shell of the Co^{2+} ion in an octahedral site fill + or up-spin states and the remaining two fill up as a down-spin state. The last electron in the doubly degenerate d_γ level has the tendency to alternate between two possible spin states, constituting a circular orbit with an orbital magnetic moment $\vec{L}$. This orbital moment interacts with the total spin $\vec{S}$ of Co^{2+}, giving rise to a spin-orbit coupling of the form $w_{SO} = \eta\vec{L}\cdot\vec{S}$. Since Co^{2+} has more than half the number of electrons that are required for a filled shell, $\vec{L}$ is parallel to $\vec{S}$ according to Hund's rule and $\eta < 0$.
In cubic crystal which has four <111> axes, if Co^{2+} ions are distributed equally on octahedral sites, the anisotropy energy is given by:

$$E_a = \frac{1}{4}\eta LS(|cos\theta_1| + |cos\theta_2| + |cos\theta_3| + |cos\theta_4|) \tag{1.48}$$

where θ_1, θ_2, θ_3, and θ_4 are the angles between $\vec{S}$ and the four <111> axes. This equation can be further transformed into:

$$E_a = -\frac{32\pi}{135}\eta LS(\alpha_1^2\alpha_2^2 + \alpha_2^2\alpha_3^2 + \alpha_3^2\alpha_1^2) \tag{1.49}$$

Since $\eta < 0$, so the factor before the parenthesis is positive and thus Eq.1.47 follows. This explains why the ferrites with Co^{2+} have the positive K_1.[49]

1.4.3 Nickel Ferrite, $NiFe_2O_4$ (NFO)

Nickel ferrite is also an inverse spinel similar to CFO (see Section(1.4.2)) with the difference that Co^{2+} is replaced by Ni^{2+}, thereby changing its magnetic and magnetostrictive properties. It has a Curie temperature of 858 K with a saturation magnetization of 271 $kA.m^{-1}$.[43]

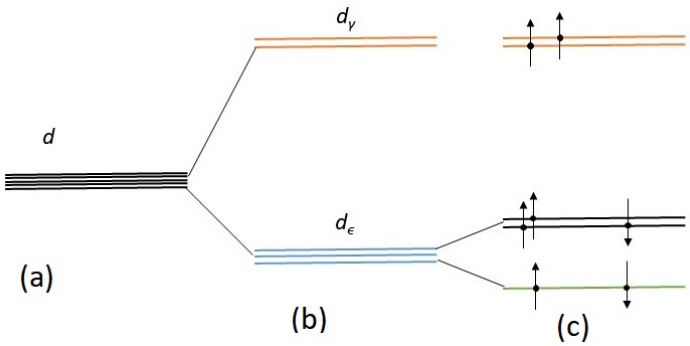

Figure 1.12: Crystal-field splitting of energy levels of 3*d* electrons: (a) free ions; (b) cubic fields; (c) trigonal fields.[49]

1.4.4 Magnetostriction

Change in dimensions of a material upon application of a magnetic field is termed as magnetostriction. This magnetically induced strain in a material is usually represented by λ which is $\lambda = \Delta l/l$. The magnetostriction occurs in all magnetic materials, however, the overall effect is quite small. The saturation magnetostriction λ_s is of the order of 10^{-6}. Quantitatively it can be compared to its thermal counterpart, where the same amount of strain occurs for just 0.5 K change of temperature.[45]

The value of λ_s can be positive, negative or even zero sometimes. Most of the magnetostrictive change in magnetic material occurs during a domain rotation process. The longitudinal magnetostriction can be measured with commercially available strain gauges. These gauges are magnetoresistive in nature, and usually, two such gauges are used in a bridge circuit. One of the gauges is directly glued to the surface of the sample while the other remains as it is. Both of them are placed under the same magnetic field. The dimensions of the gauge attached to the sample change, thereby changing its resistance while that of the other remains unaffected. Other types of magnetostrictive sensors include capacitive, inductive, and optical ones, which are non-touch sensors. These types of sensors when used with proper circuit design have a wide temperature range of operation.

Magnetostriction can be categorized into two basic types: First is *spontaneous* which occurs when a sample is cooled below the Curie point and such a change occurs in each domain individually. Second is the *forced* one which occurs when a magnetically saturated specimen is subjected to large-enough magnetic field to increase its magnetization above its saturation value. However, the ordinary field-induced magnetostriction in which λ changes from 0 to λ_s is caused by direct conversion of a demagnetized sample consisting of domains strained in different directions into a saturated single domain state strained in only one direction.

The saturation magnetostriction λ_s, which cubic crystals undergoes from a direction that is defined by the direction cosines β_1, β_2, and β_3 relative to the crystal axes to a

saturation direction with another set of direction cosines α_1, α_2, and α_3 is given by:[45]

$$\lambda_s = \frac{3}{2}\lambda_{100}(\alpha_1^2\beta_1^2 + \alpha_2^2\beta_2^2 + \alpha_3^2\beta_3^2 - \frac{1}{3}) + 3\lambda_{111}(\alpha_1\alpha_2\beta_1\beta_2 + \alpha_2\alpha_3\beta_2\beta_3 + \alpha_3\alpha_1\beta_3\beta_1) \tag{1.50}$$

Here λ_{100} and λ_{111} are saturation magnetostrictions when the applied magnetic field as well as the directions of measured strain are $\langle 100 \rangle$ and $\langle 111 \rangle$, respectively. When strain is measured in the direction of magnetization, Eq. 1.50 becomes:

$$\lambda_s = \frac{3}{2}\lambda_{100}(\alpha_1^4 + \alpha_2^4 + \alpha_3^4 - \frac{1}{3}) + 3\lambda_{111}(\alpha_1^2\alpha_2^2 + \alpha_2^2\alpha_3^2 + \alpha_3^2\alpha_1^2) \tag{1.51}$$

Which can be further reduced to

$$\lambda_s = \lambda_{100} + 3(\lambda_{100} - \lambda_{111})(\alpha_1^2\alpha_2^2 + \alpha_2^2\alpha_3^2 + \alpha_3^2\alpha_1^2) \tag{1.52}$$

Eq.1.52 is known as the *two-constant* equation for magnetostriction, and it is valid for a magnetostrictive system brought to saturation from a demagnetized state in which all the domain magnetizations were randomly oriented in all directions such that they approximately add up to give zero net value.

In polycrystalline magnetic systems such as $CoFe_2O_4$ and $NiFe_2O_4$, the situation is different where grain orientations are completely random. Thus the saturation magnetostriction of such a system can be determined by some sort of average over these orientations. Each grain when subjected to a field value that is higher than the saturation value, undergoes a strain that is different from that experienced by its neighbors owing to its orientation. If a condition of uniform strain is implied, the magnetostriction can then be averaged over all directions. This results in the following form:

$$\overline{\lambda_s} = \frac{2\lambda_{100} + 3\lambda_{111}}{5} \tag{1.53}$$

1.4.5 Multiferroics Classification

Multiferroics can be broadly classified into two classes, single phase or *intrinsic* multiferroics and multiphase or *extrinsic/hybrid* multiferroics.

1.4.5.1 Classes of Intrinsic Multiferroics

Four main mechanisms are responsible for multiferroicity in single phase intrinsic multiferroics. These include:

- **Lone-pair mechanism:** This mechanism is responsible for the room-temperature ferroelectricity observed in $BiFeO_3$. In this material, a pair of Bi^{3+} valence electrons

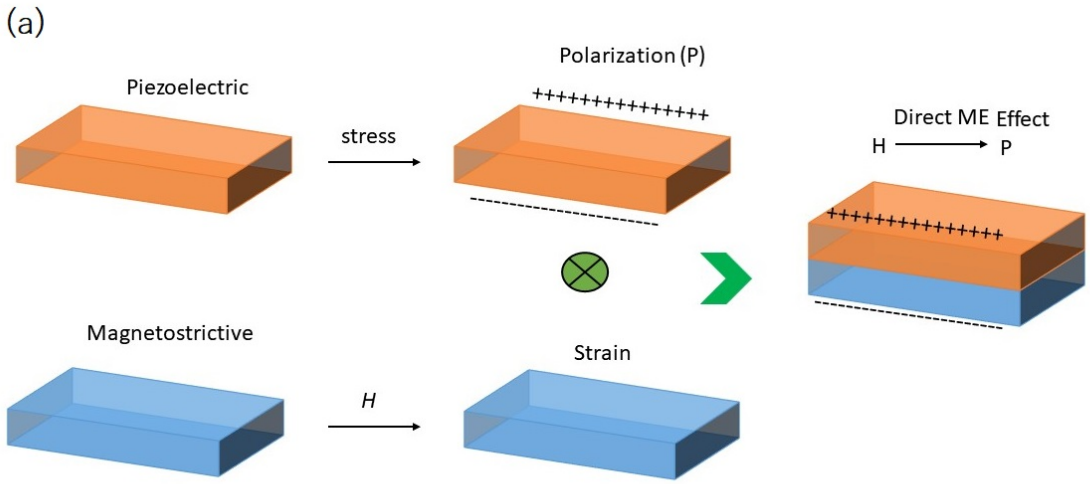

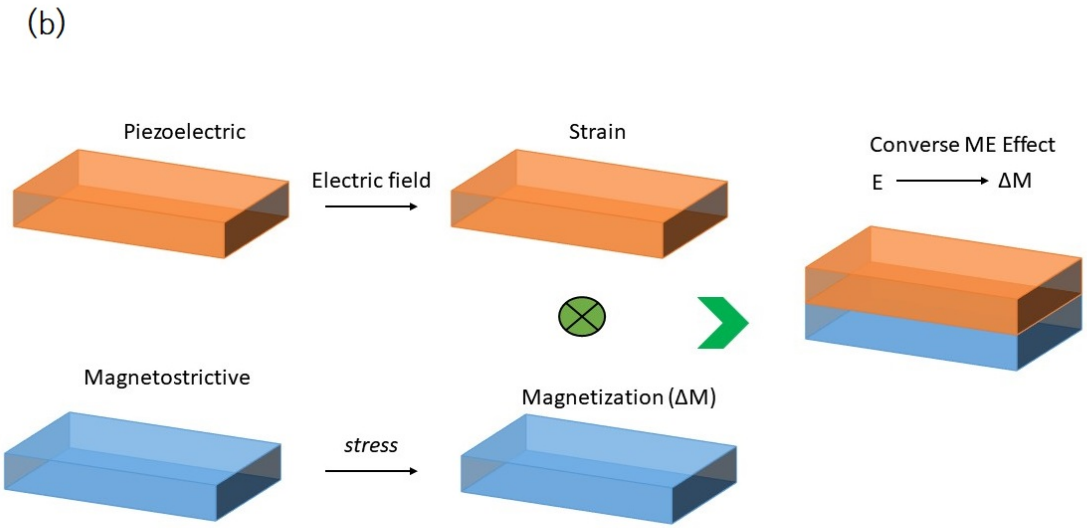

Figure 1.13: The simplest block diagrams for strain-mediated direct (a) and converse (b) magnetoelectric coupling mechanisms, adapted from Wang *et al.*[50]

Table 1.2: A brief list of some well-studied piezoelectric and magnetostrictive materials, taken from Palneedi *et al.*[11]

Piezoelectric Phase	**Magnetostrictive Phase**
Lead-based:	**Metals:**
$Pb(Zr,Ti)O_3$ (PZT)	Fe, Co, Ni
$Pb(Mg_{1/3}Nb_{2/3}])O_3$-$PbTiO_3$ (PMN-PT)	**Alloys:**
$Pb(Zn_{1/3}Nb_{2/3})O_3$-$PbTiO_3$ (PZN-PT)	FeNi-based
$Pb(Mg_{1/3}Nb_{2/3})_y(Zr_xTi_{1-x})_{1-y}O_3$ (PMN-PZT)	FeCo-based
$Pb(In_{1/2}Nb_{1/2})O_3$-$Pb(Mg_{1/3}Nb_{2/3})O_3$-$PbTiO_3$ (PIN-PMN-PT)	CoNi-based
Lead-free:	Ni_2MnGa
$BaTiO_3$ (BTO)-based	Permendur (FeCoV)
$(K_{0.5}Na_{0.5})NbO_3$ (KNN)-based	Galfenol (FeGa), FeGaB
$Na_{0.5}Bi_{0.5}TiO_3$ (NBT)-based	Samfenol ($SmFe_2$)
Others:	Terfenol-D ($Tb_{1-x}Dy_xFe_2$)
AlN	Fe-based metallic glasses (FeBSi, FeBSiC, FeCoB,
ZnO	FeCoSi, FeCoSiB, FeCuNbSiB)
$(Sr, Ba)Nb_2O_5$	**Ceramics:**
$Ba_{1-x}Sr_xTiO_3$ (BSTO)	Fe_3O_4
$Bi_{1-x}Sr_xTiO_3$ (BST)	$Zn_{0.1}Fe_{2.9}O_4$ (ZFO)
$La_3Ga_{5.5}SiO_{14}$ (LGS)	$La_xSr_yMnO_3$ (LSMO)
$La_3Ga_{5.5}Ta_{0.5}O_{14}$ (LGT)	$La_xCa_yMnO_3$ (LCMO)
Polyurethane (PU)	Ferrites or doped Ferrites e.g. $NiFe_2O_4$ (NFO)
Polyvinylidene difluoride (PVDF)	$CoFe_2O_4$ (CFO), Li ferrite, Cu ferrite, Mn ferrite)

in the 6*s* orbital does not take part in *sp* hybridization, thus creates a local dipole yielding a spontaneous polarization below the Curie temperature (T_C = 1103 K). A long-range periodic antiferromagnetic structure arises below the Néel temperature (T_N = 643 K). Among the lone-pair systems, $BiFeO_3$ is the only room-temperature single-phase multiferroic material. It had large and robust electric polarization and pronounced magnetoelectric coupling.

- **Geometric ferroelectricity:** Geometric constraints and space-filling effects may result into structural instabilities in materials, which lead to ionic shifts and the formation of a polar state. Typical examples are h-$RMnO_3$ (R = Sc, Y, In or Dy-Lu). Unit-cell tripling is responsible for the emergence of a ferroelectric order at T_C = 120 K followed by magnetic ordering at $T_N \leq$ 120 K.

- **Charge ordering:** This is an interesting concept in compounds like $LuFe_2O_4$ where it was proposed that the Fe atoms in $LuFe_2O_4$ may form a superlattice with a repetitive sequence of Fe^{2+} and Fe^{3+} ions[51] which might act as a source of ferroelectricity. However, such an origin of ferroelectricity is still under debate. Other examples demonstrating charge-ordered ferroelectricity and magnetism include mixed manganites $Pr_{1-x}Ca_xMnO_3$[52] but they have not attracted much attention.

- **Spin-driven ferroelectricity:** Magnetic order can break the inversion symmetry of electric lattice. So far there are three mechanisms that are identified in this respect; the inverse Dzyloshinskii-Moriya interactions,[53] the Heisenberg-like exchange-striction,[54] and a variation in the metal-ligand hybridization as a function of spin-orbit coupling.[55]

The most researched single phase multiferroics include: The Pb-family perovskite oxides,[3,69–74] Bismuth compounds,[75–79] rare-earth manganites, mixed perovskite solid solutions[80–86] etc. However, most of these compounds have the following drawbacks:[87–92]

- They are multiferroics at lower temperatures.

- They have weak ferroelectric and ferromagnetic response.

- Their ME coupling constants are too low for practical purposes.

1.4.5.2 Classification of Extrinsic Multiferroics

An alternative route towards the development of multiferroic systems consists in exploring the coupling that might occur at the interface between dissimilar magnetic and ferroelectric materials. By carefully engineering a coupling between the magnetic and ferroelectric order parameters across the interface, strong magnetoelectric couplings can

Table 1.3: Some well-studied laminates along with their ME-output and experimental conditions

Composition	**DC Bias, Frequency**	$\alpha_{dir.}$ (V/cm.Oe)
PZT-Terfenol D	4 kOe, 1 kHz	5.9[56]
PMN-PT and Terfenol D	4 kOe, 1 kHz	10.4[56]
AlN and Ta/Cu/$Mn_{70}Ir_{30}$/$Fe_{50}Co_{50}$	- , 1.197 kHz	96.7[57]
Terfenol-D-BTO	350 Oe, 1 kHz	2.1[58]
PZT and Fe-(20 at%)Ga	800 Oe, 1 kHz	3.5[59]
PZT-NFO	40 Oe, 1 kHz	1.5[60]
Terfenol-D + Stainless steel + PZT	-, 5 kHz	40[61]
Terfenol-D + PZT and μ-metal	240 Oe, 1 kHz	1.4[62]
Terfenol-D + PMN-PT	400 Oe, 1 kHz	4.3[63]
Metglass and PVDF	8 Oe, 1 kHz	7.2[64]
PMN-PT and Fe-(20 at%)Ga	750 Oe, 1 kHz	1.0[65]
Metglass + Piezo fiber	2 Oe, 10 Hz	22[66]
Ni-PZT-Ni	80 Oe, 1 kHz	0.45[67]
Terfenol-D + Epoxy + PZT	700 Oe, 1 kHz	7.0[68]

be attained that are orders of magnitude larger than those typical of single phase multiferroics. Another advantage of this approach is that the properties of each component of the composite can be chosen within a larger number of materials, allowing for better optimization of the properties of the system. These multiferroics are divided into four main categories as given below:

- **Exchange-mediated ME coupling.** The exchange interaction gives rise to magnetic order in ferrimagnetic and antiferromagnetic materials and is also responsible for ME coupling in intrinsic multiferroics like $BiFeO_3$. This effect is mediated through an adjacent oxygen ion and can also be used to control the properties of a ferromagnetic layer in the neighborhood of exchange coupled material through the exchange bias effect. Thus exchange bias is present in ferromagnetic/antiferromagnetic heterostructures where the antiferromagnetic material is cooled below its Néel temperature while the ferromagnet is in its saturation state. The exchange coupling at the interface between the two materials causes a shift of the $M(H)$ hysteresis loop. The exchange bias effect was first demonstrated in [Co/Pt]/Cr_2O_3(0001) films[93] where ME coupling in Cr_2O_3 was used to control the sign of the exchange bias field. Later, several other systems were explored in this connection for example NiFe/$YMnO_3$,[94] FeCo/$BiFeO_3$,[95] and $Ni_{78}Fe_{22}$/$BiFeO_3$[96] etc.

- **Charge-mediated ME coupling** There are certain systems in which magnetic properties are linked to the presence of charge thus altering the charge density can

alter the magnetic properties. In strongly correlated oxides, charge carrier doping can be achieved by using a ferroelectric as a gate dielectric, an effect known as the ferroelectric field effect in analogy to the normal semiconductor field effect.[97] In artificial multiferroics, there are three mechanisms of ME coupling:

  - Modification of magnetic moment of a system by increasing its spin imbalance at the Fermi level due to screening.[98]

  - Variation in exchange interaction such that the magnetic state of the system is altered to either a nonmagnetic state or to a state with different spin configuration.[99]

  - Change in the magnetic anisotropy of the system.[100]

- **Charge transport phenomena in heterostructures.** Presence of electric and magnetic polarizations in multiferroic heterostructures can also give rise to other non-magnetoelectric phenomenon.[101] The charge transport phenomena in multiferroic heterostructures in which both magnetic and ferroelectric order parameters are employed to control charge transport, suggest new possibilities to control the conduction paths of the electron spin, with potential for device applications. Typical examples are tunnel junction devices employing ferroelectric,[102] magnetoelectric[103] and multiferroic[104] materials.

- **Strain-mediated ME coupling** The idea of combining two different ferroic orders and utilizing strain mediated coupling was first explored by van Suchtelen[105] and later further elaborated by Ryu *et al.*[56] This idea is based on the *product* property of two materials. In two-phase composite system one of the phases might have a property so that an agent X results in an effect Y with a relationship $dY/dX = Z$, with Z being the proportionality factor (it can be linear or non-linear). For the other phase, the agent Y now acts on another property V and results in an effect W with a relationship $dV/dY = W$ where V is another type of linear or non-linear effect. Now the effect of X on V $[dV/dX]$ can be determined simply by $(dY/dX)(dV/dY)$ which is actually the product of proportionality factors $Z \cdot W$. That is why it is known as a product property. Thus the product property is utilized in the sense that an agent produces such an effect in a composite which is not present in either of the two constituent phases.

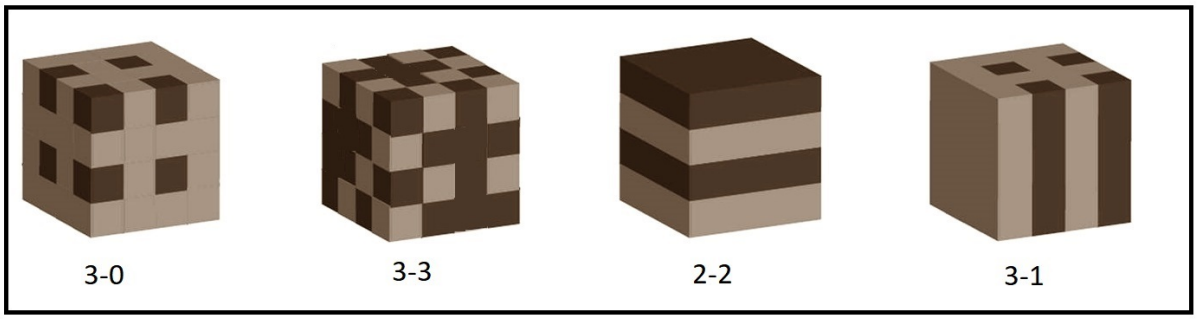

Figure 1.14: Different connectivity schemes which induce different kinds of ME coupling.

1.5 ME Effect in Extrinsic Strain-Mediated Multiferroic Magnetoelectrics

Strain-mediated two-phase multiferroics were engineered with the idea to eliminate the inherent deficiencies of single phase multiferroics. The first experiment on such composites was conducted at the Philips Research Laboratory[105] where the unidirectional solidification technique was employed to obtain eutectic compositions in the quaternary system Fe-Co-Ti-Ba-O. The obtained voltage coefficient of the magnetoelectric effect was superior to that of single phase materials.[105–108] However, the problem with this type of composite was the form of the spinel dendrites in the perovskite matrix[109] (Fig.1.15), which limits the piezoelectric and magnetoelectric coefficients because of the difficulty in electrical poling. This groundbreaking work paved the way towards the search of a variety of ferroelectric/ferromagnetic bulk composites. Extrinsic magnetoelectrics can be configured in multiple ways; a detailed and systematic approach description is presented in the following section via the connectivity schemes.

1.5.1 Connectivity Schemes

A connectivity scheme refers to a configuration which describes how two different types of phases are interconnected/joined together. Connectivity is important, because it is a crucial factor in the determination of constitutive/product properties of the resultant phase. Especially, in case of the strain mediated magnetoelectric effect, it is the most important factor. Different connectivity schemes are shown in Fig. 1.14, and are briefly described in the following section. Moreover, a brief list of most commonly used piezoelectric and magnetostrictive phases is presented in Table 1.2.

1.5.1.1 The 3-0, 0-3, 3-3 Connectivity Schemes

These connectivity schemes refer to the matrix-particle configuration, the first digit in the scheme refers to the host/matrix (in larger amount) in which particles of second phase rest. The digit 0 implies nanoparticles while 3 is referred to 3-dimensional phase. The 3-3

Table 1.4: A brief list of some of the nanocomposites studied for ME coupling.

Composition	**Synthesis**	**ME Properties**	**Ref.**
BTO - CFO	Unidirectional solidification	130 mV/Oe.cm	[105–107]
BTO - CuFO	Sol-gel	425 mV/Oe.cm	[110]
BTO - NFO	Solid-state reaction	20 mV/Oe.cm	[111]
BTO - CFO	Sol-gel	24 ps/m (Converse ME)	[112]
BTO - CFO	Spark plasma	2 ps/m (Converse ME)	[112]
0.5BTO - 0.5CFO	solid state	1.48 mV/Oe.cm	[113]
0.25BTO - 0.75CFO	Sol-gel, solid state	1.97 mV/Oe.cm (dynamic)	[114]
0.25BTO - 0.75CFO	Sol-gel, solid state	1.67 mV/Oe.cm (Pulsed H)	[114]
0.6BTO - 0.4NFO	Solid state synthesis	252 mV/Oe.cm	[115]
0.7BTO - 0.3NCoCuFO	Solid state synthesis	0.63 mV/Oe.cm	[116]
PZT@NFO	solid-state reaction	190 mV/Oe.cm	[117]
CFO@PZT	Sol-gel + electrospinning	-	[118]
Fe_3O_4@BTO	Electrochemical	-	[119]
BTO@γ-Fe_2O_3	Sol-gel	MD of 1.5 % at 300 kHz	[120]
BTO@Fe_2O_3	Sol-gel	MD of 1%	[121]
CFO@BTO	Sol-gel synthesis	2540 mV/cm.Oe @ 160 kHz	[122]
CFO@BTO	Sol-gel synthesis(core-shell)	6.7 mV/cm.Oe	[123]
BTO@LSMO	Sol-gel	54.4 mV/cm.Oe	[124]
CFO@BTO	Hydrothermal + annealing	2.23 mV/cm.Oe	[125]
CFO@BTO	Wet-chemical method	3.4 mV/cm.Oe	[126]
CFO@BTO	Wet-chemical method	-	[127]
CFO-PZT thick films	Sol-gel	30 mV/cm.Oe @ 10 kHz	[128]
CFO-BTO	Sol-gel synthesis	5.5 mV/cm.Oe	[129]
$NiFe_2O_4$@$BaTiO_3$	Sol-gel synthesis	12 mV/cm.Oe	[130]
Ferrite@perovskite	Sol-gel synthesis	-	[131]
NFO@PZT	Sol-gel	195 mV/cm.Oe	[117]
BTO-CFO covalently bonded	Sol-gel synthesis	0.3 mV/cm.Oe	[132]
NFO - BTO	Sol-gel synthesis	0.5 mV/cm.Oe	[133]
BTO@NFO	Sol-gel synthesis	MD of 28 % resonance	[134]
NFO - BTO	Sol-gel synthesis	0.4 mV/cm.Oe	[135]
BTO@NiZnFO	Chemical self-assembly	-	[136]
Fe_2O_3@BTO	Chemical self-assembly	-	[137]
CFO - PZT nanofibers	Electrospinning	Studied via PFM	[138]
NFO - PZT	Electrospinning	MD of 8 %	[139]
PZT@NFO	Sol-gel + electrochemical	-	[140]
CFO@BTO	Sol-gel	MD of 4.5 %	[141]

scheme is also included in this group because in the case of sintered particulate ceramics, the distinction between these three types is very difficult. The 3-3 connectivity also is referred to as *mixed-phase connectivity*. It is usually achieved by mixing the constituent phases in the solid state and subsequent compaction and sintering at high temperatures. The synthesis of such materials is convenient and cost-effective, however, this type of configuration suffers, at times, from poor phase connectivity.

An extensively used technique for producing 0-3 particulate composites comprises of sintering a mixture of ceramic oxide powders at high temperature. This ceramic sintering process is straightforward and the properties of the composite can be conveniently customized by picking the constituent phases, their starting particle sizes, and processing parameters. Using this process, mainly magnetic ferrites have been used with piezoelectric ceramic composites due to their high temperature stability. Currently, the measured ME coupling of the particulate composites are distinctly lower than the theoretically expected ones. Several factors influence the ME coupling which include the misfit strain at the interface arising from the thermal expansion mismatch between the two phases reducing the densification the interdiffusion and/or chemical reactions between the two phases during high-temperature sintering. However, these issues can be counteracted by using an optimum sintering regime and better piezoelectric materials that can show better coupling properties. A great number of particulate systems have been investigated for ME coupling, a brief list of these is presented in Table 1.4 which include the composites prepared by all the chemical synthesis methods available. For example, the most widely used method is sol-gel.

1.5.1.2 The 2-2 Connectivity Scheme

Here the digit 2 refers to the two-dimensional nature of both phases. Mostly it refers to alternate 2-dimensional layers which may be two or more in number. Sometimes, these structures are also called heterostructures. Two-phase thin films as well as laminates and thin films fall in this category. Laminates are usually fabricated by glueing two or more thin layers, usually a dielectric layer sandwiched between two metallic magnetostrictive layers. This results in a very high stress-mediated magnetoelectric coupling, for example, an ME coefficient of 4.68 V/cm·Oe (off-resonance) was obtained in a laminate structure of Terfenol-D/PZT/Terfenol-D.[142] A brief list of high ME-output laminates is given in Table 1.3.

In spite of good performance, they suffer from some drawbacks. The metallic magnetostrictive materials are overly expensive. Moreover, these magnetostrictive materials are brittle, have low permeability, and require a high biasing magnetic field to achieve the maximum magnetoelectric effect.

Another type of laminate consists of the polymer PVDF and Metglas.[143] They show

good room temperature ME characteristics. However, the main drawback with these laminates is their small temperature-window of operation. Hence they are not suitable for devices to be operated at high temperatures.

Bi-layered and multilayered thin films also form a part of this connectivity scheme. There has been an enormous amount of interest in thin film heterostructures, and many different types of heterostructure combinations have been reported in literature.[5,144–147] A brief list of heterostructures which employ strain-mediated magnetoelectric coupling are given in Table 1.5.

1.5.1.3 The 3-1 or 1-3 Connectivity Schemes

This is a very interesting category of connectivity schemes. The digit 1 refers to one-dimensional pillars/rods which are embedded in the other three-dimensional phase. In the past, it was predicted that this is the most useful configuration to get enhanced magnetoelectric properties.[148] A number of such films were fabricated, mostly via physical methods like pulsed-laser deposition, physical vapor deposition, and a small number of them with chemical deposition techniques. Phase self-assembly is the mechanism responsible for such structure growth during film deposition. A lot of research work has been done on these self-assembled nano-pillar structures.[149–163] It was determined that although they provide better mechanical coupling, they also suffer from the serious drawback of electrical-shortening which drastically reduces their magnetoelectric abilities.

Table 1.5: Different thin film heterostructures, along with their coupling mechanisms, and temperatures corresponding to maximum ME coefficients.

System	Coupling	T	Mechanism	Reference
$Ni/BaTiO_3$	converse	300 K	Strain	164
$CoFe_2O_4/BaTiO_3$	direct	300 K	Strain	165
$CoFe_2O_4/BiFeO_3$	direct	370 K	Strain	166
$Zn_{0.1}Fe_{2.9}O_4$/PMN-PT	direct	300 K	Strain	167
$Fe_3O_4/CoFe_2O_4$/PZT	converse	300 K	Strain	168
Fe3O4/PMN-PT	converse	300 K	Strain	169
LSMO ($x = 0.3$)/$BaTiO_3$	converse	200 K	Strain	170
LSMO ($x = 0.3$)/$BaTiO_3$	converse	300 K	Strain	170
LSMO ($x = 0.3$)/PMN-PT	converse	300 K	Strain	171
LCMO ($x = 0.3$)/PMN-PT	converse	10 K	Strain	172

1.6 Thesis Motivation

According to a recent article,[173] two main challenges are faced by modern electronic industry: cost control and environmental concerns. The electronic industry has to follow the idea of steeply declining costs of electronic products and find ways to come up with better and simultaneously cheaper products.

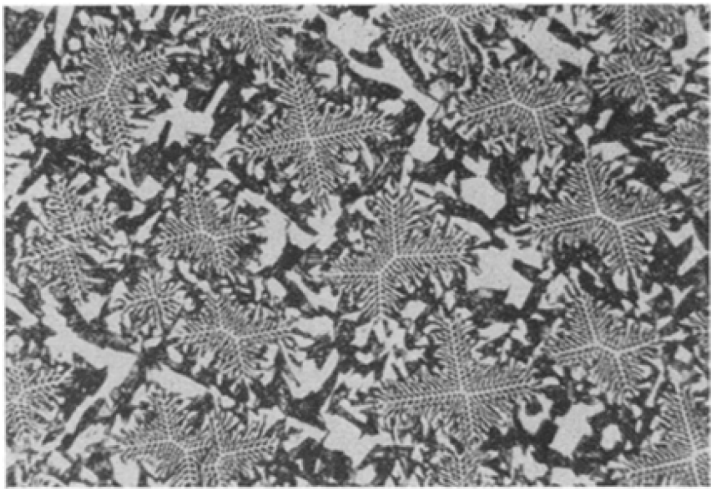

Figure 1.15: A transverse section of a BTO-CFO unidirectionally solidified rod showing four finned spinel dendrites in cell. The image was reused with permission from Kluwer Academic Publishers, ©1974 Chapman and Hall Ltd.[109]

Table 1.6: Piezoelectric, dielectric, and electromechanical coupling coefficients of BCT-50BZT.[174]

	Piezoelectric Coefficients			Dielectric Constants				Electromechanical Coupling Factors				
	d_{ij} (10^{-12} N/C)			$\varepsilon_{ij}(\varepsilon_0)$								
Mat.	d_{33}	d_{31}	d_{15}	ε_{33}^T	ε_{31}^T	ε_{33}^S	ε_{31}^S	k_{33}	k_{31}	k_{15}	k_t	k_p
BCZT	546	-231	453	4050	2732	2930	1652	0.65	0.31	0.48	0.42	0.53
$BaTiO_3$	191	-79	270	1898	1622	1419	1269	0.49	0.21	0.48	...	0.35
PZT5A	374	-171	584	1700	1730	830	916	0.70	0.34	0.68	0.49	0.60

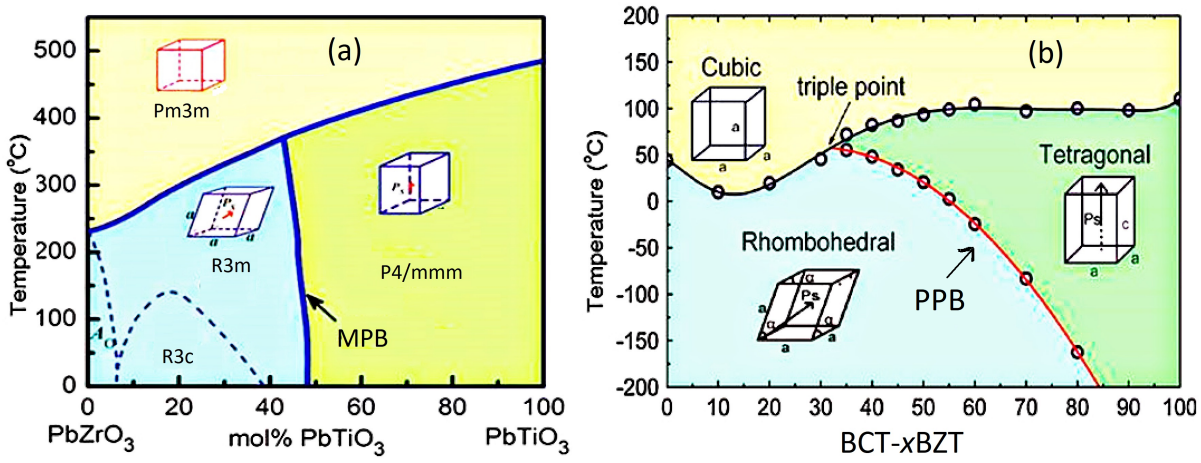

Figure 1.16: Comparsion of the phase digrams of PZT and BCT-xBZT.[186] Phase diagram of BCT-xBZT reused with permission from ©2009 American Physical Society.[187]

The solid solutions of lead zirconate titanate $Pb(Ti,Zr)O_3$ have been the focus of attention in piezoelectric industry, because all the desired features like high piezoelectric and electromechanical properties are readily achieved by either doping or modifying the crystal lattice.[175] Pb-based piezoceramics hold more than 90% share of the modern piezoelectric industry.[176] However, due to increased global awareness about a healthy environment since the late 1990's, Pb-based materials are considered to be in the list of heavily toxic materials. Moreover, the global awareness resulted in concrete steps toward the elimination of toxic materials from household and daily use from certain national and international governing bodies.[177–183] Pb and PbO were clearly categorized as toxic materials,[184,185] and since then alternatives for Pb-based materials are being sought.

Based on the discussion in the previous section, the requirements for new functional materials and the quest of achieving higher magnetoelectric coupling can be rationalized as follows:

1. There is a great need for Pb-free multiferroic composites that can replace PZT and PMN-PT-based piezoelectrics in multiferroic composites. Although the properties of Pb-based piezoelectrics are hard to beat, yet there is a lot of room for improvement, discovery, and research in Pb-free materials. Pb-based systems have been a focus of research, especially $P(Zr,Ti)O_3$ which is categorized as the one with a vertical morphotropic phase boundary MPB on its phase diagram, separating a ferroelectric rhombohedral and a ferroelectric tetragonal phase. Similarly in Pb-free systems, for example in $BaTiO_3$, in which a new piezoelectric system can be created by doping both Ba and Ti sites so that the system develops a polymorphic phase boundary (PMB). The proposed system in this case is (1-x)$(Ba_{0.7}Ca_{0.3})TiO_3$-$x$$Ba(Zr_{0.2}Ti_{0.8})O_3$ (BCT-xBZT). The end-composition $(Ba_{0.7}Ca_{0.3})TiO_3$ has a pure cubic-tetragonal phase transition and $Ba(Zr_{0.2}Ti_{0.8})O_3$ has a pure rhombohedral to

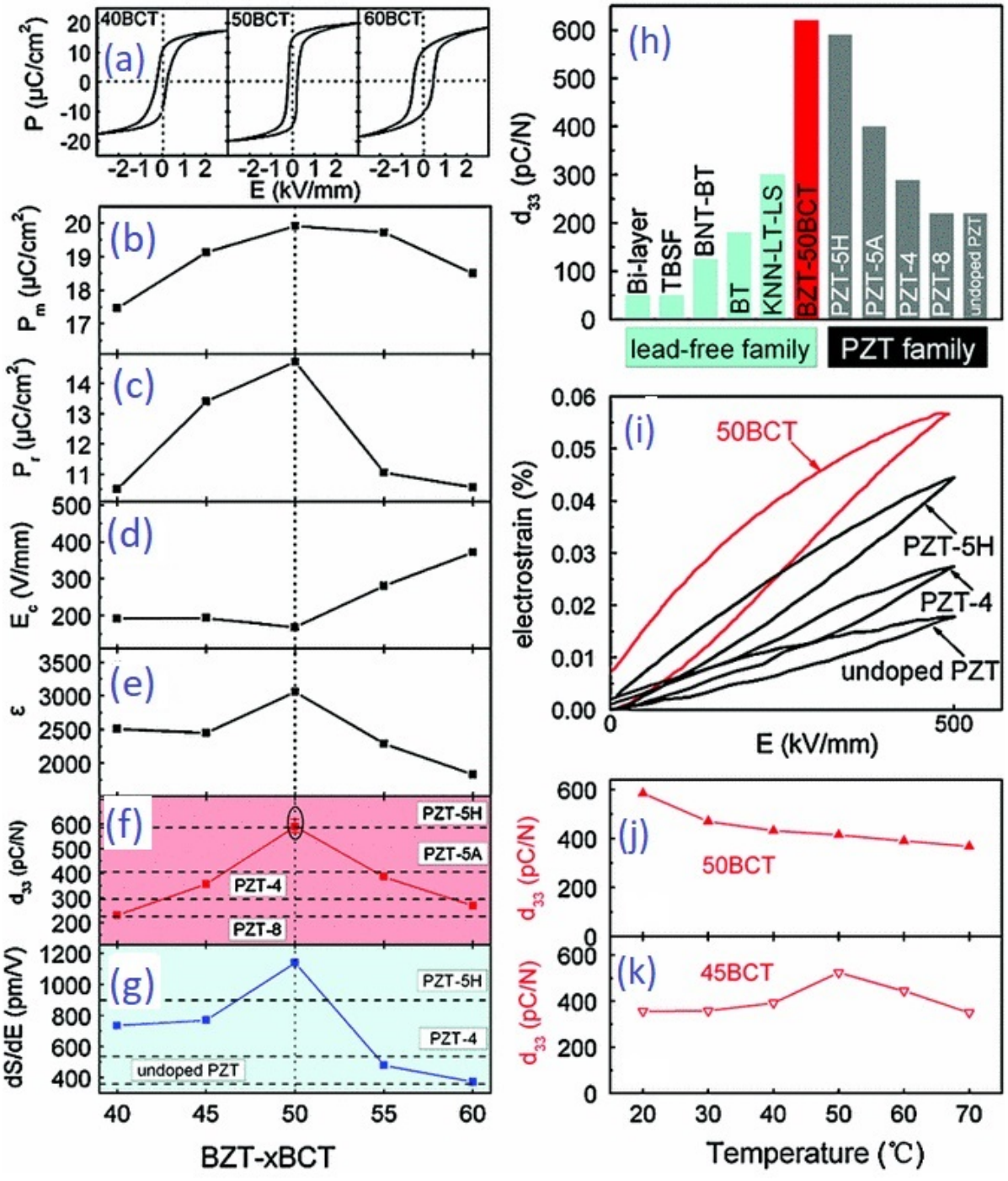

Figure 1.17: Comparison of the properties of 0.5BCT-0.5BZT with other piezoelectrics.[187] The figure was reused with permission from ©2009 American Physical Society.[187]

cubic transition. The resulting pseudo-binary phase diagram of BCT-xBZT contains some compositions at PPB boundaries. The BCT-50BZT is one such composition on the PPB phase boundary of BCT-xBZT at $x = 0.5$. It is a well-known fact now that the piezoelectric, dielectric and electromechanical properties are greatly enhanced at and around this PPB. A comparison of the properties of BCT-50BZT with other compositions on the BCT-xBZT phase diagram is depicted in Fig.1.17(a-g), while its comparison to other piezoelectric compounds of competitive properties is presented in Fig.1.17(h-k). Values of various piezoelectric, dielectric, and electromechanical constants are also given in Table 1.6. The terminology polymorphic phase boundary (PPB) is used in case of $BaTiO_3$ systems, because the systems do not possess a vertical phase boundary as in the case of PZT. The difference in phase diagrams of PZT and BCT-xBZT is shown in Fig.1.16. Other cations like Sn^{4+} when substituted at various sites have a very positive impact on the piezoelectric properties.The identification of potential piezoelectric materials is crucial, because the properties of two-phase composites also strongly depend upon the choice of piezoelectric/ferroelectric medium.

2. Many magnetostrictive materials have already been a focus of research. However, there is a lot more to be achieved by improving their magnetostrictive properties. Moreover, more research is required to find out the best combination of these new ferroelectric/magnetostrictive materials for the enhancement of the ME effect. The well-known and well-studied magnetostrictive systems are spinel ferrites, e.g., cobalt ferrite and nickel ferrite. Usually, they are used in their unmodified form. However, there are certain reports in literature about the enhancement of their magnetostrictive properties by doping/modifying them with non-magnetic cations like Al^{3+}, Ga^{3+}, Zn^{2+} etc. Hence it is possible to form new sintered composites which might consist of lead-free piezoelectric systems of significantly better properties than pure $BaTiO_3$ and improved magnetostrictive ferrites. This would result in enhanced ME coupling.

3. Materials science and solid state physics literature is replete with the synthesis and magnetoelectric characterization of two-phase sintered composites. However, little information is available on the structure-property relationships. For example, there are not so many articles available which show how the connectivity varies when the contents of both phases are altered and how does this affect the ME coupling. Moreover, there are not many reports which combine dielectric and magnetoelectric studies on these composites. For example, a study can be conducted to show the possible impact of electric permittivity of each phase on ME response of the com-

posites. It is not known to-date what kind of parameters influence the temperature dependence of ME coupling, especially when the piezoelectric component contains the PPB.

4. Electric control of magnetization, the converse ME effect, which has been measured extensively in thin film heterostructures, has not been explored that much in bulk ceramics. This dissertation will report on the converse ME coupling in bulk composites, measured with a modified super-conducting quantum interference device (SQUID).

5. There is some research avenue available in strain-mediated multiferroic thin films in which studies can show how the manipulation of the existing materials by altering their geometries/interfaces in shape of thin films would affect the ME coupling. The greatest challenge is substrate clamping in these thin film structures, which limits their strain-related properties like piezoelectricity and ME coupling. A wealth of knowledge is available on $BaTiO_3$-$CoFe_2O_4$ thin films. It is believed that there are some missing pieces of information, for example, it is needed to be seen whether or not there is an impact of changing the growth-orientations of the perovskite substrates on magnetoelectric features of bi-layered heterostructures comprising of CFO and BTO. A study in this direction may lead to new physics and improved ME coupling.

Chapter 2

Overview of Experimental Techniques

2.1 Sample Synthesis Techniques

Two main sample synthesis techniques were employed, one for the preparation of bulk ceramic samples (for 3-3 connectivity) and pulsed laser deposition for the 2-2 connectivity. Both of these techniques will be described in detail as follows:

2.1.1 Solid State Synthesis

Any chemical reaction which involves the preparation of powders that react in their solid form to result in products is known as solid-state synthesis[1]. The simplest process is shown in the flowchart in Fig. 2.1. The first step is the mixing of commercially available powders in stoichiometric ratios and then the homogenization step of the mixture. This is followed by heating the mixture of powders to elevated temperatures for ceratin time periods, the step known as calcination. The calcination step is the phase formation step, the phase checked by X-ray diffraction. The product of calcination is milled to get a fine powder. It is followed by the consolidation/pressing of the powder, afterward binding to form the desired green body, then firing the green body at elevated temperatures to form the dense ceramics.

2.1.1.1 Stoichiometric Mixing of Powders

Mostly the synthesis process initiates from a set of powders, obtained mostly from commercial resources. The purity of these commercial powders is a key to get high purity end-products. The actual starting point is a chemical equation involving powders to be mixed (called reactants) on the left-hand-side of the equation and the end-products on the right-hand-side. The chemical equation must be balanced concerning the molar masses of reactants and products. Details of some of the raw powders are given in Table 2.1. The molar masses of the reactants obtained as a result of this balancing is mixed and homogenized. The mixing is usually done in some organic liquid like acetone or ethanol,

[1]The most of the discussion in this section about calcination and sintering is based on the knowledge from the books of M.N. Rahaman[188,189] and S. J. L. Kang.[190]

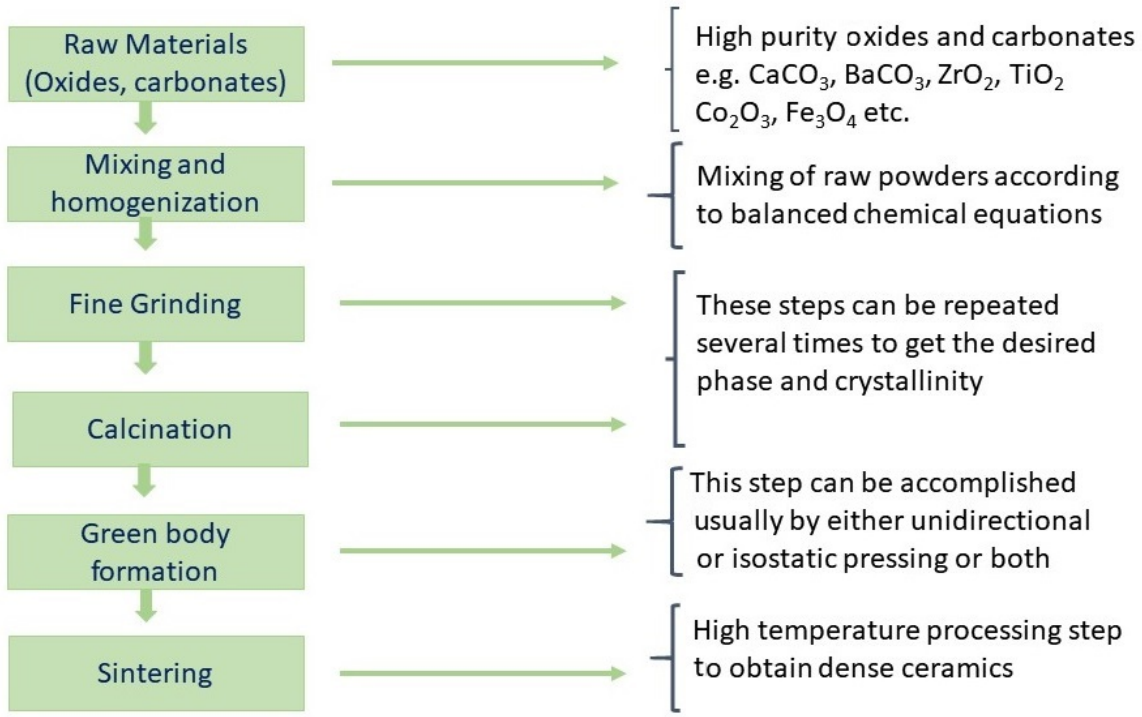

Figure 2.1: Schematic representation of the main steps involved in a solid state synthesis of polycrystalline samples.

and it is followed by a fine grinding step in a rotary ball-mill for a period of time. The resultant mixture is dried in air for an extended period to remove the solvent.

Table 2.1: Details of some of the raw materials used for the solid-state reaction.

Chemicals	**Formula**	**Purity**	**Mol. Wt.**	**Supplier**
Calcium Carbonate	$CaCO_3$	$>$ 99 %	100.08 g/mol	Avonchem
Barium Carbonate	$BaCO_3$	$>$ 99 %	197.35 g/mol	Avonchem
Titanium (IV) Oxide	TiO_2	99 %	79.87 g/mol	Riedel-de Haën
Zirconium (IV) Oxide	ZrO_2	$>$ 99 %	123.22 g/mol	Fluka
Tin Oxide	SnO_2	99 %	150.71 g/mol	Sigma-Aldrich
Cobalt (II-III) Oxide	Co_3O_4	99.9 %	240.79 g/mol	Fluka
Iron (III) Oxide	Fe_2O_3	99 %	159.69 g/mol	Sigma-Aldrich
Nickel Oxide	NiO		74.69 g/mol	Fluka

2.1.1.2 Calcination

The process which involves the decomposition of the solid reactants and, as a result, a real chemical reaction occurring between them, is known as calcination. For inorganic oxides and carbonates, it is usually obtainable at high temperatures. In case of carbonates, it results in its decomposition to simple oxides plus carbon dioxide. For example, the chemical decomposition of calcium carbonate results in calcium oxide and carbon dioxide.

$$CaCO_3(s) \xrightarrow{\text{Heat}} CaO\,(s) + CO_2(g)$$

The calcination products are usually agglomerates which need to be ground fine for the next step. The phase formation is verified at this stage with the X-ray diffraction technique.

The following balanced chemical equations were used to calculate the stoichiometric ratios of the raw materials:

- xBCT-BZT:

$$(1\text{-}x)BaCO_3 + xCaCO_3 + (1\text{-}y)TiO_2 + yZrO_2 \xrightarrow{\text{Heat}} (Ba_{1\text{-}x}Ca_x)(Ti_{1\text{-}y}Zr_y)O_3 + CO_2$$

- $CoFe_2O_4$:

$$3\,Fe_2O_3 + Co_3O_4 \xrightarrow{\text{Heat}} 3\,CoFe_2O_4 + 0.5\,O_2$$

- $Co(Fe_{1.5}Al_{0.5})O_4$:

$$9\,Fe_2O_3 + 4\,Co_3O_4 + 3\,Al_2O_3 \xrightarrow{\text{Heat}} 12\,Co(Fe_{1.5}Al_{0.5})O_4 + 2\,O_2$$

- $NiFe_2O_4$:

$$Fe_2O_3 + NiO \xrightarrow{\text{Heat}} NiFe_2O_4$$

2.1.1.3 Consolidation and Debinding Process

The consolidation is usually achieved via the standard procedure of die pressing of the powders obtained in the last step of mixing. Steel dies are used to highly compress the powder for 4-5 minutes. Sometimes it requires a binder like the aqueous solution of polyvinyl alcohol (PVA) (4g/100ml solution) in small quantity for the compaction of powders under stress. If a binder is used, then the green bodies are needed to be debinded at certain temperatures like 500 ℃ to burn out this binder.

2.1.1.4 Sintering of Green Bodies

This is the last step of the ceramic synthesis. The green bodies obtained in the previous step are transferred to a high-temperature furnace where they are heated to elevated temperatures to get the desired microstructure. This step has a key significance for the *densification* of the solid. Although the detail is quite complex, the driving force behind the sintering process is the reduction in surface free energy of the consolidated mass of particles. This reduction in energy is usually attained by atom diffusion processes which result in either densification of the body or *coarsening* of the microstructure. The densification is characterized by the transport of matter from inside the grains into the

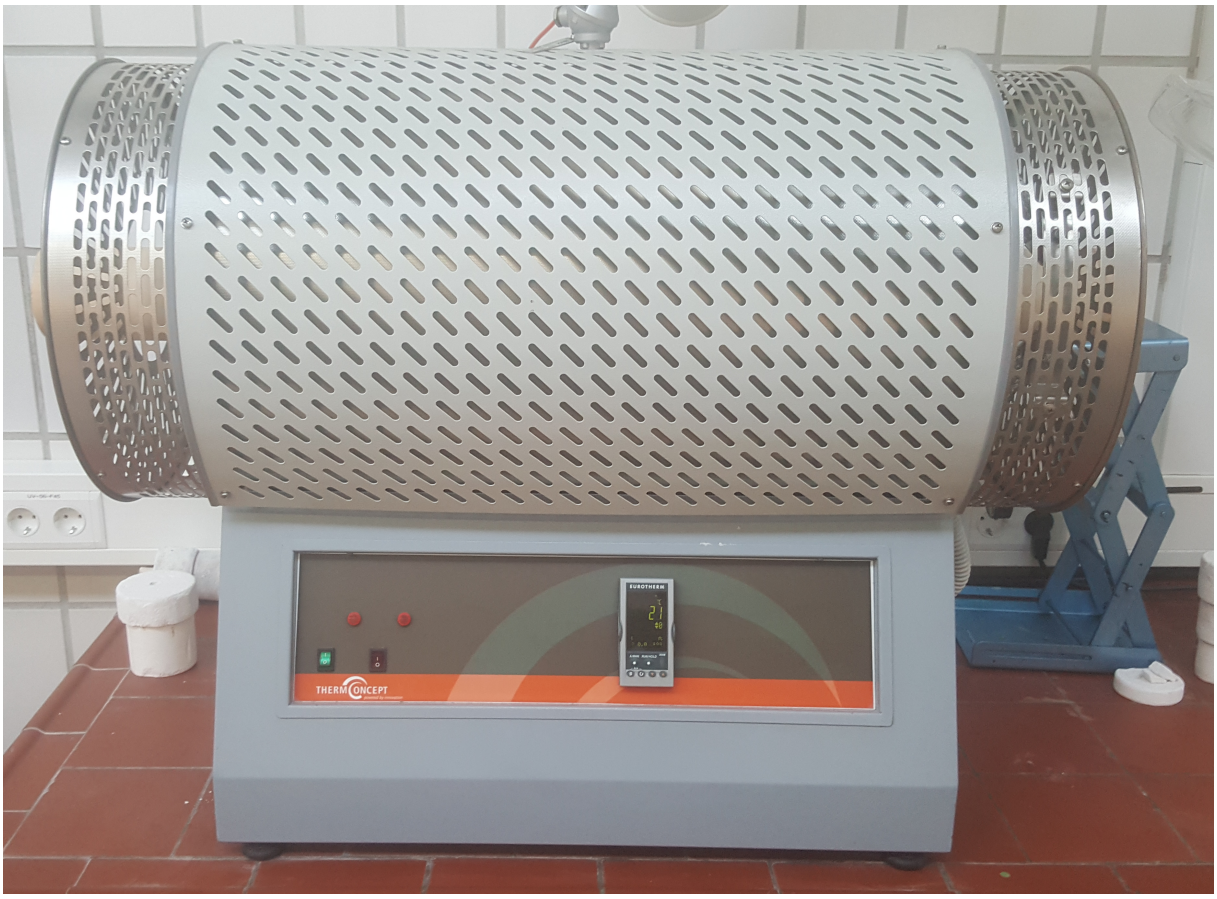

Figure 2.2: Tube furnace used for calcination and sintering of the polycrystalline samples.

pores while coarsening is marked by the redistribution of matter between different parts of the pore surfaces without actually leading to a decrease in the pore volume.

The protocols that were followed for the calcination and sintering of different compounds used in this thesis are depicted in Fig. 2.3. Two steps were usually required for calcination of BCT50-BZT and one step of calcination for ferrites, and one step for the sintering of the composites. Calcination and Sintering of all samples was done in a ThermConcept® tube-furnace (Fig. 2.2) which has a maximum temperature capability of 1500 ℃.

2.1.1.5 Density Determination

The Archimedes method was employed for density measurements of sintered samples of each composition with the Sartorius® Density Determination Kit. The dry weight of as-sintered ceramic discs (W_{air}) was measured. The samples were weighed in distilled water (W_{water}). The absolute density of each sample (ρ_{exp}) was calculated using the following formula:

$$\rho_{exp} = \frac{W_{air} \cdot \rho_{water}}{W_{air} - W_{water}}, \tag{2.1}$$

where ρ_{water} is the density of water used during the measurements. The theoretical density of the composites was determined from the volume and mass of the unit cells of each phase. The theoretical density of CFO was calculated as follows: The molecular weight of CFO is 234.63 g, and a spinel ferrite has eight formula units per unit cell. Therefore the molecular weight of one cell is 8 × (234.63) = 1877.04 g. The edge length of CFO was determined from the XRD analysis which is for example 8.34 Å, and thus its volume is $[(8.38)^3 \cdot A]$ where A is Avogadro's number (6.023×10^{23}), so the volume V is: V = $(6.022 \times 10^{23})(588.48 \times 10^{-24})$ = 354.44 cm^3 and thus
$\rho_{CFO} = mass/volume$ = 1877.04/354.44 = 5.2957 g/cm^3.

Similarly for the BCT50-BZT sample, for example in orthorhombic phase, its unit cell volume is 77.38 $Å^3$, and its molar mass is 266.9475 g. Hence its theoretical density is
$\rho_{BCT50-BZT}$ = 266.9475/[77.38 × 10^{-24} cm^3][6.022 × 10^{23}] = 5.74 g/cm^3.
Overall, the theoretical density of composites (ρ^{th}_{comp}) consisting of both BCT50-BZT and CFO was determined using
ρ^{th}_{comp} = (vol. fraction of BCT50-BZT × $\rho_{BCT50-BZT}$) + (vol. fraction of CFO × ρ_{CFO})
Moreover, after the determination of experimental and theoretical densities, the relative density (%) of the composite was determined using:

$$RTD(\%) = \frac{\rho_{exp}}{\rho^{th}_{comp}} \times 100 \tag{2.2}$$

All composite samples reported in the current study had relative theoretical densities between 90 - 94 %.

2.1.2 Pulsed laser deposition (PLD)

Pulsed laser deposition (PLD) is one of the finest methods to grow high-quality functional oxide thin films, and it is widely used for new material exploration.[191] The pulsed laser deposition, sometimes also called pulsed laser ablation, is a physical vapor deposition process. It consists of a process in which a high-energy laser is made to strike a ceramic target of the desired composition. This ablates the target and produces a plasma plume of the material. The target surface remains approximately perpendicular to the substrate surface, and a film starts to grow. Similar to the other growth processes, the substrate is pre-heated to ensure uniform growth of the film. The simplest schematic diagram for PLD is shown in the Fig. 2.4.
The process starts out in a vacuum chamber with pressures ranging from 10^{-6} mbar to 10^{-10} mbar as base pressure. However, it is then fed in with a background gas to improve stoichiometry of the film to be grown (i.e., in the case of oxides a background pressure of oxygen is used). The ability to use such background gas is one of PLD key benefits over other methods.

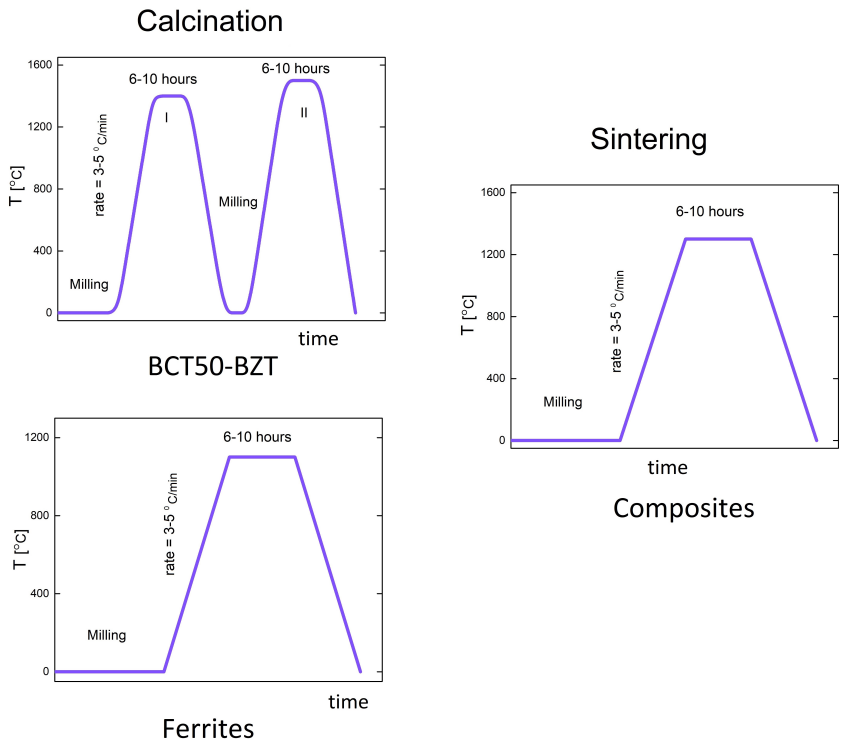

Figure 2.3: Schematic representation of the steps involved in the calcination of powders and the sintering of the ceramics.

The precise control of the stoichiometry of the PLD deposited films is linked with the utilization of the bulk target with the desired composition. This makes it superior to techniques such as molecular beam epitaxy (MBE) where the composition has to be produced by controlling the ratio of the different species arriving on the substrate. Moreover, the typical PLD deposition rate (10 Å/s) is higher than techniques (3 Å/s for MBE) with competing control over stoichiometry. PLD can be used to deposit a broad range of materials including metals, semiconductors, borides, carbides, nitrides, oxides. Many of these can be grown in multilayers, making PLD a versatile technique. The capability of PLD to operate under high background pressure of reactive gases is probably its best feature.

2.1.2.1 Film Growth Mechanisms involved in Pulsed Laser Deposition

The process of pulsed laser ablation growth of materials is quite complex. A laser pulse ablates several different types of species from the target surface including many atoms, ions, and molecules. When these species reach the substrate surface, several processes may occur. The particles are either elastically reflected or captured on the sample by transferring their kinetic energy to the surface molecules. If captured, the particles are subject to desorption and adsorption, diffusion on the surface, and finally, they become a part of the film. As a result of these processes, the film grows. Four different types of thin film growth modes can be easily recognized, depending on the factors: *the free energies*

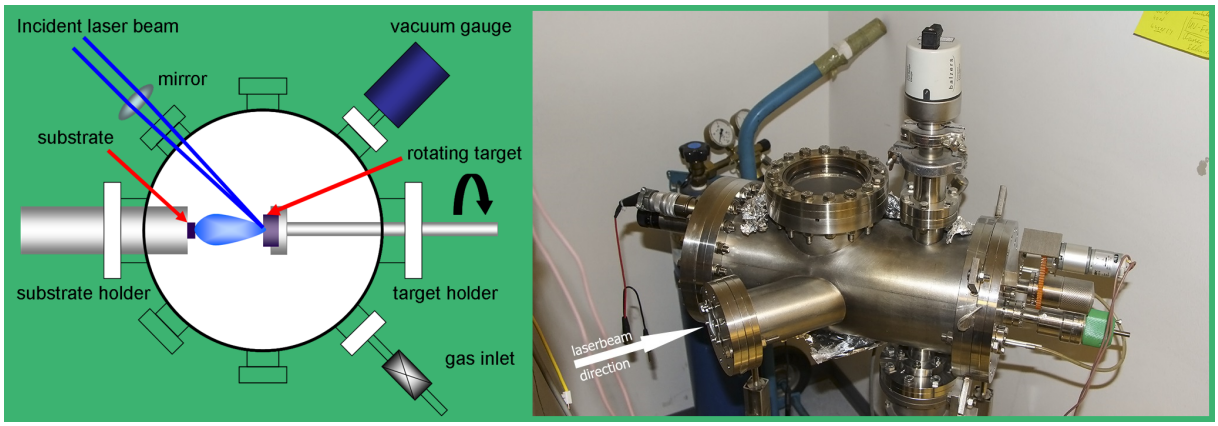

Figure 2.4: A pulsed-laser deposition chamber schematic diagram, adapted from Kai Wang[192] and the actual chamber used during current study.

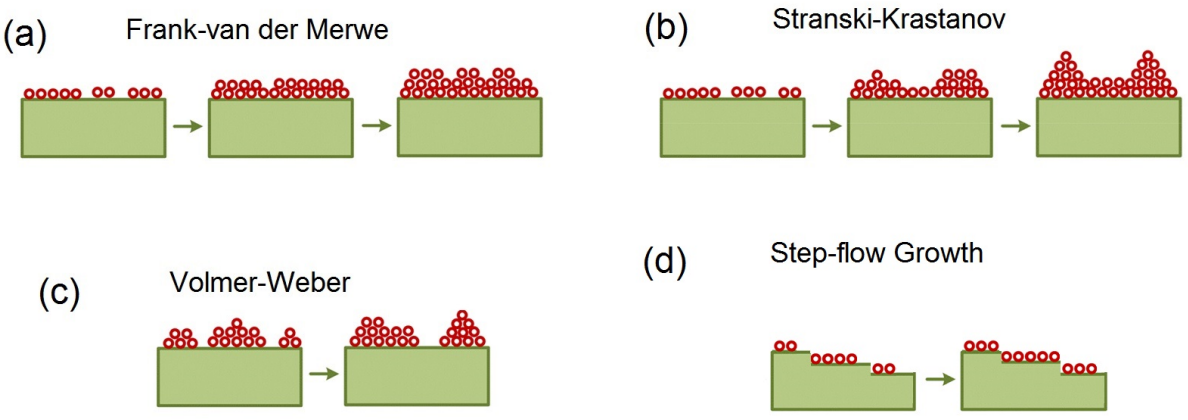

Figure 2.5: Various Thin film growth mechanisms are elaborated, the figure is adapted from Le *et al.*[193]

of the substrate surface, the film surface, and the film-substrate interface.
The four modes are:

1. **Frank-van der Merwe growth** which occurs if the total free energy of the film surface and the interface is lower than the free energy of the substrate.[194] This mode is also known as layer by layer growth mode and is shown in Fig. 2.5(a).

2. **Volmer-Weber growth** occurs due to the weak bonding between substrate and film, and hence enlarging the interface area yields no gain in free energy.[195] In this case, distinct three-dimensional islands will grow coalesce (Fig. 2.5(c)).

3. **Stranski-Krastanov growth** is the intermediate between layer growth and the island growth modes. At first, some continuous mono-layers grow, which are followed by the growth of discrete islands[196] (Fig. 2.5(b)).

4. **Step-flow growth** occurs due to fast diffusion of atoms on a terrace. The absorbed atoms move to step edges rather than nucleating on the surface (Fig. 2.5(d)).

The growth modes described regarding thermodynamic considerations above are only the limiting cases. Several other factors might also play a very crucial role which includes substrate temperature, background gas pressure, and nucleation density of particles on the sample surface. So in some cases, all of the above growth modes might coexist for the same film. For hetero-epitaxial growth, the crystallographic mismatch between film and substrate is also an important factor. The elastic energy may increase with increasing thickness due to this mismatch, which may lead to cracks or dislocation formation at the interface of layers to release the strain.

2.2 Sample Characterization Techniques

2.2.1 X-ray Diffractometry

X-ray diffractometry, commonly known as XRD, is a swift analytic technique for the phase identification of crystalline materials, whether in single crystal or polycrystalline form. It brings out information mainly about the unit cell dimensions. The technique is based on constructive interference of monochromatic X-rays and a crystalline sample. The source of X-rays is a cathode ray tube, fitted with filters to produce monochromatic radiation, and a collimator to concentrate on the sample surface. The interaction of diffracted rays from the sample produces constructive interference whenever it satisfies the famous Bragg's law: $n\lambda = 2dsin\theta$. Here λ is the X-ray wavelength, θ be the diffraction angle, and d is the lattice spacing. The diffracted rays are detected and counted, by scanning the sample through a range of 2θ angles to cover all possible orientations of randomly oriented crystallites in a polycrystalline sample.

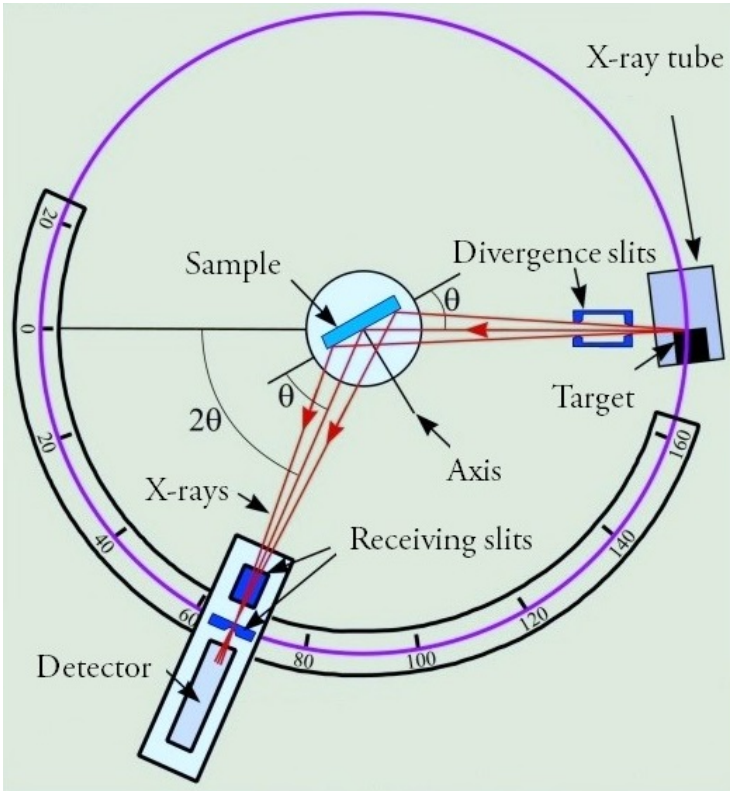

Figure 2.6: Schematic diagram portraying the setup that is used for simple powder diffraction.

All XRD instruments consist of three basic elements: an X-ray tube, a sample holder, and a detector, schematically shown in Fig. 2.6. High energy electrons are produced in cathode ray tube, which are then directed towards a metal target by applying a voltage. The bombardment of these electrons on the metal dislodges electrons from the inner shell electrons, which results in characteristic X-ray spectra. These X-rays are made monochromatic by passing them through crystal monochromators such that only K_α radiations are obtained for diffraction. Copper is the most widely used metal target in laboratory XRD apparatuses with CuK_α radiation of wavelength 1.5418 Å. These X-rays are collimated and directed onto a sample surface, and spectra are obtained as explained earlier. The detector records the x-ray signals and converts them to a count rate. A typical range of 2θ angles in which spectra are taken is 5-90° because most prominent X-ray diffractions in most materials lie in this range.

2.2.1.1 Crystal Structure Determination

Two basic principles involved in crystal structure determination are:

- The crystal structure, i.e., the shape and size of the unit cell define the angular positions of the diffraction lines. An illustration of the position of diffraction lines for some basic unit cells is depicted in Fig. 2.7.

- The arrangement of the atoms within the unit cell lattice determines the relative

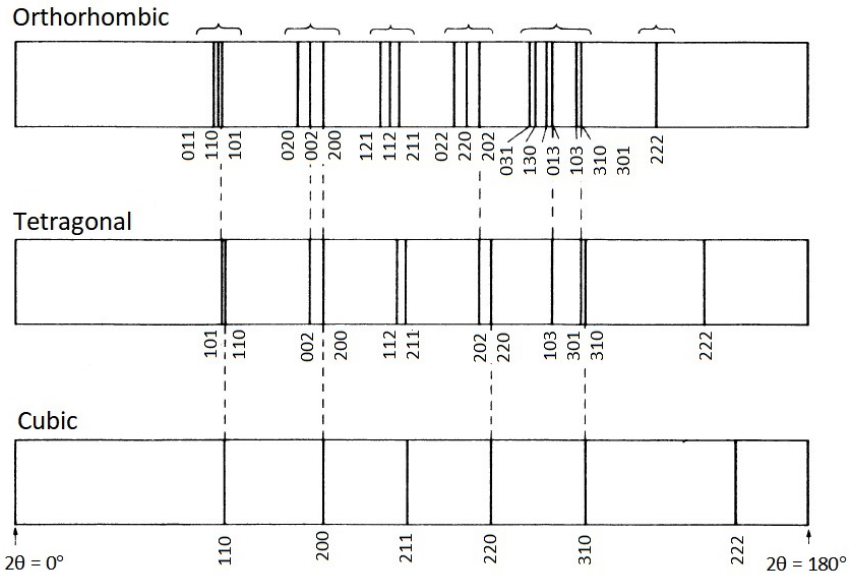

Figure 2.7: Schematic planes corresponding to different unit cells, after B.D.Cullity[197]

intensities of the lines.

The procedure used to determine the crystal structure is the one of trial and error. An educated guess is made by comparing the measured diffraction pattern to previously existing standard basic unit cell patterns. These standard patterns are available in the form of powder diffraction files (PDFs), and structure is assumed based on the close resemblance. In the next step, the corresponding diffraction pattern is calculated, the calculated pattern is compared with the observed one. If the two agree on most of the details, the assumed structure is considered to be correct; otherwise, the process is reiterated as often as is required to find the precise solution. The process of calculation and comparison of crystal structures is usually accomplished via a well-known technique known as "Rietveld refinement".

2.2.1.2 Rietveld Refinement

Rietveld refinement is useful in quantifying the different structural phases present in a sample; to estimate the amount of disorder or mixing of a Wyckoff site (a Wyckoff positions tell us where the atoms in a crystal can be found), and to determine the crystallite size and strains within a sample. Both neutron and X-ray patterns can be refined by this technique. This technique uses a *least squares* approach to refine the theoretical line profile until it matches with the measured one. There are many software programs accessible for the refinement of a crystal structure such as General Structure Analysis System (GSAS), Fullprof, MAUD, and TOPAS. In the current dissertation, all Rietveld refinements were carried out employing GSAS-II.[198]

The least squares fitting approach in Rietveld refinement minimizes the following func-

tion Δ given by:

$$\Delta = \sum_i \omega_i (y^i_{obs} - y^i_{cal})^2 \tag{2.3}$$

where y^i_{obs} and y^i_{cal} are observed and calculated intensities of the ith step while ω_i is weighing factor. For the convergence of the fitting, there are several agreement indices used; the first one is weighted-profile R factor which is defined as:

$$R_{wp}(\%) = \sqrt{\frac{\sum_i \omega_i (y^i_{obs} - y^i_{cal})^2}{\sum_i \omega_i {y^i}^2_{obs}}} \times 100 \tag{2.4}$$

$$= \sqrt{\frac{\Delta}{\sum_i \omega_i {y^i}^2_{obs}}} \times 100 \tag{2.5}$$

This R_{wp} is quite universal, and the summation can be applied to all points i or only to those points where significant diffraction intensity is present. This factor, however, is sensitive to background.

The other R-factor that is crucial for structure determination is the expected R-factor R_{exp}, which essentially deals with the quality of measured data. It is defined in the following way:

$$R_{exp}(\%) = \sqrt{\frac{N - P + C}{\sum_i \omega_i {y^i}^2_{obs}}} \times 100 \tag{2.6}$$

Where is N is the total number of points with significant intensity, P is number of parameters refined, and C is the number of total constraints applied.

The ratio of above two factors R_{wp} and R_{exp} gives the *Goodness of Fit* or χ^2 value:

$$\chi^2 = (R_{wp}/R_{exp})^2 \tag{2.7}$$

While R_{wp} is the most direct parameter for monitoring convergence of the refinement, χ^2 is useful to know whether inadequate fittings are caused by the poor structural parameters (for example a wrong model) or poor instrumental parameters. Some important sample and instruement based parameters for Rietveld refinement are given in Table. 2.2

2.2.2 Scanning Electron Microscopy

Scanning electron microscopy (SEM) is a method used to produce very high-resolution images of a sample surface. A focused electron beam scans a surface to create an image. The most sophisticated optical visualization techniques do not go beyond 250-300 nm (1000x magnification limit) theoretically, SEM is far superior to the traditional optical techniques with a resolution of around 10 nm. The working principle of SEM is illustrated

Table 2.2: Instrument/experiment and sample-based factors which must be taken into account during refinement to get the best agreement between the calculated and experimental models.

	Instrument factors	**Sample based factors**
Peak Positions	Wavelength, zero point error, and sample height	Unit cell dimensions
Peak Shapes	Diffractometer geometry, slit sizes, types of detectors, and X-ray source	Size of crystallites, strain, and defects
Intensities	Amount of the sample, Lorentz polarization and other diffractometer factors	Atomic coordinates, temperature factors, absorption and site occupancies
Background	Air scatter, detectors noise and sample holder	fluorescence and disorder

in Fig. 2.8(b).

The electron gun shown at the top of the image produces an electron beam that is made to focus into a tiny spot of the order of 1 nm in diameter on the sample surface. The sample is scanned by the beam, and the intensities of different signals which are produced by interactions between the electrons and the sample are recorded. These are imaged as variations in brightness on the image display. The most commonly used signal is the secondary electron (SE) signal, however, back-scattered electrons (BSE) are sometimes utilized. Topographically uneven areas on sample surfaces are imaged much like an aerial photograph: edges are bright, recesses are dark.

All of the SEM images reported in this dissertation were taken with an Environmental Scanning Electron Microscope (ESEM, FEI Quanta 400 FEG) as shown in Fig. 2.8(a). This microscope is equipped with a field emission gun, operating at an accelerating voltage variable from 0.5 to 30 kV, with a claimed resolution of 2 nm. The instrument can be used in high vacuum mode (HV) or low-vacuum mode (LV) mode. The instrument is fitted with an EDAX Genesis energy-dispersive X-ray spectrometer for elemental analysis. Qualitative and quantitative analysis, elemental mapping, and line scans can be performed.

2.2.3 Transmission Electron Microscopy (TEM)

TEM is also a sample probing technique based on the interaction of electrons with a sample. However, in contrast to SEM, here electrons go through the sample, so the sample should be thin enough for that purpose. It can be considered as a destructive technique because samples are ground and well thinned before measurement. The thin samples are usually prepared by mechanical polishing, followed by milling with Ar ions. The TEM images shown in the current study were taken by Dr. Markus Heidelmann

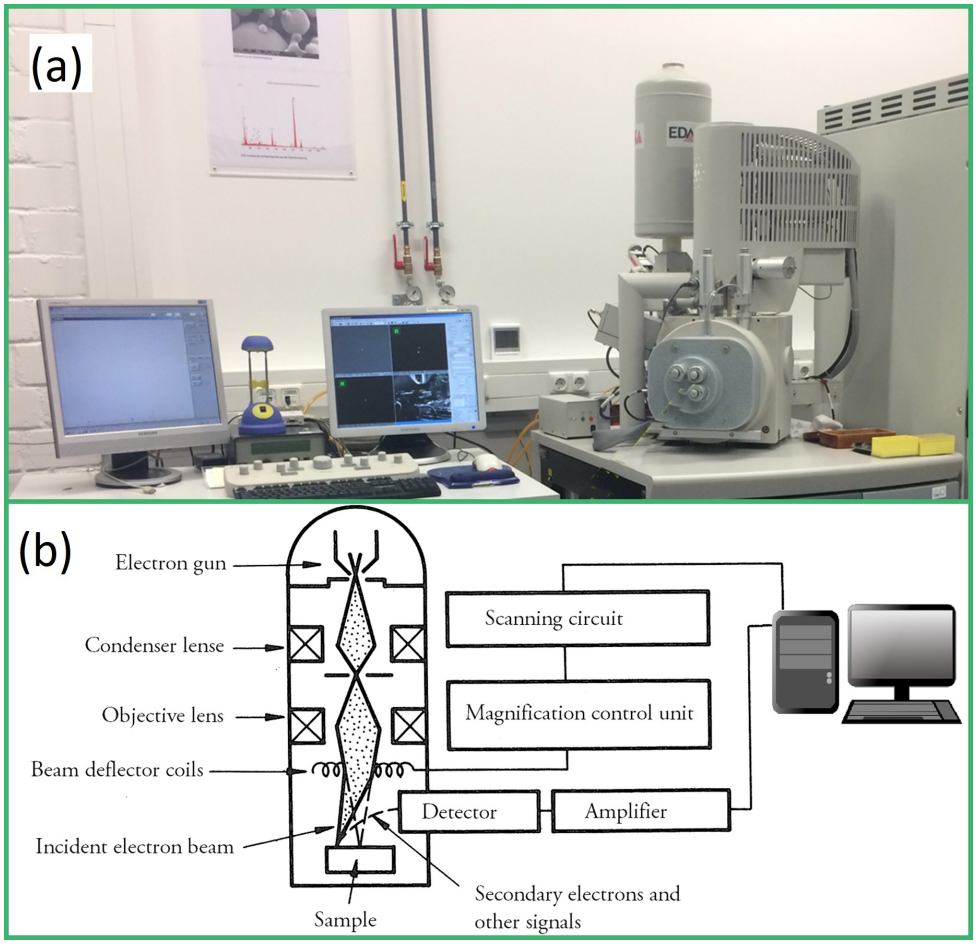

Figure 2.8: (a) FEI Quanta 400 FEG Environmental Scanning Electron Microscope and its schematic diagram in (b).

at NETZ, Universität Duisburg-Essen employing a JEOL 2200FS transmission electron microscope in high-resolution TEM (HRTEM) mode; the author highly acknowledges his support.

2.2.4 Polarization versus Field Hysteresis

A sample with a capacitance C_{sample} was connected in series with a reference capacitor C_{ref}. To minimize the voltage drop V_{ref} at the reference capacitor the condition $C_{ref} >> C_{sample}$ was fulfilled with the difference in the capacitance values of over three orders of magnitude. The reference capacitor was $V_{ref} = 1$ µF. This condition makes sure that V_{ref} remains below 1 % of the voltage drop at the sample V_{sample}. The charge Q of the reference capacitor is equivalent to the sample's charge since both capacitors are in series. A function generator (Agilent Technologies Inc., model 33220A) was used to supply an input signal to a high voltage amplifier (Trek Inc., United States). Triangular waves of some kV amplitude with frequencies between 5 Hz and 100 Hz were used as input signals for the measurements. Data were acquired via an oscilloscope (Tektronix Inc.). The polarization was calculated using Eq. 2.9.

$$Q = C_{sample} \cdot V_{sample} = C_{ref} \cdot V_{ref} \tag{2.8}$$

$$P = \frac{C_{ref} \cdot V_{ref}}{A} \tag{2.9}$$

Where A is the area of the sample. The overall circuit is known as Sawyer-Tower circuit, and its schematic setup is shown in Fig.2.9. The random error in the polarization measurements is on the order of 1 %.

2.2.5 Atomic Force Microscopy

Atomic force microscopy (AFM) is a method to map the topography of a sample by utilizing the interaction between a nanometer-sized probing tip and the sample surface when the two are brought sufficiently close to each other. The cantilever is typically made of silicon or silicon nitride with a tip radius of the order of some nanometers. When the tip is brought into the vicinity of a sample surface then according to Hooke's law, forces between the tip and the sample lead to a deflection of the cantilever. Typical forces that are measured in AFM include mechanical contact force, van der Waals forces, magnetic forces. The AFM has three major capabilities of force measurement, imaging, and manipulation at the nanoscale.

For imaging purposes, the sample is brought into contact with the tip and the sample stage rasters it in the x-y plane (see Fig. 2.10a). An electronic feedback loop is used to keep the probe-sample force constant during scanning. This feedback loop takes the

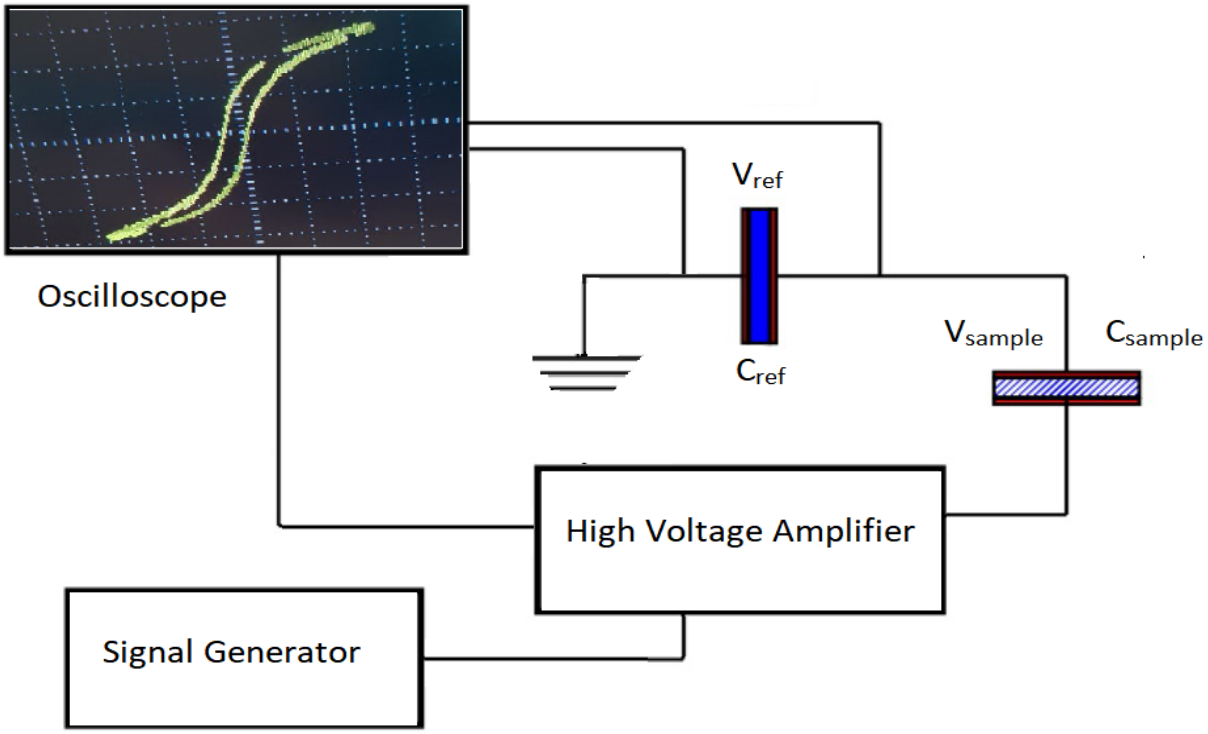

Figure 2.9: Schematic diagram of the Sawyer-Tower circuit used to measure polarization verses electric field hysteresis.

cantilever deflection as its input, and its output controls the distance along the z-axis between the tip and the sample. This force is constant, the sample is scanned in the x-y plane, and the height variations are recorded from the tip deflection. The sole purpose of feedback loops is to keep the cantilever at certain user-defined distance (also known as set-point).

The different modes of AFM operation are contact mode, tapping or intermittent contact mode and the non-contact mode. Normally, low stiffness cantilevers are employed to obtain higher deflections of the tip and also to keep the interaction forces between the sample and the tip to a minimum. The intermittent or tapping mode is useful under ambient conditions or when a sample has a liquid component. The cantilever is vibrated at a constant frequency at or close to its resonance, and at a constant amplitude. When the tip comes near to the sample surface, forces like Van der Waals forces, dipole-dipole interactions, electrostatic forces cause the amplitude of the cantilever's oscillation to change. Here this change in amplitude is used to construct the sample surface. The feedback loop is also used here to keep the amplitude of the cantilever to a certain set-point. In non-contact AFM mode, the tip of the cantilever does not come in contact with the sample surface. The cantilever oscillates at either its resonant frequency (frequency modulation) or just above (amplitude modulation) where the amplitude of oscillation is usually of the order of a few nanometers to a few picometers. Any long-range force that extends

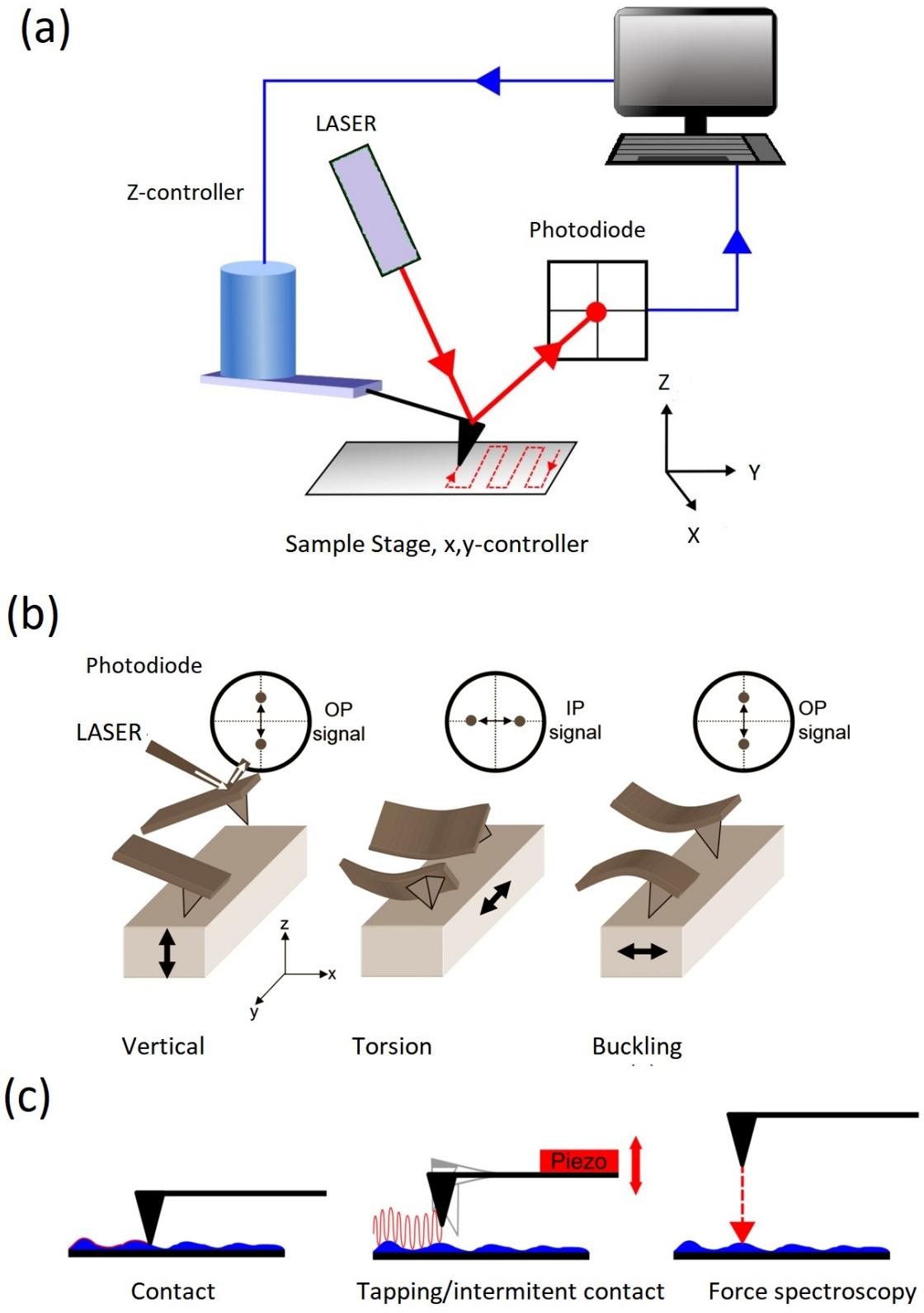

Figure 2.10: Schematic illustration of AFM and a brief working principle, adapted from Nath *et al.*[199]

beyond the sample surface would decrease the amplitude of oscillation, which again in combination with the feedback loop is used to keep the amplitude constant.

2.2.6 Piezoforce-response Microscopy (PFM)

Piezoresponse force microscopy (PFM) is a modification of AFM that allows imaging and manipulation of ferroelectric domains. A sharp conductive tip is brought in contact with a piezoelectric surface and an *ac* bias is applied to the probe tip to stimulate deformation of the sample through the converse piezoelectric effect. The resulting deflection of the cantilever is detected through a standard split photodiode detector and then demodulated by a lock-in amplifier. Thus, topography and ferroelectric domains are imaged simultaneously.

The direct piezoelectric effect from Eq. 1.33 is written (in Voigt notation) as:

$$D_i = d_{ij}\sigma_j, \tag{2.10}$$

in which d_{ij} are the components of direct piezoelectric tensor, and σ_j are the components of the stress tensor. In case of a tetragonal crystal system ($4mm$ symmetry) like $BaTiO_3$, it can be written in matrix form as:[200,201]

$$\begin{bmatrix} D_1 \\ D_2 \\ D_3 \end{bmatrix} = \begin{bmatrix} 0 & 0 & 0 & 0 & d_{15} & 0 \\ 0 & 0 & 0 & d_{24} & 0 & 0 \\ d_{31} & d_{32} & d_{33} & 0 & 0 & 0 \end{bmatrix} \begin{bmatrix} \sigma_1 \\ \sigma_2 \\ \sigma_3 \\ \sigma_4 \\ \sigma_5 \\ \sigma_6 \end{bmatrix} \tag{2.11}$$

The converse piezoelectric effect quantifies the change in shape of piezoelectric materials when an electric field is applied to it. It is given (from Eq. 1.34):

$$e_j = d_{ji}E_j \tag{2.12}$$

In which e_j is the strain tensor, $d_{ji} = d^t_{ij}$ are the elements of converse piezoelectric tensor,

and E_j are the elements of an electric field. In matrix form it is given by:

$$\begin{bmatrix} e_1 \\ e_2 \\ e_3 \\ e_4 \\ e_5 \\ e_6 \end{bmatrix} = \begin{bmatrix} 0 & 0 & d_{31} \\ 0 & 0 & d_{32} = d_{31} \\ 0 & 0 & d_{33} \\ 0 & d_{24} = d_{15} & 0 \\ d_{15} & 0 & 0 \\ 0 & 0 & 0 \end{bmatrix} \begin{bmatrix} E_1 \\ E_2 \\ E_3 \end{bmatrix} \tag{2.13}$$

When E_3 is applied,elongation is in the c-direction ($d_{33} > 0$) and contraction in a and b directions ($d_{31} < 0$) are induced. When E_1 is applied, shear strains are induced ($d_{15} > 0$). PFM uses these deformations to detect domains along with their orientations.

When a *dc* voltage applied to a piezoelectric material, it will produce a displacement, but the piezoelectric tensor coefficients are relatively small at small applied fields so that the physical displacement is small. For example, the value of the d_{33} of $BaTiO_3$ is 85.6 pm/V, which means that a change of length of 85.6 pm is produced upon the application of 1 V. This results in a small deflection of the AFM cantilever and is very difficult to separate it from the environmental noise. To separate the deformation from the environmental noise, a modulation technique is used in which a reference *ac* signal $V(\omega) = V_0 cos(\omega t)$ having a frequency ω and amplitude V_0 is applied to the cantilever so that the deformation of the sample is now:

$$d = d_0 + Dcos(\omega t + \phi) \tag{2.14}$$

where d_0 is the equilibrium position of the cantilever, D is the amplitude of vibration and ϕ is the associated phase. The oscillating deflection is recorded via the photo-diode and converted to an oscillating voltage. A lock-in amplifier is used to demodulate the amplitude and phase of the converse piezoelectric effect induced surface deformation.

The contrast mechanism in PFM images is governed by the fact that the cantilever performs three kinds of displacements as depicted in Fig. 2.10 (b).

- Vertical displacement due to out-of-plane force due to d_{33}^{eff}, also called vertical PFM (VPFM).
- Torsion caused by shear piezoelectric constant d_{15}^{eff}, also known as Lateral PFM (LPFM).
- Buckling from the interaction with the surface.

Another important technique that is utilized in PFM is known as switching spectroscopy PFM (SSPFM) in which the area underneath the PFM tip is switched with simultaneous

acquisition of a hysteresis loop that is analysed to obtain information about the sample properties.[202]

2.2.7 Magnetic Force Microscopy (MFM)

Magnetic force microscopy was invented in the backdrop of the advent of Scanning Tunneling Microscopy (STM) and of Atomic Force Microscopy in the 1980's[43] when Y. Martin and H .K. Wickramasinghe published their pioneering work.[203] The technique was developed extensively, before being available commercially in the early 1990's. It is based on the very definition of magnetism, i.e. the attraction and repulsion between two magnets. A magnetic tip is scanned over or very near the sample surface, and the stray magnetic fields from the surface are detected. The mathematical form of this interaction is given by a force of the form:

$$\vec{F} = \mu_0(\vec{m}_{tip} \cdot \nabla)\vec{H}_{sample} \tag{2.15}$$

where m_{tip} is the magnetic moment of the tip, approximated by a magnetic dipole, $\vec{H}_{sample}$ is the magnetic stray field. Alternatively, it can also be written as:

$$\vec{F} = \mu_0(\vec{H}_{sample} \cdot \nabla)\vec{m}_{tip} \tag{2.16}$$

In integral form, this interaction is given by:

$$E = -\mu_0 \iiint_{tip} M_{tip} \cdot \vec{H}_{sample} \cdot d\tau_{tip} = -\mu_0 \iiint_{sample} M_{sample} \cdot \vec{H}_{tip} \cdot d\tau_{sample} \tag{2.17}$$

As the cantilever tip is scanned over the sample, the sample is subjected to the field of the tip, and vice versa, the tip is subjected to the stray field of the sample, the obvious reason for the equivalence of the above two representations. Equation 2.17 also implies that if the field of the tip is stronger than the field of the sample (magnetically) soft samples, it may seriously perturb it, leading to erroneous MFM results.[204]

The sample preparation is not too tedious, and the magnetic resolution of 30 nm is readily achieved.[43] Its high sensitivity allows easy determination domain configurations in thin films, even below room temperature.

The tip-sample interaction as described above causes some difficulty in the determination of the actual domain structure, as it does not directly take into account the sample magnetization. Due to this, different magnetic patterns may lead to similar domain patterns when measured via MFM. Hence the previous knowledge of the magnetic properties of the sample is crucial for better analysis of the MFM images. So to reduce this effect, the field produced by the tip has to be reduced in order to avoid the disturbance

of sample magnetization. Moreover, it can also be understood from Eq. 2.17 that for samples with the magnetic response, the magnetic signal would also be weak, due to the weak tip-sample interaction. However, this seldom happens in real experiments, where a variety of tips are now commercially available for an almost whole range of magnetic responses.

2.2.8 Time of Flight Secondary Electron Mass Spectroscopy (ToF-SIMS)

The TOF-SIMS abbreviation stands for a technique that is a combination of secondary ion mass spectrometry (SIMS) and a time-of-flight (TOF) mass analysis. The sample is bombarded with primary ions with a kinetic energy of several keV. The ions collide with the surface, thereby giving off their energy and producing a collision cascade. This cascade leads to the elimination of single surface atoms and molecules, or of clusters and fragments. Some of these secondary particles are present as ions and can be analyzed in one by their mass. Due to the high spectral resolution, a very accurate image of the sample surface is obtained. With these methods, a spatial resolution of ~ 60 nm is achieved with a surface sensitivity to the first 1-2 layers of the sample. Depth profiles with a depth accuracy of ~ 1 nm and a measuring speed of up to 10 µm/h can be achieved.

2.2.9 Dielectric Constant Measurements

The low field electric permittivity ($\varepsilon_r = \varepsilon'/\varepsilon_0$) and loss tangent ($tan\delta = \varepsilon''/\varepsilon'$) are among the most important properties of a material. Most of the time, these parameters are measured on electroded discs with the aid of well-engineered commercial instruments such as LCR meters or Impedance Analyzers. Measuring fields are usually kept vanishingly low, well under 1 V/mm.

For good insulators, ε_r does not vary much from *dc* to MHz frequencies. In ferroelectrics, and particularly in poled piezoelectric samples, there is a strong dependency of ε_r on frequency. At small frequencies, non-uniform conductivity produces interfacial polarization which adds to the effective electric permittivity and loss. This effect is intensely frequency dependent. It is not intrinsically associated with ferroelectricity but is commonly encountered in ferroelectrics just as in many other imperfect dielectrics. Dipole relaxation related to impurities and domain wall motion may also contribute to the frequency dependence.

Both LCR meter and Impedance Analyzers are measuring instruments that give out the value of impedance. Impedance, which is expressed as Z^*, indicates resistance to the flow of an *ac* current. Normally, it can be calculated from the current I flowing to the object to be measured, and the voltage V developed across the object's terminals. Since impedance is expressed as a vector on a complex plane; these instruments measure the

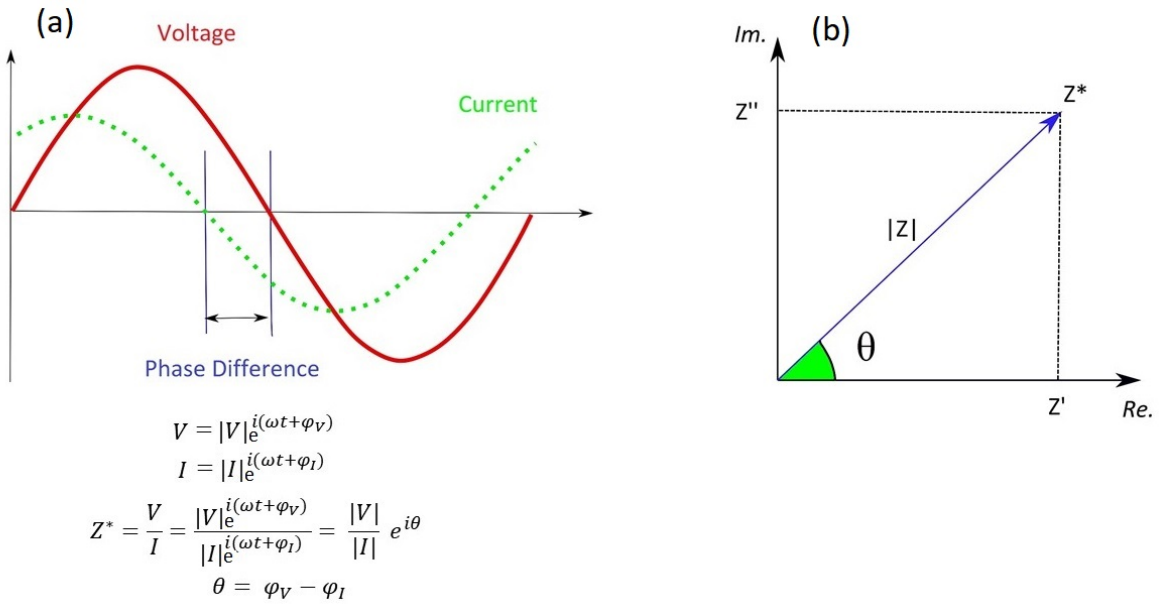

$$V = |V|e^{i(\omega t+\varphi_V)}$$
$$I = |I|e^{i(\omega t+\varphi_I)}$$
$$Z^* = \frac{V}{I} = \frac{|V|e^{i(\omega t+\varphi_V)}}{|I|e^{i(\omega t+\varphi_I)}} = \frac{|V|}{|I|}\, e^{i\theta}$$
$$\theta = \varphi_V - \varphi_I$$

Figure 2.11: (a) The relationship between *ac* voltage and current in a capacitor; (b) An *ac* electric impedance in the complex plane.

ratio of current and voltage RMS values as well as the phase difference between current and voltage waveforms. This is depicted in Fig. 2.11.

From the values of I, V, and θ, the instrument calculates measurement parameters such as C and R from the Z and θ values. The equations used to compute these measurement parameters differ subject to whether the apparatus is functioning in series equivalent circuit manner or parallel equivalent circuit manner. Series equivalent circuit manner implies that capacitance and the resistance component are treated as they are linked in series, while parallel equivalent circuit mode assumes these are connected in parallel. Usually, the series equivalent circuit mode is employed for measuring low-impedance elements (with an impedance of approximately 100 Ω or less) such as high-capacitance capacitors, whereas parallel equivalent circuit mode is used when measuring high-impedance elements (impedance ~ 10 kΩ or more) such as low-capacitance capacitors.

For the electric permittivity of the samples, a Solarton Impedance Analyzer with temperature control was used. The setup is schematically illustrated in Fig. 2.12. Circular disk-shaped ceramic samples were painted with silver paste to make electrodes and heated to 400 ℃ to dry. Electric permittivity was measured in the temperature range 300-440 K with an electric field frequency in the range from 1Hz - 1MHz.

2.2.10 Magnetic measurements

A superconducting Quantum Interference Device (SQUID) magnetometer was employed for the usual magnetic measurements ($M(H)$ hysteresis). SQUID is one of the most sensitive instruments (sensitivity of 10^{-18} Tesla) used for magnetization measure-

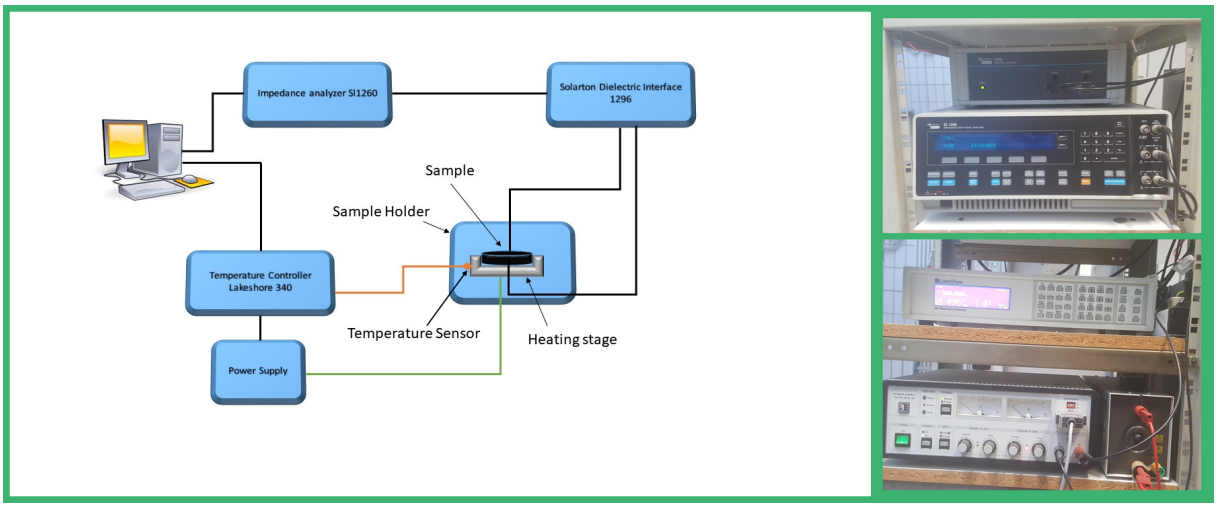

Figure 2.12: Schematic diagram of a dielectric measurement setup used in the current thesis for temperature range of 300-450 K and Solarton Impedance Analyzer with temperature control.

ments. The most important part of a SQUID device is a Josephson tunnel junction, which consists of two superconducting materials separated by thin insulating layers to form two parallel Josephson junctions.

The extraordinary sensitivity of SQUID is associated with its ability to record changes in magnetic field associated with one quantum of magnetic flux. One flux quantum is simply $\phi_0 = 2\pi\hbar/2e = 2.068 \times 10^{-15}$ Tesla.m^2. In a *dc* Josephson junction in the absence of any magnetic field, the bias current is equally divided between the two branches. As soon as a small magnetic field is applied, a small screening current I_{SC} starts to flow whose direction is the same as one of the junctions (total current $= I/2 - I_{SC}$) and opposite to the other one (total current $= I/2 - I_{SC}$). Now if the external flux is increased to one-half of the flux quantum ($\phi_0/2$), the SQUID, in this case, prefers to increase it to one flux quantum. Resultantly, the screening current changes direction whenever there is a change in flux equal to one-half of the amount of flux quantum. Thus one complete cycle of voltage implies one quantum of magnetic flux change. For $M(H)$ measurements, samples were either used in powder form inside a gelatin tube or pellet form. Two kinds of magnetic measurements were conducted, as a function of DC magnetic field at some fixed values of temperature ($M(H)$ loops), and temperature variation of zero-field cooled (ZFC) and field-cooled (FC) $M(T)$ measurements.

2.2.11 Direct Magnetoelectric Measurements

2.2.11.1 Electrical poling of the samples

To measure the ME coupling of a composite, it had to be poled electrically to optimize its piezoelectric character. The procedure is as follows: The sample was heated up in a silicone oil bath to a temperature in the range 80 - 100 ℃ (just above the Curie temperature) depending upon the ferrite content, because more ferrite content sometimes causes

a voltage drop at these temperatures. The resistances of the samples varied form 2 GΩ (for the highest ferrite content) to 12 GΩ for the lowest one. The external electric field was applied, which was also not the same for all samples, (5 - 8 kV/cm), at a maximum temperature and it was kept for 15 minutes. Afterward it was cooled to room temperature in this field at a rate of about 3 ℃/minute.

2.2.11.2 ME Measurements

The direct ME effect can be measured via three usual methods:

- In the static method in which a uniform *dc* magnetic field is applied and the voltage developed across the sample electrodes is measured. Thus, point by point application of different static magnetic fields gives an estimate of the magnetic dependence of ME coupling.
- In the quasi-static method a magnetic field is slowly varied in time, and the corresponding response is measured as the induced voltage. The typical rate of magnetic field variation is around 0.05 - 0.5 T/min.
- In the dynamic method an *ac* magnetic field with a frequency f and amplitude δH is applied to a sample in conjunction with a large *dc* magnetic field. An *ac* voltage is induced across the sample electrodes which is measured via a lock-in amplifier. The induced voltage is recorded as a function of applied *dc* magnetic field or the frequency of *ac* magnetic field.

Both direct and converse ME couplings are measured in two configurations which depend on the mutual orientations of polarization, electric field, and magnetic field. One configuration is the transverse configuration (also known as α_{31}) as shown in Fig. 2.13(a). In this configuration, the applied magnetic field is parallel to the sample surface, and the polarization direction is perpendicular to the sample surface. The second one is the longitudinal configuration (α_{33}) where the specimen surface is placed perpendicular to the applied magnetic field and electrical polarization as shown in Fig. 2.13(b).
All the direct and converse measurements on bulk ceramics reported in the current dissertation were performed in longitudinal configuration, because the transverse configuration results in a lower ME coupling[205] The direct ME measurements reported carried out in dynamic mode using the following setup.[206]
The samples were positioned in the middle of a plastic box comprising of a Helmholtz coil capable of generating *ac* magnetic fields with amplitudes δH of up to 100 Oe. A *dc* magnetic bias field in the range of 0 - 15 kOe was generated by an external electromagnet (Bruker ESP 300E) collinear with the Helmholtz coil and directed along the Z direction. This bias field is stabilized by a Hall-sensor-based regulating feedback loop.

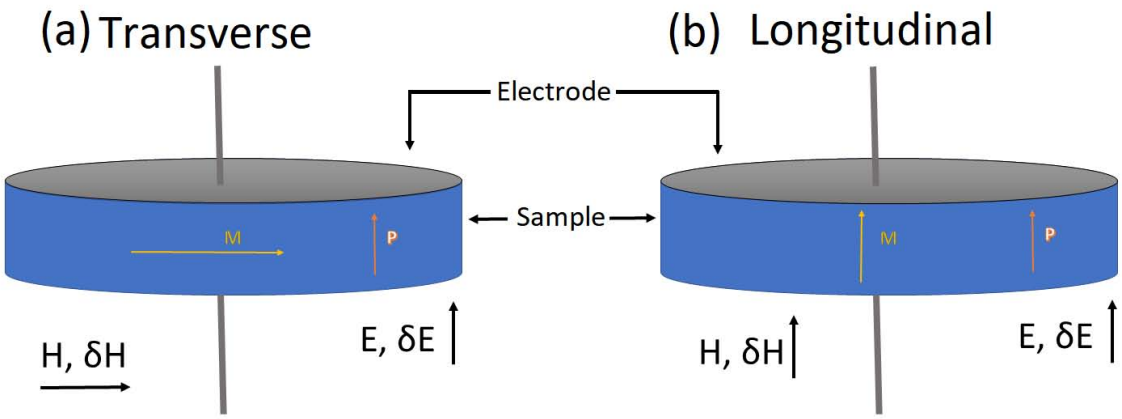

Figure 2.13: Configurations used during the measurement of direct and converse ME coupling; (a) Transverse (b) Longitudinal.

The Helmholtz coil is driven by a power amplifier (AE Techron, model 7224) with a gain between 1 and 20 and low output impedance (28 mΩ in series with 1 μH). The current flowing through the coil is stabilized by a current control loop. The amplitude and frequency of the *ac* current are set either by an external function generator (SRS, model DS345) or by the internal generator of the lock-in amplifier (Zurich Instruments model HF2LI). The AC current passing through the Helmholtz coil is continuously measured by a multimeter (Agilent, model 34401A), which is then utilized to compute the earlier calibrated magnetic field. The direct ME coefficient is calculated using the following formula $\alpha_E = \partial E/\partial H = \delta V/(\delta H \cdot t)$ where t is the thickness of the sample. α_E has units of (mV/cm.Oe). A schematic diagram is presented in Fig. 2.14. An important point here is that lock-in amplifiers have an input impedance in the range of 1 to 10 MΩ, and to achieve the condition of open-circuit, a high input impedance pre-amplifier is used.

2.2.12 Converse Magnetoelectric Measurements

Converse ME effect, also known as ME susceptibility is given by:

$$\mu_0 M = \alpha_c E \tag{2.18}$$

The converse ME was measured in a modified-SQUID setup[208] (Quantum Design MPMS5S) which is capable of applying a *dc* magnetic field up to 5 T.

The ME susceptibility was measured by applying an *ac* electric field to the sample in parallel-plate capacitor geometry. The sample was inserted into the SQUID magnetometer, fixed between two Teflon membranes in a plastic straw. The induced moment $m = m'cos\omega t + m''sin\omega t$ was detected via the pickup coil inside the SQUID setup. The value of the converse ME coefficient was obtained from the slope of induced moment versus

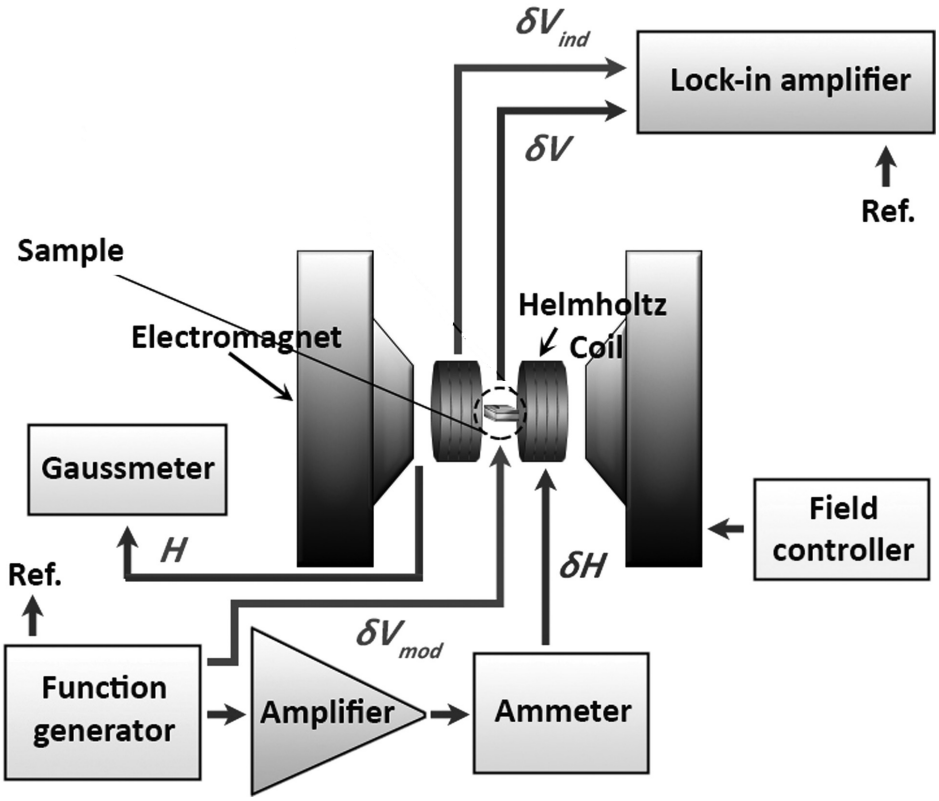

Figure 2.14: Schematic diagram of direct ME measurements setup,[207] the figure was reused with permission from ©2013 AIP Publishing LLC.

applied *ac* electric field amplitude. The setup is illustrated schematically in Fig.2.15

There are two kinds of problems when the ME coefficient is measured by applying an *ac* electric field:

- The first one is the stray pickup, the voltages that are induced in the pick-up coil due to the *ac* current flowing through the capacitor-shaped sample (Faraday's induction).[209]
- The stray capacitance present between the sample electrodes and the pickup coil.

The first issue was taken into account automatically via two-point measurement that is an essential part of SQUID measurement setup. Moreover, it is always advisable to use a low number of turns on the pickup coil (4 in this case) and low frequency of applied *ac* electric field (1 - 10 Hz in this case) to avoid both of the effects mentioned above.

2.2.13 Magnetodielectric Measurements

For low-temperature measurements, the sample was mounted on a brass sample holder with dimensions 16 × 13 mm^2 and was attached to the top end of the cold finger of the closed cycle refrigerator (Janis CS-335), with an electrical insulation of mica. An LCR meter (Wayne-Kerr 4275) was employed for the measurement of capacitance and

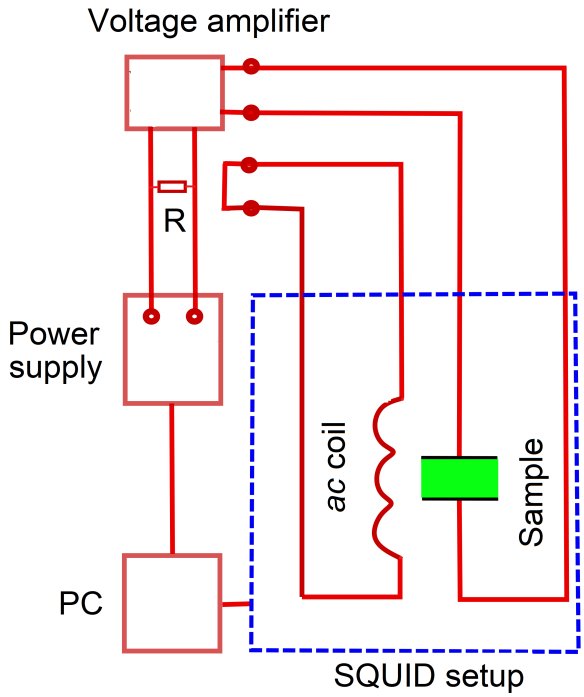

Figure 2.15: Modified super-conducting quantum interference device (SQUID) for converse ME measurements, adapted from Borisov *et al.*[208]

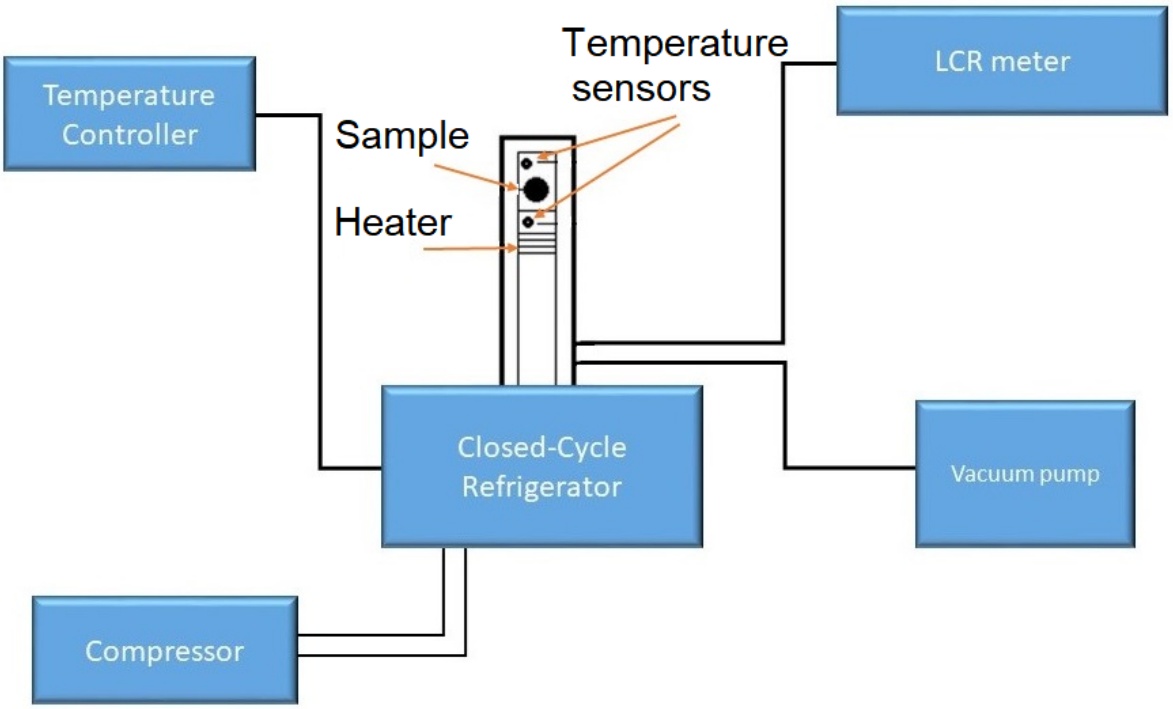

Figure 2.16: Schematic diagram of low-temperature electric permittivity measurement setup.

dissipation factor, via two copper wires attached to the sample via silver paste. A *dc* magnetic field was applied from an external electromagnet in longitudinal configuration as shown for the case of ME measurement setup in Fig. 2.13. A helium-based cryostat was used to cool the sample from room temperature down to 10 K, sample heating and cooling rates were controlled by a temperature controller (Lakeshore 331). Two sensor inputs were used for the temperature controller, the sensors being TG-120-CU GaAlAs diode thermometers. A 25 Ω heater was attached to the cold finger to regulate the temperature. One of the sensors was attached to the cold finger while the other one to the sample. Before cool-down, the refrigerator shroud was evacuated down to 1.0×10^{-4} torr using a diffusion pump for greater insulation, and resultantly shorter cool-down times. A schematic diagram of the setup (without the *dc* magnet) is shown in Fig. 2.16.

Chapter 3

Converse Magnetoelectric Effect in BCZT-CFO Composites

This chapter is divided into three main parts:
In the first part of this chapter, the synthesis and characterization of a new multiferroic magnetoelectric composite $[(Ba,Ca)(Zr,Ti)O_3]_{0.85}$-$[CoFe_2O_4]_{0.15}$ ($BCZT_{85}$-CFO_{15}) are presented. Electric permittivity data was analyzed in full detail to elucidate the relationship between microstructure and electric properties. Microscopy techniques such as PFM and MFM were utilized for the local scale study of ferroelectric and magnetic features. The converse magnetoelectric effect was explored in full detail. The sample was found to possess a good value of converse magnetoelectric coefficient.
Further ME composites were also formed with increasing the volume percentage of cobalt ferrite, however, the converse ME coupling was not increased. To circumvent this problem in these composites a new strategy of enhancing the magnetostrictive properties of CFO was devised by its modification with Al^{3+}. The second part thus deals with the comparison of structural and magnetic properties of $CoFe_2O_4$ and $Co(Fe_{1.5}Al_{0.5})O_4$.
The third portion of this chapter deals with the comparison between the properties of multiferroic composites, one $BCZT_{50}$-$(CoFe_2O_4)_{50}$ and the other being $BCZT_{50}$-$(CoFe_{1.5}Al_{0.5}O_4)_{50}$. Structural, polarization, magnetic, and magnetoelectric properties were measured independently then compared and contrasted to elucidate the effect of Al^{3+}-modification of the ME coupling of the composite.[1]

3.1 Converse Magnetoelectric Effect in $BCZT_{85}$-CFO_{15} System

3.1.1 Background and Motivation

Lead-free piezoelectric (Ba, Ca)(Zr, Ti)O_3 have been reported to exhibit piezoelectric properties similar to the conventionally used Pb(Zr, Ti)O_3 materials, and have therefore

[1]The work reported in this chapter also appeared in the form of two peer-reviewed articles published in Scientific Reports 2016[210] and Journal of Materials Science 2017.[211] Full-text permission was obtained to reuse any materials like figures and tables from the respective publishers.

been attracting much attention as potential replacements for lead-based piezoceramics. In that regard, the discovery of a large electromechanical response found at room temperature in the (1-x)$Ba(Zr_{0.2}Ti_{0.8})O_3$-$x(Ba_{0.7}Ca_{0.3})TiO_3$ solid solutions with $x = 0.50$,[187] denoted as BCZT in this thesis, is a key driving force. Its properties are compared with different present-day piezoelectrics in Chapter 1 (see Table 1.6). The origin of such large piezoelectricity is currently under debate. For example, one experimental study suggests that it arises from the vicinity of *triple* point where rhombohedral and tetragonal ferroelectric phases coexist with the paraelectric phase of cubic symmetry.[187] Another study[212] based on theoretical and experimental results suggested that highest piezoelectric coefficients were reached at the boundary of tetragonal and orthorhombic phases and are a result of a combination of reduced anisotropy energy, high polarization, and increased compliance. There exists yet another explanation which hints that the coexistence of tetragonal, orthorhombic, and rhombohedral ferroelectric phases, the electric properties of each being dependent on electric field differently, are the reasons of the large observed electromechanical response.[213,214]

The discussion above and also in Chapter 1 was the motivation to form a new composite using BCZT (85 vol. %) as a piezoelectric component and CFO (15 vol. %) as a magnetostrictive component. The detailed study of its structure and different properties is as follows:

3.1.2 Experimental Details

The BCZT powder was prepared employing a two-step solid-state reaction using reagent grade carbonates and oxides. The raw powders $CaCO_3$ (Fluka Chemie GmbH, purity > 99%), $BaCO_3$ (Alfa Aesar GmbH KG, purity 99.95%), TiO_2 (Merck KgaA, purity > 99%) and ZrO_2 (Sigma Aldrich U.K. purity 99%) were mixed according to the stoichiometric formula $0.5Ba(Zr_{0.2}Ti_{0.8})O_3$-$0.5(Ba_{0.7}Ca_{0.3})TiO_3$. All the powders were added to an alumina milling container with yttria-stabilized zirconia balls and ethanol. The suspensions were milled in a planetary ball mill (Fritsch Pulverisette 5) for 12 hours and dried at room temperature for 24 hours. The milled powder was calcined at 1400 ℃ for 6 hours with a heating rate of 5 ℃/min and subsequently ball-milled for 10 hours with the previously described parameters. The powder was again calcined for another 6 hours upto 1500 ℃ at a heating rate of 5 ℃/min and ball milled subsequently for 10 hours as previously.

$CoFe_2O_4$ was synthesized by the mixed oxide route. Powders of Fe_2O_3 (Alfa Aesar GmbH KG, purity > 99%) and Co_3O_4 (Alfa Aesar GmbH KG, purity > 99%) were mixed in ethanol in a stoichiometric ratio and milled for 10 hours. The suspension was dried and calcined for 6 hours at 1050 ℃ with a heating rate of 5 ℃/min and ball milled again with the previously described parameters. The calcined powders BCZT and CFO were

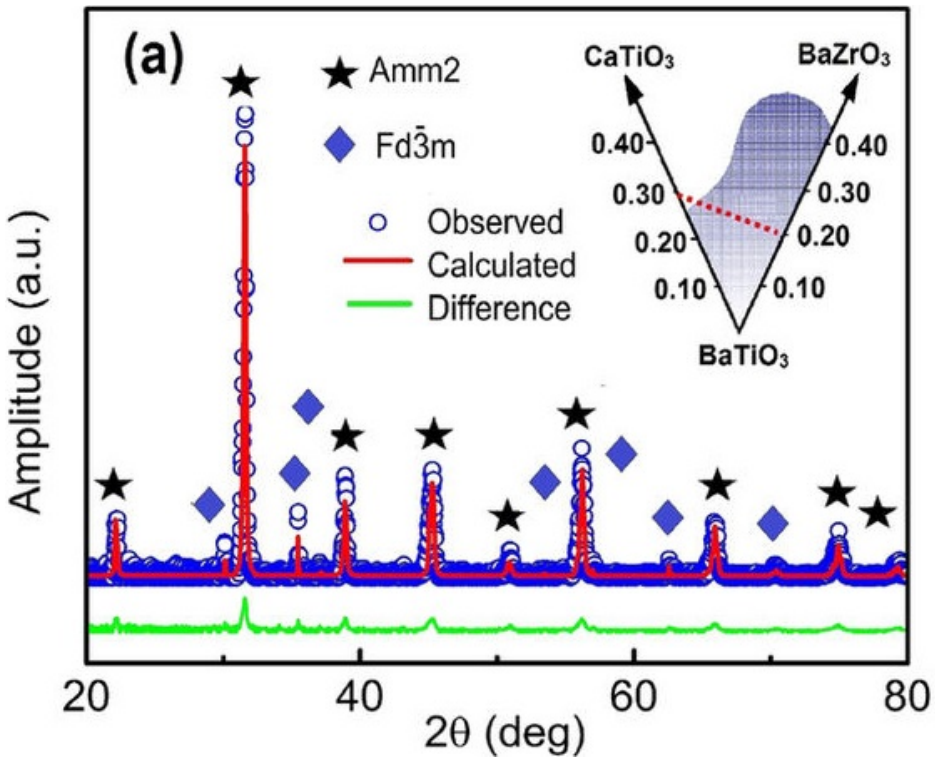

Figure 3.1: XRD spectra taken at room temperature along with Rietveld analysis of $BCZT_{85}$-CFO_{15}. Open symbols are experimental data, Rietveld two-phase model fitting is represented by a solid line superposed on the data, while the difference curve is below it. Two phases are represented by the solid symbols. Inset shows the phase diagram of the solid solution $BaTiO_3$-$CaTiO_3$-$BaZrO_3$ in which xBCT-(1-x)BZT is represented by the dashed line and BCT50-BZT is the midpoint on this line.

mixed in 85 vol.% and 15 vol.% ratios in ethanol and ground for 6 hours at 300 rpm. The suspension was dried, and the powder was pressed into pellets of 6 mm diameter and a thickness of around 1 mm using a hydraulic press under a uniaxial pressure of 300 MPa for 2-5 min. The green bodies were sintered in covered alumina crucibles in the air at 1300 ℃ for 6 hours.

X-ray diffraction was conducted at room temperature using a Siemens D5000 diffractometer both for the calcined powders and for the final sintered pellets. Rietveld refinement was performed using GSAS-II software.[198]

3.1.3 Results

The crystal structures of both phases in the composite (BCT50-BZT and CFO) were determined with the help of X-ray diffraction. The spectra were identified to have two kinds of peaks: One corresponding to the perovskite orthorhombic structure (space group $Amm2$), and the other to the cubic spinel structure (space group $Fd\bar{3}m$) for the CFO phase. Rietveld analysis was performed employing a two-phase model. The results are shown in Fig. 3.1. The symbols correspond to the observed data, the solid superposed-

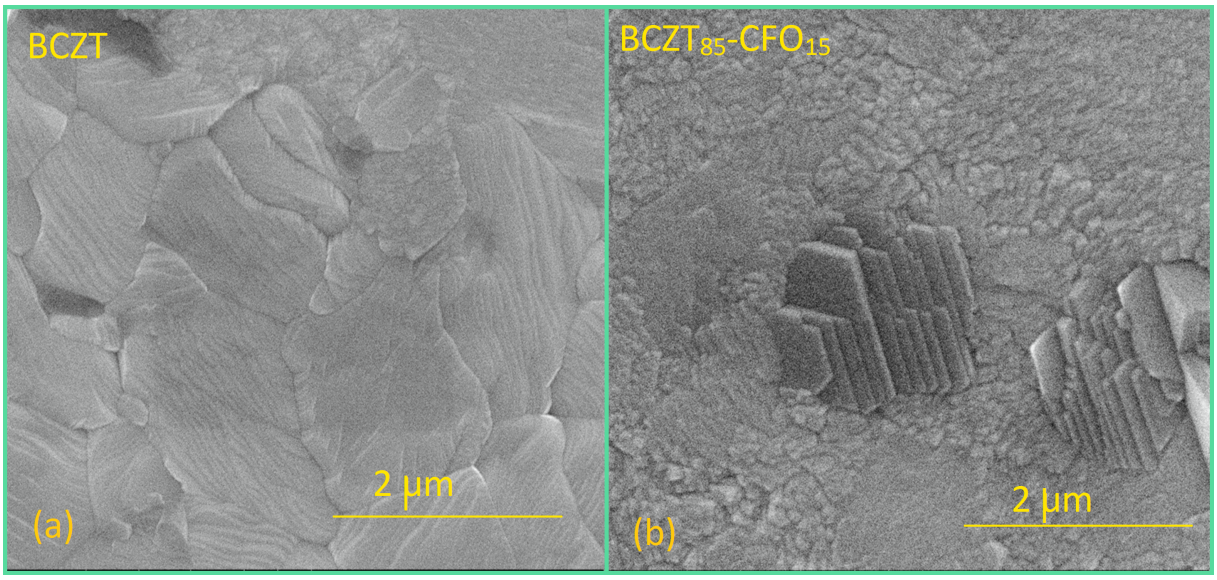

Figure 3.2: SEM images of (a) BCZT and $BCZT_{85}$-CFO_{15} taken at room temperature.

line is the fit to the two-phase model, while the lower line shows the difference between the observed and the fitting. A suitable fitting was obtained with the two-phase model as can be seen from the difference plot. Moreover, no additional phase peaks could be seen. The refinement resulted in the following lattice parameters for both the phases in the composite: $a_{BCZT} = 4.002$ Å, $b_{BCZT} = 5.676$ Å, $c_{BCZT} = 5.656$ Å, and $a_{CFO} = 8.4$ Å.

Fig. 3.2 shows the SEM images of the composite samples. Dense microstructure is evident with the mixed distribution of grain sizes. BCZT when sintered alone at 1300 ℃ 3.2(a), in general, attains a relative density of $\geq 96\%$, provided the starting particle size for sintering is ≤ 1 μm.[215] The particle shape, in this case, is irregular, and the particles of BCZT are highly fused into one another in the composite. This is visible in both Fig. 3.2 (a) and (b). As far as $CoFe_2O_4$ is concerned, it grows in the shape of regular or irregular octahedral crystals when sintered alone.[216] The irregular octahedral-shaped CFO crystals can be seen in the middle of Fig.3.2(b). So the microstructure of the composite is like ferromagnetic CFO crystals embedded in ferroelectric BCZT matrix, making it a pseudo 3-0 type connected composite.

3.1.3.1 Electric Permittivity Measurements

Electric permittivity was measured as a function of temperature and frequency. Fig. 3.3(a) shows the temperature dependence of the real part of electric permittivity ε' for pure BCZT ceramic measured at different frequencies. It exhibits a small peak around 320 K that corresponds to the orthorhombic-tetragonal phase transition while a larger maximum at around 370 K represents the ferroelectric-paraelectric phase transition. Moreover, The phase transition is not very sharp, and also there is a frequency dispersion such that ε'_m

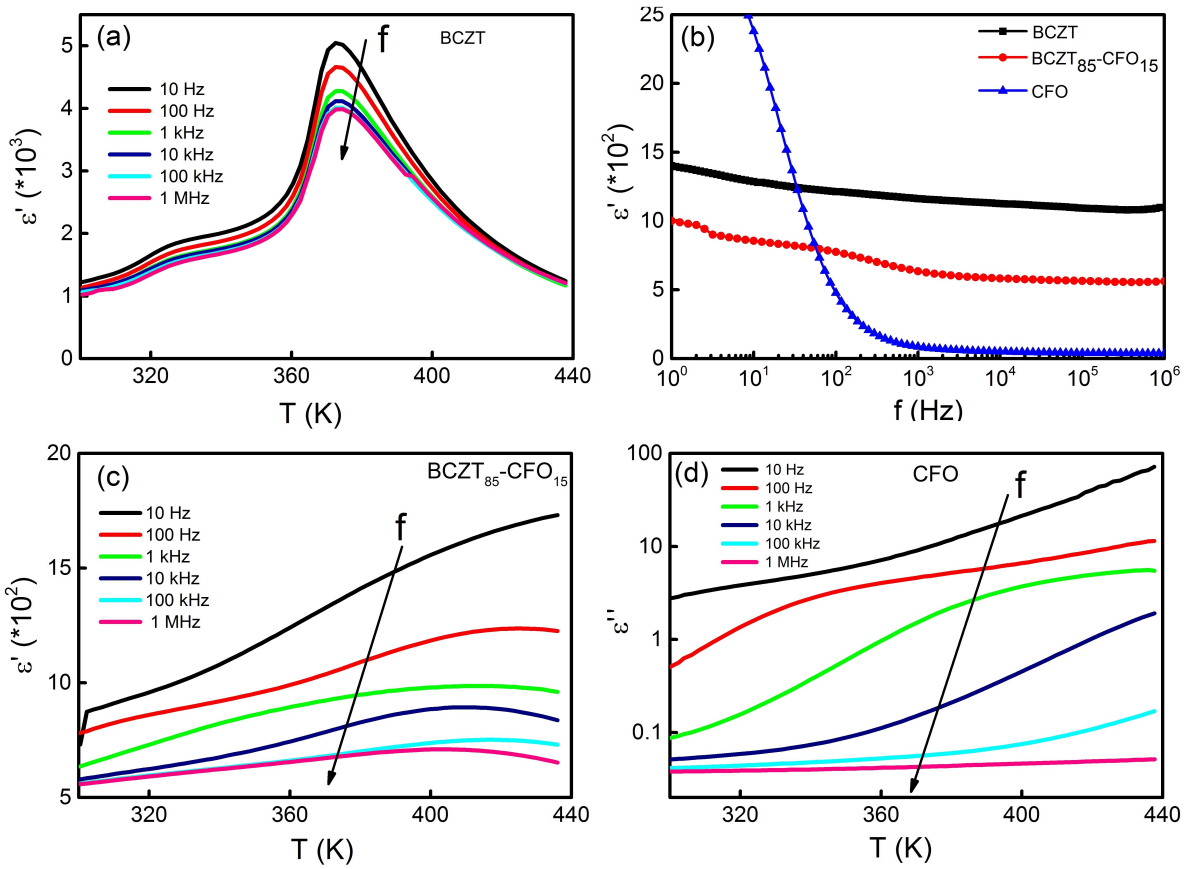

Figure 3.3: Electric permittivity of (a) BCZT versus temperature at various E-field frequencies. (b) Electric permittivity versus frequency for BCZT, CFO, and $BCZT_{85}$-CFO_{15} at room temperature. (c) Real part of electric permittivity ε' of $BCZT_{85}$-CFO_{15} versus temperature, and (d) imaginary part of electric permittivity ε'' versus temperature, measured at various E-field frequencies.

decreases with increasing frequency. This behavior is a typical signature of a ferroelectric with a diffuse phase transition.

Fig. 3.3 (c) and (d) show $\varepsilon'(T)$ and $\varepsilon''(T)$ for the composite $BCZT_{85}$-CFO_{15}. Their behavior is different from that of BCZT. One witnesses broad maxima at all the frequencies in ε' and there is no indication of any phase transition temperature in the dielectric response of the composite. Moreover, the overall values of electric permittivity are decreased in comparison with the pure sample. This behavior can be readily explained regarding the electric permittivity of BCZT and CFO and by the fact that electric permittivity is an *additive* property of BCZT and CFO. By additive property it means that it depends also upon the microstructure of both phases. For pure CFO, $\varepsilon^*(T)$ monotonically increases with increasing temperature without any peak/transition temperature,[217] in the present-studied temperature range. However, when it is combined with BCZT, one witnesses a hump in ε' and ε'', the behavior at higher temperatures is dominated by CFO due to its inferior dielectric properties, so there is a rather diffuse peak at some

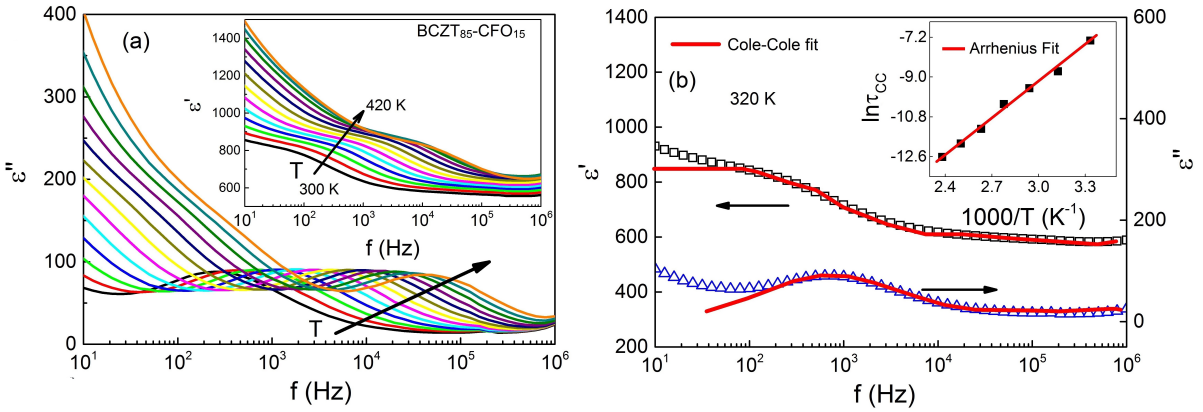

Figure 3.4: (a) Real part of electric permittivity versus frequency $\varepsilon'(f)$ measured at various temperatures for $BCZT_{85}$-CFO_{15}, inset shows $\varepsilon''(f)$. (b) Real and imaginary parts of electric permittivity for $BCZT_{85}$-CFO_{15} given by open symbols and its fitting to the Cole-Cole model given by solid line superposed to it. Inset shows a plot of the Cole-Cole time constants τ_{cc} versus inverse temperature where the solid line shows the fitting to Arrhenius law.

frequencies. This peak does not necessarily represent the phase transition temperature of the composite, but rather is a relaxation effect in a system of heterogeneous grains. A comparison of electric permittivity versus frequency of BCZT, CFO, and $BCZT_{85}$-CFO_{15} of the data taken at room temperature. To further study the relaxation behavior in the composite, electric permittivity versus frequency behavior of both samples, i.e., of BCZT and $BCZT_{85}$-CFO_{15} is required. However, a small discussion about different possible relaxation mechanisms is necessary before the analysis of data.

3.1.3.2 A Brief Introduction to Relaxation Mechanisms

Debye was the first theoretician who worked on the time evolution of polarization/relaxation when an external *ac* electric field is applied to a dielectric.[218] He considered non-interacting dipoles floating in some imaginary viscous medium so that the whole dielectric polarization has a time dependence of the following type:$P(t) = P_0 exp(-t/\tau)$, where τ is the relaxation time. Consequently the time derivative of polarization across the whole dielectric is also an exponential function of time:

$$I(t) = \frac{P(t)}{\tau} \propto exp(-\frac{t}{\tau}) \tag{3.1}$$

Practically the response encountered in real dielectric materials deviates from the ideal Debye dielectric response (Eq.3.1). A comprehensive understanding of dielectric response and its relationship to microscopic features in solids can be found in the research of Jonscher,[218] Ngai,[219] Dissado,[220] and Hill.[221] A *universal dielectric response* was introduced in which dielectric relaxation was treated as one that involves interacting electric species (be either dipoles or charges). To interpret the results of dielectric spectroscopy, one needs

to understand the process which might be involved and which type of charged species are taking part. Unlike classical dielectric response which involves only the orientation of rigid dipoles, it is *now* well understood that certain hopping mechanisms involving electronic and ionic charges might also give rise to polarization.

Dipoles are broadly divided into two groups, one which exists inherently in a material (*permanent dipoles*), and the other which are created only after the application of an electric field (*induced dipoles*). However, in terms of their dynamic response, they are divided a bit differently, i.e., *static and dynamic dipoles*. The static dipoles consist of bound charges with fixed distances between the charges of opposite sign. These only possess rotational degrees of freedom. The dynamic dipoles might involve both permanent and induced dipoles, and the resultant polarization is termed as *dipolar polarization* (also see Fig. 1.2). An interesting situation is encountered when, under certain conditions, the weakly bound charges are forced to come out of their local potential wells (e.g. increase in temperature might provide the required excitation). In that case, the charges now are able to move in a larger area than those of strongly bound ones, under the application of an electric field. The dipoles are termed as *dynamic dipoles*, and the associated polarization now called as *charge carrier polarization*. However, there also exist free charge carriers, which are responsible for *dc*-type processes, are non-localized, and therefore do not contribute to any polarization process at any frequency.[218]

A significant number of dielectric materials show relaxation-times τ that are somewhere in between 10^{-5} to 10^{-9} seconds. Current sampling at such small times is a gigantic task sometimes and not all fast processes might be resolved. This problem is circumvented by using the measurements taken in the frequency domain rather than the time domain. That is why most of the literature deals with frequency domain data, where commonly available setups can readily reach megahertz or even higher frequencies. Moreover, the conversion from one domain to the other domain is easily achieved through Fourier Transformation. In the Debye model (Eq. 3.1) the complex capacitance $C^*[\cong C_0/(1+i\omega\tau)]$ ($i=\sqrt{-1}$), can be represented by electric permittivity relation in terms on frequency domain representation ($\omega = 2\pi f$) as:

$$\varepsilon^* = \varepsilon'(\omega) - i\varepsilon''(\omega) \propto \frac{\varepsilon_s}{1+i\omega\tau} \tag{3.2}$$

where $\varepsilon_s \equiv \varepsilon'(0)$ is the static low frequency electric permittivity. The circuit combination for such a system is a series combination of a capacitor (capacitance C_0) and resistance R_0, with a relaxation time $\tau = R_0C_0$.

The Debye model deals with an ideal system with a single relaxation time, which is not consistent with most practical systems. To achieve a better agreement with the experimental data, the Debye model was improved by taking into account more than one

relaxation time. The important improvements in shape of models are Cole-Cole, Cole-Davidson, and Havriliak-Negami models. These models are expressed in terms of electric permittivity given in Table 3.1.[218]

Table 3.1: Models for the interpretation and fitting of dielectric responses, and the asymptotic behaviors of the corresponding dielectric losses.

Models	$\varepsilon^*(\omega)$	$\varepsilon''(\omega) \propto$
Debye	$\frac{\varepsilon_s}{1+i\omega\tau}$	$\omega^{+1}; \omega \ll \omega_p$ $\omega^{-1}; \omega \gg \omega_p$
Cole-Cole	$\frac{\varepsilon_s}{1+(i\omega\tau)^{1-\alpha}}$ $0 < \alpha < 1$	$\omega^{1-\alpha}; \omega \ll \omega_p$ $\omega^{-(1-\alpha)}; \omega \gg \omega_p$
Cole-Davidson	$\frac{\varepsilon_s}{(1+i\omega\tau)^{\beta}}$ $0 < \beta < 1$	$\omega^{+1}; \omega \ll \omega_p$ $\omega^{-\beta}; \omega \gg \omega_p$
Havriliak-Negami	$\frac{\varepsilon_s}{[(1+i\omega\tau)^{1-\alpha}]^{\beta}}$ $0 < (\alpha, \beta) < 1$	$\omega^{1-\alpha}; \omega \ll \omega_p$ $\omega^{-\beta(1-\alpha)}; \omega \gg \omega_p$

3.1.3.3 Analysis of Electric Permittivity versus Frequency Data

Electric permittivity was measured as a function of frequency at different fixed temperatures. The isotherms of the imaginary part $\varepsilon''(f)$ of the composite are shown in Fig.3.4(a), while the isotherms of the real part $\varepsilon'(f)$ are shown in the inset. A strong increase of both $\varepsilon'(f)$ and $\varepsilon''(f)$ at low frequencies and high temperatures can be seen, and is believed to be mainly caused by the contribution from the CFO phase inclusions as shown in the SEM image. These inclusions alter the properties of the composite from the pure BCZT via the following two mechanisms:

- Due to the conductivity of cobalt ferrite, which is high at low frequencies and higher temperatures.
- Due to the accumulation of interfacial charges between the semi-conductive ferrite and insulating BCZT phases, which generates the Maxwell-Wagner type interfacial polarization.

These mechanisms were also suggested for similar two phase systems, for example $BaTiO_3$-$Ni_{0.5}Zn_{0.5}Fe_2O_4$ composites.[136,222] Maxwell-Wagner relaxation is usually related to chemical inhomogeneities which are present mostly in two phase systems. Also, a large number of hetero-interfaces between the ferroelectric and ferrimagnetic phases act as traps for the mobile charge carriers at high temperatures. Accumulation of charges in the vicinity of the interfaces leads to the formation of inner fields. These fields might cause huge dielectric losses, especially at low frequencies where the separation distances between the positive and negative charges can be large.[222]

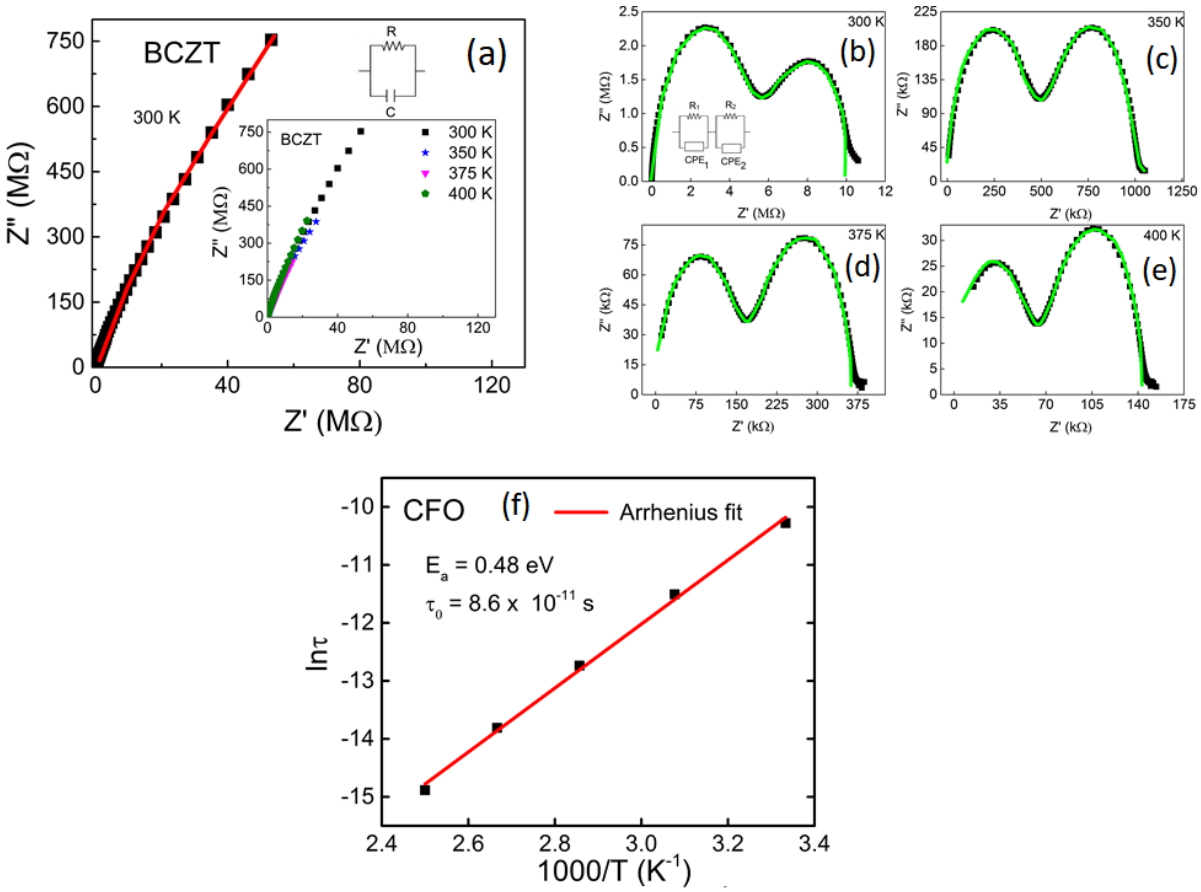

Figure 3.5: (a) Nyquist plot for BCZT at 300 K, the inset shows Nyquist plots for higher temperatures; (b - e) Nyquist plot for CFO at different temperatures fitted to the circuit shown in (b). The symbols are the experimental data while the solid lines correspond to the fitting. (f) Arrhenius fit to pure CFO data, errors in fitting results are less than 1 % of the values shown on the graph.

In addition to the low-frequency relaxation, $\varepsilon'(f)$ has a broad step while $\varepsilon''(f)$ has a broad peak in the frequency range $10^2 \leq f \leq 10^5$ Hz. The position of the $\varepsilon'(f)$ step and the peak of $\varepsilon''(f)$ shift toward higher frequency as temperature increases. This is a clear indication of a thermally-activated process. The Cole-Cole model see Table 3.1) was employed to evaluate the physical nature of the relaxation behavior, and a representative curve fitted to Cole-Cole model is shown in Fig. 3.4(b).

$$\varepsilon^* = \varepsilon_\infty + \frac{\Delta\varepsilon}{1 + (i\omega\tau_{cc})^{1-\alpha}}; \tag{3.3}$$

which can be decomposed into a real part:

$$\varepsilon' = \varepsilon_\infty + \Delta\varepsilon\Big[\frac{1 + (\omega\tau_{cc})^{1-\alpha} sin(\frac{\alpha\pi}{2})}{1 + 2(\omega\tau_{cc})^{1-\alpha} sin(\frac{\alpha\pi}{2}) + (\omega\tau_{cc})^{2-2\alpha}}\Big]; \tag{3.4}$$

and an imaginary part:

$$\varepsilon'' = \Delta\varepsilon\Big[\frac{(\omega\tau_{cc})^{1-\alpha} cos(\frac{\alpha\pi}{2})}{1 + 2(\omega\tau_{cc})^{1-\alpha} sin(\frac{\alpha\pi}{2}) + (\omega\tau_{cc})^{2-2\alpha}}\Big]; \tag{3.5}$$

ε_∞ is the high frequency electric permittivity, $\Delta\varepsilon = \varepsilon_s - \varepsilon_\infty$ is the difference between high and static low frequency permittivity ε_s, τ_{cc} is called the Cole-Cole characteristic relaxation time, and α is related to the symmetric broadening of the relaxation time distribution. $\alpha = 0$ corresponds to the classical Debye relaxation (single time constant system), while $\alpha \geq 0$ means a system with a distribution of relaxation times. The best fit parameters after fitting the data to equations 3.4 and 3.5 are given in Table 3.2. The values of τ_{cc} were further fitted to Arrhenius's law $\tau_{cc} = \tau_0 exp(\frac{E_a}{k_B T})$, where E_a is called the activation energy and k_B is Boltzmann's constant. A fitting to Arrhenius law is shown in the inset of Fig. 3.4(b), which gives $E_a = 0.47$ eV and $\tau_o = (8.4 \pm 0.2) \times 10^{-12}$ s. Pure BCZT does not show any relaxation behavior in $\varepsilon(f)$, but CFO does show relaxations. The values of E_a and τ_0 shown above very well correspond to those obtained from the relaxations of CFO sample (see Fig.3.5(f)), and also to those reported in literature for CFO[223] and ferrite containing compounds.[136,224,225]

The time constant and activation energies obtained from Arrhenius fit can be explained easily when we consider the electronic conduction phenomenon between ferric Fe^{3+} and ferrous Fe^{2+} ions. Ferrites when sintered at high temperatures (1300 °C here), develop a large number of oxygen vacancies,[225] and a possibility of reduction of Fe^{3+} to Fe^{2+}. The electronic exchange mechanism might follow $Fe^{2+} \rightleftharpoons Fe^{3+} + e^{-1}$, and a local displacement of these dipoles in the direction of an applied electric field is obtained. These displacements account for the polarization in ferrites. The activation energy given above describes the energy required by electrons for hopping between Fe^{3+} and Fe^{2+}.[226]

Table 3.2: Summary of fitting results according to the Cole-Cole equations.

T (K)	τ_{cc} (μs)	$\Delta\varepsilon$	α
300	637 ± 14	307 ± 5	0.33 ± 0.01
320	159 ± 10	301 ± 4	0.32 ± 0.01
340	74 ± 7	298 ± 5	0.31 ± 0.01
360	36 ± 4	278 ± 7	0.29 ± 0.02
380	12 ± 4	263 ± 4	0.26 ± 0.01
400	6.0 ± 0.4	252 ± 10	0.22 ± 0.01
420	3.0 ± 0.5	217 ± 11	0.16 ± 0.03

3.1.3.4 Impedance Analysis

Relaxation processes in the composite can be further studied by employing the analysis of complex impedance ($Z^* = Z' + \iota Z''$) and complex modulus ($M^* = M' + iM''$) data. Nyquist plots of impedance Z' vs. Z'' and modulus M' vs. M'' are very useful to elucidate the electric relaxation behavior. The reason for which is that the impedance Nyquist plots highlight the phenomena characterized by high resistance, while modulus plots identify electric responses with small capacitances. Fig. 3.6(a) and (b) shows the Nyquist plots for impedance and modulus, respectively, for the composite. Big semi-circular arcs are visible in impedance plots, however, it is hard to distinguish any relaxations apparently. On the other hand, modulus plots indicate two different types of relaxations. In the low-frequency regime, one sees a step like relaxation as we saw in the electric permittivity spectra, and an activated behavior in mid-frequency range with sharp maxima. In brief, it can be easily seen that impedance plots show a dominant capacitance behavior at lower frequencies (in this case it belongs to BCZT phase), while the modulus plots give a clear indication of small capacitance behavior at higher frequencies (which might be assigned to the CFO phase). These predictions can be matched with some actual calculated numbers, with the help of equivalent circuit analysis, which is presented next.

Nyquist plots can be modeled by several serially connected equivalent electrical circuits, which correspond to different relaxation processes/entities. Looking at the impedance Nyquist plots in more details, it was found to have two semicircular arcs, which are poorly resolved as indicated in Fig. 3.7(a). The equivalent circuit comprised of elements indicated in the inset of Fig. 3.7(a). C_1 and C_2 are the representative capacitors, R_1 and R_2 are resistances. And constant phase element (CPE) is an element representing a non-ideal dielectric response related to ac conductivity and also to space charge. The impedance of CPE is given by $Z_{CPE} = 1/Y_{CPE} = 1/Q(i\omega)^n$, Q is a prefactor related to the capacitance of the sample, while the exponent n has a value in between 0 (for the purely resistive circuit) and 1 (for purely capacitive one).[227]

The values of fitting parameters are given in Table 3.3. Moreover, pure Nyquist plots

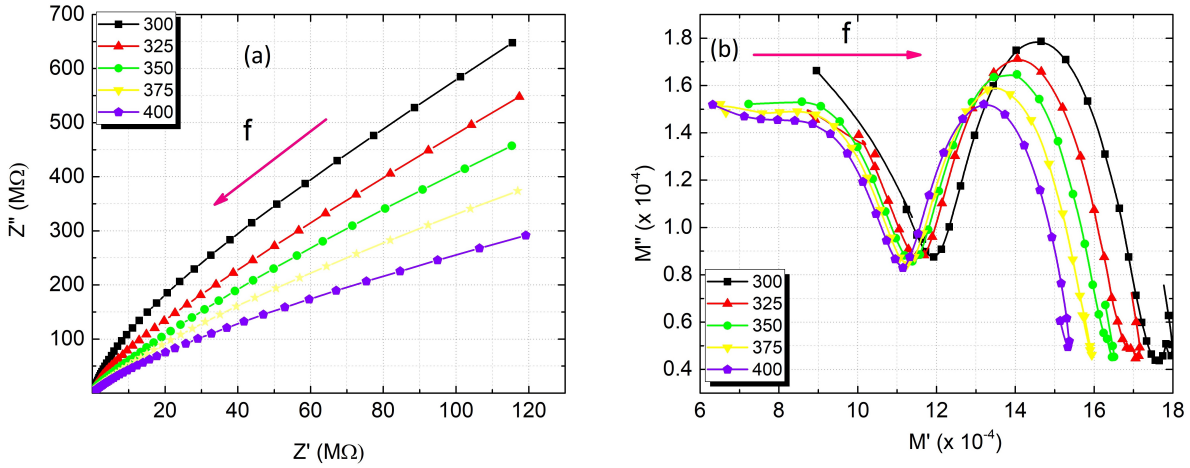

Figure 3.6: Nyquist (a) electric impedance and (b) elelctric modulus versus frequency plots for $BCZT_{85}$-CFO_{15} at various temperatures.

Table 3.3: Summary of the best fit parameters according to the circuit Fig.3.7(a).

T (K)	C_1 (nF)	C_2 (pF)	R_1 (GΩ)	R_2 (MΩ)	Q(S·s^n)*10^{-10}	n
300	18.7 ± 0.6	160 ± 10	6.20 ± 0.80	2.2 ± 0.3	1.02	0.80 ± 0.10
325	12.6 ± 0.4	250 ± 20	0.93 ± 0.03	1.6 ± 0.2	1.42	0.80 ± 0.01
350	16.7 ± 1.0	310 ± 15	0.13 ± 0.01	0.45 ± 0.05	2.10	0.78 ± 0.03
375	15.1 ± 1.0	570 ± 20	0.12 ± 0.02	0.11 ± 0.01	2.00	0.75 ± 0.02
400	11.5 ± 0.6	340 ± 20	0.09 ± 0.01	0.13 ± 0.04	1.04	0.74 ± 0.01

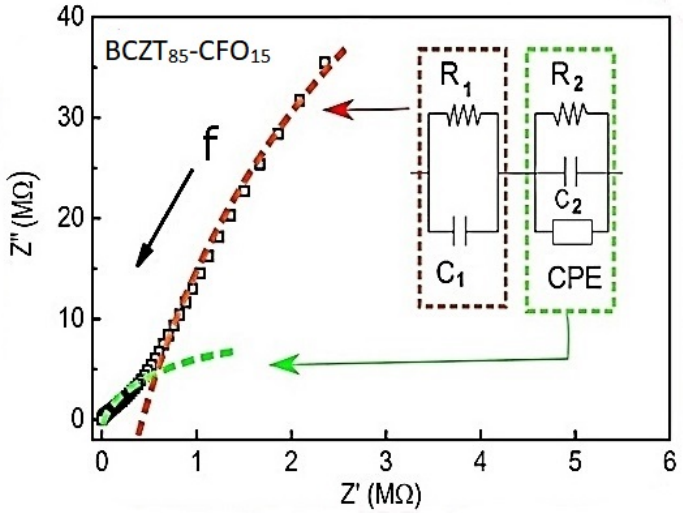

Figure 3.7: Modelling in terms of equivalent circuits for $BCZT_{85}$-CFO_{15}. A closer view of the impedance versus frequency curve at room temperature; inset displays the equivalent circuit used to model this. The circuit displayed on the right of the figure was utilized for the higher frequency part of the curve, and the one on the left for the lower frequency part.

for pure BCZT as well as CFO were also fitted to equivalent circuits (Fig. 3.5 (a) and (b - e)). It was interesting to find out that the fitting parameters related to the second circuit (inside the green box) well correspond to that of the pure ferrite phase. On the other hand, the contribution of the perovskite phase BCZT could not be singled out, so it was assumed here that the first circuit represents an effective response from the BCZT phase and any interfacial effects.

3.1.3.5 Electric Polarization

Macroscopic polarization as a function of the electric field ($P(E)$ hysteresis curve) was measured at room temperature employing a custom-built Sawyer-Tower circuit. The frequency of the *ac* field was 100 Hz. The loop is shown in Fig.3.8(b) and it was not completely saturated. For comparison, a $P(E)$ loop corresponding to BCZT ceramic (Fig.3.8(c)) which shows a typical behavior of ferroelectric hysteresis loop, saturation polarization of 10 $\mu C/cm^2$ and a coercivity of 5 kV/cm.

3.1.3.6 Magnetic Hysteresis

Magnetic hysteresis loop were measured in a SQUID at 280 K, showing slim hysteresis. Its remanent magnetization M_r is 8.32 kA/m, with a relatively small magnetic coercive field $\mu_0 H = 0.04$ T, thus proving it to be consisting of ferrimagnetic cobalt ferrite.

3.1.3.7 Microscopic Multiferroic Properties

Piezoresponse force images of the sample were acquired at room temperature. Fig.3.9(a) and (b) show the topography and lateral PFM images, respectively, of the finely polished sample surface. There exist distinct bright regions which correspond to the piezoactive BCZT phase. To verify whether it is an actual ferroelectric response, switching spectroscopy PFM (SSPFM) loops were obtained on the bright spot designated by the white circle. Hysteresis loops of local amplitude and phase measured as a function of the applied *ac* voltage are shown in Fig.3.9(c) and (d), respectively. The phase loop spans over 180°, while the amplitude loops are similar to strain-electric field hysteresis (macroscopic $S(E)$) butterfly loops for piezoelectric materials. It becomes clear from the SSPFM analysis that bright regions are indeed piezoelectrically active regions. Thus piezoelectricity is confirmed at the microscopic scale. Now the only question remains whether or not these phases are cross-coupled concerning external electric/magnetic fields, i.e., magnetoelectric coupling, which will be analyzed in the next section.

3.1.3.8 Converse Magnetoelectric Measurements

The converse magnetoelectric effect was measured in three different modes:

- Under constant *ac* electric field amplitude and constant *dc* magnetic field, sweeping the temperature only.

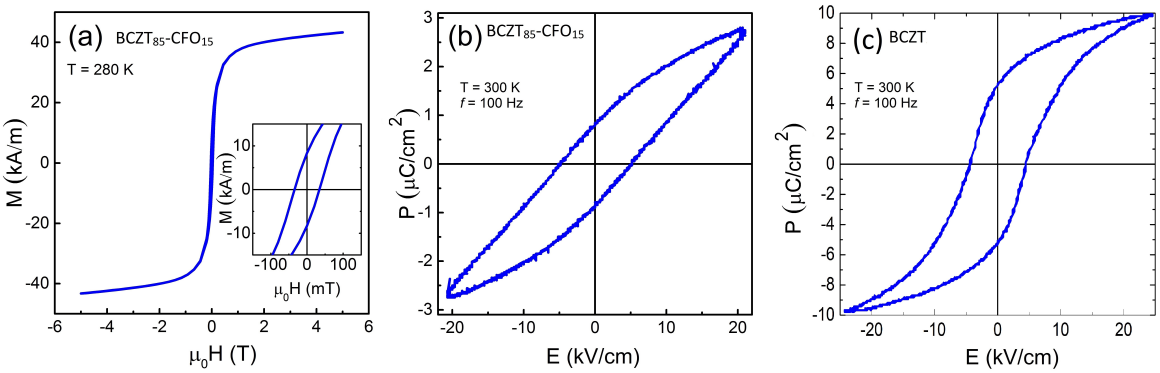

Figure 3.8: (a) Magnetization-magnetic field hysteresis $M(H)$ for $BCZT_{85}$-CFO_{15} at 280 K, (b) Polarization hysteresis $P(E)$ for $BCZT_{85}$-CFO_{15} at 300 K, and (c) Polarization hysteresis $P(E)$ for BCZT at 300 K.

- At constant temperature and fixed value of *ac* electric field, with a sweep of *dc* magnetic field.
- At constant temperature, at a fixed value of *dc* fields, however, this time ramping up the amplitude of *ac* electric field.

The data taken from all three modes will be presented as follows:
Electrically induced magnetization as a function of temperature $M_{ME}(T)$ is plotted in Fig.3.10, it increases from low values to a maximum at around 280 K, and then decreases with further increase in temperature. This behavior would be explained later, in combination with $M_{ME}(H)$ data.

Electrically induced magnetic moment M_{ME} versus applied *dc* magnetic field ($M_{ME}(H)$) was measured and plotted in Fig.3.11(a). It shows a *hysteretic* behavior by following different curves with increasing and decreasing *dc* magnetic fields as illustrated in its panel (b).

By keeping temperature and *dc* magnetic field fixed, an *ac* electric field amplitude is increased, and the corresponding induced magnetic moment is recorded. The $M_{ME}(E_{ac})$ is linear as shown in the inset of Fig.**??**. Its slope was determined from the linear fit to the relation

$$\mu_0 M_{ME} = \alpha_c E_{ac} \tag{3.6}$$

where α_c is the converse magnetoelectric coefficient expressed in units of s/m. α_c for $BCZT_{85}$-CFO_{15} comes out to be 6 ps/m, which is almost 50% larger than the value obtained for bulk magnetoelectric composite of $BaTiO_3$-$CoFe_2O_4$ with 80-20 mass-% ratio.[228] For further studies of these composites, more composites were synthesized with higher ferrite content i.e., 30 and 40 and 50 vol.% by assuming that increasing the ferrite content might lead to an increase in ME coupling. However, this did not prove to be a completely correct assumption as the compositions with 30 and 40 vol.% CFO did

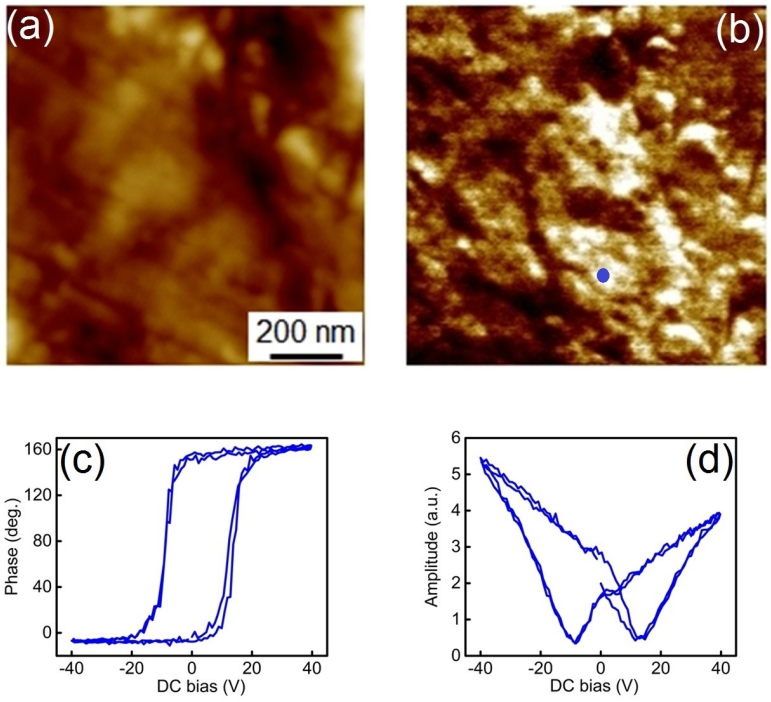

Figure 3.9: (a) PFM topography (b) PFM amplitude for $BCZT_{85}$-CFO_{15} measured at room temperature at the same area. Parts (c) and (d) show the PFM phase and amplitude versus voltage hysteresis loops for $BCZT_{85}$-CFO_{15} taken at the designated point in (b).

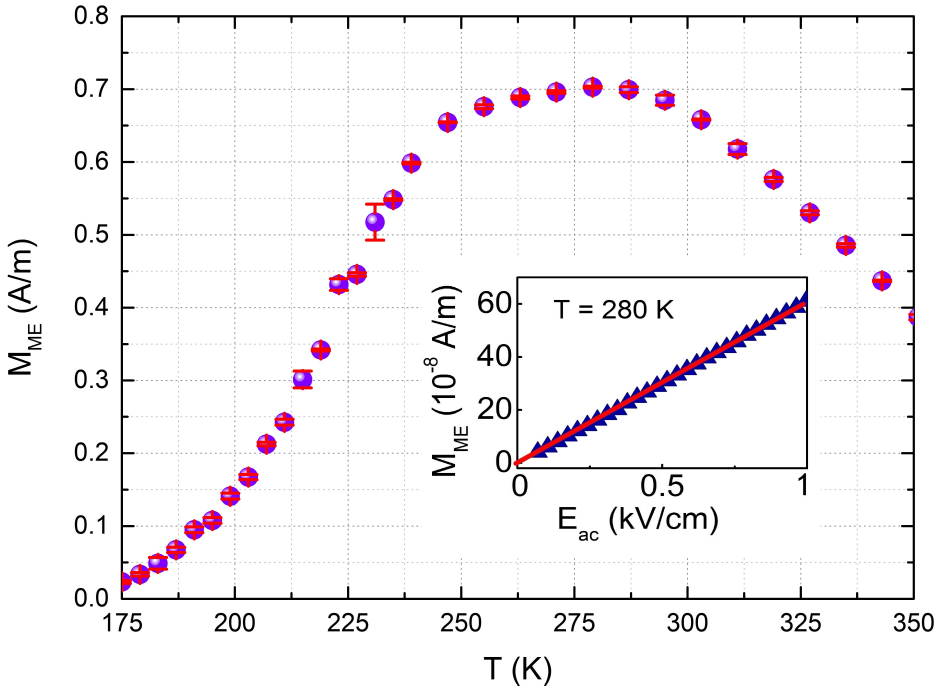

Figure 3.10: Temperature dependence of magnetoelectrically induced magnetization $M_{ME}(T)$ for $BCZT_{85}$-CFO_{15}. Inset shows the electric field induced ME coupling $M_{ME}(E_{ac})$ measured at 280 K.

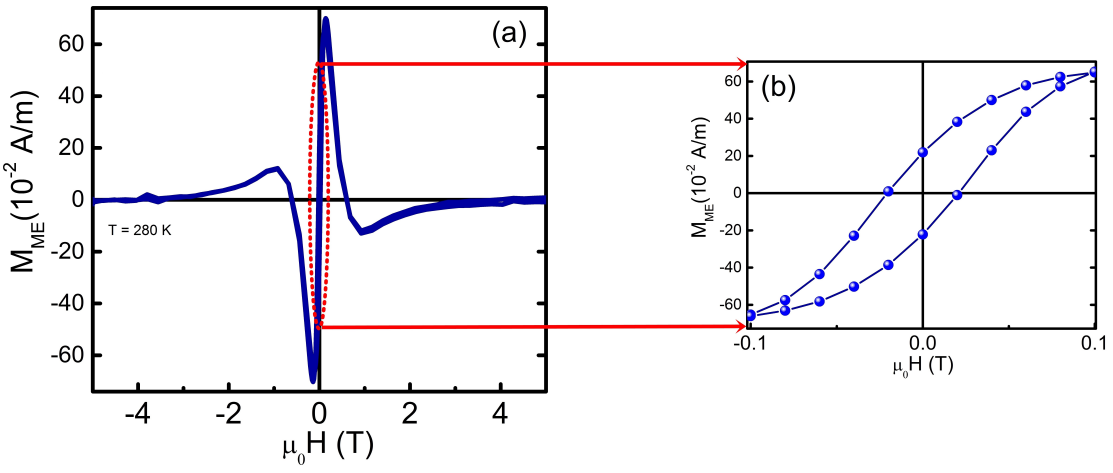

Figure 3.11: (a) Magnetic field dependence of magnetoelectrically induced magnetization $M_{ME}(H)$ for $BCZT_{85}$-CFO_{15} measured at 280 K, and (b) shows its zoomed-in view.

not show any ME coupling at all. A smaller value of converse ME coefficient of 3 ps/m was obtained for 50 % content of ferrite ($BCZT_{50}$-CFO_{50}) which is half of the value for that $BCZT_{85}$-CFO_{15} composite. Therefore, a new strategy was devised by enhancing the magnetostrictive properties of CFO. This was accomplished by modification of CFO with Al^{3+} ions, the details of which are presented in the following sections.

3.2 Structural and Magnetic Properties of $CoFe_2O_4$ and $Co(Fe_{1.5}Al_{0.5})O_4$

3.2.1 Synthesis

$Co(Fe_{1.5}Al_{0.5})O_4$ and $CoFe_2O_4$ were prepared using the mixed oxide route. The oxides of iron, cobalt, and aluminum were mixed in ethanol in stoichiometric ratios as determined from the balanced chemical equations given in Chapter 2 and milled for 10 hours in an alumina crucible with yttria-stabilized zirconia balls for 10 hours. The suspension was dried and calcined for 6 hours at 1050 ℃ at a heating rate of 5 ℃/min and ball milled again with the previously described parameters. All the properties described in the following section were measured in powder form. Mössbauer spectra of the powder samples were recorded in transmission geometry using a ^{57}Co source mounted on a Mössbauer drive operating in constant acceleration mode. A cryostat with a superconducting magnet in split-coil geometry was used to apply a magnetic field of 5 T along the gamma-ray propagation direction.

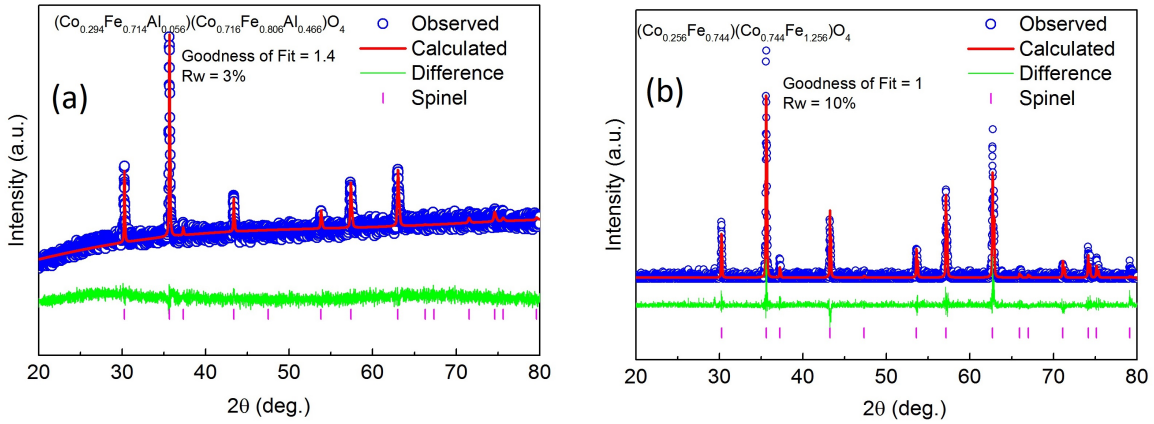

Figure 3.12: XRD data for (a) $Co(Fe_{1.5}Al_{0.5})O_4$ and (b) $CoFe_2O_4$. Symbols are actual data points whereas the solid lines are the fit-lines to the Rietveld refinemnts done according to the inverse cubic spinel ($Fd\bar{3}m$).

3.2.2 Results

Full structural and magnetic characterizations of CFO(Al) and CFO(pure) were performed including Rietveld refinement of XRD data, Mössbauer spectra, and magnetization versus magnetic field hysteresis loops. Here the difference between two kinds of samples is presented.

According to Néel's two-sublattices theory for ferromagnetic materials, the net spontaneous magnetization at 0 K is simply the numerical difference between the two sublattice's magnetizations:[229]

$$M_s = |M_A - M_B| \tag{3.7}$$

Since the properties of ferrite spinels depend on the interaction between the ions at the tetrahedral (A) and octahedral B sites, the distribution of these ions is critical. This site preference of a particular ion is strongly dependent on the temperature of preparation, the rate of cooling, and subsequent heat treatments.[229]

Cobalt ferrite (CFO) exists in the mixed-spinel form. The XRD data as shown in Fig. 3.12(b) confirm this fact where the distribution of the different ions at the terahedral and the octahedral sites is also written. The Al^{3+}-modified cobalt ferrite is also in the mixed-spinel state except the fact that the distribution of ions is altered in the presence of Al^{3+}. Al^{3+} ion is present at both A and B-sites. However, it has a preference for B-sites, which means that it replaced more number of Fe^{3+} ions from the B-site as compared with those on A-site. The total magnetic moment of cobalt ferrite according to the ion configuration obtained from Rietveld analysis can then be written as:

$$[\overrightarrow{Fe^{3+}}, \overrightarrow{Co^{2+}}]_A[\overleftarrow{Fe^{3+}}, \overleftarrow{Co^{2+}}]_B O_4 \tag{3.8}$$

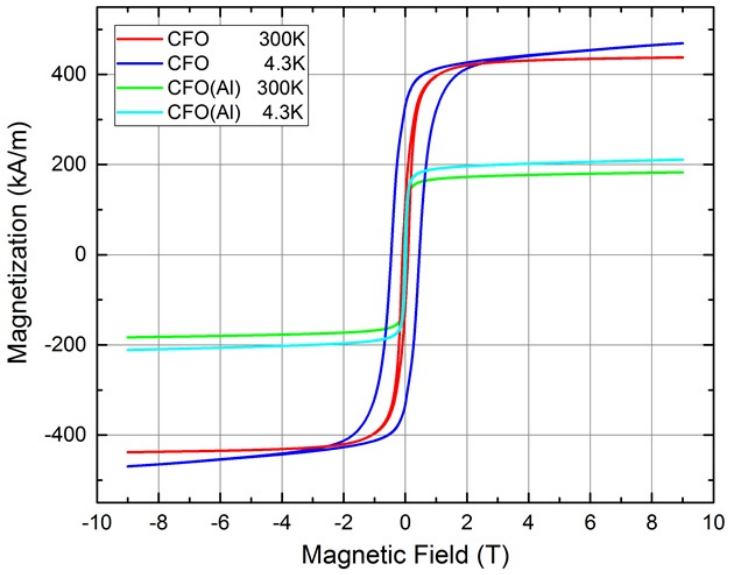

Figure 3.13: $M(H)$ curves for Al^{3+}-modified and pure CFO at different temperatures as indicated in the figure legend.

So a net magnetic moment per formula unit for CFO, in this case, is given by:

$[(0.744)5\mu_B + (0.256)3\mu_B]_A - [(0.744)3\mu_B + (1.256)5\mu_B]_B$ which sums up to 4.024 μ_B/formula unit. Here μ_B is the Bohr magneton.

In case of $Co(Fe_{1.5}Al_{0.5})O_4$, which is also in mixed spinel configuration, the calculation yields:

$[(0.714)5\mu_B + (0.294)3\mu_B + (0.056)0\mu_B]_A - [(0.716)3\mu_B + (0.8065)\mu_B + (0.0.466)0\mu_B]_B$

Which equals 1.726 μ_B/formula unit. This is a huge difference in the net magnetic moment when we compare it to pure CFO. To get a proof of this, $M(H)$ measurements on both samples were performed at 300 K as well as at 4.3 K which are shown in Fig.3.13. As anticipated, there is an actual difference of magnetizations of approximately the same order. The saturation magnetization for CFO is 470 kA/m while for CFO(Al) it is 210 kA/m. Hence the mixed spinel nature of both CFO and CFO(Al) is confirmed.

Further confirmation of magnetic properties of these two samples was obtained by Mössbauer spectra measured by Dr. Joachim Landers. Fig. 3.14 (a) and (b) show the Mössbauer spectra of CFO(Al) and CFO samples, measured at 4.3 K in an external magnetic field of 5 T. Both samples show magnetically ordered behavior, with no traces of parasitic phases visible. For pure CFO, moderate spin canting angles of 28° (B-site) and 25° (A-site) can be determined from the spectra, while CFO(Al) shows smaller canting angles of 20° (B-site) and 18° (A-site), respectively. Due to the magnetic moments being largely aligned along the external magnetic field direction, A and B-sites can be clearly resolved. In agreement with data from XRD experiments shown in Fig.3.12, we observe a preference of the Fe-atoms for the octahedral lattice positions, resulting in a ratio of spectral areas of about 60:40 in both samples. Briefly summarizing, from the X-

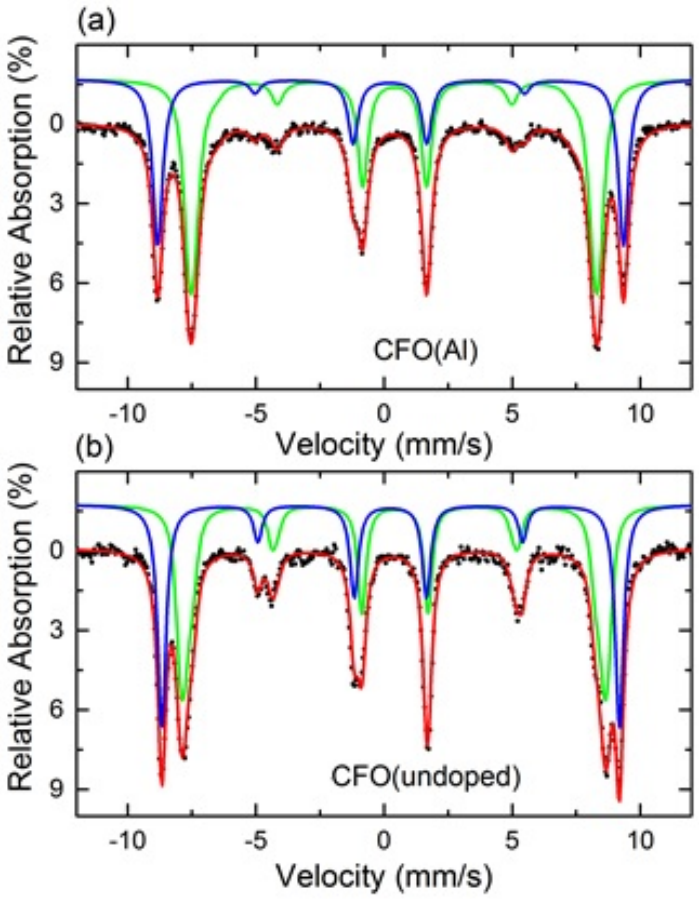

Figure 3.14: Mössbauer data for (a) $Co(Fe_{1.5}Al_{0.5})O_4$, and (b) for $CoFe_2O_4$. Spectra courtesy: Dr. Joachim Landers, M.Sc. Soma Salamon.

ray analysis, it became clear that $CoFe_2O_4$ has a mixed spinel structure which can be represented by an approximate formula:

$$[Co_{0.256}Fe_{0.744}]_A[Co_{0.744}Fe_{1.256}]_BO_4.$$

It has a saturation magnetization M_s of 470 kA/m, which is in good agreement with the literature of mixed spinel cobalt ferrites.[230] On the other hand, Al^{3+} substituted cobalt ferrite has an approximate formula:

$$[Co_{0.294}Fe_{0.174}Al_{0.056}]_A[Co_{0.716}Fe_{0.806}Al_{0.466}]_BO_4,$$

as determined from Rietveld analysis. The saturation magnetization as determined from the $M(H)$ loops came out to be 210 kA/m. The Rietveld analysis and the $M(H)$ measurements complement each other meaning that Al^{3+} has a preference of B-site. This results in the reduction of inherent magnetization imbalance of A and B sublattices of un-modified cobalt ferrite. This eventually leads to a net magnetization decrease. The Mössbauer spectra also confirmed this finding.

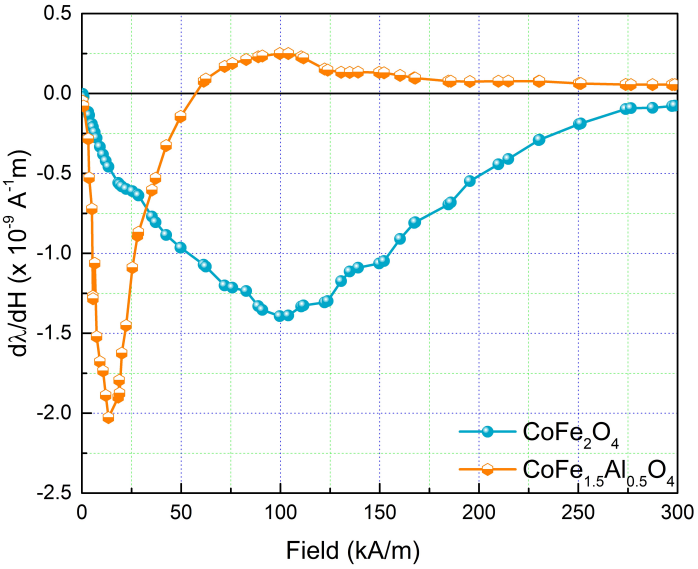

Figure 3.15: Magnetostriction properties of of CFO and CFO(Al), after Nlebedim *et al.*[231]

3.3 Magnetoelectric Effect in $BCZT_{50}$-$CFO(Al)_{50}$ Composites

3.3.1 Background and Motivation

In a pursuance of better ME coupling, it was realized that the magnetostrictive properties of cobalt ferrite can be tuned by different methods which include magnetic annealing and cation substitution of cobalt and iron. In literature the effect of different cation substitutions on the magnetostrictive properties of cobalt ferrite have been studied, some examples include substitutions with Zr^{4+},[232] Mn^{3+},[233] Al^{3+},[231] Ga^{3+},[234] and Zn^{2+}.[235] Nlebedim *et al.*[231] studied magnetic and magnetomechanical properties of $CoAl_xFe_{2-x}O_4$ with x ranging from 0 to 0.9. They found enhanced values of $d\lambda/dH_{max}$ for the Al^{3+} for samples with x upto 0.5. The comparison of their study for $x = 0$ and $x = 0.5$ is presented in Fig.3.15. Keeping this in mind, $CoFe_{1.5}Al_{0.5}O_4$ was selected as a magnetostrictive material for the bi-phase composite, while BCZT was kept as piezoelectric component as before.

3.3.2 Experimental Methods

The solid state method was followed for the synthesis of two composites, $BCZT_{50}$-CFO_{50} and $BCZT_{50}$-$CFO(Al)_{50}$, where $CFO(Al) = Co(Fe_{1.5}Al_{0.5})O_4$. The rest of the characterizations stayed the same as discussed for $BCZT_{85}$-CFO_{15}.

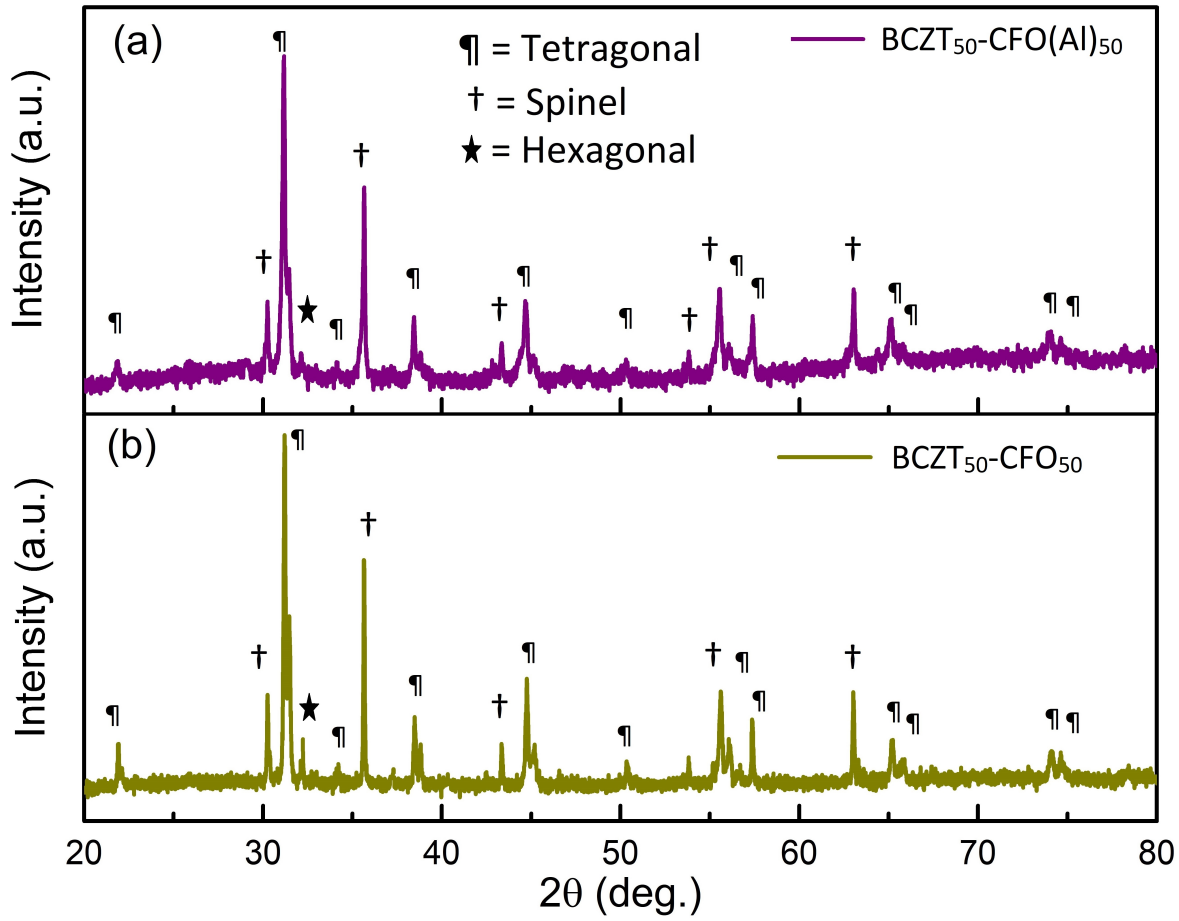

Figure 3.16: XRD Spectra of the $BCZT_{50}$-CFO_{50} and $BCZT_{50}$-$CFO(Al)_{50}$. Both BCZT and ferrite phases along with the impurity phase are indicated with different symbols.

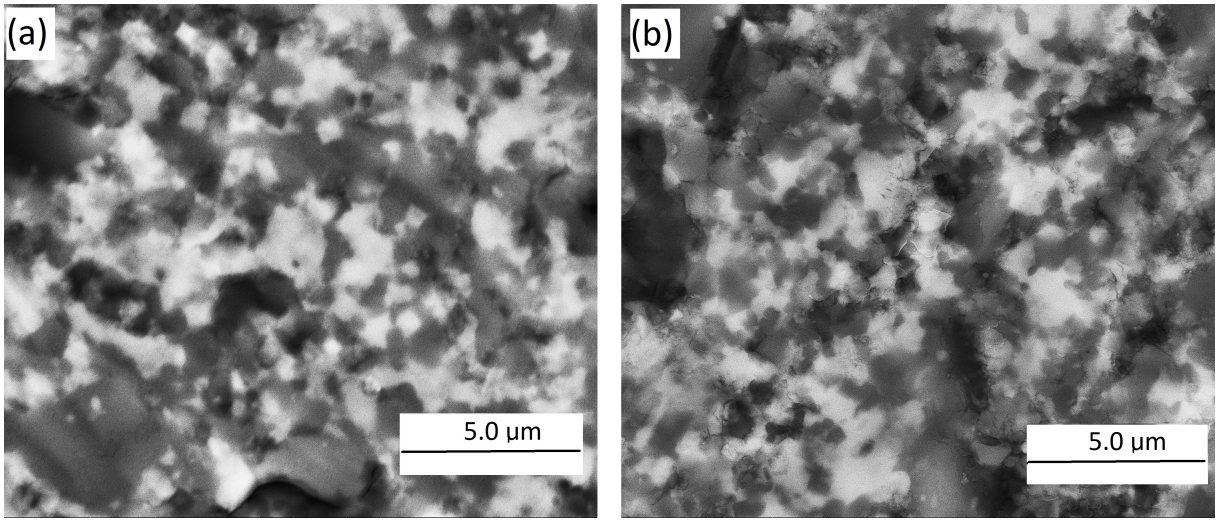

Figure 3.17: SEM Spectra of the $BCZT_{50}$-$CFO(Al)_{50}$ and (b) $BCZT_{50}$-CFO_{50} in backscattering mode.

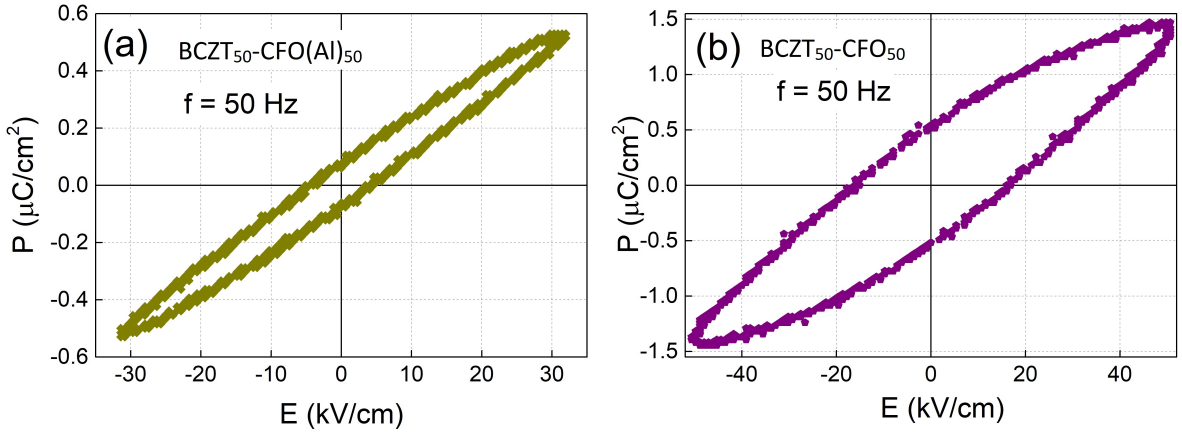

Figure 3.18: $P(E)$ loops of the (a) $BCZT_{50}$-$CFO(Al)_{50}$ and (b) $BCZT_{50}$-CFO_{50} measured at room temperature.

3.3.3 Results

3.3.3.1 X-ray Diffraction

XRD spectra were collected at room temperature for both samples, and are plotted as shown in Fig.3.16(a) and (b). All peaks were identified either belonging to the tetragonal perovskite crystal system ($P4mm$) for BCZT and cubic spinel system $Fd\bar{3}m$ for both CFO and CFO(Al). These phases are indicated with different symbols in Fig.3.16. There are a couple of small peaks that were identified to be belonging to the hexagonal phase $Ba(TiCo)_xFe_{12-x}O_{19}$, as also indicated in the figure. This impurity phase is also a ferromagnetic as studied by Jie *et al.*[236]

Scanning electron microscopy used in backscattering mode is quite useful for differentiating between two phases. The spectra which are shown in Fig.3.17 indicate two thoroughly mixed phases. The brighter phase was attributed to the piezoelectric phase (BCZT), while the dark one corresponded to CFO.

3.3.3.2 Electric Polarization Measurements

Polarization was determined at room temperature for both samples and $P(E)$ curves are plotted in Fig. 3.18 (a) and (b). The loop for $BCZT_{50}$-$CFO(Al)_{50}$ is slimmer than that of $BCZT_{50}$-CFO_{50}. Both loops are unsaturated, due to which saturation polarization could not be determined. This type of polarization behavior is quite common in two-phase composites.[237,238] Since the polarization loops do not supply the necessary information about the exact ferroelectric properties of the composite, local piezoresponse of the composite $BCZT_{50}$-$CFO(Al)_{50}$ was necessary to be measured. This was done at room temperature. The images of topography and lateral PFM are shown in Fig. 3.19 (a) and (b), respectively. The bright area corresponds to the piezoactive BCZT, while the dark area is most probably the non-piezoactive CFO(Al) phase. The distribution of

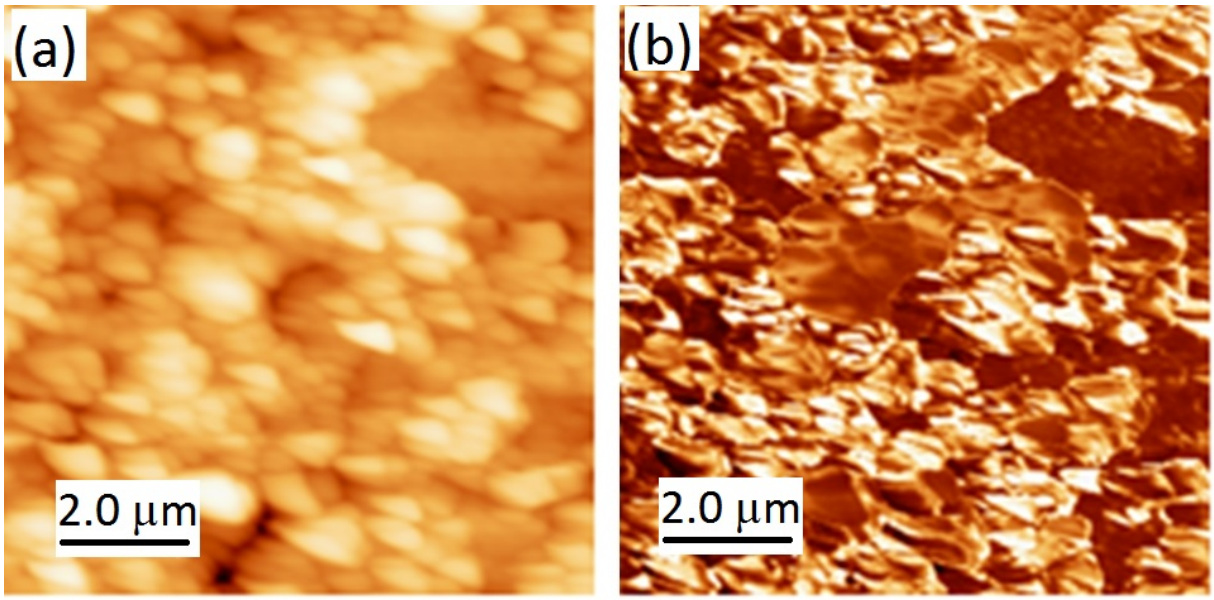

Figure 3.19: (a) Topography, (b) Lateral PFM image of the $BCZT_{50}$-$CFO(Al)_{50}$

the two phases as seen via PFM images is in agreement with the SEM image 3.17 (b). Moreover, the bright area is not continuous, while the dark/less bright area consists of continuous path like structures. This confirms that the non-piezoactive ferrite phase percolates, forming continuous portions. This agglomeration is a key factor when the sample is required to be electrically poled for piezoelectric and magnetoelectric measurements. Electric poling is hindered by these semiconducting continuous paths of the ferrite phase when the voltage which is supplied to orient the piezoelectric grains is dropped on these continuous paths, and a type of charge flow is created at poling temperatures ($>$ 100 ℃).

3.3.3.3 Magnetic and Magnetoelectric Characterizations

Magnetization as a function of *dc* magnetic field was measured at room temperature. The $M(H)$ curves are shown in Fig. 3.20 (a) and (b) for $BCZT_{50}$-CFO_{50} and $BCZT_{50}$-$CFO(Al)_{50}$, respectively. The important thing to note is that the saturation magnetization for $BCZT_{50}$-CFO_{50} has a lower value (91 kA/m) than the one for $BCZT_{50}$-$CFO(Al)_{50}$ (106 kA/m). This discrepancy might be attributed to the presence of extra-phase as detected in the XRD spectrum of $BCZT_{50}$-$CFO(Al)_{50}$. This hexagonal phase is also ferrimagnetic, but is ferromagnetically hard with a saturation magnetization value much lower than in cobalt ferrite. Also, there is a possibility of perovskite $BaFeO_{3-x}$ phase as demonstrated by Van Hook.[239] This phase has a tetragonal unit cell similar to BCZT and is indistinguishable from it owing to its very similar lattice parameters,[240] but is not ferromagnetic. The saturation magnetization of $BCZT_{50}$-CFO_{50} is lower than that of $BCZT_{50}$-$CFO(Al)_{50}$ which might not contain the impurity $BaFeO_{3-x}$ phase.

The magnetoelectric signal is induced as a result of the applied *ac* electric field. Its *dc* magnetic field dependence is shown in Fig.3.21(a) and (b) for $BCZT_{50}$-$CFO(Al)_{50}$ and

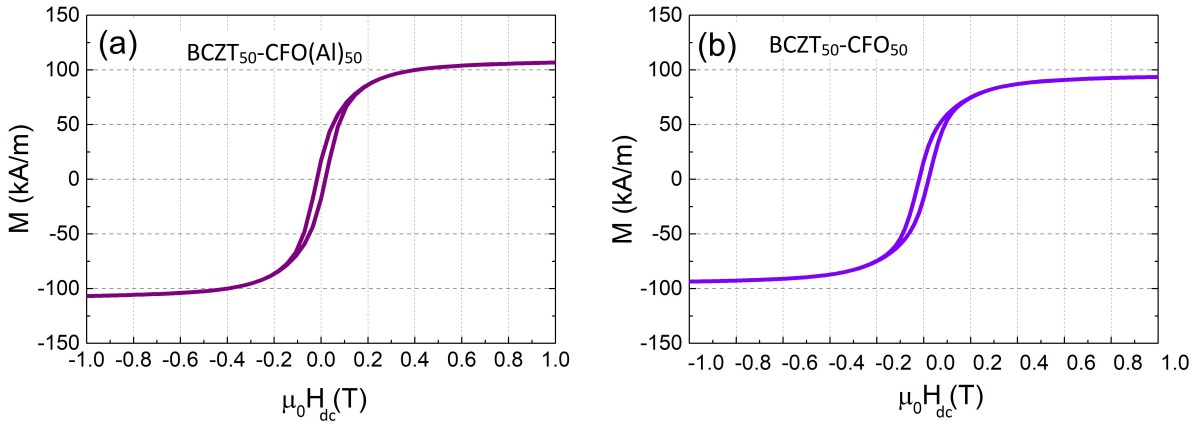

Figure 3.20: $M(H)$ loops of the (a) $BCZT_{50}$-$CFO(Al)_{50}$ and (b) $BCZT_{50}$-CFO_{50} measured at room temperature.

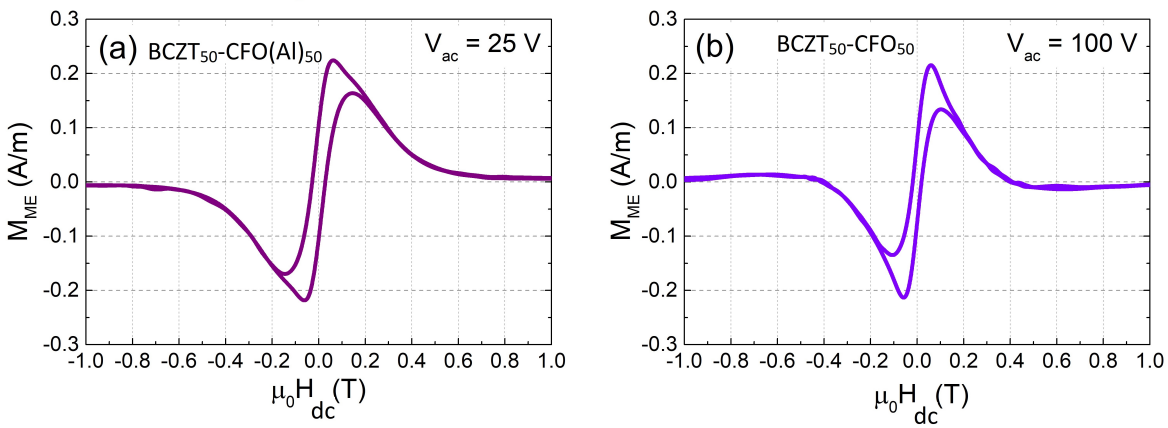

Figure 3.21: $M_{ME}(H)$ loops of the (a) $BCZT_{50}$-$CFO(Al)_{50}$ and (b) $BCZT_{50}$-CFO_{50}. The maximum value of induced ME magnetization for $BCZT_{50}$-$CFO(Al)_{50}$ is 8.4 $\times$ 10^{-3} A/m per volt while it is 2.1 $\times$ 10^{-3} A/m per volt in $BCZT_{50}$-CFO_{50}.

$BCZT_{50}$-CFO_{50}, respectively. $M_{ME}(H)$ have similar shapes at low magnetic fields. The common feature is a presence of some induced ME at zero *dc* magnetic field)known in literature as self-biasing effect and a small hysteresis at low magnetic fields. Increasing field from zero value, the induced signal increases monotonically, reaches a maximum, and then decreases again with a further increase in the field. The maximum value of induced ME magnetization for $BCZT_{50}$-$CFO(Al)_{50}$ is 8.4 $\times$ 10^{-3} A/m per volt while it is 2.1 $\times$ 10^{-3} A/m per volt in $BCZT_{50}$-CFO_{50}. For $BCZT_{50}$-$CFO(Al)_{50}$, the signal reduces to zero at around $\mu_0 H = \pm$ 1 T (known as zero-crossing in literature). However, in case of $BCZT_{50}$-CFO_{50}, it changes sign at around $\mu_0 H = \pm$ 0.4 T, and upon further increase in field, becomes zero again.

The temperature dependence of the induced ME signal was also determined. In this case, the amplitude of the *ac* electric field as well as the magnitude of the *dc* magnetic field were kept constant. The temperature dependence was monitored from 250 K to

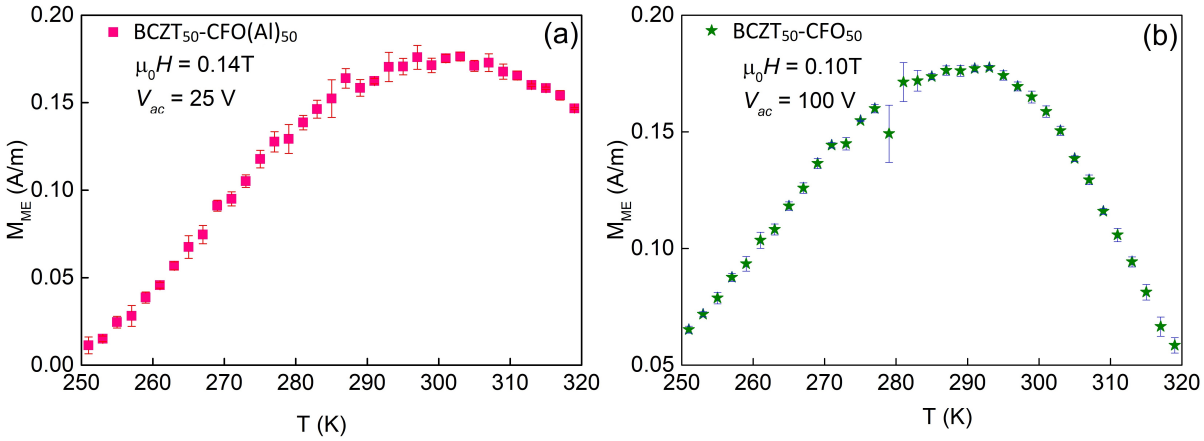

Figure 3.22: $M_{ME}(T)$ curves of the (a) BCZT$_{50}$-CFO(Al)$_{50}$ and (b) BCZT$_{50}$-CFO$_{50}$.

320 K. It is shown in Fig. 3.22. The induced magnetization increases with increment in temperature, passes through a broad maximum and then decreases again with further increasing temperature. Both samples have maximum values of induced ME close in the temperature range of 270 - 310 K, approximately. These plots confirm decent ME coupling at or close to room temperature.

To determine the converse ME coefficient, the electric field amplitude was incremented in regular steps. The resultant induced magnetization was recorded under a constant *dc* magnetic bias. The behavior is linear for both samples. However, the slopes of the lines are different. The slope gives the value of ME coefficient α_c according to the Relation 3.6 i.e., $\mu_0 M_{ME} = \alpha_c E_{ac}$. The values of α_c for BCZT$_{50}$-CFO(Al)$_{50}$ and BCZT$_{50}$-CFO$_{50}$ are 11 $\times$ 10^{-12} s/m and 3 $\times$ 10^{-12} s/m, respectively. So we see a significant enhancement of about four times of the converse ME coefficient in case of Al^{3+} modification to cobalt ferrite. This enhancement is also remarkable when compared to samples with 15 % cobalt ferrite, which was 6 $\times$ 10^{-12} s/m. This also shows that ME coupling does not depend on the volume percentage of the ferrite phase. In fact, it is the improvement of magnetostrictive properties of cobalt ferrite due to Al^{3+} substitution that causes this enhancement in the ME coupling of the composite.

3.3.3.4 Direct ME Characterizations via PFM under Magnetic Field

Direct ME effect was also explored by applying *dc* magnetic field and performing point by point piezoforce microscopy. Fig. 3.24 shows the sequence of such PFM images along with topography for BCZT$_{50}$-CFO(Al)$_{50}$. The PFM response was initially measured without a magnetic field. After that, an in-plane *dc* magnetic field was applied to the ceramic composite in one direction with a magnitude of 500 Oe (50 mT) with subsequent measurement of PFM response. A similar procedure was repeated for the field applied in the opposite direction to the previous step. The contrast improved with the application

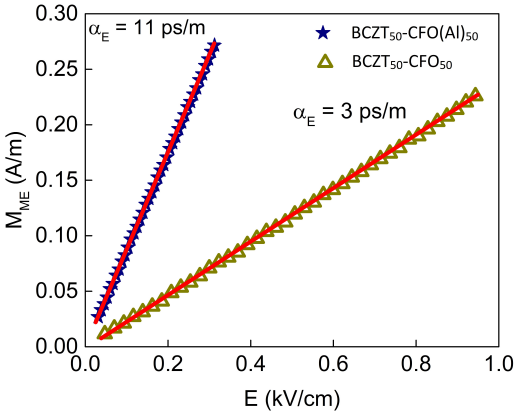

Figure 3.23: Electric field induced magnetization $M_{ME}(E)$ curves of the (a) $BCZT_{50}$-$CFO(Al)_{50}$ and (b) $BCZT_{50}$-CFO_{50}. The solid lines are the fittings to the relation 3.6.

of a magnetic field in one direction diminished when the field was removed and enhanced again in the opposite orientation of the field. The surface areas, where the contrast changes visibly, are highlighted for clarity in Fig. 3.24. For a further proof of direct ME effect, switching spectroscopy polarization loops were also measured under various magnetic fields at certain different spots, one such example is illustrated in Fig. 3.25 (b-e). There is a clear variation in amplitude under different values of magnetic field. Similar loops were also observed when the direction of the magnetic field was reversed (not shown here). Both these measurements, i.e., PFM images and SSPFM loops under magnetic field are a clear indication of direct ME coupling at the local scale in this composite.

3.4 Discussion

Let us discuss the decrease of saturation magnetization for CFO(Al) as compared with CFO as shown in Fig.3.13. CFO in its unmodified form is a mixed spinel of the $[Co^{2+}, Fe^{3+}]_A[Co^{2+}, Fe^{3+}]_BO_4$. The saturation magnetization (M_S) depends upon the strongest super-exchange coupling (antiparallel coupling) between the tetrahedral (A) and Octahedral (B) sites, given by the relation:[241] $E_{ex} = -J_{AB} < S_A \cdot S_B >$ where S_A and S_B are the spins on nearest neighbor ions and J_{AB} is Heisenberg's exchange integral for two nearest neighbors A and B. It is clear from the analysis of CFO(Al) in Section 3.2.2 that Al^{3+} has a strong preference for the B-site in the AB_2O_4 spinel lattice. So there is an overall decrease in the number of Fe^{3+} ions at B-sites due to their replacement with Al^{3+} ions, as a result of which now fewer Fe^{3+} ions at B-sites are linked via superexchange to A-site Fe^{3+} ions. Thus, a decrease in the strength of the A-B inter-sublattice super-exchange interactions resulted, and eventually, this weakening of super-exchange interaction would lead to a decrease in saturation magnetization of CFO(Al).

For stress-mediated ME coupling, magnetic field dependence of the magnetoelectri-

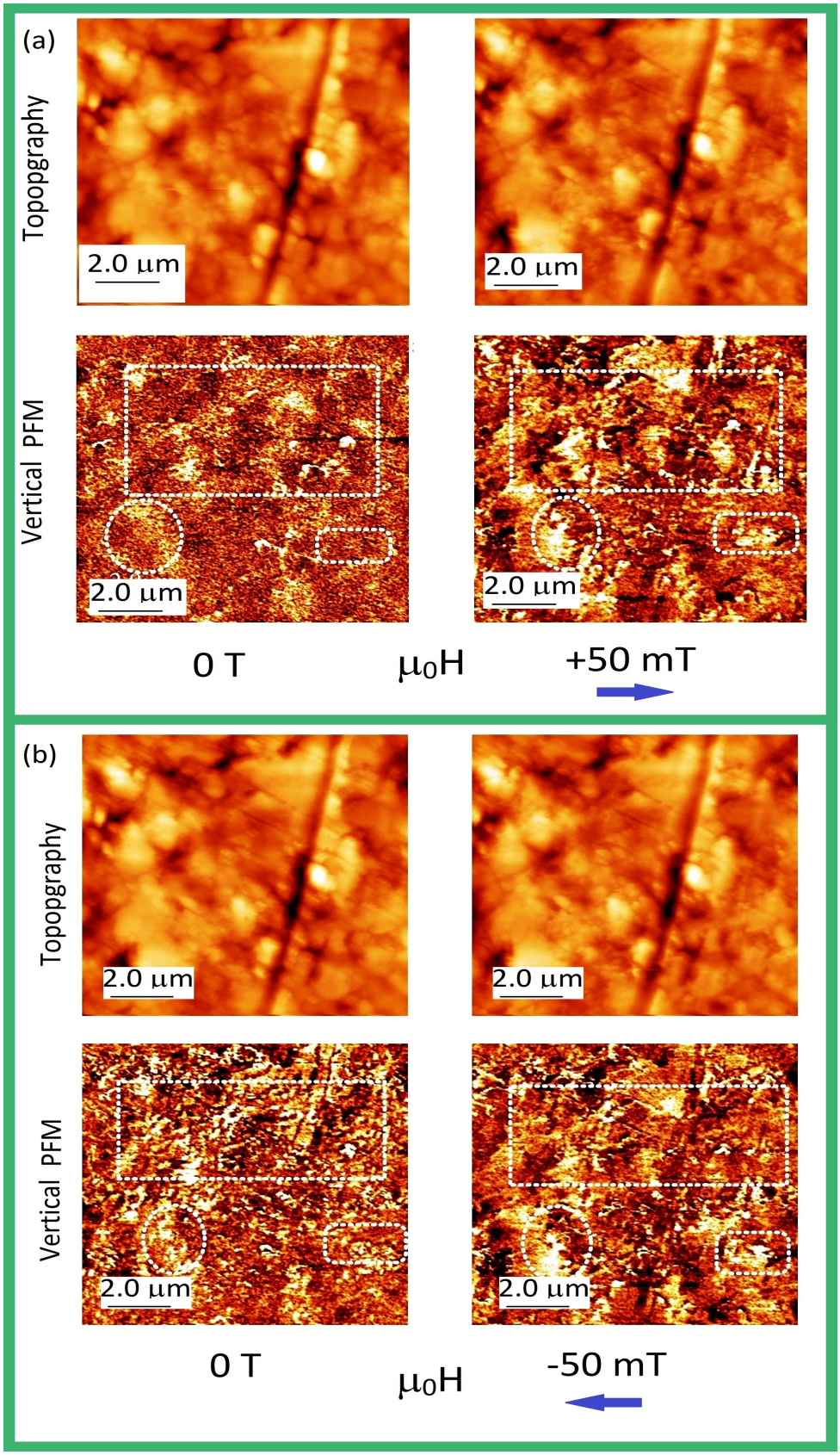

Figure 3.24: Magnetic field induced changes in the vertical PFM response for $BCZT_{50}$-$CFO(Al)_{50}$. In-plane *dc* field applied in opposite directions (also indicated by arrows) is marked with positive in (a) and negative in (b). The areas where there is a maximum change in PFM contrast are highlighted for clarity.

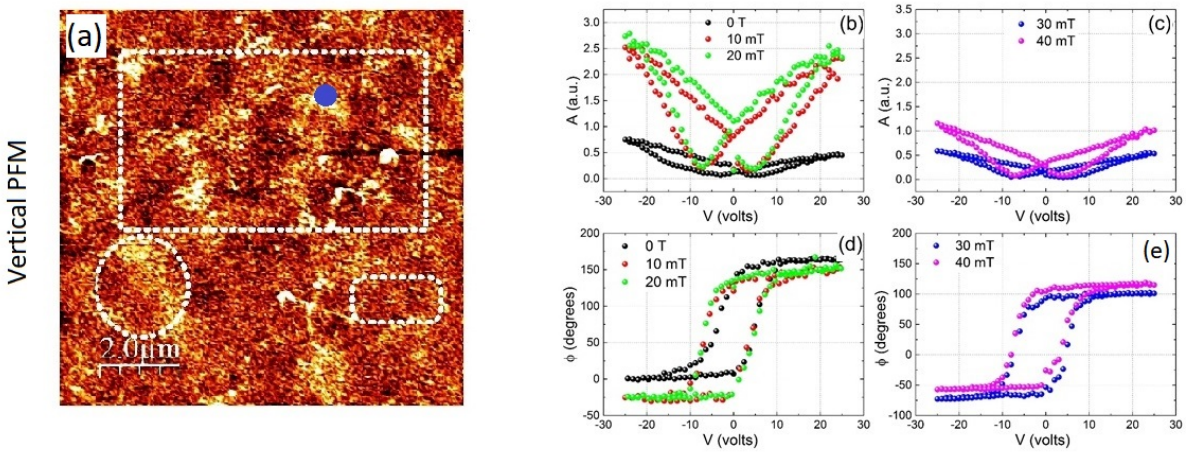

Figure 3.25: SSPFM phase and amplitude loops measured at various *dc* magnetic values, to explore the direct ME coupling in $BCZT_{50}$-$CFO(Al)_{50}$, the point where all these loops were taken is marked with a blue symbol in the vertical PFM image.

cally induced moment (i.e. $M_{ME}(H)$) is given by the product of piezoelectric times the *effective piezomagnetic* tensors, and the effective piezomagnetic tensor is itself magnetic field dependent. So converse ME coupling might be decomposed as:[242]

$$\alpha_{conv} = \frac{\mu_0 dM_i}{dE_j} = q_{imn} \cdot c_{mnkl} \cdot d_{jkl} \tag{3.9}$$

where d_{jkl} is the piezoelectric tensor and c_{mnkl} is the *effective stiffness* of the material microstructure, and q_{imn} is the piezomagnetic tensor. q_{imn} is a symmteric tensor as can be seen from Eq: 1.32. It is proportional to $d\lambda_{im}/dH_n$ where λ_{im} are the components of magnteostrictive tensor. Thus the shape of the $M_{ME}(H)$ curves can be conveniently explained by taking into consideration the shapes of the $\lambda(H)$ and $d\lambda/dH$ curves as shown schematically in Fig. 3.26 (a) and (b), respectively. The shape of the $d\lambda/dH$ curve in Fig. 3.26 (b) is similar to the $M_{ME}(H)$ curves shown in Fig. 3.11 (a), and to those shown in Fig. 3.21 (a) and (b). Thus $M_{ME}(H)$ tracks the behavior of $d\lambda/dH$ in a *dc* magnetic field. As given by Eq. 1.53, the overall magnetostriction behavior depends on the collective behavior of λ_{100} and λ_{111}. In Fig. 3.26(a), the slope of the $\lambda(H)$ curve was initially negative and later positive. The initial of the curve represents a region in which the contribution of λ_{100} to its amplitude is dominant. This continues until all magnetic domains align parallel to the easy axes. After this, on further rise of magnetic field value, the contribution of λ_{111} to the amplitude of is observed. That is also the reason of change in sign of the $M_{ME}(H)$ curves for the composites which contain unmodified CFO.

A small self-biasing effect is present at low magnetic fields especially when the field was swept from higher values. This effect is not first-hand, the early observation of this self-biased ME effect can be traced to the year 2002 when it was first observed

in $La_{0.3}Sr_{0.3}MnO_3$-PZT laminates by Srinivasan *et al.*[243] Other systems with similar hysteretic behavior include Co-PZT-Co and Fe-PZT-Fe trilayers.[67] These interesting characteristics of hysteresis and the self-biased effect at low fields can be explained in terms of $d\lambda/dH$ of the magnetostrictive phase especially when considering the dynamic response when a *dc* magnetic field is superposed on an *ac* magnetic field. Therefore, the *ac* magnetomechanical response has a different form than its *dc* and it can be given as:[244]

$$\frac{d\lambda}{dH} = \frac{4\pi\mu_r\lambda'}{Y} \tag{3.10}$$

Where λ' is the *ac* magnetostrictive constant, μ_r is the reversible permeability, and Y is Young's modulus. Thus, the shape of low field induced ME curve or the magnetostriction hysteresis based self-biasing effect can be influenced by several factors, the most probable factors that might cause the hysteresis are:

1. The demagnetization field of the magnetostrictive phase. If the demagnetization field is high, it causes the *effective* magnetic induction to be reduced and therefore influences the slef-biasing effect.

2. The composition gradients that might arise due to either chemical reaction between the ferromagnetic and ferroelectric or due to their inter-diffusion. These inter-diffused regions which might contain built-in self-biasing, and therefore the hysteresis.

3. Residual stress might also arise at the interfaces of the two phases due to high temperature sintering process. This might be due to lattice mismatching of the constituent phases or might be due to thermal mismatch. This mismatch serves multipurposely, by providing mechanical coupling and can be possible reason of unique behavior like self-biasing effect.

Two important quantities to be considered here the electromechanical coupling coefficients of BCZT and the magnetomechanical coupling coefficient of the ferrite. These are important criteria for evaluating and are a measure of the conversion of magnetic/electric to mechanical energy and vice versa. These are defined as[245] the square root of the ratio of the converted stored energy to the input stored energy provided there are no losses or radiation.

$$k_m^2 = \frac{\lambda_s^2 Y}{|K_1| + |\lambda_s\sigma_{int}| + K_{shape}}; \tag{3.11}$$

where σ_{int} is the internal stress anisotropy and K_{shape} is the shape anisotropy. The internal-stress anisotropy depends on the sample preparation technique. The magnetocrystalline anisotropy energy is controlled by the chemical composition and is a func-

tion of the temperature. K_1 of cobalt ferrite is positive while other ferrites have negative values of K_1 at room temperature. Internal stresses are always present due to the high temperature sintering and unequal thermal expansion coefficients, and phase transition temperature. It is well-known that the components of electromechanical coupling factor (k_{ij}) might be written as:[18,246]

$$k_{ij} = \frac{d_{ij}}{\sqrt{\varepsilon_{ii} S_{jj}}} \tag{3.12}$$

Where k_{ij} is electromechanical coupling factor, ε_{ii} is the component of electric permittivity, and S_{jj} is the component of elastic compliance, and the indices ij correspond to 33, 31 and 15. Cordero *et al.* measured the elastic properties of BCT-50BZT which proved to be quite useful in studying the intermediate phase at the polymorphic phase boundaries and its role in increasing the piezoelectric response.[247] The measurements are shown in Fig. 3.27, the real part of compliance for BCT-50BZT peaks at the tetragonal to orthorhombic phase transition (290-295 K); and an additional broader maximum at 250-260 K suggesting orthorhombic to rhombohedral transition, while the Curie temperature is identified as 360 K as a sharp step. From Relation 3.12, it is evident that there might be some temperature dependence in k_{ij} due to the strong temperature dependence in S.

Therefore the temperature dependence of induced ME magnetization (M_{ME}) for $BCZT_{85}$-CFO_{15} (Fig. 3.10) and also for $BCZT_{50}$-$CFO(Al)_{50}$ and $BCZT_{50}$-CFO_{50} (Fig. 3.22(a) and (b)) would have a dependence on the compliance of BCZT because it has already been discusssed that magnetomechanical coupling factor κ_m is slightly temperature dependent. And the broad maximum in $M_{ME}(T)$ of all samples is a manifestation of competing properties of the piezoelectric and magnetostrictive phases. At low magnetic fields λ can be approximated by $\lambda \sim M^2$, so one could write:[45]

$$\frac{\lambda}{\lambda_s} = \frac{M^2}{M_s^2} \tag{3.13}$$

Considering the rotation of magnetization against anisotropy in an untextured polycrystalline material with random distribution of easy axes, one has:

$$\frac{dM}{dH} = \frac{\mu_0 M_s^2}{N K_1} \tag{3.14}$$

Where N = -3 for cubic anisotropy and $\lambda < 0$. And

$$\frac{d\lambda}{dH} = \frac{d\lambda}{dM} \cdot \frac{dM}{dH} \tag{3.15}$$

and therefore,

$$\frac{d\lambda}{dH} = \frac{2\mu_0 \lambda_s M}{N K_1} \tag{3.16}$$

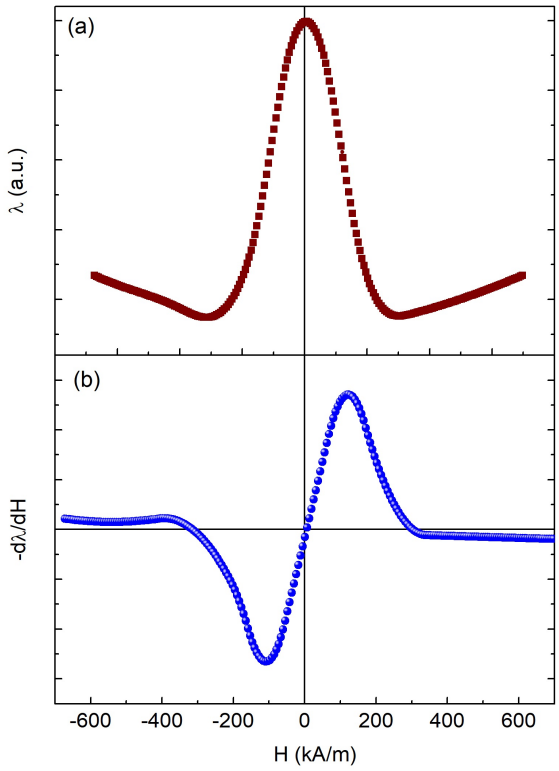

Figure 3.26: Schematic diagram showing (a) $\lambda(H)$ for CFO; (b) its derivative. The shape of the curve in (a) was copied from an article by Nlebedim *et al.*[231]

Which shows that the anisotropy constant K_1 is inversely proportional to $\frac{d\lambda}{dH}$. This is because of the fact that magnetostriction and magnetocrystalline anisotropy in spinel ferrites are both dependent on spin orbit coupling. The magnetocrystalline anisotropy in CFO was explained in terms of *one ion model*. i.e., Co^{2+} ion on B-sites produces a positive value of anisotropy constant K_1 in Section 1.4.2.3. As shown in Section 3.2.2, the Co^{2+} concentration at octahedral sites was decreased form 0.744/unit cell in unmodified CFO to 0.716/unit cell in CFO(Al). Resultantly, the effect of spin-orbit coupling would also decrease, thereby decreasing the crystal anisotropy constant of CFO(Al). This decrease in anisotropy constant, and the anisotropy field which is responsible for higher magnetostriction in a certain orientation thus would decrease. However, $d\lambda/dH$ would increase according to relationship 3.16. Thus the enhanced converse ME coefficient in $BCZT_{50}$-$CFO(Al)_{50}$ might be attributed to the improved $d\lambda/dH$ behavior of cobalt ferrite after its modification with Al^{3+}.

The evidence of direct ME presented in the last section can also be explained from the fact that in PFM, the effective value of d_{33} is measured by the tip, which can be given by:

$$d^{eff} = \varepsilon_0 Q \varepsilon(E) P \tag{3.17}$$

where $\varepsilon(E)$ is the field dependent electric permittivity and $P(E)$ is the static or *dc*

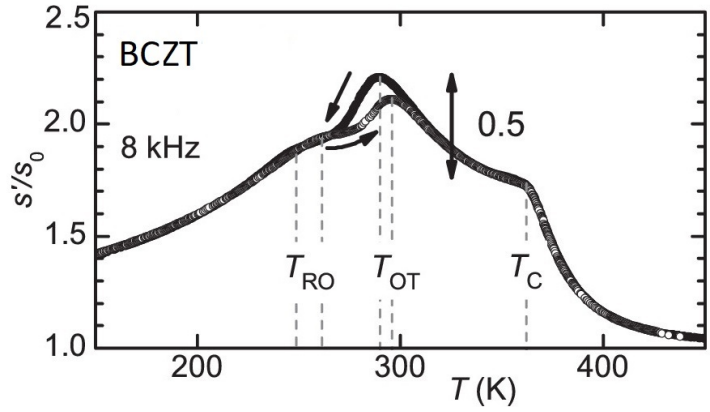

Figure 3.27: Elastic compliance of BCZT measured at 8 kHz during heating and cooling.[247] Image reused with permission from © 2014 AIP Publishing LLC.

polarization which shows that $d_{33} \propto P$. The PFM response or ΔP in this case is excited by *dc* magnetoelectric coupling $\alpha(H_{static})$ which can be given by:

$$\Delta P = \alpha(H_{static})\Delta H_{static} \tag{3.18}$$

Here $\alpha(H_{static})$ is the *dc* coupling coefficient different from the dynamic *bulk* ME coefficient that is normally measured with *ac* electric/magnetic fields. The effective d_{33} on the application of magnetic field for the whole system is given by $d^{eff} = d_0 + \Delta d^{eff}$, where

$$\Delta d^{eff} = \varepsilon\varepsilon_0\alpha(H_{static}) \tag{3.19}$$

There is a small complexity here that the observed PFM variation with a magnetic field can be intrinsic (strain-mediated ME coupling) or extrinsic (might be due to the electrostatic interaction between the tip and the sample or hysteretic charging of the sample surface). To remove this complexity, switching spectroscopy PFM was performed on various spots of the sample, one example of which is shown in Fig.3.25(a-e). The SSPFM amplitude was measured at different points on the sample surface with and without an in-plane magnetic field. The SSPFM analysis confirmed that the PFM response was indeed strain mediated, because all the amplitude loops, either with or without external magnetic field being applied, are symmetric concerning the direction of the applied voltage. These loops might have been asymmetric in the presence of extrinsic effects which was not the case in this sample.

3.5 Summary and Conclusions

In the first part of this chapter, synthesis, and characterization of a new multiferroic magnetoelectric system $BCZT_{85}$-CFO_{15} were presented. Electrical analysis revealed that there exist two types of relaxation mechanisms in these two phase composites. These

two categories of relaxation might be explained equivalently using either grain boundary effects or by the presence of electric heterogeneity due to a less conductive piezoelectric and a more conductive ferrite phase. Equivalent circuit analysis suggested that two types of relaxations fit best to the latter, namely, the two-phase model. Further analysis of dielectric data revealed that Maxwell-Wagner type space charge polarization was responsible for dielectric dispersion at low-frequencies and at high temperatures, the origin of this space charge polarisation is the temperature-activated behavior of charged species due to the ferrite phase. The converse magnetoelectric coefficient for $BCZT_{85}$-CFO_{15} had a value of 6 ps/m which represented an enhancement over the two-phase magnetoelectric composites prepared via similar solid state method. In other samples with higher CFO vol.% no enhancement of ME coupling was achieved. Therefore, CFO was modified to enhance it.

Cobalt ferrite was modified by the substitution of Al^{3+} for Fe^{3+}. Al^{3+} favored more octahedral sites rather than the tetrahedral ones, thus decreasing the saturation magnetization as compared to the unmodified one. However, the advantage of such modification was achieved in terms of stress sensitivity ($dB/d\sigma$) which is equivalent to the magnetic field derivative of magnetostriction ($d\lambda/dH$).

To observe the effect of such modification on magnetoelectric effect, two samples were prepared with the same volume percentage of cobalt ferrite (50 %) and BCZT. However, one sample contained Al^{3+}-modified cobalt ferrite while the other contained the unmodified one. Both samples contained small amounts of a hexagonal phase as it was detected from the XRD measurements. Magnetization hystereses looked similar with small coercive magnetic fields. The difference in saturation magnetization was also not very large due to the possibility of non-magnetic perovskite phase in $BCZT_{50}$-CFO_{50}. However, there was a significant difference between the electrically induced magnetization, i.e., the converse magnetoelectric coupling. The value of converse magnetoelectric coefficient was 12 ps/m $BCZT_{50}$-$CFO(Al)_{50}$ which was 4 times as large as for the composite that contained unmodified cobalt ferrite $BCZT_{50}$-CFO_{50}(3 ps/m). This improvement is believed to be originating from the improvement of $d\lambda/dH$ in Al^{3+}-modified cobalt ferrite. The Al^{3+} replacing Fe^{3+} ions on the octahedral sites not only led to the weakening of superexchange interaction between A and B-site cations but also resulted in the weakening of spin-orbit coupling. This weakening of exchange interaction reduced the saturation magnetization, and weakening of the spin-orbit coupling enhances the stress sensitivity of cobalt ferrite that can be given by $d\lambda/dH$. Thus the ME coupling is enhanced in $BCZT_{85}$-CFO_{15} because the coupling is directly related to $d\lambda/dH$. The temperature dependent ME coupling was attributed to depend on the behaviors of magnetomechanical and electromechanical coupling factors of ferrite and piezoelectric phases.

Chapter 4

Direct and Converse Magnetoelectric Effect in BCZT-NFO system

Replacement of Co^{2+} ions in $CoFe_2O_4$ with Ni^{2+} (NFO) ions leads to the formation of another magnetostrictive material known as $NiFe_2O_4$ with excellent properties. This chapter deals with a complete study including synthesis, structure, and magnetoelectric characterization of a new multiferroic ME composite system consisting of BCZT and NFO in various proportions.

4.1 Background and Motivation

Cobalt ferrite and its derivatives are extensively discussed in connection to their magnetostrictive properties in the previous chapters. $NiFe_2O_4$ has an identical structure with that of CFO and is a mixed-spinel ferrite with a saturation magnetostriction value ~ -27 ppm for the polycrystalline sample.[248] Although this value of magnetostriction is not significant as compared with that of CFO, however, the properties that matter the most for multiferroic ME composites are the initial permeability, the effective piezomagnetic coefficient of magnetostrictive strain ($d\lambda/dH$), and the magnetomechanical coupling factor. The initial permeability of NFO is 39 as compared with 1-2 for CFO.[249] It also possesses a decent strain derivative as well as magnetomechanical coupling factor values.[248] Therefore it was chosen to be combined with BCZT to make piezoelectric/magnetostrictive composites for the enhancement of magnetoelectric coupling.

4.2 Synthesis and Experimental Techniques

The BCZT powder was synthesized by using a two-step solid state reaction as described in earlier chapters. $NiFe_2O_4$ (NFO) was also prepared by the solid-state reaction method. The oxides of iron and nickel, i.e., Fe_2O_3 (Alfa Aesar GmbH KG, purity > 99%) and NiO (Alfa Aesar GmbH KG, purity > 99%) were mixed in ethanol in stoichiometric amounts and milled for 10 hours in an alumina crucible with yttria-stabilized zirconia balls. The mixture was dried and calcined for 6 hours at 1050 ℃ with a heating rate of 5 ℃/min and ball-milled again with the previously described parameters.

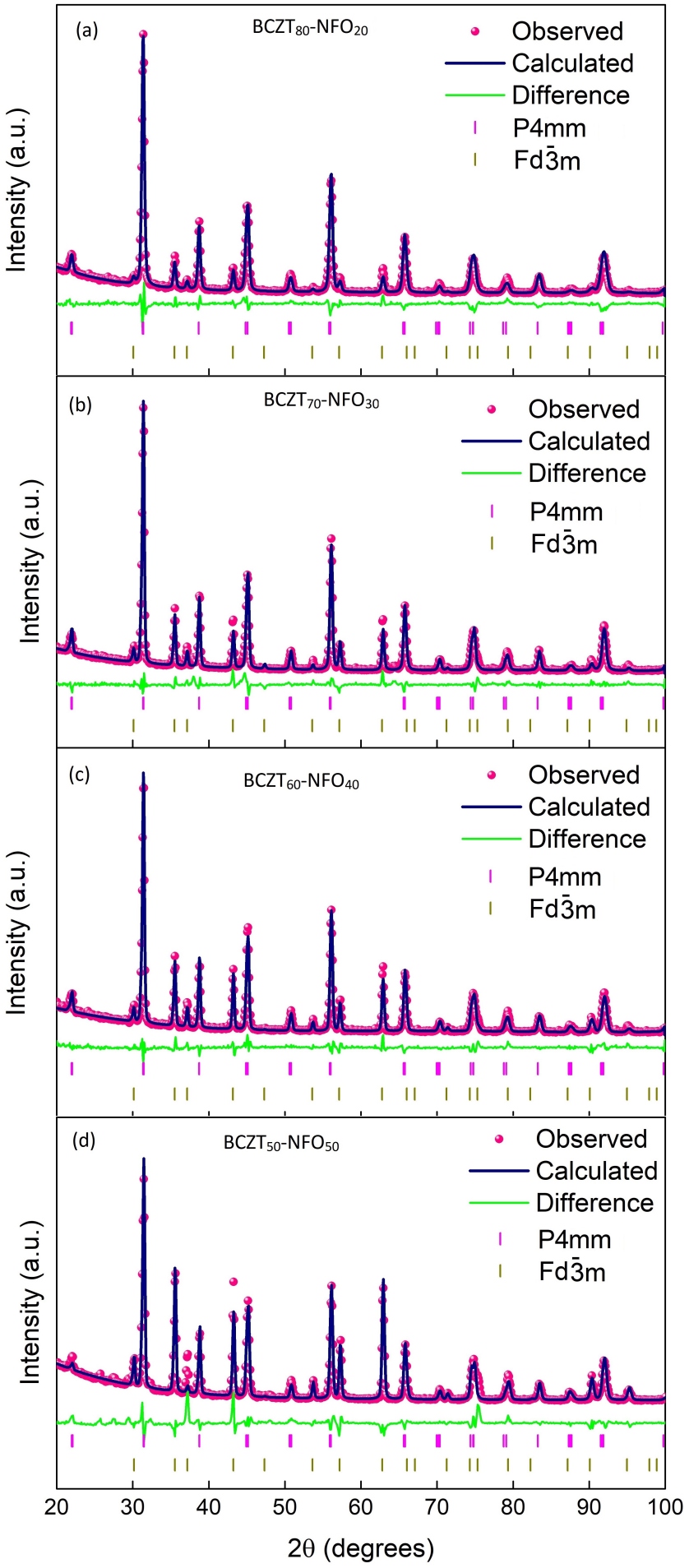

Figure 4.1: XRD spectra along with Rietveld analysis of $BCZT_{1-x}$-NFO_x ceramics. XRD spectra were taken at room temperature. The refinement was performed using freeware GSAS-II.[198]

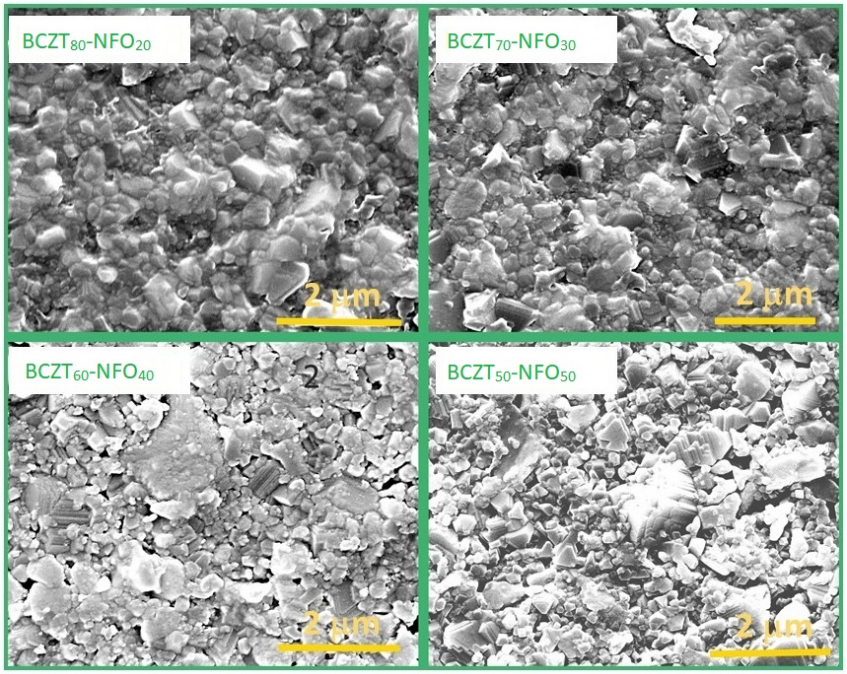

Figure 4.2: SEM surface images of all samples acquired at room temperature.

The calcined powders BCZT and NFO were mixed in respective vol.% ratios in ethanol and milled in a rotary ball mill for 6 hours at 300 rpm. The final sintering was done at 1200 ℃ for 6 hours in covered crucibles. The following four compositions were investigated:

- 0.8BCZT-0.2NFO ($BCZT_{80}$-NFO_{20})
- 0.7BCZT-0.3NFO ($BCZT_{70}$-NFO_{30})
- 0.6BCZT-0.4NFO ($BCZT_{60}$-NFO_{40})
- 0.5BCZT-0.5NFO ($BCZT_{50}$-NFO_{50})

The rest of the characterizations were the same as described for BCZT-CFO samples in previous chapters.

4.3 Structural Characterizations

The results of X-ray diffraction performed on all samples are shown in Fig. 4.1. The peaks in each spectrum correspond to two phases, one of them being the tetragonal BCZT phase, while the other one being cubic spinel NFO phase. For further analysis of the spectra, Rietveld analysis was carried out, using a two-phase model. The space groups used for fitting were P4mm and $Fd\bar{3}m$ for BCZT and NFO, respectively. The two-phase model was successful as can be seen from the fitted spectra and difference plots in Fig. 4.1. The complete set of unit cell parameters along with the goodness of fitting (GoF) parameter in each case are listed in Table 4.1. The XRD analysis has confirmed

the purity of each phase, and also the absence of any extra phase. SEM images of all samples are shown in Fig. 4.2, showing the grain distribution in the composites.

Table 4.1: Calculated parameters and fitting values as obtained from Rietveld analysis of the XRD data for all the samples.

Composition	$P4mm$ (Å)	**Vol. (Å^3)**	$Fd\bar{3}m$ **(Å)**	**Vol. (Å^3)**	**GoF**
$BCZT_{80}$-NFO_{20}	a = 4.00399 c = 4.02598	64.54	a = 8.34534	581.2	1.03
$BCZT_{70}$-NFO_{30}	a = 4.01190 c = 4.02942	64.86	a = 8.36360	585	1.14
$BCZT_{60}$-NFO_{40}	a = 4.00558 c = 4.02435	64.57	a = 8.35252	582.7	1.01
$BCZT_{50}$-NFO_{50}	a = 4.0106 c = 4.0311	64.48	a = 8.36299	584.9	1.15

4.4 Surface and Sub-surface Characterizations with the ToF-SIMS Technique

Fig. 4.3 (a) and (b) show the TOF-SIMS 3D reconstruction for the BCZTNF20 and BCZTNF30 samples. The top-surface shown was recorded at a depth of 200 nm below the actual sample surface. Red areas in the image represent the phase containing Fe-ions and the blue areas, on the other hand, represent the Ba-ion rich regions. These color proportions essentially signify the volume proportion of the two phases, i.e., blue for the ferroelectric BCZT and red for the NFO. The ferrite phase noticeably looks to be embedded in the piezoelectric phase, giving rise to a pseudo 3-0 connectivity in $BCZT_{80}$-NFO_{20} and $BCZT_{70}$-NFO_{30} samples. The higher concentration BCZT ferroelectric phase acts as a matrix, while the lower concentration ferrite phase acts as the embedded one. However, the connectivity scheme is not an ideal distribution of 3-0 matrix-particle one, as we see the ferrite phase forming continuous stripes and not the ideal distinct round particles (0-D configuration).

Similar ToF-SIMS images for samples $BCZT_{60}$-NFO_{40} and $BCZT_{50}$-NFO_{50} are shown in Fig. 4.3 (c) and (d). It is obvious that increasing the ferrite content during the synthesis step results in an increase of the ferrite-volume (red color) in the images. In the case of $BCZT_{60}$-NFO_{40} and $BCZT_{50}$-NFO_{50} the two phases are in nearly equal volume proportions. Here the two phases are bicontinuous giving rise to a kind of 3-3 type of connectivity, rather than the 3-0 as we see in $BCZT_{80}$-NFO_{20} and $BCZT_{70}$-NFO_{30}. The ferrite phase interconnections which were already present in $BCZT_{70}$-NFO_{30}, increased

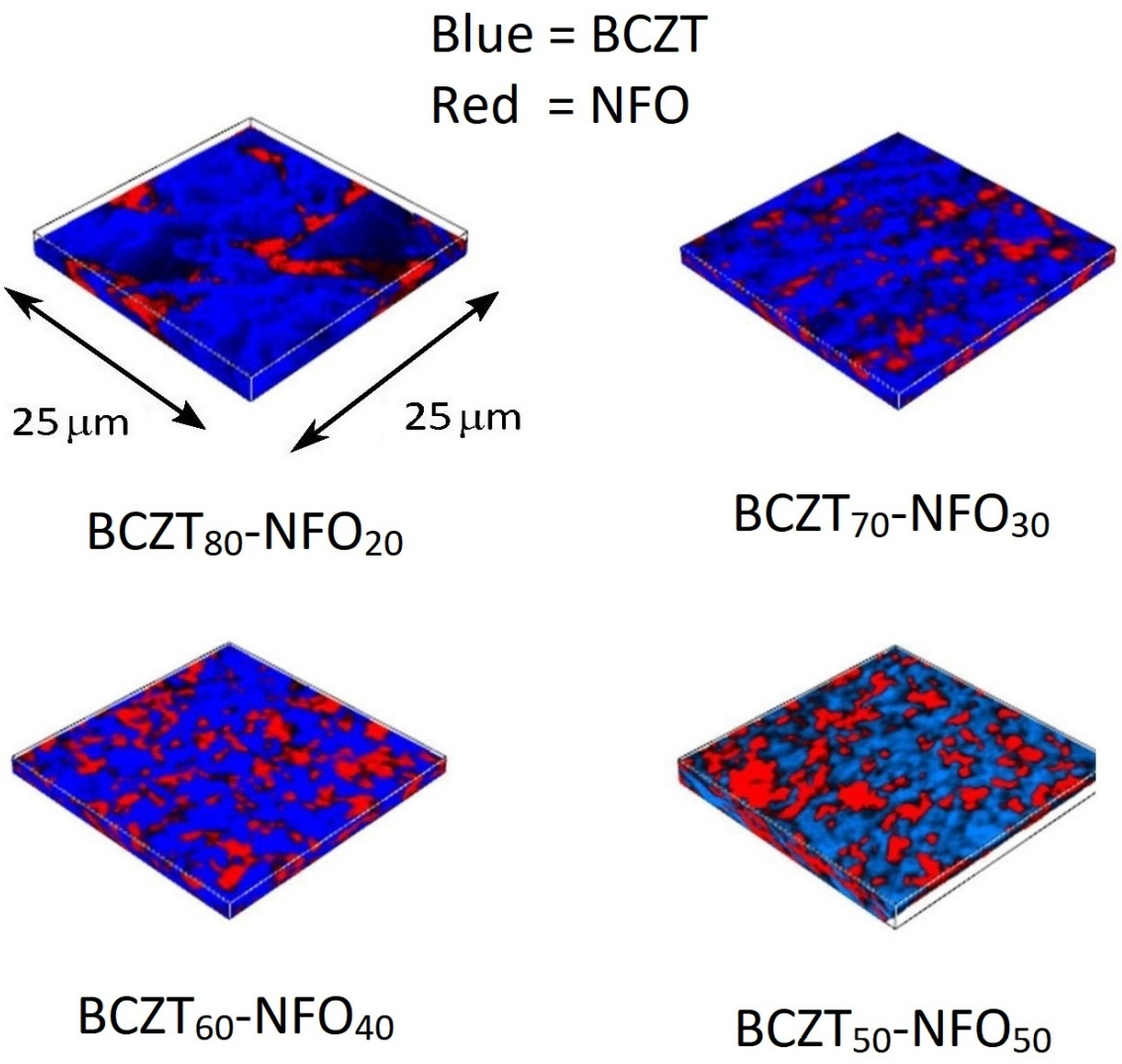

Figure 4.3: Time of Flight-Secondary-Ion Mass-Spectrometer (ToF-SIMS) images all samples. All images were acquired at room temperature.

greatly in number and intensity. These interconnections, which are the result of percolation of the ferrite phase, play a very decisive role in electrical and magnetoelectric properties. This phase connectivity hinders the electrical poling resulting in a poor magnetoelectric effect that will be discussed later.

4.5 Local Piezoelectric and Magnetic Characterizations

Due to the presence of the magnetic phase, the electric polarization properties of the composites are not easily singled out. The bulk response in these composites might originate from certain extrinsic effects like space-charge accumulation at grain boundaries. However, measuring the local piezoelectric response is a method to establish the presence of piezoelectricity. Piezoforce response microscopy (PFM) has been proven to be a powerful technique. The principle of PFM is that the tip makes contact with the sample surface and the piezoresponse is detected as a tip deflection. Due to a strong coupling between polarization and electromechanical response in piezo/ferroelectric materials, the information on local ferroelectric behavior can be collected. Both vertical and lateral PFM modes were utilized for the current investigation.

PFM images were taken at room temperature for all samples are shown in Fig. 4.4. It is divided into four panels. Each panel comprises of four images, which consist of (a) topography, (b) vertical and (c) lateral PFM, and (d) MFM images. All the images in Fig. 4.4 demonstrate appreciable local piezoelectric character of the samples, with a decent number of vertical as well as lateral piezo-domains. The number of those areas which are highly active (enhanced contrast) decreases consistently with the decrease in piezoelectric content from 80 % for $BCZT_{80}$-NFO_{20} to 50 % for $BCZT_{50}$-NFO_{50}. Moreover, comparing the PFM images with the topography in each case, it is quite clear that the response is intrinsic, and is not originating from any type of topological defect. The magnetic response was also measured at the same spot, and is shown in Fig. 4.4 (d) in each panel. The magnetic response is also quite pronounced, which again confirms the coexistence of two phases. Hence it has been verified with local measurements that the composites are multiferroics, with simultaneous piezoelectric and magnetic responses, in agreement with TOF-SIMS images in Fig. 4.3.

4.6 Magnetic measurements

All samples were inserted into the SQUID magnetometer, and magnetization versus magnetic field hysteresis $M(H)$ curves were measured. The DC magnetic field was swept between ± 5 T, and the resultant magnetization was recorded as displayed in Fig. 4.5 and the inset shows its zoomed-in view at low field values. All samples exhibit very slim

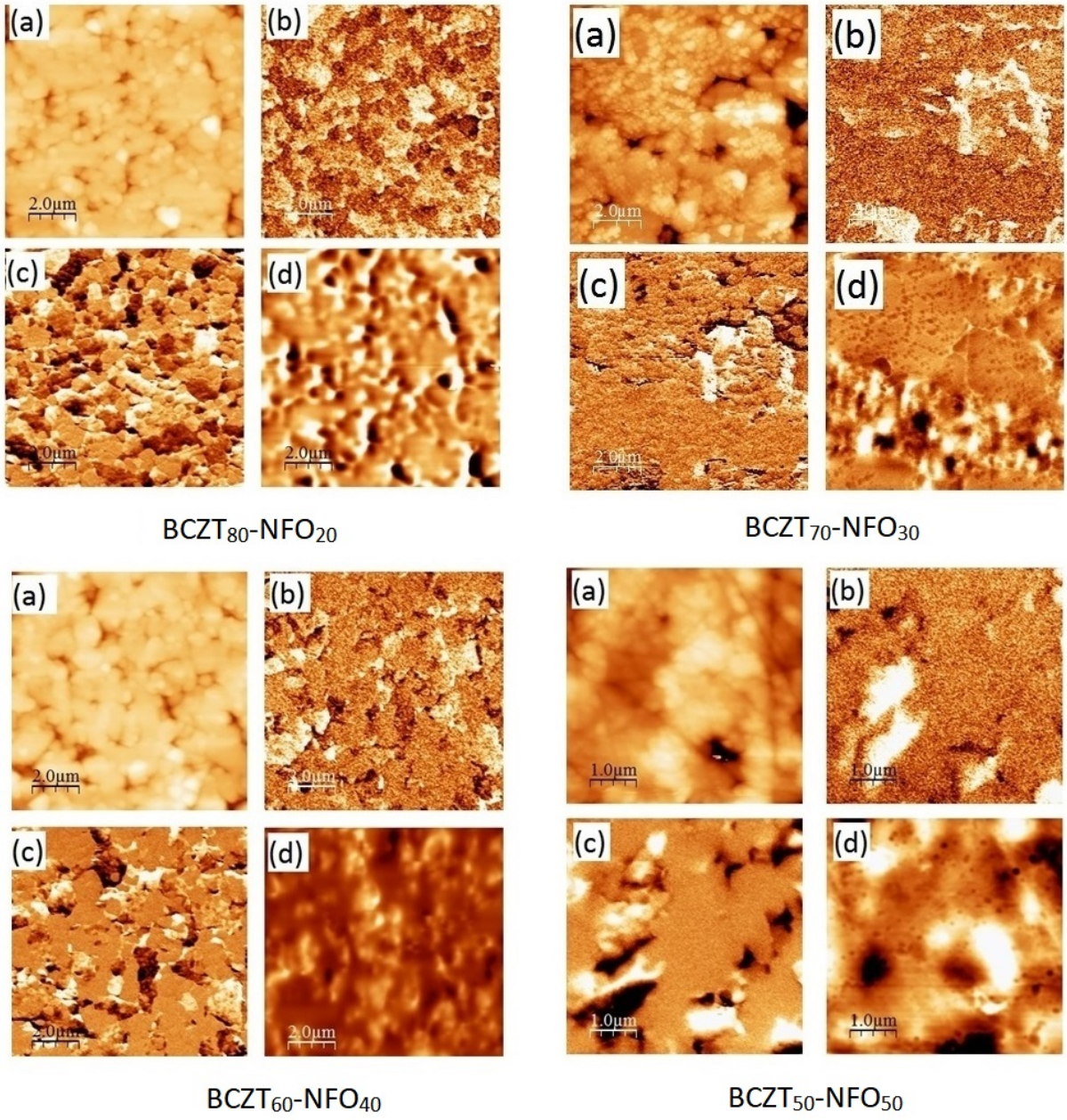

Figure 4.4: PFM images of the composites taken at room temperature: Panel 1-4 for $BCZT_{80}$-NFO_{20}, $BCZT_{70}$-NFO_{30}, $BCZT_{60}$-NFO_{40}, and $BCZT_{50}$-NFO_{50}, respectively. In each panel, the details are: part (a) for topography, part (b) for vertical PFM, part (c) for lateral PFM, and part (d) for MFM.

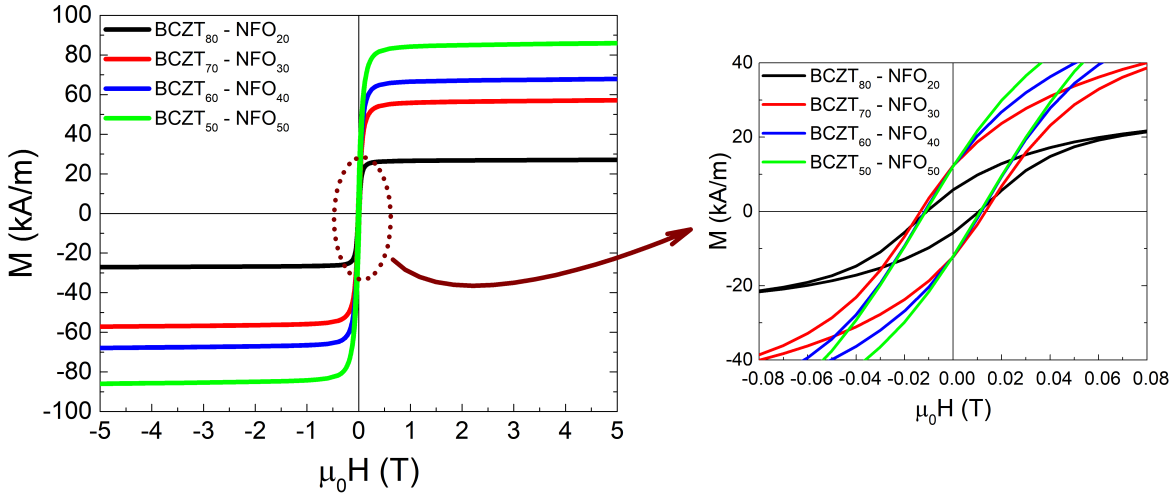

Figure 4.5: $M(H)$ curves for all samples measured at room temperature.

hysteresis, which is characteristic of NFO. All the samples have a low coercive magnetic field of almost the same value ($\mu_0 H = 0.02$ T). The values of saturation magnetization increase with the NFO-content in each case from 20 kA/m for $BCZT_{80}$-NFO_{20} to 80 kA/m for $BCZT_{50}$-NFO_{50}.

4.7 Magnetoelectric Measurements

Both the direct and the converse ME couplings were measured for all these compositions.

4.7.1 Direct ME Measurements at Room Temperature

4.7.1.1 Induced Voltage as a Function of Static Magnetic Field

The voltage induced as a result of an applied magnetic field, i.e., the direct magnetoelectric effect was probed at room temperature in all samples. The resultant values are plotted in Fig. 4.6. The full setup for this measurement is described in Chapter 2. Briefly describing, a *dc* magnetic field superposed on a small *ac* magnetic field (in this case 1 Oe) with a frequency of 1 kHz was applied to the sample, and the resultant induced voltage due to strain mediated ME coupling was recorded as a function of *dc* magnetic field sweep. The *dc* magnetic field was increased in small steps to a maximum value in one direction, decreased back to zero, increased in the opposite direction in the same manner and then decreased down to zero value again. The variation in induced voltage was recorded for this whole sequence. It is interesting to observe that with the increase in the magnetic field in either of the two directions, the induced voltage initially increased, went through a maximum and then decreased with further increase in the field. The induced voltage also displays a hysteretic behavior; its value is high when the *dc* magnetic field is decreased from higher values. This effect can be a manifestation of magnetic field

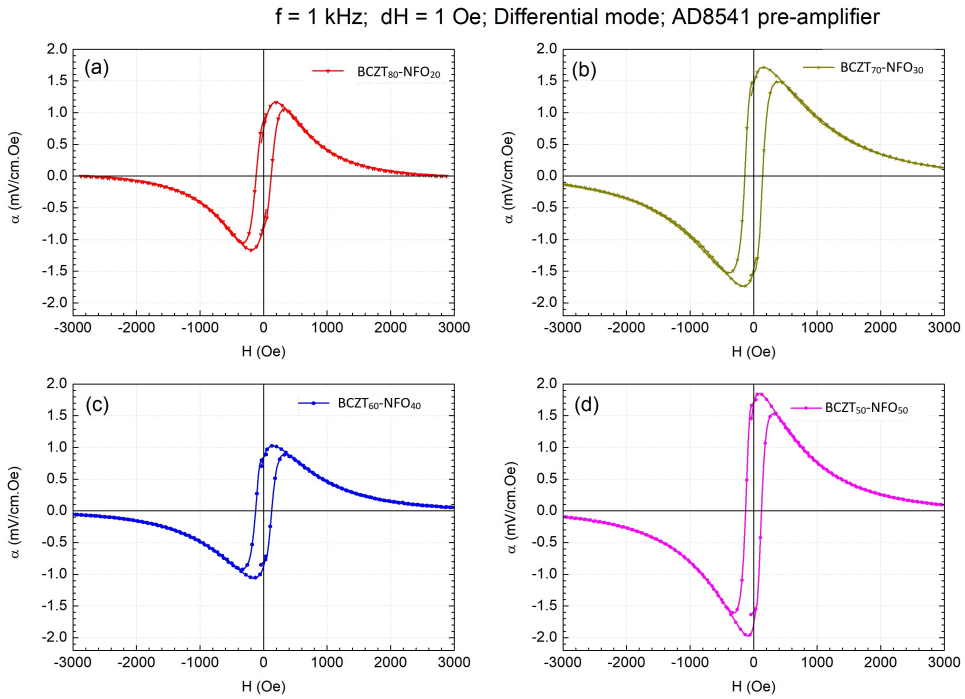

Figure 4.6: $\alpha_{direct}(H)$ curves of all the samples measured at room temperature, the parameters used to measure direct ME are also mentioned on top of the figure.

poling. The samples also had a non-zero value of induced ME voltage even at zero *dc* magnetic field value, which can be attributed to the exchange-bias effect that might be present in these samples. The maximum value of direct ME coefficient was obtained for $BCZT_{50}$-NFO_{50} sample (50 % ferrite) and is equal to 1.9 mV/Oe.cm which is comparable to those of $BaTiO_3$-$NiFe_2O_4$ composites.[115,116,133]

4.7.1.2 Induced Voltage as a Function of Frequency

When a pure piezoelectric ceramic is exposed to an *ac* field, it changes dimensions periodically, at the frequency of the field. The frequency at which the ceramic element converts the electrical energy input into mechanical energy most efficiently is the resonance frequency. The composition of the sample and the shape and volume of the element determine the resonance frequency. A thicker element has a lower resonance frequency than a thinner element of the same shape. All ceramic samples were checked for such resonance modes and only the $BCZT_{80}$-NFO_{20} ceramic showed one such resonance mode at 362 kHz.

The direct ME coupling coefficient was also measured as a function of *ac* magnetic field frequency. $BCZT_{80}$-NFO_{20} (see Fig. 4.7) had a maximum value of direct ME coefficient of 273 mV/Oe.cm at resonance which is almost 200-times larger than its off-resonance value. The reason for the absence of resonance in other samples might be due to less amount of piezoelectric phase where non-piezoelectric NFO contributes to the poor mechanical

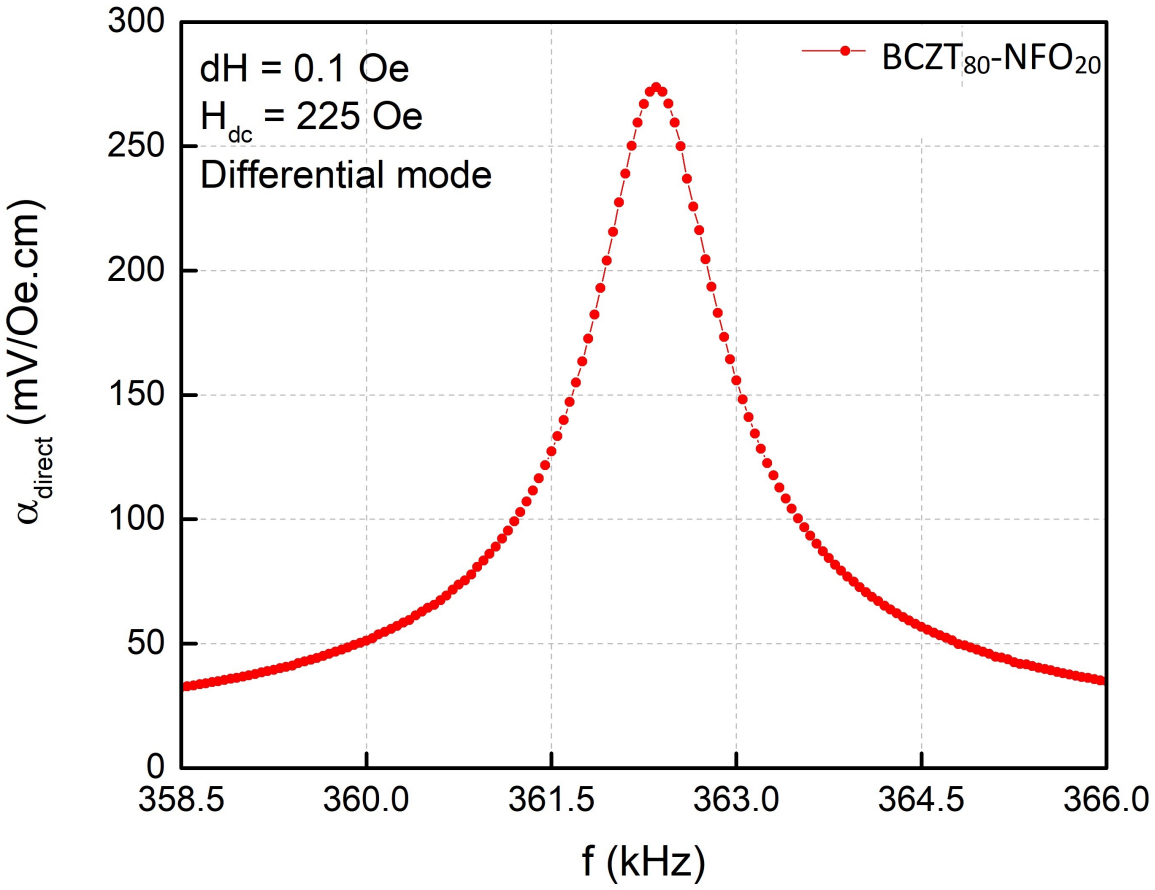

Figure 4.7: Direct ME coupling coefficient measured at resonance and at room temperature for $BCZT_{80}$-NFO_{20} sample.

properties of the composites.

4.7.2 Converse Magnetoelectric Measurements

Temperature dependence, *dc* magnetic field dependence, and the *ac* electric field dependence of the converse ME coupling was measured. The results will be described in detail below.

4.7.2.1 DC magnetic field dependence of electric field induced magnetization $M_{ME}(H)$

This was the first step to determine the optimum *dc* magnetic field value at which maximum induced magnetization might be obtained. To accomplish this, an *ac* electric field of fixed amplitude was applied to the sample at room temperature, and *dc* magnetic field is swept from zero to maximum value in opposite directions. The resultant induced magnetization is plotted as a function of H_{dc} as shown in Fig. 4.8 for all samples. In each of the curves in Fig. 4.8, $M_{ME}(H)$ increases rapidly at low magnetic field values, reaches a maximum, and then decreases also rapidly with further increase in magnetic field. It becomes zero at magnetic field values above 400 mT. There is a marked hysteresis

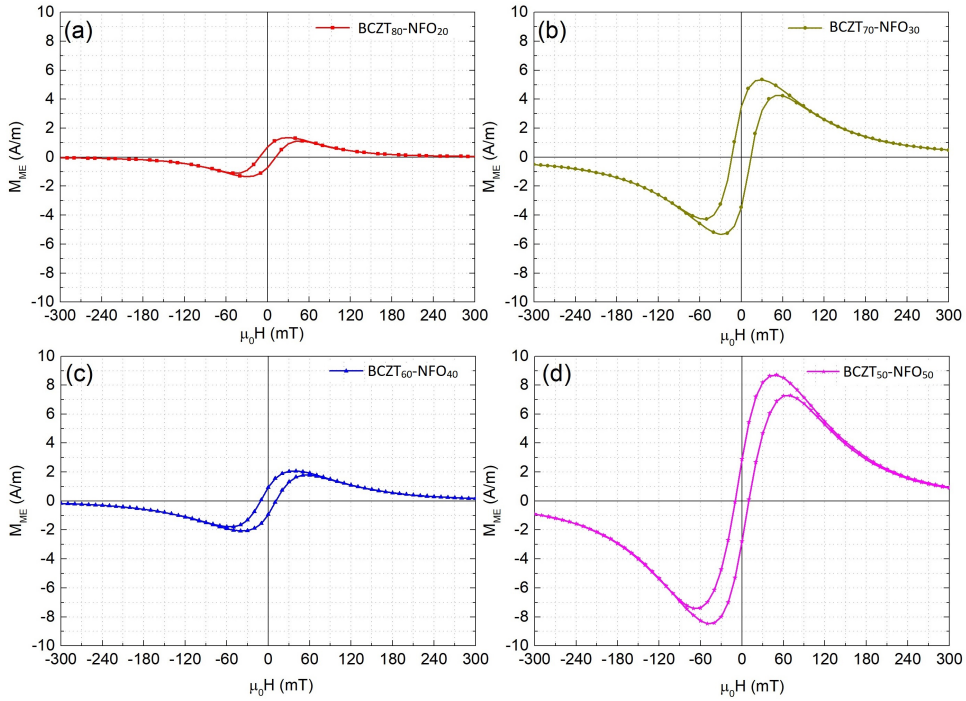

Figure 4.8: Electric voltage induced magnetization $M_{ME}(H)$ curves of all samples.

when the curve is traced back from the higher magnetic field values, with higher values of $M_{ME}(H)$ at lower magnetic fields. The behavior is similar in both directions of magnetic field. M_{ME} is an odd function of H. Later this behavior of $M_{ME}(H)$ would be discussed in connection with the behavior of strain derivative $(d\lambda/dH)$ of NFO.

4.7.2.2 Temperature dependence of electric field induced magnetization $M_{ME}(T)$

The temperature dependence of induced magnetization in each sample is shown separately in Fig. 4.9 (a-d). The $M_{ME}(T)$ was measured at constant amplitude of electric field and at a fixed value of *dc* magnetic field. The induced magnetization increases as a function of temperature in the range 150-250 K, passes through a broad maximum in the range 275-325 K, and then decreases with further increase in temperature. For each sample there is a unique temperature range in which it shows a maximum value.

4.7.2.3 Calculation of converse magnetoelectric coefficient, variation of induced magnetization as a function of *ac* electric field

First order converse magnetoelectric effect can be described by Eq. 3.6 i.e., $\mu_0 M_{ME} = \alpha_c E_{ac}$; the induced magnetization as a result of a change in *ac* field amplitude is plotted in Fig. 4.10. The behavior is linear and fitting it with Eq. 3.6 is also displayed. The slope of the straight line yielded values of α_c which are given in Table 4.2. The highest value of α_c for $BCZT_{70}$-NFO_{30} is almost two times as large as for those composites based on $BaTiO_3$-$CoFe_2O_4$,[112,228,250] and almost 4 times larger than that of $BCZT_{50}$-$CFO(Al)_{50}$ (11 ps/m).[210]

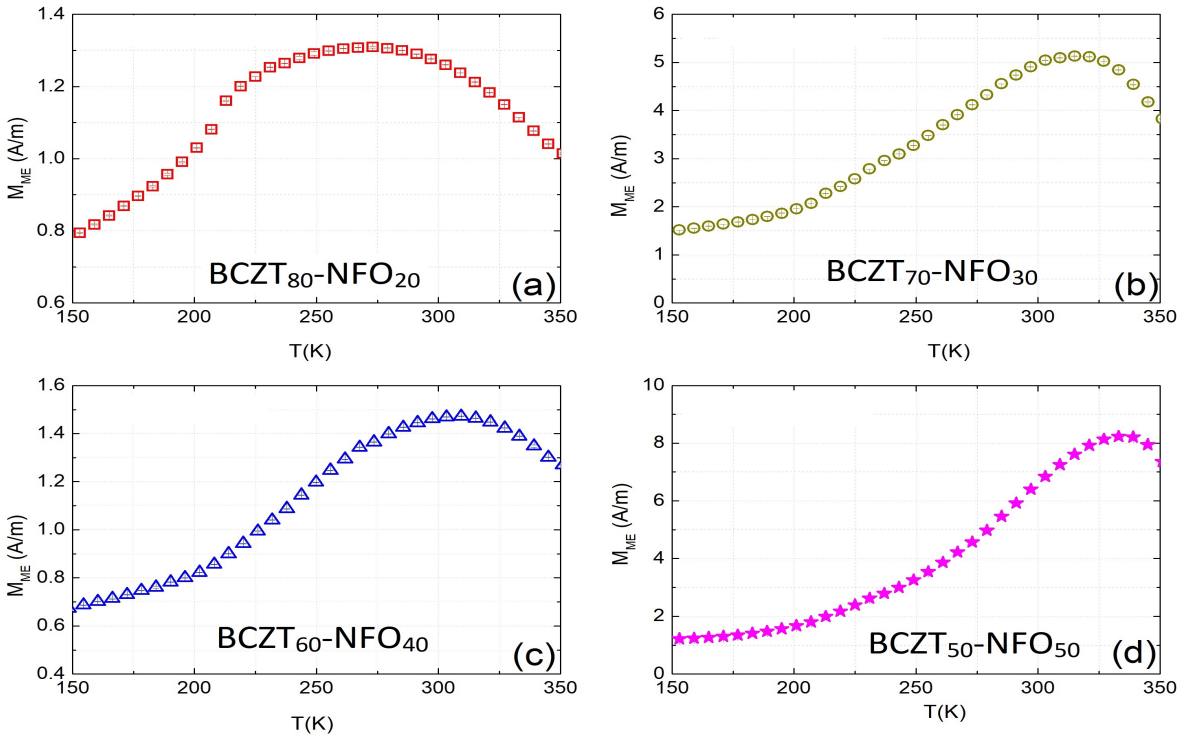

Figure 4.9: $M_{ME}(T)$ curves of all the samples measured constant values of *dc* magnetic field from the $M_{ME}(H)$ curves.

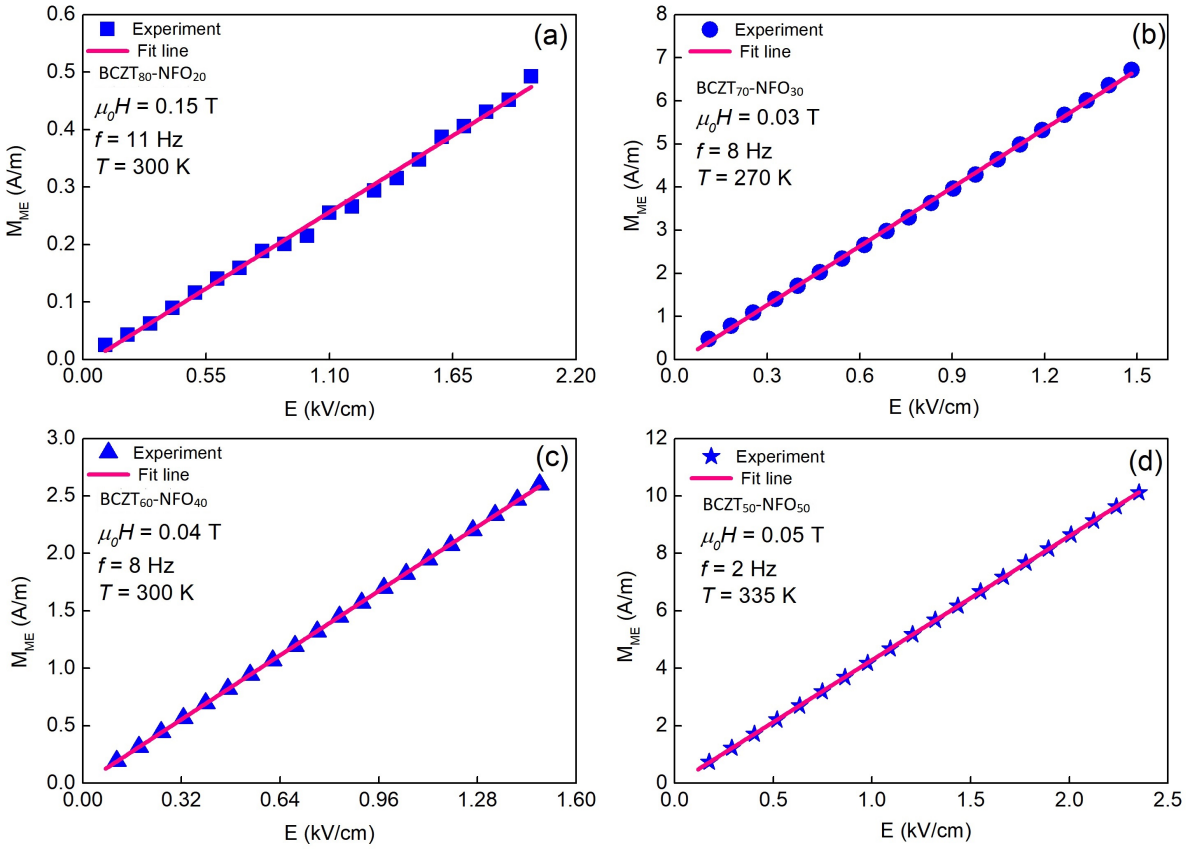

Figure 4.10: $M_{ME}(E)$ plots of all the samples and their fitting to Eq.**??**. The values calculated from the straight line slopes are given in Table 4.2.

Table 4.2: Calculated values of converse ME.

Sample	$BCZT_{80}$-NFO_{20}	$BCZT_{70}$-NFO_{30}	$BCZT_{60}$-NFO_{40}	$BCZT_{50}$-NFO_{50}
α_c (ps/m)	2.41 ± 0.03	45.44 ± 0.16	17.42 ± 0.02	43.14 ± 0.02

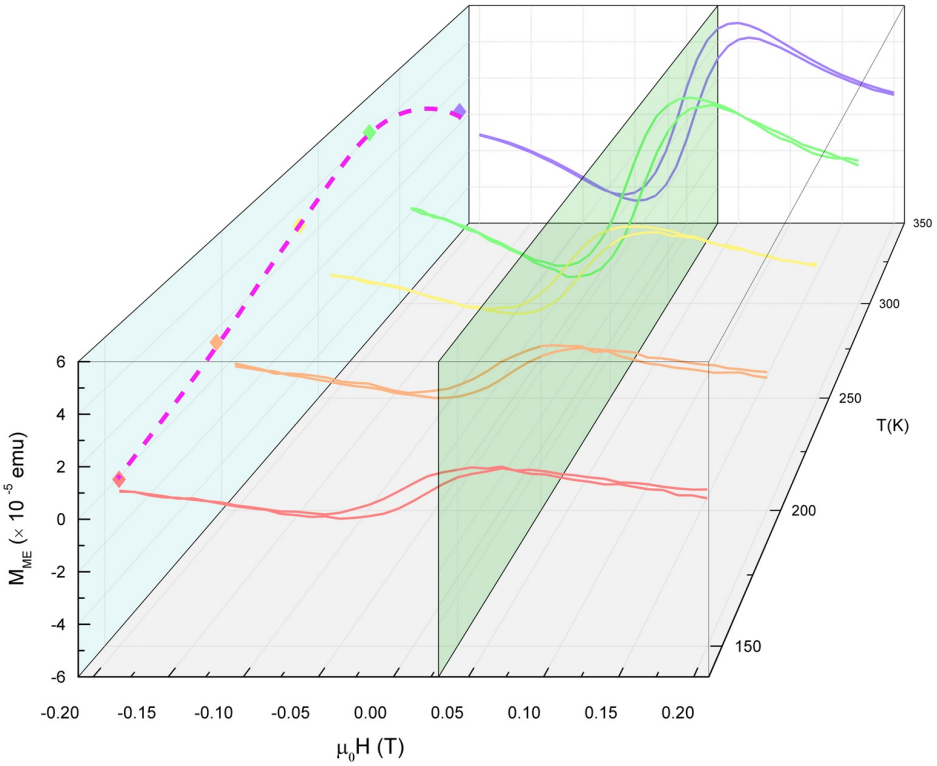

Figure 4.11: Schematic illustration of $M_{ME}(T)$ (the dashed line) in terms of $M_{ME}(H)$ curves that were taken at different temperatures. The green plane designates the value of *dc* magnetic field at which $M_{ME}(T)$ was measured for the sample, the dashed line shows the locus of points where each $M_{ME}(H)$ curve intersects the green plane.

4.8 Discussion

The magnetic field and temperature behavior of the induce magnetization as shown in the figures4.8 and 4.9 follows the same discussion as in case of the BCZT-CFO composites (see Section: 3.4). Briefly, the $M_{ME}(H)$ follows the magnetic field dependence of $d\lambda/dH$ of NFO.

$$\alpha_{ij}^{c} = q_{imn} \cdot c_{mnkl} \cdot d_{jkl} \tag{4.1}$$

The temperature dependence of M_{ME} was further explored by measuring $M_{ME}(H)$ curves for $BCZT_{50}$-NFO_{50} from low temperature to room temperature after fixed intervals of 50 K increase in temperature. The $M_{ME}(H)$ curves at lower temperatures keep the same shape as that at room temperature. However, the maximum values are low at lower temperatures and increase progressively to a maximum value and decrease on further increase in temperature. It becomes feasible to explain the shape of $M_{ME}(T)$ curves

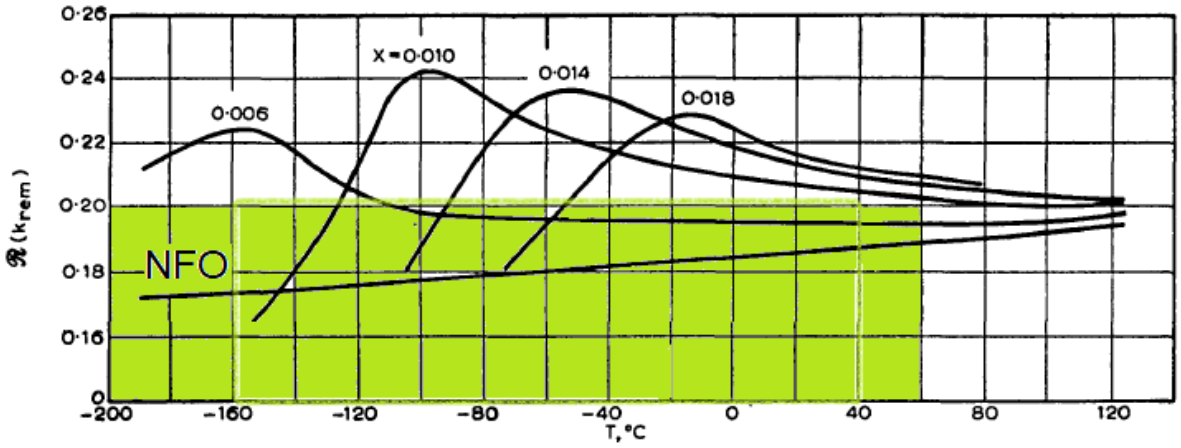

Figure 4.12: Temperature dependence of the real part of the magnetomechanical coupling factor for $(Ni_{1-x}Co_x)Fe_2O_4$.[251] The highlighted area is the the temperature range of interest.

(Fig. 4.9) considering the discussion in Section 3.4. The maximum in the $M_{ME}(T)$ curve is related to the maximum of the $M_{ME}(H)$ curve, as shown in Fig. 4.11 in the light of the discussion in the previous chapter. The shape of the $M_{ME}(H)$ curve depends on the effective behavior of the magnetomechanical coupling factor of NFO combined with the electromechanical coupling factor of BCZT. The real part of magnetomechanical coupling factor for NFO increases continuously from 160 K all the way up to 550 K[251] as shown in Fig. 4.12. However, data for the $M_{ME}(T)$ curve is measured at a constant *dc* magnetic field, which is important in explaining the reason why the maximum of the $M_{ME}(T)$ curve can only occur at a unique temperature.

Below the maximum in $M_{ME}(T)$, the dominating factor is only the temperature dependence of the magnetomechanical coupling factor. Above the maxima, in the range 310-350 K, the electromechanical coupling factor also plays its role. Beyond the Curie temperature of BCZT (~ 360 K), the electromechanical coupling factor decreases very fast and dominates the overall ME coupling, hence the shape of curves as shown in Fig. 4.9.

As we see in Table 4.2, the highest value of the converse ME coefficient was found to be for the sample $BCZT_{70}$-NFO_{30} (30% ferrite). Two factors are believed to play very important roles, which include the demagnetization factor,[252] and the overall dielectric coefficient of the sample.[242] Intrinsically, magnetostriction in the ferrite phase is proportional to its magnetization, so from material's perspective, it is important to know how an external magnetic field would influence the local magnetization. For this, the effect of external magnetic field on the material is needed to be figured out.

This effect is two-fold, the global effect on the whole sample, and the local effect on individual magnetic grains.[250,253] Now the critical role of demagnetizing factor comes into play. In micro-structures with low ferrite content (e.g. $BCZT_{80}$-NFO_{20} and $BCZT_{70}$-

NFO_{30}) as shown in Fig. 4.3, almost isolated inclusions are apparent. The case of disordered particles in non-magnetic matrix, in case of uniformly magnetized finite bodies (ellipsoids, elongated cylinders) leads to a uniform demagnetizing field inside the particle as discussed by J.-L. Mattei *et al.*[254] For a magnetic ellipsoid (an ideal case) characterized by a permeability μ_i and its shape factor $\overleftrightarrow{A}$ (a second rank tensor) which is represented by a diagonal matrix with components A_α where $\alpha = x, y,$ or z in particles reference frame. The effective magnetic field inside such a material due to the demagnetizing tensor $\overleftrightarrow{N}$ is given by:

$$\vec{H}_{eff} = \vec{H}_{ext} - \overleftrightarrow{N}\vec{M} \tag{4.2}$$

And it is established that the diagonal componenets N_α are givcen by:[255]

$$N_\alpha = \frac{\mu_i - \mu}{\mu(\mu_i - 1)} A_\alpha \tag{4.3}$$

where μ_i is the magnetic permeability of the embedded particles and μ is the permeability of the matrix. Equation 4.3 shows that the demagnetizing factors depend on the shape of the body (through A_α) as well as the magnetic properties of its surrounding medium (through μ). In the limit when $\mu_i >> 1$, Eq. 4.3 can be written as $N_\alpha \simeq A_\alpha/\mu$.

Now lets take into consideration the effect of percolation. Belwo the percolation limit, the demagnetziation effects only exist locally (at the scale of magnetic inclusions) and there is almost none macroscopic demagneiztaion. With the inccrease of magnetic content, the magnetic particles start to cluster, and after a certain concentartion (also called percolation limit), the magnetic poles are expelled form the interior of the composite to its ends. This leads to non-zero demagnization factor at the scale of percolative cluster.[254]

Now the role of piezoelectric (PE) part to the ME coefficient, when an external ac magnetic field is applied to it, is also crucial in these bi-phase composites. The polarization/charge value of the PE material would change locally as a result of a change in material strain due to its converse piezoelectric effect. Voltage is applied to the sample via an external power supply which is responsible for the establishment of the desired electric field, no matter how much charge is required by the sample. The dielectric losses, if any, would always be compensated this way externally. On a local scale, the piezoelectric effect is determined by the local electric field. If partially conducting magnetic grains are in series with the PE part, the field seen by PE medium would be enhanced. Contrarily, it would be reduced if they are in parallel to it. Hence samples with higher percolation (e.g., $BCZT_{50}$-NFO_{50}), are not good for converse ME scenario. They generate partial short circuits in parallel with the piezoelectric component, reducing the overall piezoelectric as well ME response. Less number of percolating structures ($BCZT_{70}$-NFO_{30} in this case) are beneficial to the electric part of the sample by reducing the effective electric thick-

ness of the sample, meaning higher electric fields in the piezoelectric material, generating better converse ME response. Therefore, it is the role of magnetic field percolation which increases both the demagnetization field as well as leakage paths in samples with higher ferrite content.

4.9 Conclusions

A new set of compositions (1-x)BCZT-xNFO ($x = 0.2$-0.5) was successfully synthesized with the solid state method. Phase purity, as well as lattice parameters of the respective phases, were determined using X-ray diffraction, combined with Rietveld analysis technique. TOF-SIMS maps acquired at room temperature give interesting information about the phase connectivity. The samples which contain higher volume percentage of one of the two phases show approximately 3-0 type connectivity, on the other hand, composites with an equal volume of both phases show a 3-3 connectivity, approximately. Piezoforce response microscopy and magnetic force microscopy have led us to conclude that the two phases coexist locally. The cross-coupling between the two phases was determined by applying an *ac* electric field, and the resultant induced magnetization was measured. The induced magnetization tracks the behavior of $d\lambda/dH$ in an applied magnetic field. The $M_{ME}(T)$ curve has been shown to depend on the *effective* coupling of electromechanical and magnetomechanical coefficients of BCZT and NFO phases and the highest value is obtained in the range where both of these show their best values. The highest value of direct ME was obtained for the $BCZT_{50}$-NFO_{50} sample. The converse magnetoelectric effect was determined for each composition, and the maximum value was obtained for the sample with 30 % NFO. The samples show an enhancement of converse magnetoelectric coefficient, because the maximum value is at least twice as large as similar two-phase composites obtained via solid state reaction. The role of demagnetization factor and the connectivity of two phases toward the enhancement of ME coefficient has also been discussed in detail.

Chapter 5

Magnetoelectric Effect in Sn-doped $BaTiO_3$-CFO Composite

This chapter is all about synthesis and characterization of a composite consisting of Sn-doped $BaTiO_3$ and cobalt ferrite i.e. $[Ba(Sn_{0.3}Ti_{0.7})O_3]_{0.8}$-$[CoFe_2O_4]_{0.2}$[1]. Introduction of Sn into the crystal lattice of BTO induced certain special properties which include a decrease of Curie temperature, broadening of the permittivity maximum, and frequency dependence of electric permittivity. All these features are collectively known as relaxor properties (relaxors are discussed in Chapter 1). Sample synthesis was done by solid-state reaction method. Electric permittivity was measured as a function of temperature, with and without external dc magnetic field and it was found to change by the application of dc magnetic field. A relationship was established between the change in electric permittivity in response to external magnetic field and the strain mediated magnetoelectric effect.

5.1 Background and Motivation

Usman *et al.*[257] reported magnetic control of relaxor features in $(BaZr_{0.5}Ti_{0.5}O_3)_{0.65}$-$(CoFe_2O_4)_{0.35}$. They demonstrated that magnetic field can modulate the behavior of polar nanoregions in relaxor $BaZr_{0.5}Ti_{0.5}O_3$ to decrease its Burns temperature. Later Sahoo *et al.*[258] studied composition control of magnetoelectricity in the relaxor-ferrimagnetic composite $BaZr_{0.4}Ti_{0.6}O_3/CoFe_2O_4$. The control of relaxor features in $Ba(Sn_{0.3}Ti_{0.7}O_3)$-$CoFe_2O_4$ has not been demonstrated previously. From a technological perspective, these materials have gained attention due to their possible application for small antenna applications.[259–262] For example Kim *et al.* showed that the size of an antenna can be reduced by using magneto-dielectric materials without the decrease of bandwidth.[263,264]

$Ba(Ti_{1-x}Sn_x)O_3$ (BSnT) offers an interesting and feature-rich phase diagram[265] as depicted in Fig. 5.1. Briefly describing, there exists a steady crossover from normal ferroelectric to relaxor behavior in it. Below $x = 0.175$, it exists in a normal ferroelectric state and relaxor features related to the reorientation of polar nanoregions appearing in

[1]The work reported in this chapter also appeared in the form of a published article in *Journal of Alloys and Compounds*, 2015.[256] Full-text permission was obtained for reuse of figures and tables from ©2015 Elsevier B.V.

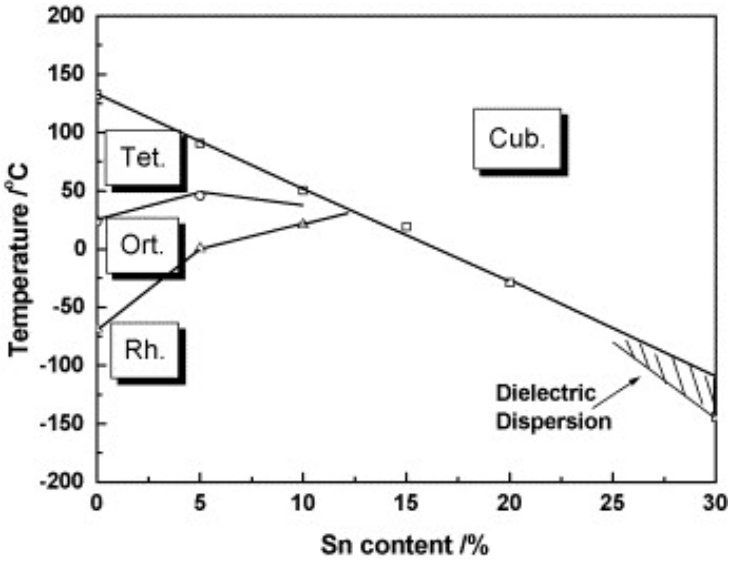

Figure 5.1: (x-T) diagram of $Ba(Ti_{1-x}Sn_x)O_3$.[265] The figure was reused with permission from © 2006 Elsevier B.V.

compositions with higher Sn content. In the composition range $0.175 \leq x \leq 0.25$, its exists in a mixed state with features of normal as well as relaxor ferroelectrics.[38] The pure relaxor state has its onset around $x = 0.30$. The relaxor properties in BSnT are thought to be induced by weak random fields.

Keeping in mind the above discussed issues, a study about the synthesis, structural, dielectric and magnetoelectric properties of the two-phase composite $[Ba(Sn_{0.3}Ti_{0.7})O_3]_{0.8}$-$[CoFe_2O_4]_{0.2}$ ($BSnT_{80}$-CFO_{20}) was conducted.

5.2 Sample Synthesis

Both BSnT and CFO were synthesized separately using solid-state reaction. To prepare composites of $BSnT_{80}$-CFO_{20}, the BSnT and CFO powders were mixed in the proportion: BSnT at 80 vol.% and CFO at 20 vol.% , and ground again to fine powder form. After that, the mixture was pressed under 3 MPa into disk-shaped pellets (diameter 10.0 mm and thickness 1.0 mm) using a hydraulic press with the addition of some drops of polyvinyl alcohol (PVA) solution as a binder. The pellets were sintered in air at 1300 ℃ for 6 hours in a tube furnace with a heating rate of 5 ℃/min. For dielectric measurements, the sintered disks were painted on both sides with silver paste. Contacts were made with copper wire and fired in an oven at 200 ℃ for 1 h to ensure good contacts. The samples were placed inside a cryostat from Janis Research (model CCS-350) attached with a Lakeshore 331 temperature controller. The real and imaginary parts of the dielectric permittivity were measured with a Wayne Kerr 4275 LCR meter in the frequency range 0.2-500 kHz in the temperature range 10-300 K with and without different *dc* magnetic fields in longitudinal configuration.

Table 5.1: Best fit Rietveld refinement parameters for $BSnT_{80}$-CFO_{20}.

Phase	**Space Group**	**Lattice Parameters (Å)**	**GoF**
$Ba(Sn_{0.3}Ti_{0.7})O_3$	$Pm\bar{3}m$	a = 4.05888	1.23
$CoFe_2O_4$	$Fd\bar{3}m$	a = 8.39672	

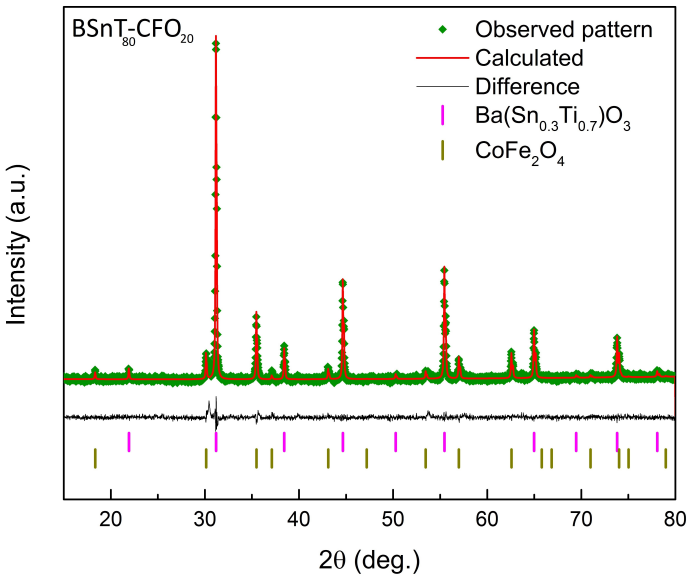

Figure 5.2: XRD spectra along with Rietveld analysis of $BSnT_{80}$-CFO_{20}.

5.3 Structural Characterization with XRD

The phase and structure of the ceramics were verified with X-ray diffraction at room temperature and. The resultant pattern is displayed in Fig. 5.2. All peaks in the XRD spectrum were identified belonging to either the cubic perovskite phase $Pm\bar{3}m$ for BSnT or to the cubic spinel $Fd\bar{3}m$ for CFO. Rietveld refinement was carried out with the software *GSAS II*.[198] The fitting results are shown as the solid line superposed on the data points in Fig. 5.2. The observed spectrum fits very well to the two phase model containing perovskite and spinel phases as it is evident from the difference plot in Fig. 5.2. Lattice parameters obtained from the Rietveld fitting as well as the goodness of fit (GoF) parameter are given in Table 5.1.

5.4 Electric Permittivity Measurements

Electric permittivity was measured as a function of temperature from 10 K to 300 K at different electric field frequencies. The plots are shown in Fig. 5.39a) for BSnT, in which both real and imaginary parts of electric permittivity are shown simultaneously. A diffuse phase transition at all the frequencies is visible and both $\varepsilon'(T)$ and $\varepsilon''(T)$ are frequency dependent. The maximum point on ε'(T) curve shifts to higher temperatures

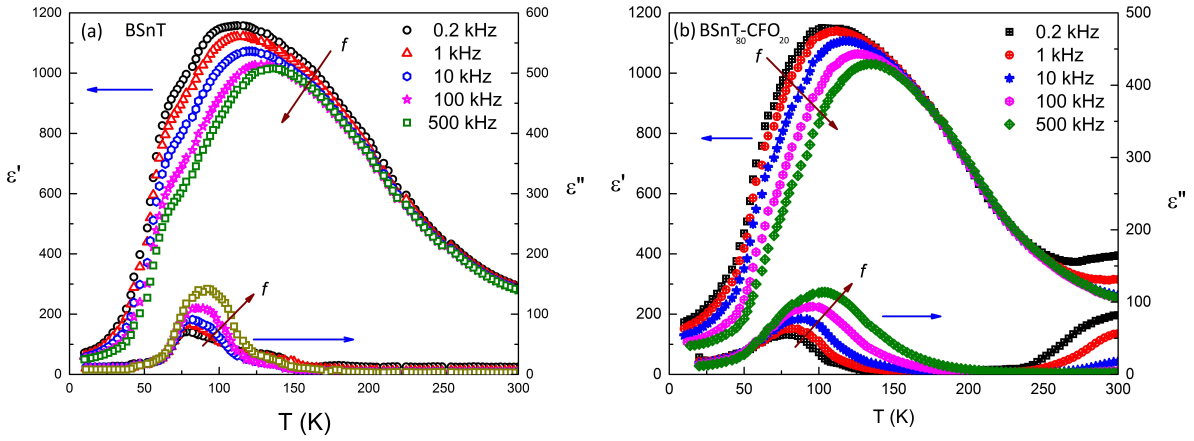

Figure 5.3: Real and imaginary parts of electric permittivity as a function temperature measured at various frequencies (a) for BSnT nad (b) for $BSnT_{80}$-CFO_{20}.

with increasing frequency. A similar type of behavior was seen in the imaginary part of the electric permittivity. All these features correspond to typical relaxor-ferroelectric materials. Electric permittivity-temperature profiles were also measured for the composite $BSnT_{80}$-CFO_{20} and are shown in Fig. 5.3(b). Behavior identical to that of BSnT is witnessed. Similar frequency dispersion as well as a shift of electric permittivity maxima ε'_m to higher temperatures with increasing frequency. Hence a clear indication of relaxor ferroelectricity in pure BSnT, as well as the composite, is there.

The second most important step towards the analysis of the relaxor nature of materials is the analysis of the dielectric data using suitable parameters and models. The first parameter in this context is ΔT_m which gives the width of the diffuse phase transition, and is the difference between the temperature maximum of the highest and lowest frequencies i.e. in our case is: T_m(500 kHz) - T_m(0.2 kHz). The value of ΔT_m for BSnT and BSnT-CFO comes out to be 22 K and 30 K, respectively. Similar values were also obtained for T''_m i.e. the maximum temperature in the imaginary part of electric permittivity. These values well correspond to the ones previously available in literature about the dielectric properties of $Ba(Sn_{0.3}Ti_{0.7})O_3$.[266–269]

The diffuse phase transition as witnessed in Fig. 5.3(a) and Fig. 5.3(b) can be better understood in terms of a variable power law as suggested by Santos *et al.*:[270]

$$\frac{1}{\varepsilon'} = \frac{1}{\varepsilon'_m} + \left(\frac{T - T_m}{C'}\right)^{\gamma}; (1 \leqslant \gamma \leqslant 2) \tag{5.1}$$

Here ε'_m is maximum electric permittivity and T_m is the corresponding temperature to it. γ and C' are fitting parameters. The most important information about the type of phase transition is provided by the factor γ: a value close to unity corresponds to a *normal* ferroelectric transition while values close to 2 are an indicator of a diffuse phase

transition. To fit the data to Eq. 5.1, a graph between $ln(1/\varepsilon' - 1/\varepsilon'_m)$ and the reduced temperature $ln(T - T_m)$ was plotted for each sample BSnT and BSnT-CFO as it is shown in the insets of Fig. 5.4(a) and (b) with their fittings to Eq. 5.1 depicted with the solid lines. The value of γ for BSnT is 2.01 and for BSnT-CFO, it is 2.13. Both of these values well correspond to a highly diffuse type phase transition which is one of the main characteristics of relaxor-ferroelectrics.

Now let's go back to the frequency dependence of T_m and T'_m, which is another basic feature of a relaxor-ferroelectric. This frequency dependence is directly related to the distribution of relaxation times of polar nanoregions, which was already discussed briefly in Section 1.2.10. The polar nanoregions are highly temperature dependent entities. Above the transition temperature T_m, the number of these polar nanoregions is not so high. However, with decreasing temperature, the volume fraction as well as their sizes increase.[40,271,272] Moreover, the interactions between the individual polar nanoregions increase.[273,274] All the above mentioned factors contribute toward the slowing down of the relaxation mechanisms with the decrease in temperature. At transition temperature T_m, the whole system of polar nanoregions goes into a state of totally frozen static polarization, which is known as the *non-ergodic* relaxor state. In order to get an insight into the relaxation phenomena, a well-known approach is the use of the Vogel-Fulcher relationship given by:

$$f = f_0 exp(-\frac{E_a}{k_B(T'_m - T_{VF})}) \tag{5.2}$$

Table 5.2: Fitting paramters to Vogel-Fulcher law for BSnT and $BSnT_{80}$-CFO_{20}.

Parameters	E_a **(meV)**	f_0 **(Hz)**	T_{VF} **(K)**
BST	47 ± 4	6.6×10^9	89 ± 3
$BSnT_{80}$-CFO_{20}	85 ± 8	7.2×10^{10}	53 ± 3

Here f_0 is a constant, E_a is known as the activation energy, and T_{VF} is called the Vogel-Fulcher temperature, which is believed to correspond to the static freezing temperature of polar nanoregions dynamics. The relation 5.2 was derived with an idea that the temperature dependence of relaxation times in relaxors is associated with the volume distribution of polar nanoregions.[275] Fig. 5.5 (a) and (b) show the curves between $T_m(f)$ and $ln(f)$ for BSnT and $BSnT_{80}$-CFO_{20}, respectively. The data was fit to Eq.5.2 and is indicated by solid lines in both curves, and the best fit parameters are given in Table 5.2. The values of all the parameters of fitting i.e. E_a, T_{VF}, and f_0 are in accordance with the values of similar samples reported in literature.[276]

As discussed earlier, the relaxor dynamics are characterized by a distribution of relaxation times. The relaxation that occurs in different materials can be imagined as follows:

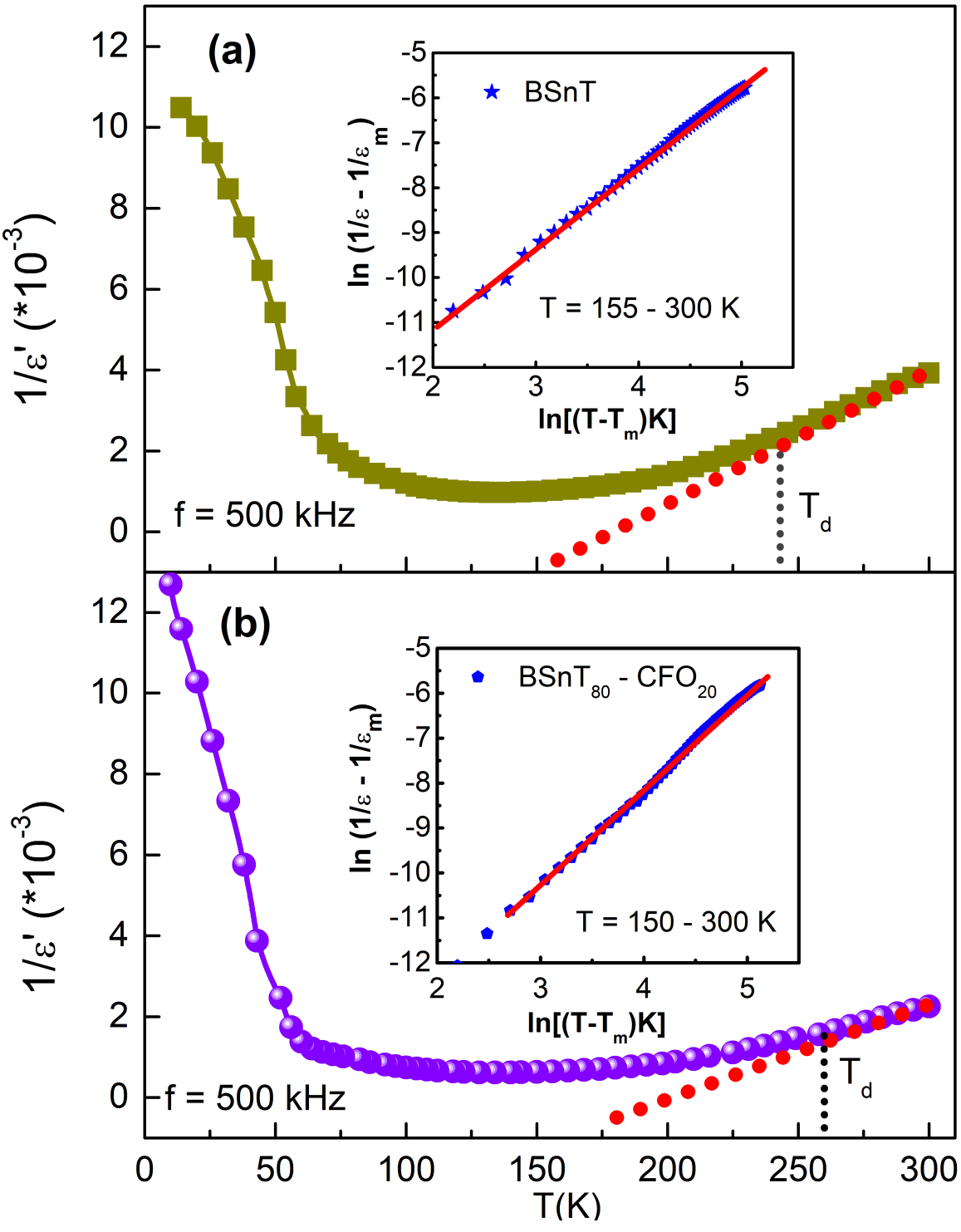

Figure 5.4: Inverse electric permittivity versus temperature and their fitting to Curie-Weiss law of (a) BSnT and (b) $BSnT_{80}$-CFO_{20}, respectively. Inset in (a) and (b) show inverse electric permittivity versus temperature and their fitting to Modified Curie-Weiss law (Eq. 5.1) of BSnT and $BSnT_{80}$-CFO_{20}, respectively. The data fitting to Modified Curie-Weiss law was done in the temperature range indicated in the insets.

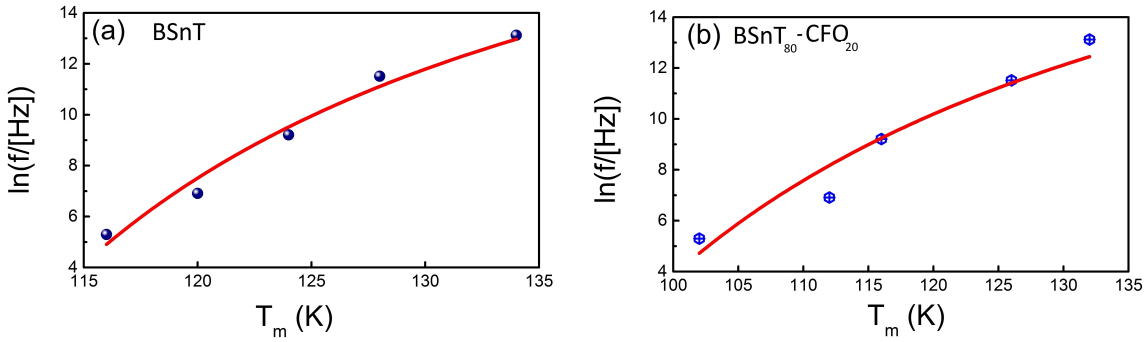

Figure 5.5: Plots of frequency versus temperature corresponding to electric permittivity maxima for (a) BSnT and (b) $BSnT_{80}$-CFO_{20}. The symbols are data points while the solid lines are fittings to Vogel-Fulcher Law.

At a temperature below characteristic freezing temperature T_d, a relaxor consists of a network of polar nanoregions which are assumed to be embedded in a highly polarizable medium. Ideally, the polarizable medium itself might be thought of as consisting of a number of fluctuating dipoles which corresponds to the case of dipolar glasses and order-disorder type relaxors. On the other hand, it might also be considered to consist of small sized polar clusters, which is true for displacive type relaxors. However the ideal cases do not occur always, and there can be materials in which both types of behaviors (i.e. glassy and displacive) might exist simultaneously.[277] So in case of the displacive relaxors, each PNR is associated with a characteristic correlation length, which increases with a decrease in temperature. The correlation length keeps on increasing until the PNRs of similar size start to merge and transform into polar clusters. Eventually, all of these PNRs freeze due to the size growth as well as increased interactions between them.[278]

5.5 Magnetodielectric Effect

Electric permittivity of the composite $BSnT_{80}$-CFO_{20} was measured as a function of temperature under different *dc* magnetic fields. The values of magnetic fields were 5 kOe and 7 kOe, respectively. Under the applied magnetic fields, electric permittivity was measured with decreasing temperature from 300 K down to 10 K. $\varepsilon'(T)$ and $\varepsilon''(T)$ curves under the designated magnetic fields are shown in Fig. 5.6. The following features in Fig. 5.6 are noteworthy:

- The magnitude of the electric permittivity (i.e. both real and imaginary electric permittivity) decreases with the application of the magnetic field over a wide temperature range (between 50 K to 300 K).

- The maxima of the electric permittivity (both ε'_m and ε''_m) shift to higher temperatures under higher *dc* magnetic fields.

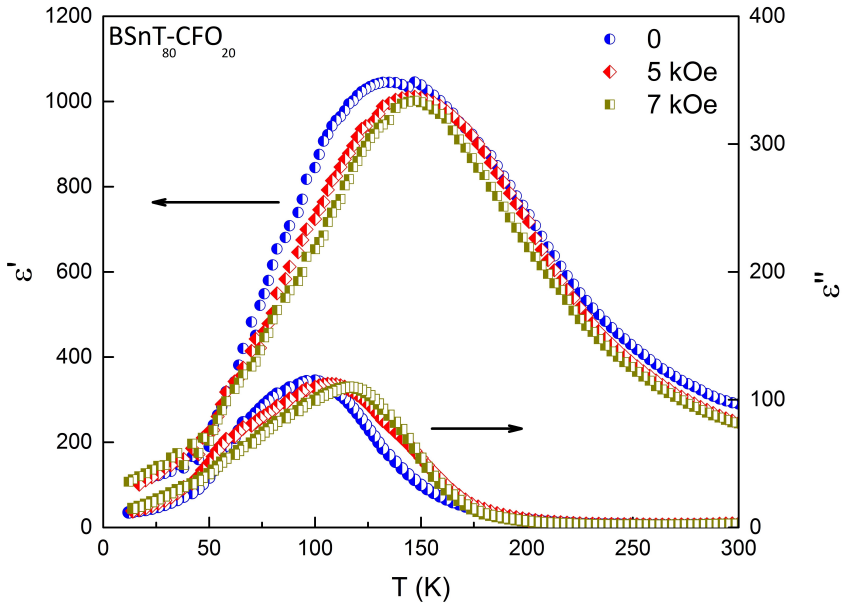

Figure 5.6: Electric permittivity versus temperature measured at various *dc* magnetic fields for $BSnT_{80}$-CFO_{20}.

To quantify the effect of magnetic field on the electric permittivity, the magnetoelectric effect (magneto-dielectric effect here) can be defined as:

$$MD\% = \frac{\varepsilon'(H) - \varepsilon'(0)}{\varepsilon'(0)} \times 100 \tag{5.3}$$

Here H denotes the magnitude of magnetic field. The MD% is plotted as a function of temperature in Fig. 5.7. It is positive below 50 K, and above this, it increases in the negative direction to a value of about 23 % at 104 K. This value of 23 % is, roughly, at least one order of magnitude higher than reported for other nano-composite systems e.g. $BaTiO_3$-$SrFe_{12}O_{19}$,[279] $BiFeO_3$-$CoFe_2O_4$-$PbTiO_3$,[280] $Ni_{0.5}Zn_{0.5}Fe_2O_4$-$BaTiO_3$,[281] and $Co_{1.2-x}Mn_xFe_{1.8}O_4$-$Pb_{0.2}Ba_{0.8}TiO_3$.[282]

5.6 Discussion

The effect of a slight decrease in electric permittivity can be understood from the magnetoelectric effect in these two-phase materials which arises due to strain coupling. The magnetostrictive phase, cobalt ferrite, is a good magnetostrictive material. As soon as a magnetic field is applied, a strain is produced in it, which due to interface coupling, transfers to the ferroelectric phase (BSnT in this case). The strain state of the ferroelectric phase changes, which results in a variation in its polarization/dielectric constant.

Two factors (magnetomechanical coupling factor and the electroemchanical coupling factors) on which the ME coupling depends were already discussed in Chapter 4. The anisotropy constant K_1 for cobalt ferrite is positive and decreases only above 150 K. Thus

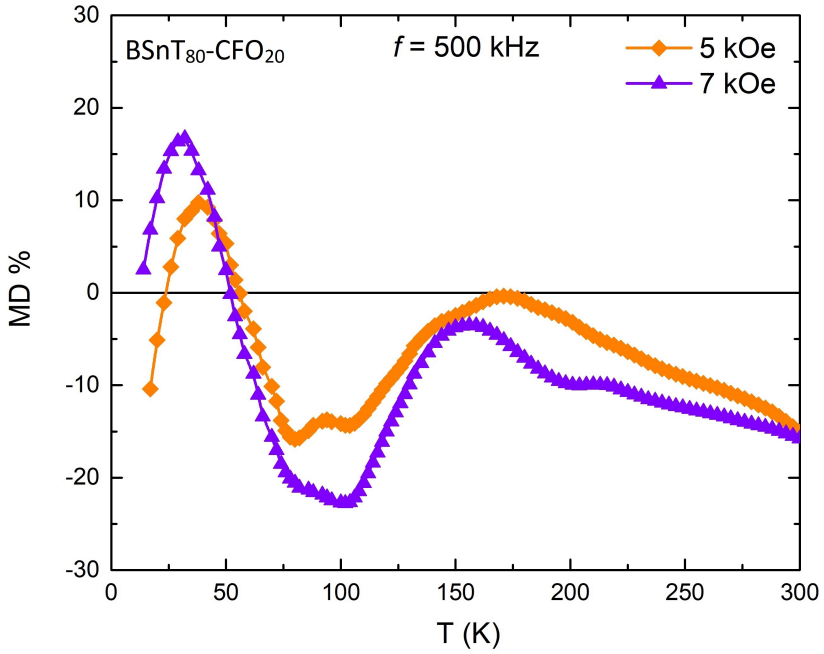

Figure 5.7: Magnetodielectric coefficient (MD%) for two different field values as a function of temperature for $BSnT_{80}$-CFO_{20}.

the initial susceptibility and magnetomechanical coupling have moderate values between 50-150 K.[283] The studies about the elastic properties of $Ba(Ti_{1-x}Sn_x)O_3$ as documented by Geske *et al.*[284] show that this system possesses interesting elastic properties. For example, it was found that peaks corresponding to elastic compliance maximum and dielectric constant maximum coincide only for $x \leq 0.1$, beyond this, they are decoupled. The elastic compliance peak occurs at temperatures much lower than the Curie temperature maximum. Our system $Ba(Ti_{1-x}Sn_x)O_3$ at $x = 0.3$ should, in principle, correspond to a maximum of compliance constant at around 100 K. Thus clear analogy of the maximum of MD might correspond to the stress-mediated direct ME coupling, which is maximized when the stress transfer is maximum due to the elastically soft BSnT. This explanation also caters for the influences of any non-stress-mediated effects on electric permittivity such as the effects due to magneto-resistance.

There is another possible explanation for the change in MD which is given as follows: The Curie-Weiss law is given by:

$$\varepsilon' = \frac{C}{T - T_{CW}} \tag{5.4}$$

and it is obeyed by normal-ferroelectrics at temperatures above the temperature for maximum ε_m. Here the constants C and T_{CW} are known as Curie-Weiss constant and Curie-Weiss temperature, respectively. However, relaxors obey it only at temperatures well above the temperature of maximum electric permittivity. This is displayed for BSnT

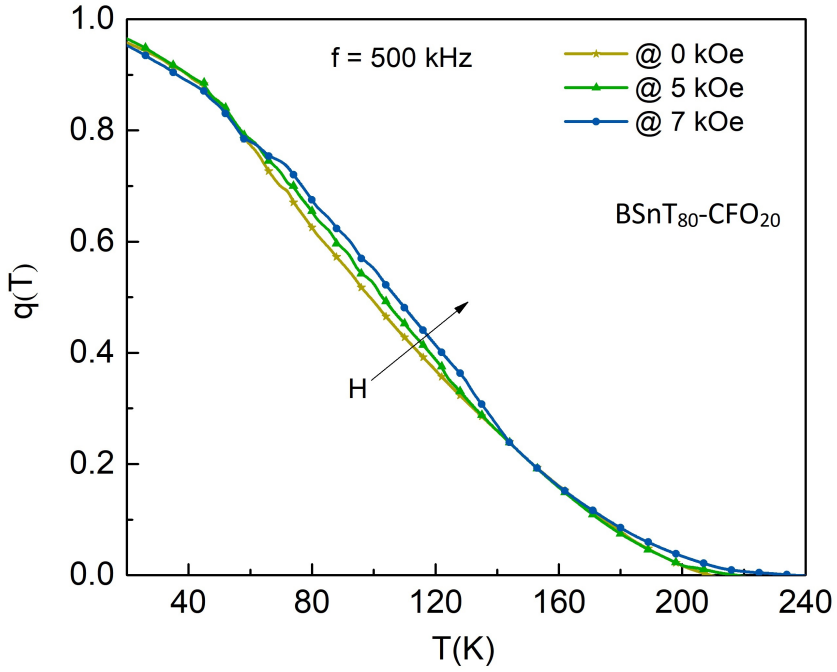

Figure 5.8: Variation of q with temperature. q was calculated from Eq. 5.5 at various *dc* magnetic fields. The arrow points to the increase magnetic field direction.

and $BSnT_{80}$-CFO_{20} in Fig. 5.4, where the inverse electric permittivity is plotted against temperature for both samples. The fit to the Curie-Weiss law is depicted by the dotted lines. The temperature at which the data start to deviate from it is marked by T_d, known as deviation temperature. Below T_d, polar nano-regions are believed to start freezing.

As already discussed, the polarization entities in a relaxor material are the polar nanoregions (PNRs). The existence of these entities has been well-documented in literature by Shvartsman *et al.*[285,286] The effect of magnetic field on these PNRs can be taken into account for the explanation of the shift of the electric permittivity maxima (T_m) in Fig. 5.6. For this, a different form of the Curie-Weiss law is employed, which is given by:[287]

$$\varepsilon'(T) = \frac{C[1 - q(T)]}{T - T_{CW}[1 - q(T)]} \tag{5.5}$$

Where C and T_{CW} are the constants obtained by the high temperature fit of $\varepsilon'(T)$ (see Fig. 5.4). The original Curie-Weiss law is followed only at much higher temperatures, however, Eq. 5.5 is useful below the temperature T_d, where PNRs are believed to start freezing. By definition, the parameter $q(T)$ is defined as $q \propto \langle P_i \cdot P_j \rangle$, which can act as a order-parameter for relaxors in terms of freezing of PNR dynamics. Here P_i and P_j are polarizations of neighboring PNRs and its temperature dependence as determined from Eq. 5.5 is shown in Fig. 5.8. Like any other order-parameter, its value is unity at certain low temperature, signifying complete freezing of PNRs. It slowly decreases, reaching zero at a certain high temperature, same as T_d. The slow decrease is also in accordance with

the relaxor behavior.

The unity value of $q(T)$ signifies the highest interaction possible among the PNRs. As increase in the interaction of these PNRs also increases their size, this leads to a "frozen" state of PNRs.[288] Upon the application of a magnetic field, the interaction parameter $q(T)$ increases slightly, in the temperature range 60-150 K. This enhanced interaction may have its origin in flexoelectricity. *Flexoelectricity is the coupling between mechanical strain gradient and electric polarization. In principle, flexoelectricity is present universally in any crystal symmetry.*[289] The flexoelectric effect is observed in several non-polar crystal systems, for example in (Ba,Sr)TiO_3 system,[290] in relaxor lead magnesium niobate (PMN) in its paraelectric state,[291] and also in paraelectric state of $BaTiO_3$.[289] Due to mixed-phase nature of our sample, there may exist regions of inhomgeneous phase distribution. These inhomogeneities may result in strain gradients upon the strain transfer from the magnetostrictive phase (after the application of a magnetic field). These strain gradient, in turn, would result into enhanced flexoelectricity, which promotes the interaction among the PNRs. This might have caused an enhanced $q(T)$ even above the lowest temperature in Fig. 5.8.

5.7 Summary and Conclusions

The very last system that studied for the effect of cation substitution of barium-titanate was the one where Ti^{4+} was substituted partially by Sn^{4+}. This Ba(Ti,Sn)O_3 system was investigated in pure form as well as a composite with cobalt-ferrite. Some properties like crystal structure, electric permittivity and magnetoelectric coupling were studied.

The Sn^{4+}-substituted system turned out to be a relaxor-ferroelectric in comparison with the pure barium tinatate which is a normal ferroelectric. At room temperature, the system is in its paraelectric cubic state (unit cell $Pm\bar{3}m$) and a phase transition temperature well below it. The relaxor properties of pure as well as the composite system were investigated with the help of electric permittivity versus temperature data in the temperature range of 10-300 K. Both systems have frequency dependent $\varepsilon'(T)$ and maxima of $\varepsilon''(T)$ shifting with frequency of electric field. The well-known Vogel-Fulcher law was used to explore the freezing properties associated with polar-nanoregions of both systems.

Interesting properties were observed when an external *dc* magnetic field was applied and $\varepsilon(T)$ was studied. Two remarkable features were:

- The overall value of electric permittivity was decreased throughout the temperature range.
- The maximum of $\varepsilon(T)$ was shifted to higher temperatures in comparison with their values without an applied magnetic field.

Both these properties were explained considering the effect of strain mediated magnetoelectric coupling on the polar-nanoregions of the Ba(Ti, Sn)O_3 relaxor-ferroelectric. Overall, the applied external magnetic field causes a part of polar-nanoregions on the average to interact more than the rest and thus *freeze* in terms of their polarziation response. This might be due to the piezoelectric strain that had been transferred from the magnetostrictive cobalt ferrite through interface coupling between the two phases. Moreover, in a certain temperature range above the phase transition temperature, the magnetic field further enhances the interaction among the PNRs due to flexoelectric properties of the paraelectric phase above phase transition temperature. This strain mediated magnetoelectric coupling was quantified in terms of the magneto-dielectric effect $\frac{\varepsilon(H)-\varepsilon(0)}{\varepsilon(0)}$, which turns out to be 23 % just around the phase transition temperature. This value is one order of magnitude higher than the previously studied two-phase multiferroic systems prepared employing similar synthesis techniques.

Chapter 6

Magnetoelctric Coupling in CFO-BTO bilayered Thin Films

6.1 Motivation and Background

The direct magnetoelectric effect in multiferroic heterostructures is very useful from a device point of view as it allows conversion between a magnetic signal and an electric voltage without requiring any source-currents or low temperatures. Thus magnetic field sensors designed on the basis of direct magnetoelectric effect are expected to be cost-effective,[292] with high sensitivity,[6] compactness, and a broad operational temperature bandwidth.[293] Advanced heterostructured nanomaterials, such as embedded nanoparticles, and heteroepitaxial composite layers with a functional response, are progressively investigated for their potential applications.[294] In multiferroic magnetoelectric composites, interfaces also play an important role. The composite system $CoFe_2O_4/BaTiO_3$ has been studied in many different configurations, such as $BaTiO_3$ nanopillars vertically clamped to a $CoFe_2O_4$ matrix,[148] self-assembled nanostructures,[149,161] two-phase ceramics,[106–108] and planar (i.e. layered) heterostructures.[295] It should be pointed out that, despite the vertical nanopillars have less clamping to the substrate and the matrix, conductive paths can form and, thus, can electrically shut down the application.[296] As a result, much effort is focused on layered heterostructures.

For such magnetoelectric composites in layered-form, theoretical models predict that a perfect elastic interface between the magnetostrictive and piezoelectric layers provides maximal magnetoelectric coupling,[297] provided the properties of the parent materials in the composite be unchanged during processing. Any variation at the interface that will induce structural changes in the individual phases will also alter the strain-mediated magnetoelectric coupling. One of the strategies used so far for ME enhancement in these layered composites includes efforts to reduce substrate clamping.[165] It was achieved by growing a thicker first layer on the substrate followed by a thinner layer on top of it. Following the same strategy, this chapter presents two thin films with thicker $CoFe_2O_4$ layer followed by a thinner $BaTiO_3$ layer, such that to reduce the effect of substrate clamping. However, these two films would differ in terms of two differently oriented

substrates (One along (100) direction and the other along (111)). Moreover, the effect of such orientation on the strain-mediated ME coupling will be studied in detail.

6.2 Experimental

Thin films were prepared using a custom-built pulsed laser deposition (PLD) setup with commercial ceramic targets of $BaTiO_3$ and $CoFe_2O_4$. One side polished $SrTiO_3$(100) and $SrTiO_3$(111), both doped with 0.5wt% Nb were purchased from MaTeck GmbH (Jülich, Germany). The purchased substrates had the dimensions 10mm × 10mm× 0.5 mm. Before the thin film deposition, the *as received* substrates were cleaned in acetone and then in ethanol in an ultrasound bath for 5 minutes each. Soon after the cleaning, they were dried in air. After the insertion of targets and substrates, the PLD chamber was pre-evacuated using a turbo pump to a pressure of 10^{-6} mbar. The temperature was increased to the desired value (650 ℃ for $CoFe_2O_4$ layer and 750 ℃ for $BaTiO_3$ layer, respectively) and then the turbo was switched off, but a rotary backing pump continued to run, and fresh oxygen was introduced to a pressure level of $\sim 10^{-1}$ mbar. This was the working pressure which was maintained for the full deposition process. A KrF Excimer laser was used for the laser pulses (256 nm wavelength, 25-30 kV laser voltage, and 90-100 mJ of laser pulse energy). The substrate was ablated 20 minutes for the CFO layer and 12 minutes for the BTO layer. Two such films were prepared at similar conditions. STO(100)//CFO//BTO (here onward will be called BLF100) and STO(111)//CFO//BTO (here onward will be called BLF111). After the BTO layer deposition at 850 ℃ for 30 minutes, each film was annealed in ample oxygen and afterward removed from the chamber.

6.3 Results and Discussions

6.3.1 Structural Characterizations

6.3.1.1 XRD Analysis

X-ray diffraction spectra of BLF100, STO(100)//CFO, and $SrTiO_3$ (STO)(100) substrate are shown in Fig.6.1(a), (b), and (c), respectively. In panel (b), all the detected peaks can be identified to be belonging to STO and CFO. The CFO film appears to be (l00) oriented, because the detected peaks are labeled as CFO(400) and CFO(008), respectively. In panel (a), the XRD scan of STO(100)//CFO//BTO is given. Reflections from both CFO and BTO were identified and indexed accordingly. The BTO film does not appear to be textured, but rather it is polycrystalline. The strongest reflections for BTO are (200) and (004), while other strong reflection peaks include (110), (111), (112), and (003).

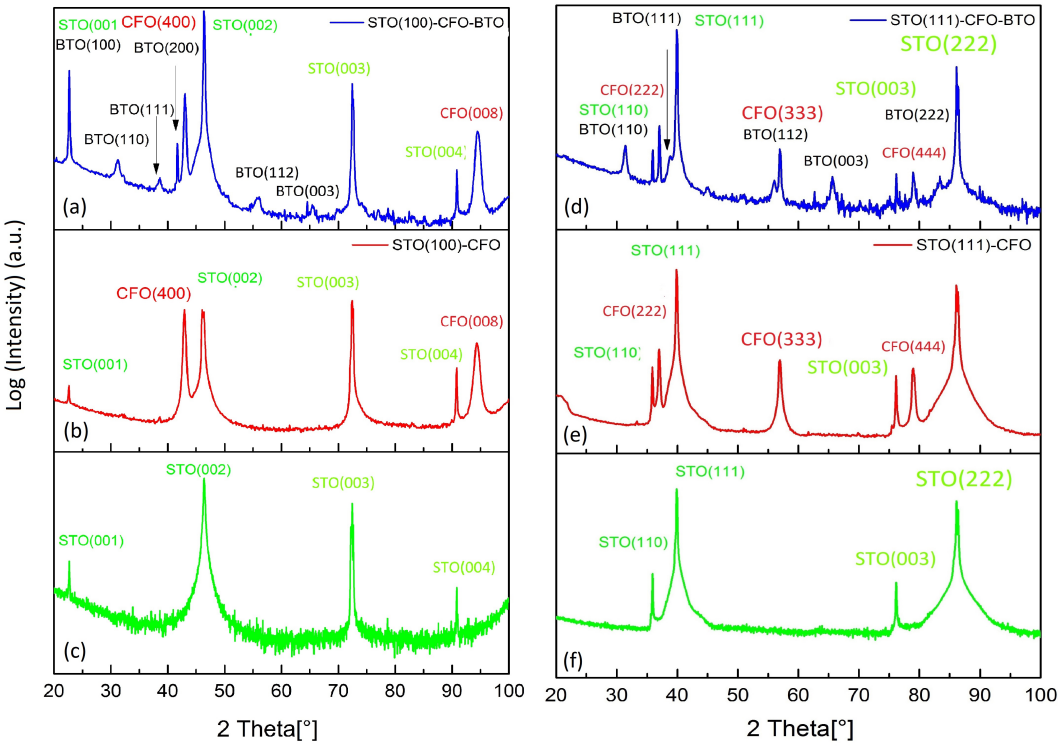

Figure 6.1: XRD spectra of thin films (a) BLF100 (b) BLF111, (c) STO(100)//CFO (d) STO(111)//CFO, (e) STO(100), and (f) STO(111), respectively.

XRD spectra of BLF111, STO(111)//CFO film, and STO(111) substrate are displayed in Fig.6.1(d), (e) and (f), respectively. The CFO film on STO(111), i.e., STO(111)//CFO displays strong texture, with the strongest reflections being CFO(222), CFO(333) and CFO(444). The STO(111)//CFO//BTO film (BLF111) as shown in panel (c) is, however, polycrystalline with randomly oriented crystallites. The strongest reflections are BTO(111) and BTO(112), however, other reflections are also present which include BTO(003) and BTO(222).

6.3.1.2 TEM Analysis

Transmission electron microscopy was utilized to elucidate the structure and especially the interfaces of the thin films. Fig.6.2 shows a cross-sectional view of the film. The thickness of CFO intermediate layer is about 90-100 nm while that of top BTO layers is around 50-70 nm.

To further elucidate how the interfaces look like, High-Resolution TEM (HRTEM) images were acquired at both interfaces, i.e., the STO//CFO interface and CFO//BTO interface for each film. The STO//CFO interface for the bi-layer thin film grown on STO(111) substrate is shown in Fig. 6.3(a). The interfaces are sharp enough, and the planes corresponding to different phases are visible. The analysis of the planes was done by fast Fourier filtering (FFT-filtering) of the selected area of the film as depicted in

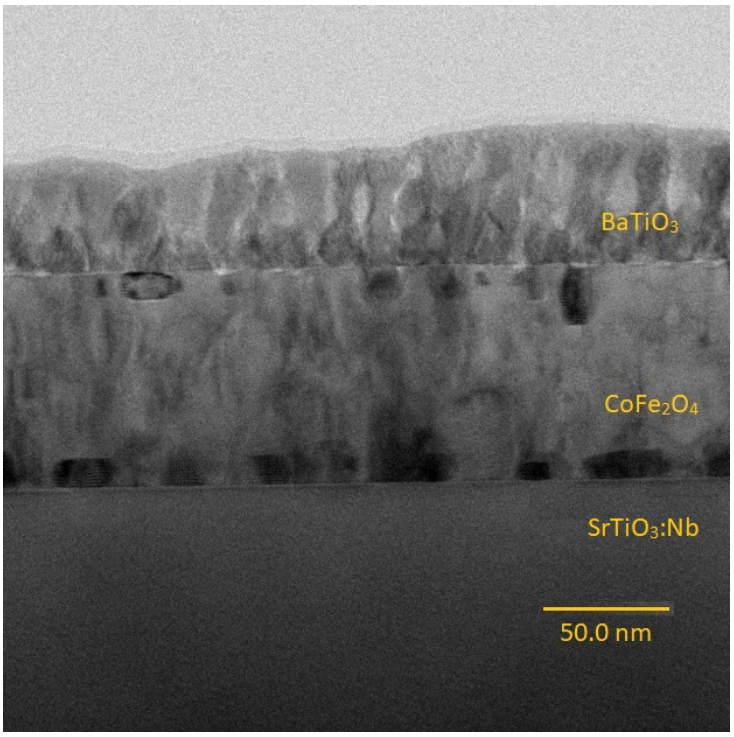

Figure 6.2: Cross-sectional image of BLF100 showing the growth pattern of the different layers.

the image. This yielded the interplanar distances corresponding to the plane STO(110) ($d_{110} = 2.79$Å) and CFO(111) ($d_{111} = 4.65$Å) at this interface. Similar analysis was also performed on the CFO//BTO interface as shown in Fig. 6.3(b), where the interplanar distances calculated form FFT-analysis came out to be CFO(111) ($d_{111} = 4.65$Å) and BTO(101) ($d_{101} = 2.89$Å). This means that the CFO layer has a texture along the {111} direction while at the interface the BTO layer is {101} oriented. Similar analyses were done for the film grown on STO(100) substrate as shown in figures 6.4(a) and 6.4(b) for STO//CFO and CFO//BTO interfaces, respectively. For the STO//CFO interface, the FFT analysis showed that CFO is oriented along the {220} direction ($d_{220} = 2.92$Å) while from the CFO//BTO interface analysis, it was revealed that at this interface CFO is in direction {220} while BTO has an orientation along the {101} ($d_{101} = 2.92$Å) direction.

6.3.2 Magnetic Measurements

Magnetization versus magnetic field hystereses normalized to maximum magnetization for BLF100 and BLF111 are displayed in Fig. 6.5(a) and (b) (measured at 5K), and (c) and (d) (measured at 300 K), respectively. Coercivity for both thin films increases with decreasing temperature, pointing out towards the highly ordered ferrimagnetic state of CFO at 5 K. It is also evident that the $M(H)$ loop for BLF111 at 300 K is slimmer compared to that of BLF100. BLF100 has a higher value of coercivity (~ 1983 Oe) as compared to BLF111 which has a value of $H_C = 1234$ Oe. The corresponding $M(T)$ curves measured in field-cooling(FC) and zero-field-cooling (ZFC) modes are shown for BLF100

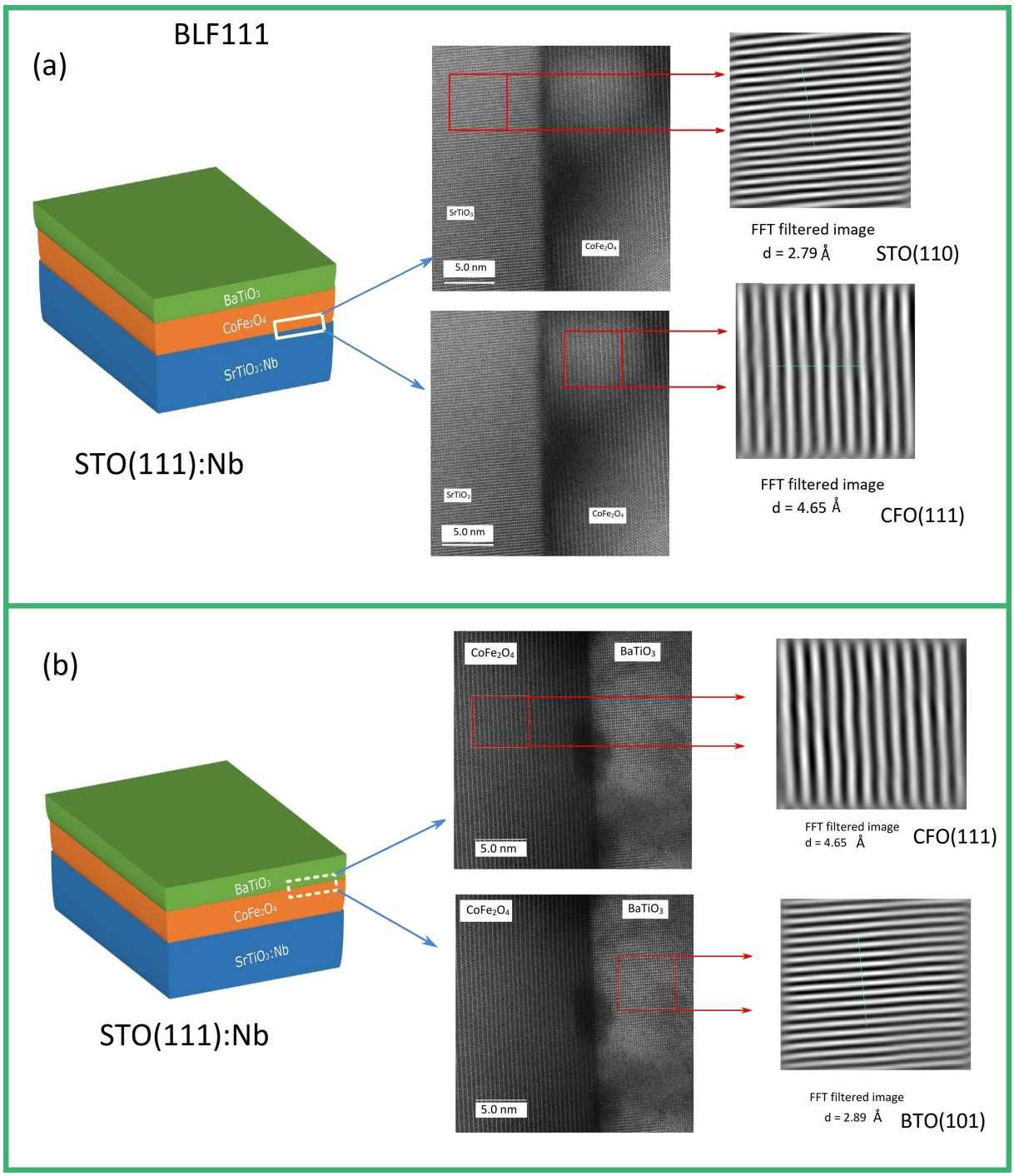

Figure 6.3: TEM analysis of BLF111. Analysis of (a) STO//CFO interface via high-resolution dark-field TEM images along with their Fourier-filtered images: and (b) analysis of CFO//BTO interface. The interplanar distances calculated from Fourier analysis are also given.

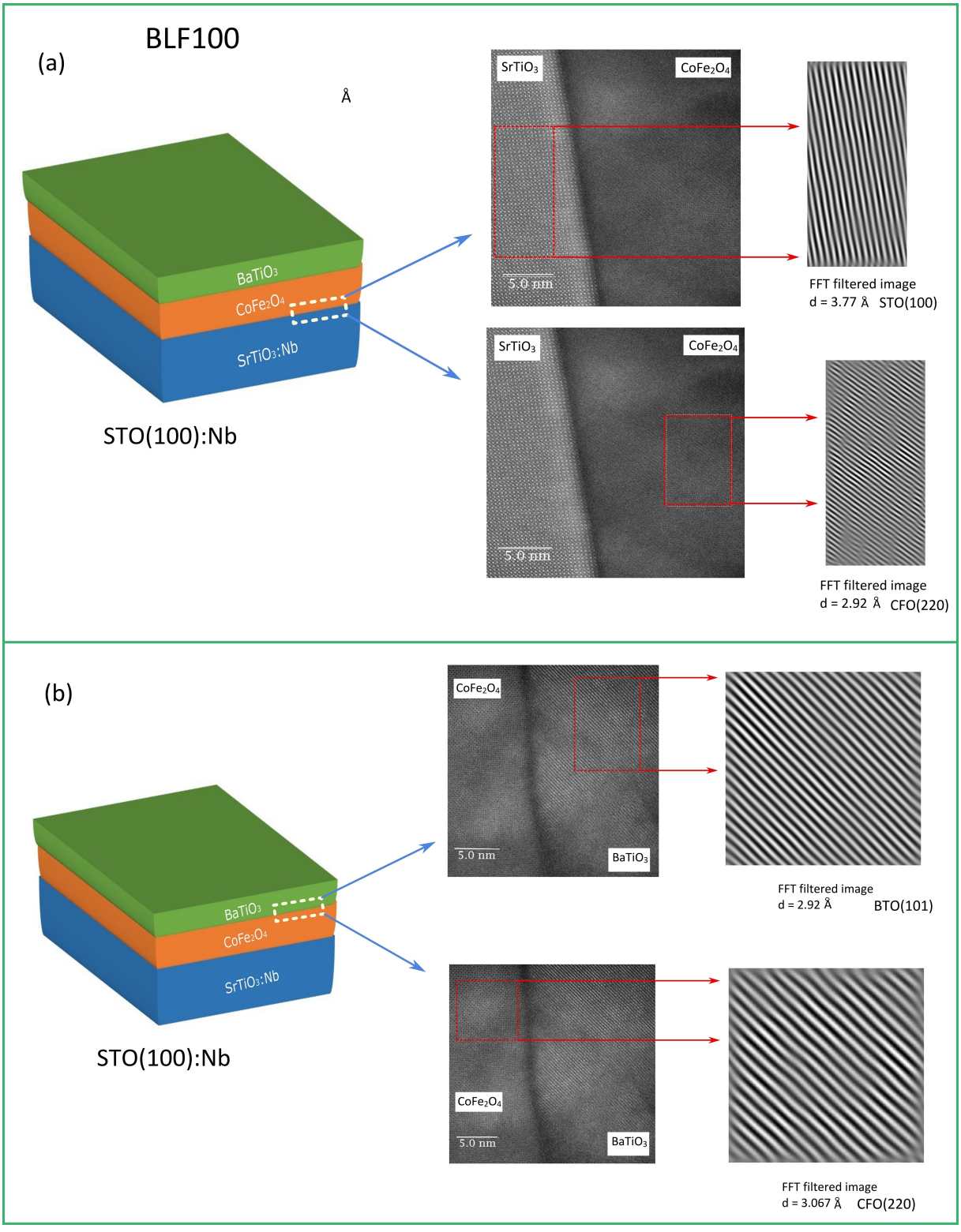

Figure 6.4: TEM analysis of BLF100. Analysis of (a) STO//CFO interface via high-resolution dark-field TEM images along with their Fourier-filtered images: and (b) analysis of CFO//BTO interface. The interplanar distances calculated from Fourier analysis are also given.

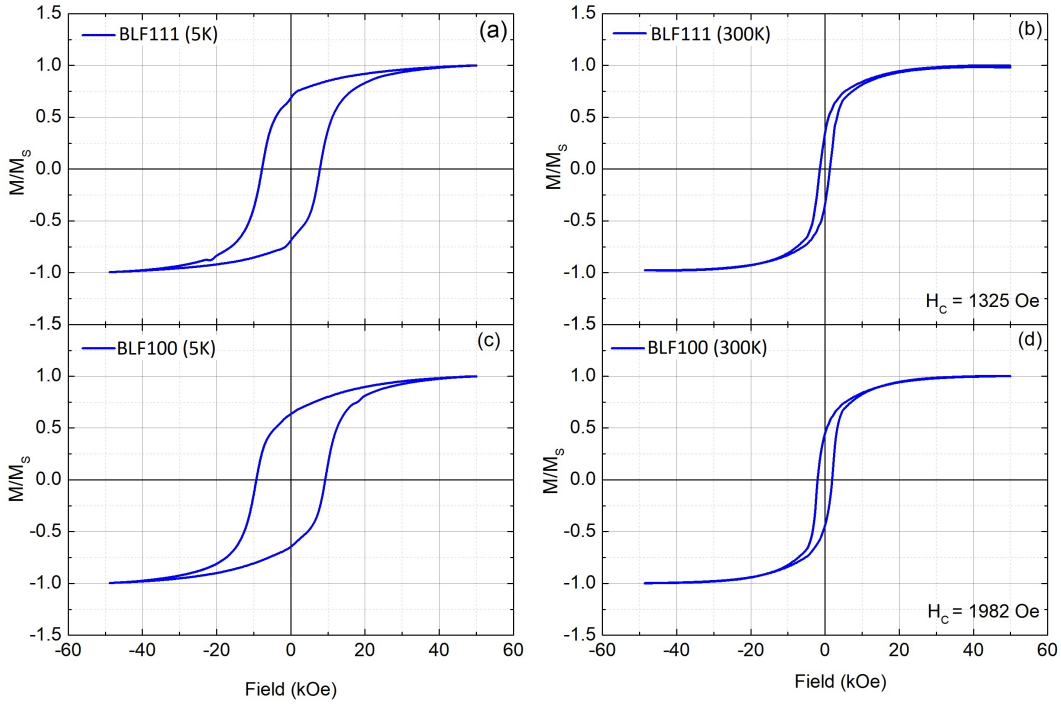

Figure 6.5: Normalized magnetic hystereses for both the films. (a) and (b) $M(H)$ curves for BLF111 measured at 5 K and 300 K, respectively. (c) and (d) $M(H)$ curves for BLF100 measured at 5 K and 300 K, respectively.

and BLF111 in Fig. 6.6(a) and (b), respectively. Both curves were measured at 100Oe of *dc* bias. For BLF111 FC magnetization initially increases with decreasing temperature and then saturates on the further decrease in temperature. The ZFC curve for BLF111 shows a decrease all the way down to 5 K. This decrease in ZFC magnetization can be attributed to randomization of different magnetic grains and the absence of long-range order. For BLF100, the FC behavior of $M(T)$ is similar to that of BLF111. However, the ZFC $M(T)$ is different. Here the $M(T)$ curve goes through a maximum with a decrease in temperature. This maximum is a clear indication of the blocking point (see the vertical arrow in Fig.6.6 (a)). The blocking phenomenon is normally present in the system of nanoparticles. However, this blocking can be explained a bit differently. The blocking behavior derives itself from the single magnetic domain structure of grain with size in the range of several tens of nanometers. These single-domain particles are hard to magnetize so a magnetic blocking point is encountered.[298, 299] This can be interpreted in terms of the TEM data as follows.

As shown in TEM analysis, CFO in BLF111 has a homogeneous growth. The lattice planes corresponding to CFO at the STO//CFO interface are the same as those at the CFO//BTO interface and also inside the bulk. This is not the case for BLF100. Differently oriented grains inside the bulk of the CFO layer as well as both interfaces are visible in the TEM images. These randomly oriented grains give rise to a situation similar to a

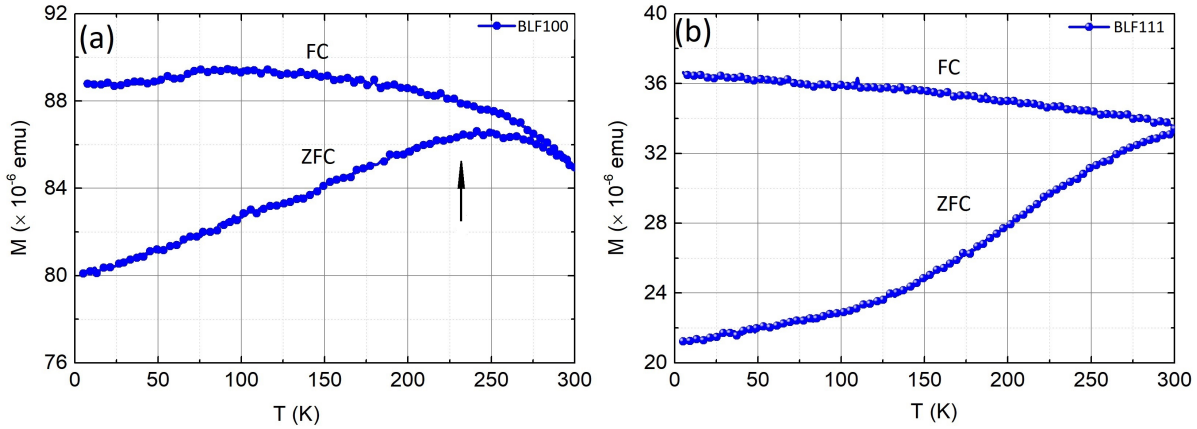

Figure 6.6: (a) Zero-field-cooled (ZFC) and Field-Cooled (FC) $M(T)$ curve for BLF100. (b) Zero-field-cooled (ZFC) and field-cooled (FC) $M(T)$ curve for BLF111. Both curves in (a) and (b) were measured under a magnetic bias of 100 Oe.

distribution of single domain particles as already mentioned. As these grains inside the CFO are harder to magnetize as compared with almost similarly oriented particle as is the case with BLF111, therefore, a higher coercive magnetic field was noted for BLF100 as compared with that of BLF111. Moreover, the smaller size of these particles can also be inferred from the overlapping of the ZFC and FC curves for BLF100 just above the blocking temperature T_B.[300]

6.3.3 Piezoresponse Force Microscopy Under A Magnetic Field

In recent years, PFM studies have been consistent in showing that upon application of magnetic field to composites, the ferroelectric phase shows a proportional change of the locally measured piezoelectric coupling (d^{eff}).[301] However, the techniques used so far are not statistically sound and scientifically robust. Thus a more rigorous approach in the form Principal Component Analysis (PCA) to study the local magnetoelectric coupling in composites was proposed.[302] The principal components produce linear combinations or dimensions of the data that are really high in variance and that are uncorrelated. In the current study, PCA was used to analyze the sequential images acquired at different magnetic fields. The task of PCA here is to identify a statistically significant pattern/s in the measured piezoresponse as a function of magnetic field. The details about the PCA application to the ME coupling process were published elsewhere.[303] As a result of PCA, the relevant patterns in the piezoresponse versus magnetic field behavior were identified, indicating a change in the local piezoelectric coupling d^{eff} as a function of magnetic field. The differences in the observed patterns were analyzed concerning the two different orientations of the substrates. The image acquiring sequence was such that the in-plane magnetic field was applied to a maximum value (600 Oe in this case) and the vertical PFM image was acquired at that value. Then the magnetic field was sequentially

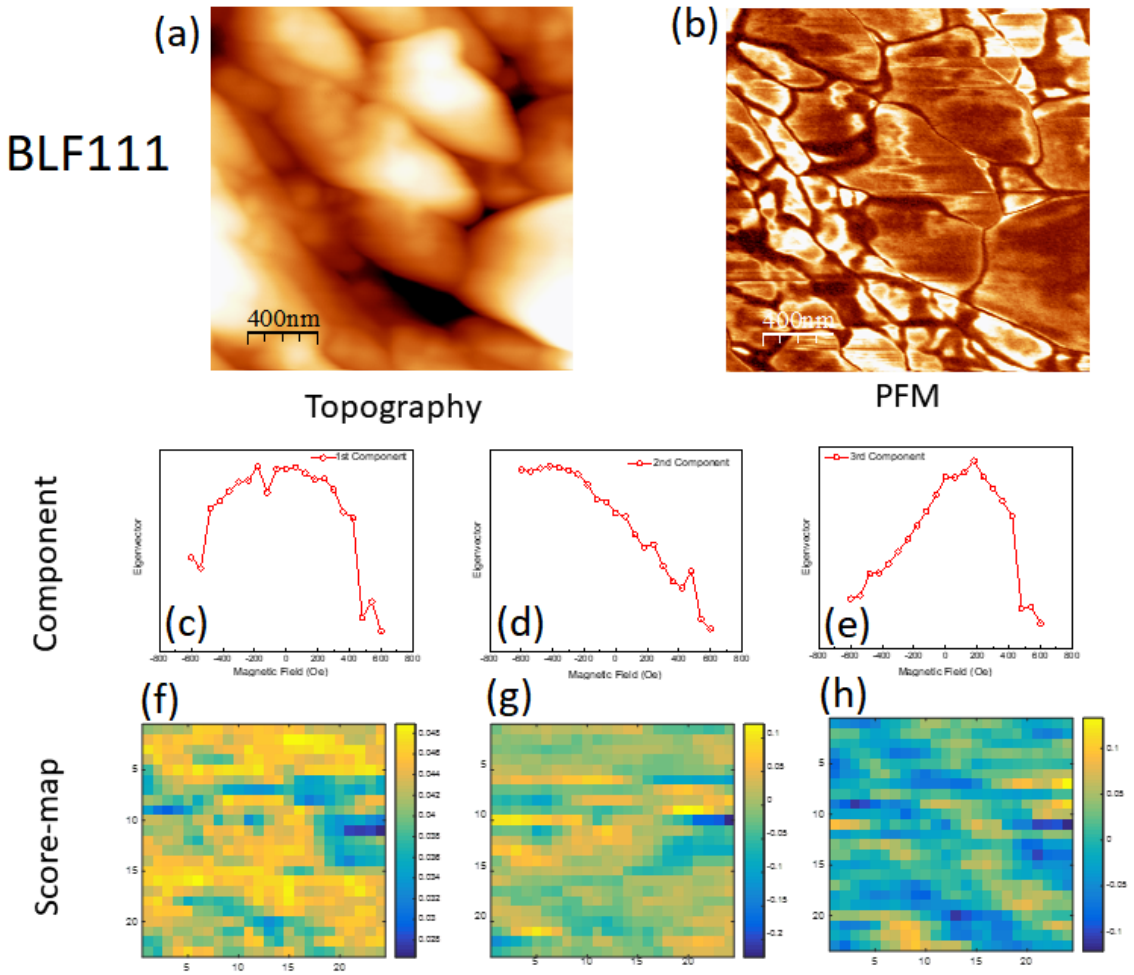

Figure 6.7: (a) Topography; (b) vertical PFM; and (c) PCA first component; (d) PCA second component; (e) PCA third component; (f) First component score map; (g) Second component score map; (h) Third component score map, for BLF111.

decreased in small steps (60 Oe step). After stabilization of the field, PFM images were acquired. This procedure was continued for field reversal to a maximum point (-600 Oe). A set of 21 images was obtained. Special care was taken to adjust the images to any shift of the measuring spot. Later the PCA procedure was applied to all these images.

To understand the results of PCA analysis, we presume that each of the locally participating constitutive phenomena, namely magnetostriction, elasticity, and piezoelectricity, lie within linear (small field) regime. The direct ME coupling is conventionally defined as $\alpha_{ME} = \frac{\partial E}{\partial H}$ and electric polarization in a dielectric material is usually given by $P = \varepsilon E$. The effective piezocoefficient for a piezoelectric is given by Eq. 3.17 i.e., $d^{eff} = \varepsilon\varepsilon_0 Q P(E)$. Thus, one gets:

$$\alpha_{ME} = \frac{1}{\varepsilon_0 \varepsilon^2 Q} \frac{\partial (d^{eff})}{\partial H} \tag{6.1}$$

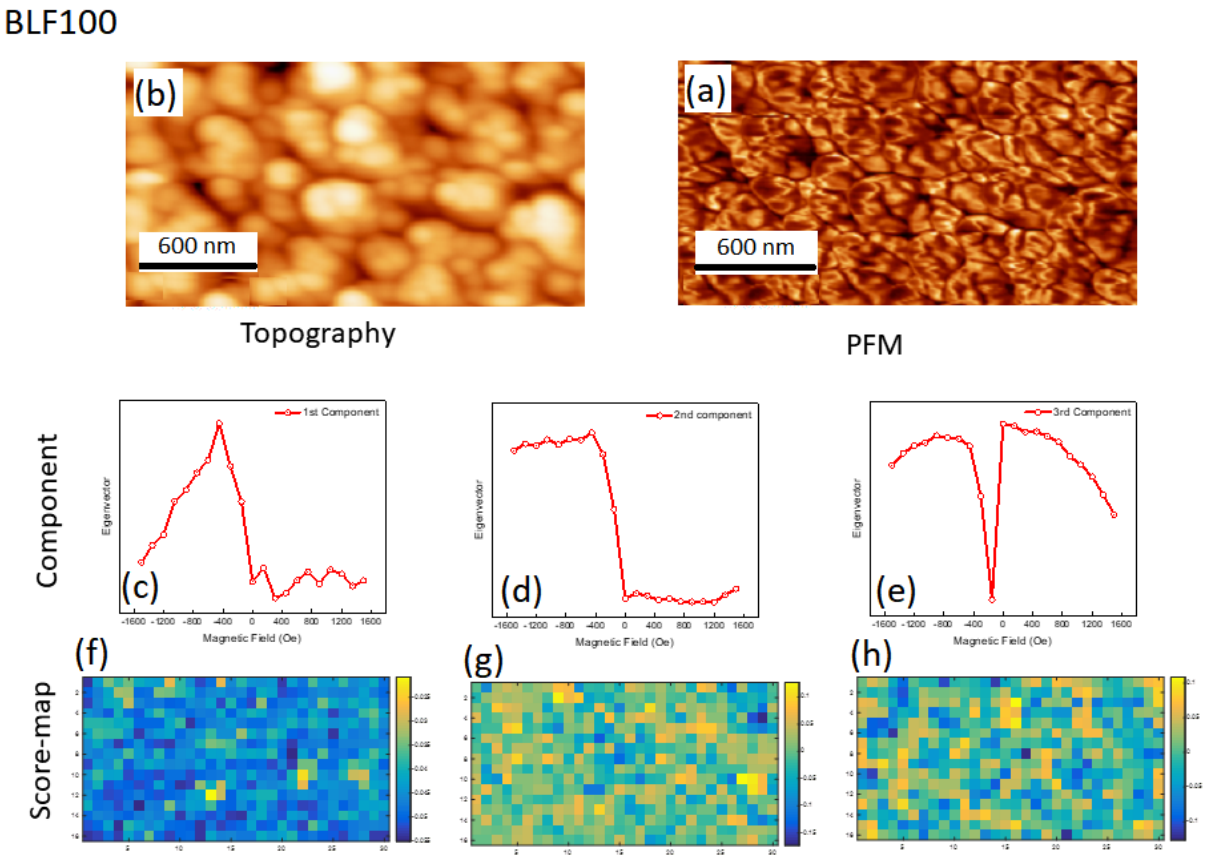

Figure 6.8: (a) Topography; (b) vertical PFM; and (c) PCA first component; (d) PCA second component; (e) PCA third component; (f) First component score map; (g) Second component score map; (h) Third component score map, for BLF100.

Thus the variation of d^{eff} with the magnetic field is a manifestation of stress-mediated ME coupling.[301] For BLF111, the 1st component of the PCA is interesting (Fig. 6.7 (c) and its score map is displayed in Fig. 6.7 (f). The PCA component drops quite sharply with the increase of the magnetic field in either direction. The 2nd and 3rd components in Fig. 6.7 (d) and (e) do not give any reasonable information. It can be speculated that these components might give a correlation between environmental noise and some drift that might still be present even after removing it manually before the analysis, without any relation to the ME coupling. On the other hand, PCA gives a bit different results in case of BLF100. Here 1st and 2nd components are strange in shape, providing almost zero information about any physical phenomenon. This is understandable if these components are compared with the mean-vector of BLF100 as shown in Fig. 6.9 (b). A mean vector is an average piezoresponse of the whole image area. One notices in Fig. 6.8 (c) that around zero magnetic field, there is a sharp spike. This peak might be due to the mean-vector response as depicted in Fig. 6.9(b). The 2nd component also does not convey any valuable information. The 3rd component, however, shows a behavior that has some physical sense regarding our two-phase system. Here a slow decrease is noted when the

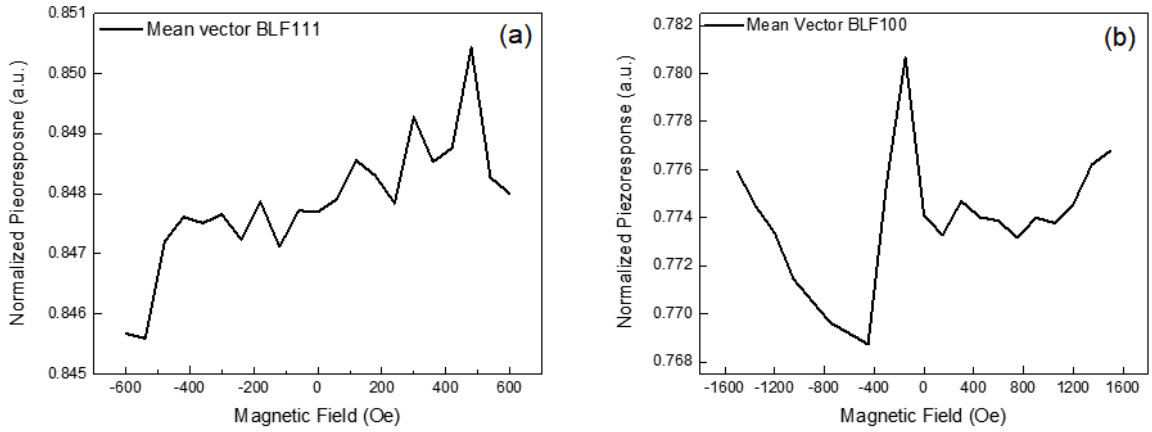

Figure 6.9: Mean-vector as a function of applied magnetic field (a) BLF111; (b) BLF100.

field was increased in either of the two directions. This response can even be compared with the 1st component of BLF111. The common feature of the two components is the inflection around the zero magnetic value and then a slow decreasing trend with increasing magnetic field values.

By looking at the score maps of both films, one realizes that why 1st component in BLF111 is more reasonable while for BLF100, it is the 3rd component which makes more sense. The score map of the 1st component in BLF111 shows essentially the areas whose PFM response was affected most by the magnetic field. It is clear that a high response was found only in those regions where grains were distinct. The other two components show no correlation with PFM grains. Similarly in case of BLF100, the score maps of the first two components show no correlation with the PFM response of the film, while the 3rd score map is correlated with the PFM response.

6.3.4 Discussion

It is a well-known lattice-matching epitaxy fact that when lattice mismatch is small (≤ 8 %), the film grows pseudomorphically up to a certain critical thickness, after that, it becomes energetically favorable for it to contain dislocations.[304] This critical thickness is on the order of 25-30 nm in most of cases. Thus, when the film thickness is beyond this critical value, the misfit is divided into both strain and dislocations. In case of BLF111, the misfit between STO and CFO causes dislocations, but only up to a thickness of 35-40 nm, and afterward, the CFO layer relaxes completely as is evident from the cross-sectional TEM analysis of the top portion of the CFO layer (Fig. 6.3(b)) where it is proven that the CFO layer is [111] oriented. When an in-plane magnetic field is applied to this [111] oriented film, the most probable direction of the field will be either along [-110] or [1-10] as depicted in Fig. 6.10. These two axes are at right angle to [111] and at 45° to the [100] direction. By looking at the *two-constant equation* (Eq. 1.52), it is easy to realize that

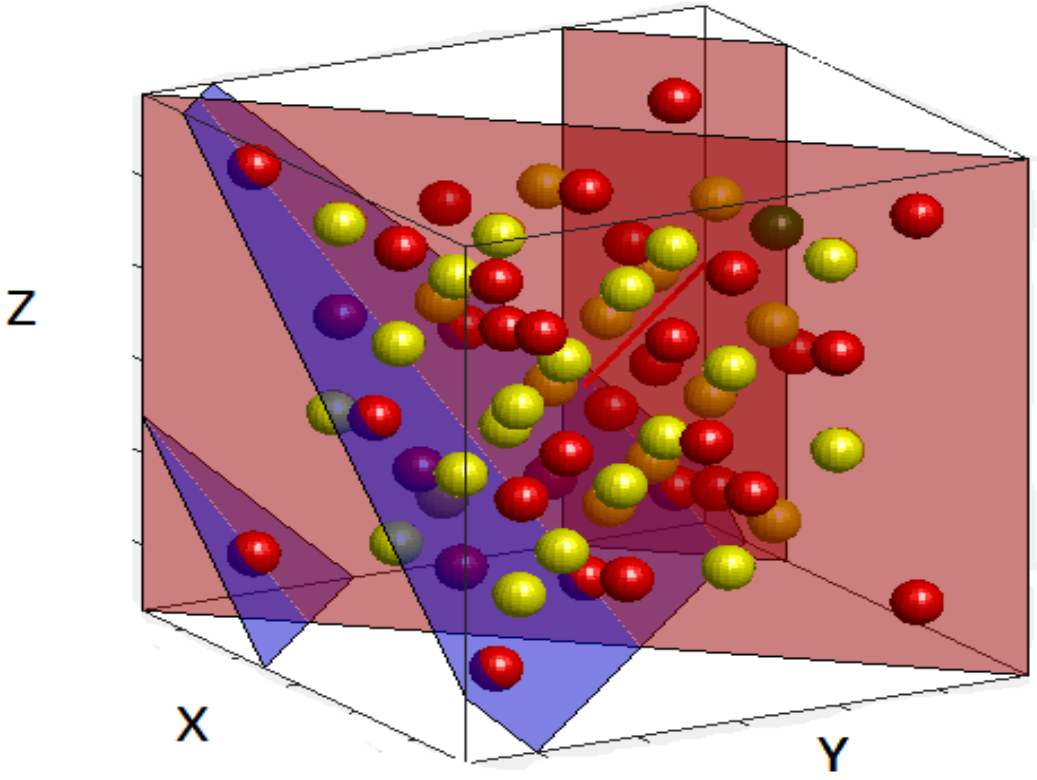

Figure 6.10: Schematic depiction of (111) plane (in blue color) in a CFO unit cell. The plane in red color shows the orientation of the in-plane magnetic field whose direction is into this plane or out of it.

the only contribution to magnetostriction would come from λ_{100}. As it is well-known in case of CFO that λ_{100} has a greater slope as compared with λ_{111} in a *dc* magnetic field.[305] The 1st component for BLF111, thus, can be associated with a qualitative sense of ME response. The variation of this component follows the behavior of magnetostriction in a *dc* magnetic field.

On the other hand, in BLF100, the CFO layer is strained in the in-plane direction, creating a distribution of differently strained domains. Thus, the interface of CFO and BTO in BLF100 is also not very smooth. When an in-plane magnetic field is applied to BLF100, due to the random orientation of magnetic grains, the situation becomes quite complex. Here both λ_{100} and λ_{111} contribute to the overall magnetostriction. Due to the randomly oriented grains and crystal defects/dislocations in the CFO layer as discussed in TEM analysis of BLF100, the magnetostrictive strain is not efficiently transferred to the BTO layer. This might be the most probable reason for the ME response as depicted by the 3rd PCA component in BLF100. The slope of the principal component in *dc* magnetic field is smaller as compared with that of BLF111. Thus, it can be concluded that the

overall ME response for BLF100 is smaller as compared with that of BLF111.

6.4 Conclusions

In summary, the stress-mediated magnetoelectric coupling in two ferrite-perovskite heterostructured thin films grown on differently oriented substrates, which was induced locally by a *dc* magnetic field, was investigated. The experimental procedure involved the measurement of the changes in the piezoresponse of the multiferroic sample when a static magnetic field was applied in the plane of the film. Due to the magnetostriction of the ferrite layer, the stress produced is transferred across the interface to the ferroelectric layer, thereby changing its piezoresponse which could be detected experimentally by a PFM tip. From the magnetic field variation of the static piezoelectric response, a simple relationship was deduced with the help of the principal component analysis technique. The principal components for both thin films showed the effect of stress-mediated ME coupling. However, the variation of the component for BLF111 was much higher than BLF100 indicating a strong ME coupling between the electrostrictive and magnetic layers at room temperature. The ME coupling has an orientational dependence in addition to the quality of the interface between the magnetostrictive and the ferroelectric layer. The outcomes indicate that this experimental procedure can be extended to other multiferroic magnetoelectric structures with different dimensionalities and connectivity schemes between the ferroelectric and magnetostrictive phases.

Chapter 7

Conclusions and Future Outlook

7.1 Conclusions

In this work, the magnetoelectric coupling in extrinsic multiferroic systems, which consist of lead-free $BaTiO_3$-based piezoelectrics and spinel ferrites, $CoFe_2O_4$ and $NiFe_2O_4$, has been investigated to identify the best combination and the best configuration of them. The systems which were studied include three bulk systems: $0.5Ba(Zr_{0.2}Ti_{0.8})O_3$-$0.5(Ba_{0.7}Ca_{0.3})TiO_3$ (BCZT) combined with $CoFe_2O_4$ (BCZT-CFO) and $NiFe_2O_4$ (BCZT-NFO); one system consisting of $Ba(Ti_{0.7}Sn_{0.3})O_3$ combined with CFO ($BSnT_{80}$-CFO_{20}); and a thin film system consisting of bilayered thin films of $CoFe_2O_4$ and $BaTiO_3$. To understand the structure-property relationship and its impact on ME coupling in these composites, direct and converse ME effects were measured. Several techniques including direct and converse measurements on a large scale as well as the local scale measurements with PFM were used. A detailed analysis of field dependent as well as temperature dependent ME properties was performed to find the appropriate relationship between intrinsic properties like magnetostriction in ferrite and piezoelectricity in piezoelectric phases. A wide-range of experiments including solid state sample synthesis, PLD thin film growth, X-ray diffraction, SEM, TEM, ToF-SIMS, PFM , MFM, direct ME measurement at room temperature, and converse effect measurement with a modified SQUID setup in a broad-range of temperatures were employed. Below is a list of significant findings and conclusions which resulted from these studies.

7.1.1 BCZT-CFO Composites

1. From frequency and temperature dependences of electric permittivity, it was found that the samples had dielectric contributions from both the piezoelectric and the ferromagnetic phases. It was concluded that the dielectric response was dominated by the contribution from CFO at low frequencies and high temperatures. The main reason for such a dielectric behavior is the large difference in electric conductivity of the phases i.e., the BCT50-BZT phase is a good electric insulator while the CFO phase is a semiconductor. When these two are combined in the shape of 3-3 composite, the difference in electric conductivities generate interfacial charges. This

interfacial polarization (Maxwell-Wagner polarization) causes dielectric relaxation.

2. The temperature variation of electrically induced ME magnetization showed a broad maximum in a particular temperature range, irrespective of the ferrite content in that composition. This maximum was attributed to the maximum on the electric compliance constant versus temperature curve of BCZT phase. Important to note is that the elastic compliance constant for BCZT ceramics is maximum at their polymorphic phase boundaries and is not directly related to its maximum of electric permittivity or its Curie temperature. Therefore it was concluded that it is the elastic compliance of the piezoelectric phase, which is responsible for the maximum in the induced ME coupling and not the maximum of electric permittivity, which occurs at the Curie temperature and was previoulsy considered to be coinciding with the $M_{ME}(T)_{max}$.

3. The behavior of induced magnetization in a *dc* magnetic field tracks the behavior of derivative of magnetostriction of the ferrite phase ($d\lambda/dH$). It was found that $M_{ME}(H)$ goes through a maximum in both directions of magnetic field (with a reversal of the sign). It was also found that there exists a special fixed value of *dc* magnetic field for each composition where this maximum ($M_{ME}(H)_{max}$) occurs, and which is related to magnetic anisotropy constant of the ferrite phase. In fact, there is an inverse relationship between the maximum of $d\lambda/dH$ and the anisotropy constant of cobalt ferrite. The anisotropy constant increases with decrease in temperature which implies that $M_{ME}(H)$ would decrease with decreasing temperature.

4. The behavior of magnetostriction derivative $d\lambda/dH$ in a *dc* magnetic field was modified by inserting non-magnetic Al^{3+} ions inside the cubic spinel lattice of cobalt ferrite. Al^{3+} tend to occupy preferentially the octahedral sites rather than the tetrahedral sites of CFO, as it was proved by the combined analysis of the data from XRD, magnetization, and Mösbauer measurements. Thus Al^{3+} modification of CFO reduces its saturation magnetization by replacing a large number of Fe^{3+} on the octahedral sites which results into a weaker superexchange coupling between the octahedral Fe^{3+} ions and the tetrahedral Fe^{3+} ions. This superexchange coupling which is responsible for antiferromagnetic coupling between these two sites is a decisive factor for the saturation magnetization of spinel ferrites.

5. Another important consequence of Al^{3+} modification on CFO was that it also displaced some of the Co^{2+} ions for the octahedral sites. These Co^{2+} ions are usually responsible for high anisotropy and the magnetostriction properties of the ferrite phase due to their spin-orbit coupling. Thus Al^{3+} had also caused reduction of the

spin-orbit coupling, thereby reducing the anisotropy constant. This in turn resulted in the enhanced stress sensitivity which is proprtional to $d\lambda/dH$ and thus a superior converse ME coefficient for the composite with Al-modified CFO. The converse ME coefficient for BCZT-CFO(Al) sample was 11 ps/m which is almost four times larger than its counterpart with unmodified CFO.

7.1.2 BCZT-NFO Composites

Continued from the last section of BCZT-CFO composites, keeping in consideration the superior electromechanical properties of BCZT, this new series of composites were formed with variable volume fractions of $NiFe_2O_4$ (20-50 vol.%). NFO is also a spinel ferrimagnetic material and is obtained by replacing the Co^{2+} by Ni^{2+} completely in the lattice of CFO. NFO is believed to have better magneto-mechanical properties as compared with CFO.

1. The samples were shown to have good multiferroic characteristics both in bulk and on the microscopic level. The piezoelectricity in these samples was verified by measuring their local piezoresponse at room temperature. The saturation magnetization was seen to be proportional to the nickel ferrite volume content per sample.

2. Time of flight secondary electron mass spectrometry (ToF-SIMS) was used to elucidate the 3D distribution of two phases in the ceramics down to certain depth. It was found that the sample connectivity varied from pseudo 0-3 at lower ferrite content to pseudo 3-3 at higher content. It was also seen that higher ferrite content resulted into continuous patches which are detrimental to the piezoelectric properties of the overall composite because it hinders the electric poling by creating conductive paths for charge flow.

3. Direct ME effect was measured as a function of *dc* magnetic field, and the sample with highest ferrite content shows the maximum value of the coupling constant which is around 1.9 mV/Oe.cm. from the frequency dependent measurements of direct ME effect, it was found that one of the samples with 20% ferrite content shows the effect of piezoelectric resonance of BCZT on the ME coupling. The direct ME coupling coefficient at a resonance frequency (362 kHz) was found to be 273 mV/Oe.cm for this sample. No other sample shows such resonance frequency effect which might be attributed to the high ferrite content which suppresses this electromechanical feature of BCTZT.

4. Converse ME effect was measured as a function of temperature and *dc* magnetic field. The temperature as well as the magnetic field behavior of induced ME magnetization were the same as that in the case of BCZT-CFO composites i.e., the

temperature behavior followed the elastic compliance constant behavior of BCZT and the magnetic field behavior tracked the $d\lambda/dH$ behavior. The converse ME coefficient was the highest for the sample with 30 vol.% of the ferrite, while the direct ME coefficient was not the highest. This means that the mechanisms responsible for the direct and the converse ME couplings behavior are not exactly the same even when the ferrite content are the same. This is explained by considering the real microstructure of these samples. In case of the direct ME coupling, the off-resonance ME effect is the largest for highest ferrite content (50 vol.%) which is related to the demagnetization factor. In this case, the shape of magnetic particles does not matter because the agent that is producing this effect is the magnetic field. On the other hand, when the agent that is producing the change is an electric field (converese ME coupling), the scenario is different. We believe that sample with less ferrite content (30 vol.% and 40 vol.%) can be treated by an equivalent *series* circuit of piezoelectric and ferromagnetic grains, resultantly, the piezoelectric grains would experience more *effective* electric field as compared with the samples that contained higher ferrite content. On the other hand, the piezoelectric and ferromagnetic grains can be treated as being connected in *parallel* to each other in case of samples with higher ferrite content, thus reducing the *effective* electric field and hence the reduced effect of inverse piezoelectric effect.

5. A comparison of ME coupling among the BCZT-CFO and BCZT-NFO ceramics can be made here. The BCZT-NFO composites show overall better ME properties as compared with those of the BCZT-CFO composites. The highest value of converse ME coupling coefficient for BCZT-CFO samples is 11 ps/m [for $BCZT_{50}$-$CFO(Al)_{50}$] and the maximum value for BCZT-NFO composites was 45 ps/m [for $BCZT_{70}$-NFO_{30} 30 vol.% NFO]. This is a large enhancement (~ 400 %) if we consider that both types of compositions were fabricated using the similar solid state syntheses. The enhancement in case of NFO containing composites can be attributed to the larger initial magnetic permeability of NFO.[306] The initial permeability of any ferrite determines the ease with which the magnetic domains can be switched/altered. The values of initial permeabilities of NFO and CFO are 1 and 39, respectively.[249] Thus it can be concluded that the initial permeability of a magnetic material is the most important parameter than the magnetostriction itself.

6. Thus the two most important conclusions drawn from the studies of these composites are that the properties like electromechanical coupling coeffiecient of the piezoelectric phase and the magnetomechanical coupling factor of the ferrite phase are the key factors for optimum ME coupling.

7.1.3 BSnT-CFO Composite

This composite was designed by keeping in mind the excellent relaxor properties of $Ba(Ti_{0.7}Sn_{0.3})O_3$. This composition has a Curie temperature in the range of 100-200 K.

1. The relaxor properties of BSnT were retained even in the composite, this is unique from what was observed in case of BCZT-based composites where the electric permittivity behavior was altered from that of the pure one. The composite with 20 vol.% of CFO also showed all the relaxor features of the pure BSnT.

2. The ME coupling in these composites was measured by measuring the magnetocapacitance as a function of temperature. The sample showed enhanced magnetodielectric coefficient in the temperature range around the diffused maximum of the electric permittivity. Here again, the most probable reasons of the enhancement of the ME coupling might be following:
   The coincidence of elastic compliance maximum with the magnetocapacitance maximum in the temperature range;
   and the possible effect of magnetic field on polar nanoregions by freezing mechanism and thus changing the strain state of the ferroelectric phase.

7.1.4 BTO-CFO Bilayered Thin Films

1. It was found from the TEM and XRD analysis that (111) oriented $SrTiO_3$ substrate offers a better landscape for the growth of $CoFe_2O_4$ layer as compared with that of (100) oriented substrate. The most probable reason for that might be the strain relaxation mechanism which favors the (111) orientation rather than the (100). Resultantly, the growth of CFO on STO(100) consists of many small domains throughout the thickness of the CFO layer while that of CFO on STO(111) consists of comparatively larger sized domains and a smooth growth beyond a particular thickness, which affects the growth of a top layer of $BaTiO_3$.

2. The magnetic studies showed that the coercivity is higher for BLF100 as compared with BLF111. The most probable reason are the randomly oriented grains of the former which make it harder for domains to be aligned parallel to the field.

3. Direct magnetoelectric coupling studied with the help of piezoresponse force microscopy under an applied magnetic field is higher in case of BLF111 film as compared with that of BLF100 film. It was attributed to the fact that smooth interface between the CFO and BTO layers offers a better medium to transfer the magnetostrictive stress from the CFO layer to the BTO layer.

7.2 Future Outlook

1. Considering the implications of polymorphic phase boundaries, it presents a very interesting scenario for the development of new two-phase piezoelectric-magnetostrictive composites. Until now, not much attention has been paid to the enhanced piezoelectricity at the morphotropic phase boundaries for use as an ingredient to increase the ME coupling. Thus there are several systems with polymorphic phase boundaries which can be investigated as ferroelectric components. One very obvious example is the system $Ba(Sn,Ti)O_3$, which also possesses a polymorphic phase boundary around ~10% of Sn doping. A complete study which may comprise of electric, magnetic and magnetoelectric properties is suggested.

2. Metal-piezoelectric-metal combination of laminates, also known as graded magnetoelectrics, has also not been studied to date with BCT50-BZT and magnetostrictive Metglas. This might offer a great possibility toward the ME coupling enhancement. The manufacturing of such a graded composite is already underway.

3. The first step of synthesis and study of CFO//BTO bilayered thin films has been achieved. This would be extended to BCZT//CFO and BCZT//NFO bilayers that can be grown by PLD technique on various substrates to explore the possibility of enhanced ME coupling. This can be combined with theoretical modeling to get a complete physical picture.

List of Figures

List of Tables

Bibliography

[1] V. Wadhawan. *Introduction to Ferroic Materials*. Taylor & Francis, 2000.

[2] D. B. Litvin. Ferroic classifications extended to ferrotoroidic crystals. *Acta Crystallographica Section A*, 64(2):316–320, Mar 2008.

[3] Hans Schmid. Multi-ferroic magnetoelectrics. *Ferroelectrics*, 162(1):317–338, 1994.

[4] Manuel Bibes and Agnes Barthelemy. Multiferroics: Towards a magnetoelectric memory. *Nature Materials*, 7(6):425–426, 2008.

[5] Jing Ma, Jiamian Hu, Zheng Li, and Ce-Wen Nan. Recent progress in multiferroic magnetoelectric composites: from bulk to thin films. *Advanced Materials*, 23(9):1062–1087, 2011.

[6] Junyi Zhai, Zengping Xing, Shuxiang Dong, Jiefang Li, and D. Viehland. Detection of pico-Tesla magnetic fields using magneto-electric sensors at room temperature. *Applied Physics Letters*, 88(6):062510, 2006.

[7] Jason R. Hattrick-Simpers, Liyang Dai, Manfred Wuttig, Ichiro Takeuchi, and Eckhard Quandt. Demonstration of magnetoelectric scanning probe microscopy. *Review of Scientific Instruments*, 78(10):106103, 2007.

[8] Xianzhi Dai, Yumei Wen, Ping Li, Jin Yang, and Gaoyong Zhang. Modeling, characterization and fabrication of vibration energy harvester using Terfenol-D/PZT/Terfenol-D composite transducer. *Sensors and Actuators A: Physical*, 156(2):350–358, 2009.

[9] J. Lou, D. Reed, M. Liu, and N. X. Sun. Electrostatically tunable magnetoelectric inductors with large inductance tunability. *Applied Physics Letters*, 94(11):112508, 2009.

[10] Shuxiang Dong, J. F. Li, D. Viehland, J. Cheng, and L. E. Cross. A strong magnetoelectric voltage gain effect in magnetostrictive-piezoelectric composite. *Applied Physics Letters*, 85(16):3534–3536, 2004.

[11] Haribabu Palneedi, Venkateswarlu Annapureddy, Shashank Priya, and Jungho Ryu. Status and perspectives of multiferroic magnetoelectric composite materials and applications. *Actuators*, 5(1):9, 2016.

[12] W. C. Röntgen. Über die durch Bewegung eines im homogenen electrischen Felde befindlichen Dielectricums hervorgerufene electrodynamische Kraft. *Annalen der Physik*, 271(10):264–270, 1888.

[13] H. A. Wilson. On the electric effect of rotating a dielectric in a magnetic field. *Philosophical Transactions of the Royal Society of London Series a-Containing Papers of a Mathematical or Physical Character*, 204:121–137, 1905.

[14] I E Dzyaloshinkii. On the magneto-electrical effect in antiferromagnets. *Soviet Physics JETP-USSR*, 10(3):628–629, 1960.

[15] D. N. Astrov. The magnetoelectric effect in antiferromagnets. *Soviet Physics JETP-USSR*, 11(3):708–709, 1960.

[16] V. J. Folen, G. T. Rado, and E. W. Stalder. Anisotropy of magnetoelectric effect in cr2o3. *Physical Review Letters*, 6(11):607–610, 1961.

[17] C. Kittel. *Introduction to Solid State Physics*. Wiley, 2004.

[18] B. Jaffe, W.R. Cook, and H.L. Jaffe. *Piezoelectric ceramics*. Non-metallic solids. Academic Press, 1971.

[19] K.M. Rabe, C.H. Ahn, and J.M. Triscone. *Physics of Ferroelectrics: A Modern Perspective*. Topics in Applied Physics. Springer Berlin Heidelberg, 2010.

[20] B.A. Strukov and A.P. Levanyuk. *Ferroelectric Phenomena in Crystals: Physical Foundations*. Springer Berlin Heidelberg, 2012.

[21] M.E. Lines and A.M. Glass. *Principles and Applications of Ferroelectrics and Related Materials*. International series of monographs on physics. OUP Oxford, 1977.

[22] K.C. Kao. *Dielectric Phenomena in Solids: With Emphasis on Physical Concepts of Electronic Processes*. Referex Engineering. Academic Press, 2004.

[23] R. Waser, U. Böttger, and S. Tiedke. *Polar Oxides: Properties, Characterization, and Imaging*. Wiley, 2006.

[24] F. Cardarelli. *Materials Handbook: A Concise Desktop Reference*. Springer London, 2008.

[25] R.E. Newnham. *Properties of Materials: Anisotropy, Symmetry, Structure*. OUP Oxford, 2004.

[26] R.E. Newnham. *Structure-property relations*. Crystal chemistry of non-metallic materials. Springer-Verlag, 1975.

[27] Gregg Jaeger. The Ehrenfest Classification of Phase Transitions: Introduction and Evolution. *Archive for History of Exact Sciences*, 53(1):51–81, May 1998.

[28] Tao Shi, Gen Li, and Jing Zhu. Compositional design strategy for high performance ferroelectric oxides with perovskite structure. *Ceramics International*, 43(3):2910 – 2917, 2017.

[29] Nicole A. Benedek and Craig J. Fennie. Why are there so few perovskite ferroelectrics? *The Journal of Physical Chemistry C*, 117(26):13339–13349, 2013.

[30] V. M. Goldschmidt. Die gesetze der krystallochemie. *Naturwissenschaften*, 14(21):477–485, 1926.

[31] Serhiy O Leontsev and Richard E Eitel. Progress in engineering high strain lead-free piezoelectric ceramics. *Science and Technology of Advanced Materials*, 11(4):044302, 2010.

[32] Adam A. Heitmann and George A. Rossetti. Thermodynamics of ferroelectric solid solutions with morphotropic phase boundaries. *Journal of the American Ceramic Society*, 97(6):1661–1685, 2014.

[33] D. Damjanovic. Comments on origins of enhanced piezoelectric properties in ferroelectrics. *IEEE Transactions on Ultrasonics, Ferroelectrics, and Frequency Control*, 56(8):1574–1585, 2009.

[34] A.G. Khachaturyan. Ferroelectric solid solutions with morphotropic boundary: Rotational instability of polarization, metastable coexistence of phases and nanodomain adaptive states. *Philosophical Magazine*, 90(1-4):37–60, 2010.

[35] Yoshihiro Ishibashi and Makoto Iwata. Morphotropic phase boundary in solid solution systems of perovskite-type oxide ferroelectrics. *Japanese Journal of Applied Physics*, 37(8B):L985, 1998.

[36] Z. K. Liu, Xinyu Li, and Q. M. Zhang. Maximizing the number of coexisting phases near invariant critical points for giant electrocaloric and electromechanical responses in ferroelectrics. *Applied Physics Letters*, 101(8):082904, 2012.

[37] M. J. Haun, E. Furman, S. J. Jang, and L. E. Cross. Thermodynamic theory of the lead zirconate-titanate solid solution system, part i: Phenomenology. *Ferroelectrics*, 99(1):13–25, 1989.

[38] V.V. Shvartsman, J. Dec, Z.K. Xu, J. Banys, P. Keburis, and W. Kleemann. Crossover from ferroelectric to relaxor behavior in $BaTi_{1-x}Sn_xO_3$ solid solutions. *Phase Transitions*, 81(11-12):1013–1021, 2008.

[39] Wolfgang Kleemann, George A. Samara, and Jan Dec. *Relaxor Ferroelectrics - from Random Field Models to Glassy Relaxation and Domain States*, pages 275–301. Wiley-VCH Verlag GmbH Co. KGaA, 2005.

[40] A. A. Bokov and Z.-G. Ye. Recent progress in relaxor ferroelectrics with perovskite structure. *Journal of Materials Science*, 41(1):31–52, 2006.

[41] GA Smolenskii and VA Isupov. * segnetoelektricheskie svoistva tverdykh rastvorov stannata bariya v titanate bariya. *Zhurnal Tekhnicheskoi Fiziki*, 24(8):1375–1386, 1954.

[42] Naohiko Yasuda, Hidehiro Ohwa, and Shigeto Asano. Dielectric properties and phase transitions of $Ba(Ti_{1-x}Sn_x)O_3$ solid solution. *Japanese Journal of Applied Physics*, 35(9S):5099, 1996.

[43] E. Du Trémolet de Lacheisserie, D. Gignoux, and M. Schlenker. *Magnetism.* Number v. 1 in Collection Grenoble Sciences. Springer, 2005.

[44] Vincent G. Harris. Chapter one - microwave magnetic materials. In K.H.J. Buschow, editor, *Handbook of Magnetic Materials*, volume 20 of *Handbook of Magnetic Materials*, pages 1 – 63. Elsevier, 2012.

[45] B.D. Cullity and C.D. Graham. *Introduction to Magnetic Materials*. Wiley, 2 edition, 2011.

[46] Koichi Momma and Fujio Izumi. *VESTA3* for three-dimensional visualization of crystal, volumetric and morphology data. *Journal of Applied Crystallography*, 44(6):1272–1276, Dec 2011.

[47] Sam Jin Kim, Seung Wha Lee, and Chul Sung Kim. Mössbauer studies on exchange interactions in $CoFe_2O_4$. *Japanese Journal of Applied Physics*, 40(8R):4897, 2001.

[48] G. Hu, J. H. Choi, C. B. Eom, V. G. Harris, and Y. Suzuki. Structural tuning of the magnetic behavior in spinel-structure ferrite thin films. *Phys. Rev. B*, 62:R779–R782, Jul 2000.

[49] S. Chikazumi. *Physics of Ferromagnetism*. International Series of Monographs on Physics. Oxford University Press, Oxford, 1996.

[50] Yao Wang, Jiamian Hu, Yuanhua Lin, and Ce-Wen Nan. Multiferroic magnetoelectric composite nanostructures. *NPG Asia Materials*, 2(2):61–68, 2010.

[51] Naoshi Ikeda, Hiroyuki Ohsumi, Kenji Ohwada, Kenji Ishii, et al. Ferroelectricity from iron valence ordering in the charge-frustrated system $LuFe_2O_4$. *Nature*, 436(7054):1136, 2005.

[52] C Jooss, L Wu, T Beetz, RF Klie, M Beleggia, MA Schofield, S Schramm, J Hoffmann, and Y Zhu. Polaron melting and ordering as key mechanisms for colossal resistance effects in manganites. *Proceedings of the National Academy of Sciences*, 104(34):13597–13602, 2007.

[53] Hosho Katsura, Naoto Nagaosa, and Alexander V Balatsky. Spin current and magnetoelectric effect in noncollinear magnets. *Physical Review Letters*, 95(5):057205, 2005.

[54] Ivan A Sergienko and E Dagotto. Role of the Dzyaloshinskii-Moriya interaction in multiferroic perovskites. *Physical Review B*, 73(9):094434, 2006.

[55] Taka-hisa Arima. Ferroelectricity induced by proper-screw type magnetic order. *Journal of the Physical Society of Japan*, 76(7):073702–073702, 2007.

[56] Jungho Ryu, Shashank Priya, Kenji Uchino, and Hyoun-Ee Kim. Magnetoelectric effect in composites of magnetostrictive and piezoelectric materials. *Journal of Electroceramics*, 8(2):107–119, 2002.

[57] Enno Lage, Christine Kirchhof, Viktor Hrkac, Lorenz Kienle, Robert Jahns, Reinhard Knöchel, Eckhard Quandt, and Dirk Meyners. Exchange biasing of magnetoelectric composites. *Nature materials*, 11(6):523, 2012.

[58] Ning Zhang, Junfeng Fan, Xiaofang Rong, Hongxia Cao, and Jianjun Wei. Magnetoelectric effect in laminate composites of $Tb_{1-x}Dy_xFe_{2-y}$ and Fe-doped $BaTiO_3$. *Journal of Applied Physics*, 101(6):063907, 2007.

[59] Shuxiang Dong, Junyi Zhai, Feiming Bai, JieFang Li, D. Viehland, and T. A. Lograsso. Magnetostrictive and magnetoelectric behavior of Fe-20 at.% Ga/Pb(Zr,Ti)O_3laminates. *Journal of Applied Physics*, 97(10):103902, 2005.

[60] G. Srinivasan, E. T. Rasmussen, and R. Hayes. Magnetoelectric effects in ferrite-lead zirconate titanate layered composites: The influence of zinc substitution in ferrites. *Phys. Rev. B*, 67:014418, Jan 2003.

[61] Zengping Xing, Shuxiang Dong, Junyi Zhai, Li Yan, Jiefang Li, and D. Viehland. Resonant bending mode of Terfenol-D/steel/Pb(Zr,Ti)O_3 magnetoelectric laminate composites. *Applied Physics Letters*, 89(11):112911, 2006.

[62] Shuxiang Dong, Jungyi Zhai, Jie-Fang Li, and D. Viehland. Magnetoelectric effect in Terfenol-D/Pb(Zr,$TiO)_3$- μ-metal laminate composites. *Applied Physics Letters*, 89(12):122903, 2006.

[63] Shuxiang Dong, Jie-Fang Li, and D. Viehland. A longitudinal-longitudinal mode Terfenol-D/Pb($Mg_{1/3}Nb_{2/3}$)O_3-$PbTiO_3$ laminate composite. *Applied Physics Letters*, 85(22):5305–5306, 2004.

[64] Junyi Zhai, Shuxiang Dong, Zengping Xing, Jiefang Li, and D Viehland. Giant magnetoelectric effect in Metglas/polyvinylidene-fluoride laminates. *Applied Physics Letters*, 89(8):083507, 2006.

[65] Shuxiang Dong, Junyi Zhai, Naigang Wang, Feiming Bai, JieFang Li, D. Viehland, and T. A. Lograsso. Fe-Ga/Pb($Mg_{1/3}Nb_{2/3}$)O_3-$PbTiO_3$ magnetoelectric laminate composites. *Applied Physics Letters*, 87(22):222504, 2005.

[66] Shuxiang Dong, Junyi Zhai, Jiefang Li, and D. Viehland. Near-ideal magnetoelectricity in high-permeability magnetostrictive/piezofiber laminates with a (2-1) connectivity. *Applied Physics Letters*, 89(25):252904, 2006.

[67] V. M. Laletin, N. Paddubnaya, G. Srinivasan, C. P. De Vreugd, M. I. Bichurin, V. M. Petrov, and D. A. Filippov. Frequency and field dependence of magnetoelectric interactions in layered ferromagnetic transition metal-piezoelectric lead zirconate titanate. *Applied Physics Letters*, 87(22):222507, 2005.

[68] Gang Liu, Ce-Wen Nan, Ning Cai, and Yuanhua Lin. Dependence of giant magnetoelectric effect on interfacial bonding for multiferroic laminated composites of rare-earth-iron alloys and lead-zirconate-titanate. *Journal of Applied Physics*, 95(5):2660–2664, 2004.

[69] R. Pirc, R. Blinc, and J. F. Scott. Mesoscopic model of a system possessing both relaxor ferroelectric and relaxor ferromagnetic properties. *Physical Review B*, 79(21), 2009.

[70] S. Nomura, H. Takabayashi, and T. Nakagawa. Dielectric and magnetic properties of $Pb(Fe_{1/2}Ta_{1/2})O_3$. *Japanese Journal of Applied Physics*, 7(6):600–, 1968.

[71] Wolf Brixel, Jean-Pierre Rivera, Anton Steiner, and Hans Schmid. Magnetic field induced magnetoelectric effects, (ME)H, in the perovskites Pb_2CoWO_6 and Pb_2FeTaO_6. *Ferroelectrics*, 79(1):201–204, 1988.

[72] N. Lampis, C. Franchini, G. Satta, A. Geddo-Lehmann, and S. Massidda. Electronic structure of $PbFe_{1/2}Ta_{1/2}O_3$: Crystallographic ordering and magnetic properties. *Physical Review B*, 69(6), 2004.

[73] V. R. Palkar and S. K. Malik. Observation of magnetoelectric behavior at room temperature in $Pb(Fe_xTi_{1-x})O_3$. *Solid State Communications*, 134(11):783–786, 2005.

[74] R. Martinez, R. Palai, H. Huhtinen, J. Liu, J. F. Scott, and R. S. Katiyar. Nanoscale ordering and multiferroic behavior in $Pb(Fe_{1/2}Ta_{1/2})O_3$. *Physical Review B*, 82(13), 2010.

[75] W. Eerenstein, N. D. Mathur, and J. F. Scott. Multiferroic and magnetoelectric materials. *Nature*, 442(7104):759–765, 2006.

[76] Nicola A. Hill. Why are there so few magnetic ferroelectrics? *The Journal of Physical Chemistry B*, 104(29):6694–6709, 2000.

[77] J. Wang, J. B. Neaton, H. Zheng, V. Nagarajan, S. B. Ogale, B. Liu, D. Viehland, V. Vaithyanathan, D. G. Schlom, U. V. Waghmare, N. A. Spaldin, K. M. Rabe, M. Wuttig, and R. Ramesh. Epitaxial $BiFeO_3$ multiferroic thin film heterostructures. *Science*, 299(5613):1719–1722, 2003.

[78] W. Eerenstein, F. D. Morrison, J. Dho, M. G. Blamire, J. F. Scott, and N. D. Mathur. Comment on "epitaxial $BiFeO_3$ multiferroic thin film heterostructures". *Science*, 307(5713):1203–1203, 2005.

[79] Ying-Hao Chu, Lane W. Martin, Mikel B. Holcomb, and Ramamoorthy Ramesh. Controlling magnetism with multiferroics. *Materials Today*, 10(10):16–23, 2007.

[80] G. A. Smolenskii, V. A. Isupov, and A. I. Agranovskaya. New ferroelectrics of complex composition of the type $A_{22}(Bi_3Bi_5)O_6$. *Soviet Physics-Solid State*, 1(1):150–151, 1959.

[81] Ashok Kumar, I. Rivera, R. S. Katiyar, and J. F. Scott. Multiferroic $Pb(Fe_{0.66}W_{0.33})_{0.80}Ti_{0.20}O_3$ thin films: A room-temperature relaxor ferroelectric and weak ferromagnetic. *Applied Physics Letters*, 92(13), 2008.

[82] B. J. Fang, C. L. Ding, W. Liu, L. Q. Li, and L. Tang. Preparation and electrical properties of high-curie temperature ferroelectrics. *European Physical Journal-Applied Physics*, 45(2), 2009.

[83] L. Mitoseriu, D. Marre, A. S. Siri, A. Stancu, C. E. Fedor, and P. Nanni. Magnetoelectric coupling in the multiferroic $PbFe_{2/3}W_{1/3}O_3$-$PbTiO_3$ system. *Journal of Optoelectronics and Advanced Materials*, 6(2):723–728, 2004.

[84] Dilsom A. Sanchez, Nora Ortega, Ashok Kumar, G. Sreenivasulu, Ram S. Katiyar, J. F. Scott, Donald M. Evans, Miryam Arredondo-Arechavala, A. Schilling, and J. M. Gregg. Room-temperature single phase multiferroic magnetoelectrics: $Pb(Fe, M)_{(x)}(Zr,Ti)_{(1-x)}O_3$ M = Ta, Nb. *Journal of Applied Physics*, 113(7), 2013.

[85] D. M. Evans, A. Schilling, Ashok Kumar, D. Sanchez, N. Ortega, R. S. Katiyar, J. F. Scott, and J. M. Gregg. Switching ferroelectric domain configurations using both electric and magnetic fields in $Pb(Zr,Ti)O_3$-$Pb(Fe,Ta)O_3$ single-crystal lamellae. *Philosophical Transactions of the Royal Society a-Mathematical Physical and Engineering Sciences*, 372(2009), 2014.

[86] Barbara Maraston Fraygola, Adelino de Aguiar Coelho, Ducinei Garcia, and Jose Antonio Eiras. Magnetic and dielectric properties of multiferroic (1-x)$Pb(Fe_{2/3}W_{1/3})O_3$-x$PbTiO_3$ ceramics prepared via a modified two-stage solid-state reaction. *Materials Research-Ibero-American Journal of Materials*, 14(4):434–441, 2011.

[87] W. Prellier, M. P. Singh, and P. Murugavel. The single-phase multiferroic oxides: from bulk to thin film. *Journal of Physics-Condensed Matter*, 17(30):R803–R832, 2005.

[88] M. Fiebig. Revival of the magnetoelectric effect. *Journal of Physics D-Applied Physics*, 38(8):R123–R152, 2005.

[89] Nicola A. Spaldin, Sang-Wook Cheong, and Ramamoorthy Ramesh. Multiferroics: Past, present, and future. *Physics Today*, 63(10):38–43, 2010.

[90] Silvia Picozzi and Claude Ederer. First principles studies of multiferroic materials. *Journal of Physics-Condensed Matter*, 21(30), 2009.

[91] James F. Scott. Room-temperature multiferroic magnetoelectrics. *NPG Asia Materials*, 5, 2013.

[92] N. A. Spaldin. Materials science: The renaissance of magnetoelectric multiferroics. *Science*, 309(5733):391–392, 2005.

[93] A Hochstrat, Ch Binek, Xi Chen, and W Kleemann. Extrinsic control of the exchange bias. *Journal of Magnetism and Magnetic Materials*, 272:325 – 326, 2004. Proceedings of the International Conference on Magnetism (ICM 2003).

[94] V. Laukhin, X. Marté, V. Skumryev, D. Hrabovsky, F. Sánchez, M.V. García-Cuenca, C. Ferrater, M. Varela, U. Lüders, J. F. Bobo, and J. Fontcuberta. Electric field effects on magnetotransport properties of multiferroic Py/$YMnO_3$/Pt heterostructures. *Philosophical Magazine Letters*, 87(3-4):183–191, 2007.

[95] Y.-H. Chu, L.W. Martin, M.B. Holcomb, M. Gajek, S.-J. Han, Q. He, N. Balke, C.-H. Yang, D. Lee, W. Hu, Q. Zhan, P.-L. Yang, A. Fraile-RodrÃŋguez, A. Scholl, S.X. Wang, and R. Ramesh. Electric-field control of local ferromagnetism using a magnetoelectric multiferroic. *Nature Materials*, 7(6):478–482, 2008.

[96] D. Lebeugle, A. Mougin, M. Viret, D. Colson, and L. Ranno. Electric Field Switching of the Magnetic Anisotropy of a Ferromagnetic Layer Exchange Coupled to the Multiferroic Compound $BiFeO_3$. *Phys. Rev. Lett.*, 103:257601, Dec 2009.

[97] C. H. Ahn, A. Bhattacharya, M. Di Ventra, J. N. Eckstein, C. Daniel Frisbie, M. E. Gershenson, A. M. Goldman, I. H. Inoue, J. Mannhart, Andrew J. Millis, Alberto F. Morpurgo, Douglas Natelson, and Jean-Marc Triscone. Electrostatic modification of novel materials. *Rev. Mod. Phys.*, 78:1185–1212, Nov 2006.

[98] Chun-Gang Duan, S. S. Jaswal, and E. Y. Tsymbal. Predicted Magnetoelectric Effect in Fe/$BaTiO_3$ Multilayers: Ferroelectric Control of Magnetism. *Phys. Rev. Lett.*, 97:047201, Jul 2006.

[99] C.A.F. Vaz, J. Hoffman, Y. Segal, J.W. Reiner, R.D. Grober, Z. Zhang, C.H. Ahn, and F.J. Walker. Origin of the magnetoelectric coupling effect in $Pb(Zr_{0.2}Ti_{0.8})O_3/La_{0.8}Sr_{0.\ 2}MnO_3$ multiferroic heterostructures. *Physical Review Letters*, 104(12), 2010.

[100] Manish K. Niranjan, Chun-Gang Duan, Sitaram S. Jaswal, and Evgeny Y. Tsymbal. Electric field effect on magnetization at the Fe/MgO(001) interface. *Applied Physics Letters*, 96(22):222504, 2010.

[101] Carlos AF Vaz, Jason Hoffman, Charles H Ahn, and Ramamoorthy Ramesh. Magnetoelectric coupling effects in multiferroic complex oxide composite structures. *Advanced Materials*, 22(26-27):2900–2918, 2010.

[102] M. Ye. Zhuravlev, S. S. Jaswal, E. Y. Tsymbal, and R. F. Sabirianov. Ferroelectric switch for spin injection. *Applied Physics Letters*, 87(22):222114, 2005.

[103] Ch Binek and B Doudin. Magnetoelectronics with magnetoelectrics. *Journal of Physics: Condensed Matter*, 17(2):L39, 2005.

[104] M. Gajek, M. Bibes, A. Barthélémy, K. Bouzehouane, S. Fusil, M. Varela, J. Fontcuberta, and A. Fert. Spin filtering through ferromagnetic $BiMnO_3$ tunnel barriers. *Phys. Rev. B*, 72:020406, Jul 2005.

[105] Van Suchtelen. Product properties: a new application of composite materials. *J. Philips Res. Rep.*, 27:28–37, 1972.

[106] Amjg Vanrun, D. R. Terrell, and J. H. Scholing. In-situ grown eutectic magnetoelectric composite materials: 2 physical properties. *Journal of Materials Science*, 9(10):1710–1714, 1974.

[107] J. Van den Boomgaard, Amjg Vanrun, and J. Vansuchtelen. Magnetoelectricty in piezoelectric-magnetostrictive composites. *Ferroelectrics*, 10(1-4):295–298, 1976.

[108] Van den Boomgaard, J. and Born, R. A. J. A sintered magnetoelectric composite material $BaTiO_3$-Ni(Co,Mn)Fe_2O_4. *Journal of Materials Science*, 13(7):1538–1548, 1978.

[109] J. Van Den Boomgaard, D. R. Terrell, R. A. J. Born, and H. F. J. I. Giller. An in situ grown eutectic magnetoelectric composite material: Part 1. *Journal of Materials Science*, 9(10):1705–1709, 1974.

[110] R. P. Mahajan, K. K. Patankar, M. B. Kothale, and S. A. Patil. Conductivity, dielectric behaviour and magnetoelectric effect in copper ferrite-barium titanate composites. *Bulletin of Materials Science*, 23(4):273–279, Aug 2000.

[111] G Srinivasan, G Sreenivasulu, Crystal Benoit, VM Petrov, and F Chavez. Magnetic field directed assembly of superstructures of ferrite-ferroelectric core-shell nanoparticles and studies on magnetoelectric interactions. *Journal of Applied Physics*, 117(17):17B904, 2015.

[112] Morad Etier, Carolin Schmitz-Antoniak, Soma Salamon, Harsh Trivedi, Yanling Gao, Ahmadshah Nazrabi, Joachim Landers, Devendraprakash Gautam, Markus Winterer, Detlef Schmitz, Heiko Wende, Vladimir V. Shvartsman, and Doru C. Lupascu. Magnetoelectric coupling on multiferroic cobalt ferrite-barium titanate ceramic composites with different connectivity schemes. *Acta Materialia*, 90:1–9, 2015.

[113] V. Corral-Flores, D. Bueno-Baques, D. Carrillo-Flores, and J. A. Matutes-Aquino. Enhanced magnetoelectric effect in core-shell particulate composites. *Journal of Applied Physics*, 99(8):08J503, 2006.

[114] M. E. Botello-Zubiate, D. Bueno-Baqués, J. De Frutos Vaquerizo, L. E. Fuentes Cobas, and J. A. Matutes-Aquino. Magnetoelectric Measurements by Two Different Methods of Cobalt Ferrite-Barium Titanate Composites. *Ferroelectrics*, 338(1):247–253, 2006.

[115] G. Sreenivasulu, V. Hari Babu, G. Markandeyulu, and B. S. Murty. Magnetoelectric effect of (100-x)$BaTiO_3$-(x)$NiFe_{1.98}O_4$ (x=20-80 wt%) particulate nanocomposites. *Applied Physics Letters*, 94(11):112902, 2009.

[116] R. S. Devan and B. K. Chougule. Effect of composition on coupled electric, magnetic, and dielectric properties of two phase particulate magnetoelectric composite. *Journal of Applied Physics*, 101(1):014109, 2007.

[117] Rashed A. Islam, Vishwas Bedekar, Narayan Poudyal, J. Ping Liu, and Shashank Priya. Magnetoelectric properties of core-shell particulate nanocomposites. *Journal of Applied Physics*, 104(10):104111, 2008.

[118] Shuhong Xie, Feiyue Ma, Yuanming Liu, and Jiangyu Li. Multiferroic $CoFe_2O_4$-$Pb(Zr_{0.52}Ti_{0.48})O_3$ core-shell nanofibers and their magnetoelectric coupling. *Nanoscale*, 3:3152–3158, 2011.

[119] HK Park, SH Choi, JH Oh, and T Ko. Preparation and characteristics of a magnetic-dielectric (Fe_3O_4/$BaTiO_3$) composite by ferrite plating with ultrasound irradiation. *physica status solidi (b)*, 241(7):1693–1696, 2004.

[120] Y. S. Koo, T. Bonaedy, K. D. Sung, J. H. Jung, J. B. Yoon, Y. H. Jo, M. H. Jung, H. J. Lee, T. Y. Koo, and Y. H. Jeong. Magnetodielectric coupling in core/shell $BaTiO_3/\gamma$-Fe_2O_3 nanoparticles. *Applied Physics Letters*, 91(21):212903, 2007.

[121] Y. S. Koo, K. M. Song, N. Hur, J. H. Jung, T.-H. Jang, H. J. Lee, T. Y. Koo, Y. H. Jeong, J. H. Cho, and Y. H. Jo. Strain-induced magnetoelectric coupling in $BaTiO_3/Fe_2O_3$ core/shell nanoparticles. *Applied Physics Letters*, 94(3):032903, 2009.

[122] SQ Ren, LQ Weng, S-H Song, F Li, JG Wan, and M Zeng. $BaTiO_3/CoFe_2O_4$ particulate composites with large high frequency magnetoelectric response. *Journal of materials science*, 40(16):4375–4378, 2005.

[123] V. V. Shvartsman, F. Alawneh, P. Borisov, D. Kozodaev, and D. C. Lupascu. Converse magnetoelectric effect in $CoFe_2O_4$-$BaTiO_3$ composites with a core-shell structure. *Smart Materials and Structures*, 20(7):075006, 2011.

[124] Chiranjib Nayek, Kishor Kumar Sahoo, and P Murugavel. Magnetoelectric effect in $La_{0.7}Sr_{0.3}MnO_3$-$BaTiO_3$ core-shell nanocomposite. *Materials Research Bulletin*, 48(3):1308–1311, 2013.

[125] Giap V Duong and R Groessinger. Effect of preparation conditions on magnetoelectric properties of $CoFe_2O_4$-$BaTiO_3$ magnetoelectric composites. *Journal of Magnetism and Magnetic Materials*, 316(2):e624–e627, 2007.

[126] Giap V Duong, R Groessinger, and R Sato Turtelli. Effect of structure on magnetoelectric properties of $CoFe_2O_4$-$BaTiO_3$ multiferroic composites. *Journal of Magnetism and Magnetic Materials*, 310(2):e361–e363, 2007.

[127] Giap V Duong, R Groessinger, and R Sato Turtelli. Driving mechanism for magnetoelectric effect in $CoFe_2O_4$-$BaTiO_3$ multiferroic composite. *Journal of Magnetism and Magnetic Materials*, 310(2):1157–1159, 2007.

[128] Jian-guo Wan, Hao Zhang, Xiuwei Wang, Dengyu Pan, Jun-ming Liu, and Guanghou Wang. Magnetoelectric $CoFe_2O_4$-lead zirconate titanate thick films prepared by a polyvinylpyrrolidone-assisted sol-gel method. *Applied physics letters*, 89(12):122914, 2006.

[129] Giap V Duong, Turtelli Sato, and R Groessinger. Magnetoelectric properties of $CoFe_2O_4$-$BaTiO_3$ core-shell structure composite studied by a magnetic pulse method. *Journal of Magnetism and Magnetic Materials*, 322(9):1581 – 1584, 2010. Proceedings of the Joint European Magnetic Symposia.

[130] Jian-Ping Zhou, Li Lv, Qian Liu, Yu-Xiang Zhang, and Peng Liu. Hydrothermal synthesis and properties of $NiFe_2O_4$@$BaTiO_3$ composites with well-matched interface. *Science and technology of advanced materials*, 13(4):045001, 2012.

[131] Rongzheng Liu, Yuzhen Zhao, Rongxia Huang, Yongjie Zhao, and Heping Zhou. Multiferroic ferrite/perovskite oxide core/shell nanostructures. *Journal of Materials Chemistry*, 20(47):10665–10670, 2010.

[132] Gary Evans, Giap V Duong, Michael J Ingleson, Zhongling Xu, James TA Jones, Yaroslav Z Khimyak, John B Claridge, and Matthew J Rosseinsky. Chemical bonding assembly of multifunctional oxide nanocomposites. *Advanced Functional Materials*, 20(2):231–238, 2010.

[133] G Sreenivasulu, Maksym Popov, Ferman A Chavez, Sean L Hamilton, Piper R Lehto, and Gopalan Srinivasan. Controlled self-assembly of multiferroic core-shell nanoparticles exhibiting strong magneto-electric effects. *Applied Physics Letters*, 104(5):052901, 2014.

[134] M Popov, G Sreenivasulu, VM Petrov, FA Chavez, and G Srinivasan. High frequency magneto-dielectric effects in self-assembled ferrite-ferroelectric core-shell nanoparticles. *AIP Advances*, 4(9):097117, 2014.

[135] G Sreenivasulu, VM Petrov, FA Chavez, and G Srinivasan. Superstructures of self-assembled multiferroic core-shell nanoparticles and studies on magneto-electric interactions. *Applied Physics Letters*, 105(7):072905, 2014.

[136] L. P. Curecheriu, M. T. Buscaglia, V. Buscaglia, L. Mitoseriu, P. Postolache, A. Ianculescu, and P. Nanni. Functional properties of $BaTiO_3$-$Ni_{0.5}Zn_{0.5}Fe_2O_4$ magnetoelectric ceramics prepared from powders with core-shell structure. *Journal of Applied Physics*, 107(10):104106, 2010.

[137] Maria Teresa Buscaglia, Vincenzo Buscaglia, Lavinia Curecheriu, Petronel Postolache, Liliana Mitoseriu, Adelina C Ianculescu, Bogdan S Vasile, Zhao Zhe, and Paolo Nanni. Fe_2O_3@$BaTiO_3$ core - shell particles as reactive precursors for the preparation of multifunctional composites containing different magnetic phases. *Chemistry of Materials*, 22(16):4740–4748, 2010.

[138] Shuhong Xie, Feiyue Ma, Yuanming Liu, and Jiangyu Li. Multiferroic $CoFe_2O_4$-$Pb(Zr_{0.52}Ti_{0.48})O_3$ core-shell nanofibers and their magnetoelectric coupling. *Nanoscale*, 3(8):3152–3158, 2011.

[139] G Sreenivasulu, Maksym Popov, Ru Zhang, K Sharma, C Janes, A Mukundan, and G Srinivasan. Magnetic field assisted self-assembly of ferrite-ferroelectric core-shell nanofibers and studies on magneto-electric interactions. *Applied Physics Letters*, 104(5):052910, 2014.

[140] Ming Liu, Xin Li, Hassan Imrane, Yajie Chen, Trevor Goodrich, Zhuhua Cai, Katherine S Ziemer, Jian Y Huang, and Nian X Sun. Synthesis of ordered arrays of multiferroic $NiFe_2O_4$-$Pb(Zr_{0.52}Ti_{0.48})O_3$ core-shell nanowires. *Applied physics letters*, 90(15):152501, 2007.

[141] Kalyan Raidongia, Angshuman Nag, A Sundaresan, and CNR Rao. Multiferroic and magnetoelectric properties of core-shell $CoFe_2O_4$@$BaTiO_3$ nanocomposites. *Applied Physics Letters*, 97(6):062904, 2010.

[142] Jungho Ryu, Alfredo Vazquez Carazo, Kenji Uchino, and Hyoun-Ee Kim. Magnetoelectric properties in piezoelectric and magnetostrictive laminate composites. *Japanese Journal of Applied Physics*, 40(8R):4948, 2001.

[143] Jon Gutiérrez, Andoni Lasheras, Pedro Martins, NÃľlson Pereira, Jose M. BarandiarÃąn, and Senentxu Lanceros-Mendez. Metallic Glass/PVDF Magnetoelectric Laminates for Resonant Sensors and Actuators: A Review. *Sensors*, 17(6), 2017.

[144] C.A.F. Vaz. Electric field control of magnetism in multiferroic heterostructures. *Journal of Physics Condensed Matter*, 24(33), 2012.

[145] L.W. Martin and R. Ramesh. Multiferroic and magnetoelectric heterostructures. *Acta Materialia*, 60(6-7):2449–2470, 2012.

[146] S. Dong, J.-M. Liu, S.-W. Cheong, and Z. Ren. Multiferroic materials and magnetoelectric physics: Symmetry, entanglement, excitation, and topology. *Advances in Physics*, 64(5-6):519–626, 2015.

[147] J.-M. Hu, L.-Q. Chen, and C.-W. Nan. Multiferroic heterostructures integrating ferroelectric and magnetic materials. *Advanced Materials*, 28(1):15–39, 2016.

[148] H. Zheng, J. Wang, S. E. Lofland, Z. Ma, L. Mohaddes-Ardabili, T. Zhao, L. Salamanca-Riba, S. R. Shinde, S. B. Ogale, F. Bai, D. Viehland, Y. Jia, D. G. Schlom, M. Wuttig, A. Roytburd, and R. Ramesh. Multiferroic $BaTiO_3$-$CoFe_2O_4$ nanostructures. *Science*, 303(5658):661–663, 2004.

[149] H. Zheng, J. Wang, L. Mohaddes-Ardabili, M. Wuttig, L. Salamanca-Riba, D.G. Schlom, and R. Ramesh. Three-dimensional heteroepitaxy in self-assembled $BaTiO_3$-$CoFe_2O_4$ nanostructures. *Applied Physics Letters*, 85(11):2035–2037, 2004.

[150] H. Zheng, Q. Zhan, F. Zavaliche, M. Sherburne, F. Straub, M.P. Cruz, L.-Q. Chen, U. Dahmen, and R. Ramesh. Controlling self-assembled perovskite-spinel nanostructures. *Nano Letters*, 6(7):1401–1407, 2006.

[151] C. Zhong, Q. Jiang, J. Fang, and X. Jiang. Thickness and magnetic field dependence of ferroelectric properties in multiferroic $BaTiO_3$-$CoFe_2O_4$ nanocomposite films. *Journal of Applied Physics*, 105(4), 2009.

[152] L. Yan, Z. Xing, Z. Wang, T. Wang, G. Lei, J. Li, and D. Viehland. Direct measurement of magnetoelectric exchange in self-assembled epitaxial $BiFeO_3$-$CoFe_2O_4$ nanocomposite thin films. *Applied Physics Letters*, 94(19), 2009.

[153] Y. Deng, J. Zhou, D. Wu, Y. Du, M. Zhang, D. Wang, H. Yu, S. Tang, and Y. Du. Three-dimensional phases-connectivity and strong magnetoelectric response of self-assembled feather-like $CoFe_2O_4$-$BaTiO_3$ nanostructures. *Chemical Physics Letters*, 496(4-6):301–305, 2010.

[154] S.-C. Liao, P.-Y. Tsai, C.-W. Liang, H.-J. Liu, J.-C. Yang, S.-J. Lin, C.-H. Lai, and Y.-H. Chu. Misorientation control and functionality design of nanopillars in self-assembled perovskite-spinel heteroepitaxial nanostructures. *ACS Nano*, 5(5):4118–4122, 2011.

[155] Z. Wang, R. Viswan, B. Hu, V.G. Harris, J.-F. Li, and D. Viehland. Tunable magnetic anisotropy of $CoFe_2O_4$ nanopillar arrays released from $BiFeO_3$ matrix. *Physica Status Solidi-Rapid Research Letters*, 6(2):92–94, 2012.

[156] Y. Li, Y. Yang, J. Yao, R. Viswan, Z. Wang, J. Li, and D. Viehland. Controlled growth of epitaxial $BiFeO_3$ films using self-assembled $BiFeO_3$-$CoFe_2O_4$ multiferroic heterostructures as a template. *Applied Physics Letters*, 101(2), 2012.

[157] Z. Wang, Y. Li, R. Viswan, B. Hu, V.G. Harris, J. Li, and D. Viehland. Engineered magnetic shape anisotropy in $BiFeO_3$-$CoFe_2O_4$ self-assembled thin films. *ACS Nano*, 7(4):3447–3456, 2013.

[158] Y.-J. Chen, Y.-H. Hsieh, S.-C. Liao, Z. Hu, M.-J. Huang, W.-C. Kuo, Y.-Y. Chin, T.-M. Uen, J.-Y. Juang, C.-H. Lai, H.-J. Lin, C.-T. Chen, and Y.-H. Chu. Strong magnetic enhancement in self-assembled multiferroic-ferrimagnetic nanostructures. *Nanoscale*, 5(10):4449–4453, 2013.

[159] H.-J. Liu, V.-T. Tra, Y.-J. Chen, R. Huang, C.-G. Duan, Y.-H. Hsieh, H.-J. Lin, J.-Y. Lin, C.-T. Chen, Y. Ikuhara, and Y.-H. Chu. Large magnetoresistance in magnetically coupled $SrRuO_3$-$CoFe_2O_4$ self-assembled nanostructures. *Advanced Materials*, 25(34):4753–4759, 2013.

[160] A. Imai, X. Cheng, H.L. Xin, E.A. Eliseev, A.N. Morozovska, S.V. Kalinin, R. Takahashi, M. Lippmaa, Y. Matsumoto, and V. Nagarajan. Epitaxial $Bi_5Ti_3FeO_{15}$-$CoFe_2O_4$ pillar-matrix multiferroic nanostructures. *ACS Nano*, 7(12):11079–11086, 2013.

[161] D.H. Kim, N.M. Aimon, X. Sun, and C.A. Ross. Compositionally modulated magnetic epitaxial spinel/perovskite nanocomposite thin films. *Advanced Functional Materials*, 24(16):2334–2342, 2014.

[162] J. Huang, L. Li, P. Lu, Z. Qi, X. Sun, X. Zhang, and H. Wang. Self-assembled Co-$BaZrO_3$ nanocomposite thin films with ultra-fine vertically aligned co nanopillars. *Nanoscale*, 9(23):7970–7976, 2017.

[163] T. Amrillah, Y. Bitla, K. Shin, T. Yang, Y.-H. Hsieh, Y.-Y. Chiou, H.-J. Liu, T.H. Do, D. Su, Y.-C. Chen, S.-U. Jen, L.-Q. Chen, K.H. Kim, J.-Y. Juang, and Y.-H. Chu. Flexible multiferroic bulk heterojunction with giant magnetoelectric coupling via van der waals epitaxy. *ACS Nano*, 11(6):6122–6130, 2017.

[164] S. Geprägs, A. Brandlmaier, M. Opel, R. Gross, and S. T. B. Goennenwein. Electric field controlled manipulation of the magnetization in ni/batio3 hybrid structures. *Applied Physics Letters*, 96(14):142509, 2010.

[165] I. Fina, N. Dix, J. M. Rebled, P. Gemeiner, X. Marti, F. Peiro, B. Dkhil, F. Sanchez, L. Fabrega, and J. Fontcuberta. The direct magnetoelectric effect in ferroelectric-ferromagnetic epitaxial heterostructures. *Nanoscale*, 5(17):8037–8044, 2013.

[166] H. Zheng, J. Wang, S. E. Lofland, Z. Ma, L. Mohaddes-Ardabili, T. Zhao, L. Salamanca-Riba, S. R. Shinde, S. B. Ogale, F. Bai, D. Viehland, Y. Jia, D. G. Schlom, M. Wuttig, A. Roytburd, and R. Ramesh. Multiferroic $BaTiO_3$-$CoFe_2O_4$ Nanostructures. *Science*, 303(5658):661–663, 2004.

[167] Ming Liu, Ogheneyunume Obi, Jing Lou, Stephen Stoute, Zhuhua Cai, K Ziemer, and Nian X Sun. Strong magnetoelectric coupling in ferrite/ferroelectric multiferroic heterostructures derived by low temperature spin-spray deposition. *Journal of Physics D: Applied Physics*, 42(4):045007, 2009.

[168] Shenqiang Ren and Manfred Wuttig. Magnetoelectric nano-$Fe_3O_4/CoFe_2O_4||PbZr_{0.53}Ti_{0.47}O_3$ composite. *Applied Physics Letters*, 92(8):083502, 2008.

[169] Ming Liu, Ogheneyunume Obi, Jing Lou, Yajie Chen, Zhuhua Cai, Stephen Stoute, Mary Espanol, Magnum Lew, Xiaodan Situ, Kate S. Ziemer, Vince G. Harris, and Nian X. Sun. Giant electric field tuning of magnetic properties in multiferroic ferrite/ferroelectric heterostructures. *Advanced Functional Materials*, 19(11):1826–1831, 2009.

[170] W Eerenstein, M Wiora, JL Prieto, JF Scott, and ND Mathur. Giant sharp and persistent converse magnetoelectric effects in multiferroic epitaxial heterostructures. *Nature materials*, 6(5):348, 2007.

[171] C. Thiele, K. Dörr, O. Bilani, J. Rödel, and L. Schultz. Influence of strain on the magnetization and magnetoelectric effect in $La_{0.7}A_{0.3}MnO_3$/PMN-PT(001) (A = Sr; Ca). *Phys. Rev. B*, 75:054408, 2007.

[172] Z. G. Sheng, J. Gao, and Y. P. Sun. Coaction of electric field induced strain and polarization effects in $la_{0.7}ca_{0.3}mno_3$/PMN-PT structures. *Phys. Rev. B*, 79:174437, May 2009.

[173] Dimitrios Matsoulis. Four challenges for the electronics industry, 2015.

[174] Dezhen Xue, Yumei Zhou, Huixin Bao, Chao Zhou, Jinghui Gao, and Xiaobing Ren. Elastic, piezoelectric, and dielectric properties of $Ba(Zr_{0.2}Ti_{0.8})O_3$-$50(Ba_{0.7}Ca_{0.3})TiO_3$ Pb-free ceramic at the morphotropic phase boundary. *Journal of Applied Physics*, 109(5):054110, 2011.

[175] Gene H. Haertling. Ferroelectric ceramics: History and technology. *Journal of the American Ceramic Society*, 82(4):797–818, 1999.

[176] Innovative Research and Products Inc. Piezoelectric Actuators and Motors - Types, Applications, New Developments, Industry Structure, and Global Markets, 2010.

[177] United Nations: RIO DECLARATION ON ENVIRONMENT AND DEVELOPMENT, 1992.

[178] Restriction on the use of certain hazardous substances in some electronic devices (RoHS), 2003.

[179] EU-Directive 2002/96/EC: Waste Electrical and Electronic Equipment (WEEE, 2003.

[180] Prohibition on certain hazardous substances in consumer products, 2004.

[181] Ministry of Information Industry China. Measures for the Administration on Pollution Control of Electronic Information Products, 2006.

[182] Environment and Labor Committee of the National Assembly of Korea . Act for Resource Recycling of Electrical and Electronic Equipment and Vehicles, 2007.

[183] EU-Directive 2011/65/EU: Restriction of the use of certain hazardous substances in electrical and electronic equipment (RoHS), 2011.

[184] Lyn Patrick. Lead toxicity, a review of the literature. Part I: exposure, evaluation, and treatment. *Alternative medicine review*, 11(1):2–23, 2006.

[185] Foster W. Meen J. and Fox D. The effect of physiologic aqueous solutions on the perovskite material lead-lanthanum-zirconium titanate (PLZT): potential retinotoxicity. *Cutaneous and ocular toxicology*, 32:18, 2013.

[186] Jinghui Gao, Dezhen Xue, Wenfeng Liu, Chao Zhou, and Xiaobing Ren. Recent progress on batio3-based piezoelectric ceramics for actuator applications. *Actuators*, 6(3), 2017.

[187] Wenfeng Liu and Xiaobing Ren. Large piezoelectric effect in pb-free ceramics. *Phys. Rev. Lett.*, 103:257602, Dec 2009.

[188] M.N. Rahaman. *Ceramic Processing and Sintering*. Materials Engineering. Taylor & Francis, 2003.

[189] M.N. Rahaman. *Sintering of Ceramics*. CRC Press, 2007.

[190] S.J.L. Kang. *Sintering: Densification, Grain Growth and Microstructure*. Elsevier Science, 2004.

[191] T. Ohnishi, H. Koinuma, and M. Lippmaa. Pulsed laser deposition of oxide thin films. *Applied Surface Science*, 252(7):2466 – 2471, 2006.

[192] Kai Wang. Laser based fabrication of graphene. *Advances in Graphene Science*, pages 77–95, 2013.

[193] Phuoc Huu Le and Chih Wei Luo. Thermoelectric and topological insulator bismuth chalcogenide thin films grown using pulsed laser deposition. In *Applications of Laser Ablation-Thin Film Deposition, Nanomaterial Synthesis and Surface Modification*. InTech, 2016.

[194] FC Frank and Jan H van der Merwe. One-dimensional dislocations. i. static theory. In *Proceedings of the Royal Society of London A: Mathematical, Physical and Engineering Sciences*, volume 198, pages 205–216. The Royal Society, 1949.

[195] M Volmer and A Weber. Nucleus formation in supersaturated systems. *Z. phys. Chem*, 119(1926), 1926.

[196] IN Stranski. Krastanov theory of orientation separation of ionic crystals. *Acad. Wiss. Math.-Naturw. Klasse IIb*, 146:797, 1938.

[197] B.D. Cullity. *Elements of X-ray Diffraction*. Addison-Wesley series in metallurgy and materials. Addison-Wesley Publishing Company, 1978.

[198] Brian H. Toby and Robert B. Von Dreele. *GSAS-II*: The genesis of a modern open-source all purpose crystallography software package. *Journal of Applied Crystallography*, 46(2):544–549, Apr 2013.

[199] Ramesh Nath, Seungbum Hong, Jeffrey A. Klug, Alexandra Imre, Michael J. Bedzyk, Ram S. Katiyar, and Orlando Auciello. Effects of cantilever buckling on vector piezoresponse force microscopy imaging of ferroelectric domains in $BiFeO_3$ nanostructures. *Applied Physics Letters*, 96(16):163101, 2010.

[200] J.F. Nye. *Physical Properties of Crystals: Their Representation by Tensors and Matrices*. Oxford science publications. Clarendon Press, 1985.

[201] A. L. Kholkin, N. A. Pertsev, and A. V. Goltsev. Piezoelectricity and crystal symmetry. In Ahmad Safari and E. Koray Akdogan, editors, *Piezoelectric and Acoustic Materials for Transducer Applications*, pages 17–38. Springer US, Boston, MA, 2008.

[202] Brian J Rodriguez, Stephen Jesse, Arthur P Baddorf, T Zhao, YH Chu, R Ramesh, Eugene A Eliseev, Anna N Morozovska, and Sergei V Kalinin. Spatially resolved mapping of ferroelectric switching behavior in self-assembled multiferroic nanostructures: strain, size, and interface effects. *Nanotechnology*, 18(40):405701, 2007.

[203] Y. Martin and H. K. Wickramasinghe. Magnetic imaging by "force microscopy" with 1000 Å resolution. *Applied Physics Letters*, 50(20):1455–1457, 1987.

[204] L. Belliard, A. Thiaville, S. Lemerle, A. Lagrange, J. Ferré, and J. Miltat. Investigation of the domain contrast in magnetic force microscopy. *Journal of Applied Physics*, 81(8):3849–3851, 1997.

[205] Morad Etier. *Preparation and Magnetoelectric Effect of Multiferroic Cobalt Ferrite-Barium Titanate Composites*. PhD thesis, Universität Duisburg-Essen, Germany, 2015.

[206] João V. Vidal, Andrey A. Timopheev, Andrei L. Kholkin, and Nikolai A. Sobolev. *Dynamic Measurements of Magnetoelectricity in Metglas-Piezocrystal Laminates*, pages 227–265. Springer International Publishing, Cham, 2016.

[207] A. A. Timopheev, J. V. Vidal, A. L. Kholkin, and N. A. Sobolev. Direct and converse magnetoelectric effects in Metglas/$LiNbO_3$/Metglas trilayers. *Journal of Applied Physics*, 114(4):044102, 2013.

[208] P. Borisov, A. Hochstrat, V. V. Shvartsman, and W. Kleemann. Superconducting quantum interference device setup for magnetoelectric measurements. *Review of Scientific Instruments*, 78(10):106105, 2007.

[209] T.H. O'Dell. *The electrodynamics of magneto-electric media.* Series of monographs on selected topics in solid state physics. North-Holland Pub. Co., 1970.

[210] M. Naveed-Ul-Haq, Vladimir V. Shvartsman, Soma Salamon, Heiko Wende, Harsh Trivedi, Arif Mumtaz, and Doru C Lupascu. A new (Ba,Ca)(Ti,Zr)O_3 based multiferroic composite with large magnetoelectric effect. *Scientific reports*, 6, 2016.

[211] M. Naveed-Ul-Haq, Vladimir V. Shvartsman, Gabriel Constantinescu, Harsh Trivedi, Soma Salamon, Joachim Landers, Heiko Wende, and Doru C. Lupascu. Effect of Al^{3+} modification on cobalt ferrite and its impact on the magnetoelectric effect in BCZT-CFO multiferroic composites. *Journal of Materials Science*, 52(23):13402–13413, 2017.

[212] Matias Acosta, Nasser Khakpash, Takumi Someya, Nikola Novak, Wook Jo, Hajime Nagata, George A Rossetti Jr, and Jürgen Rödel. Origin of the large piezoelectric activity in (1-x)Ba($Zr_{0.2}Ti_{0.8}$)O_3-x($Ba_{0.7}Ca_{0.3}$)TiØ$_3$ ceramics. *Physical Review B*, 91(10):104108, 2015.

[213] Kumar Brajesh, Khagesh Tanwar, Mulualem Abebe, and Rajeev Ranjan. Relaxor ferroelectricity and electric-field-driven structural transformation in the giant lead-free piezoelectric (Ba,Ca)(Ti,Zr)O_3. *Physical Review B*, 92(22):224112, 2015.

[214] Kumar Brajesh, Mulualem Abebe, and Rajeev Ranjan. Structural transformations in morphotropic-phase-boundary composition of the lead-free piezoelectric system, Ba($Ti_{0.8}Zr_{0.2}$)O_3-($Ba_{0.7}Ca_{0.3}$)TiO_3. *Phys. Rev. B*, 94:104108, Sep 2016.

[215] Yang Bai, Ales Matousek, Pavel Tofel, Vijay Bijalwan, Bo Nan, Hana Hughes, and Tim W. Button. (Ba,Ca)(Zr,Ti)O_3 lead-free piezoelectric ceramics-the critical role of processing on properties. *Journal of the European Ceramic Society*, 35(13):3445 – 3456, 2015.

[216] Guangbin Ji, Xiaohui Lin, Yanyan Sun, Syed Ahmed Ali Trimizi, Hailin Su, and Youwei Du. Molten salt growth and magnetic properties of octahedral $CoFe_2O_4$ crystals: effects of synthesis conditions. *CrystEngComm*, 13(21):6451–6456, 2011.

[217] MA Ahmed, U Seddik, and NG Imam. First-order studies of nanometric biferroic. *World Journal of Condensed Matter Physics*, 2(02):66, 2012.

[218] Andrzej Ka Jonscher. *Dielectric Relaxation in Solids.* Chelsea Dielectrics Press Limited, London, 1983.

[219] K. L. Ngai. Universality of low-frequency fluctuation, dissipation, and relaxation properties of condensed matter. *Comment.Solid State Phys.*, 9(4):127–140, 1979.

[220] LA Dissado and RM Hill. Non-exponential decay in dielectrics and dynamics of correlated systems. *Nature*, 279:685–689, 1979.

[221] R M Hill and L A Dissado. Dielectric relaxation in a transition-metal glass. *Journal of Physics C: Solid State Physics*, 17(33):6001, 1984.

[222] Zhi Yu and Chen Ang. Maxwell-Wagner polarization in ceramic composites $BaTiO_3$-$(Ni_{0.3}Zn_{0.7})Fe_2O_4$. *Journal of Applied Physics*, 91(2):794–797, 2002.

[223] G. H. Jonker. Analysis of the semiconducting properties of cobalt ferrite. *Journal of Physics and Chemistry of Solids*, 9(2):165–175, 1959.

[224] A. Sakanas, R. Grigalaitis, J. Banys, L. Mitoseriu, V. Buscaglia, and P. Nanni. Broadband dielectric spectroscopy of $BaTiO_3$-$Ni_{0.5}Zn_{0.5}Fe_2O_4$ composite ceramics. *Journal of Alloys and Compounds*, 602:241–247, 2014.

[225] Haibo Yang, Hong Wang, Li He, Li Shui, and Xi Yao. Polarization relaxation mechanism of $Ba_{0.6}Sr_{0.4}TiO_3/Ni_{0.8}Zn_{0.2}Fe_2O_4$ composite with giant dielectric constant and high permeability. *Journal of Applied Physics*, 108(7):074105, 2010.

[226] I.H. Gul and A. Maqsood. Structural, magnetic and electrical properties of cobalt ferrites prepared by the sol-gel route. *Journal of Alloys and Compounds*, 465(1):227 – 231, 2008.

[227] Wei Li and Robert W Schwartz. Maxwell-Wagner relaxations and their contributions to the high permittivity of calcium copper titanate ceramics. *Physical Review B*, 75(1):012104, 2007.

[228] M. Etier, Y. Gao, V. V. Shvartsman, A. Elsukova, J. Landers, H. Wende, and D. C. Lupascu. Cobalt ferrite/barium titanate core/shell nanoparticles. *Ferroelectrics*, 438(1):115–122, 2012.

[229] R.A. McCurrie. *Ferromagnetic Materials: Structure and Properties*. World Folklore Series; 3. Academic, 1994.

[230] Feng Li, Junjie Liu, David G. Evans, and Xue Duan. Stoichiometric synthesis of pure MFe_2O_4 (M = Mg, Co, and Ni) spinel ferrites from tailored layered double hydroxide (hydrotalcite-like) precursors. *Chemistry of Materials*, 16(8):1597–1602, 2004.

[231] IC Nlebedim, N Ranvah, Y Melikhov, PI Williams, JE Snyder, AJ Moses, and DC Jiles. Magnetic and magnetomechanical properties of $CoAl_xFe_{2-x}O_4$ for stress sensor and actuator applications. *IEEE Transactions on magnetics*, 45(10):4120–4123, 2009.

[232] Vinitha Reddy Monaji and Dibakar Das. Influence of Zr doping on the structural, magnetic and magnetoelastic properties of cobalt-ferrites. *Journal of Alloys and Compounds*, 634:99–103, 2015.

[233] Chien-Yie Tsay, Yi-Hsiang Lin, and Shien-Uang Jen. Magnetic, magnetostrictive, and ac impedance properties of manganese substituted cobalt ferrites. *Ceramics International*, 41(4):5531–5536, 2015.

[234] I. C. Nlebedim, Y. Melikhov, J. E. Snyder, N. Ranvah, A. J. Moses, and D. C. Jiles. Dependence of magnetomechanical performance of $CoGa_xFe_{2-x}O_4$ on temperature variation. *Journal of Applied Physics*, 109(7):07A908, 2011.

[235] P. N. Anantharamaiah and P. A. Joy. Tuning of the magnetostrictive properties of cobalt ferrite by forced distribution of substituted divalent metal ions at different crystallographic sites. *Journal of Applied Physics*, 121(9):093904, 2017.

[236] Jie Li, Huaiwu Zhang, Yinong Liu, Yulong Liao, Guokun Ma, and Hong Yang. Co–Ti co-substitution of M-type hexagonal barium ferrite. *Materials Research Express*, 2(4):046104, 2015.

[237] X. L. Zhong, J. B. Wang, M. Liao, G. J. Huang, S. H. Xie, Y. C. Zhou, Y. Qiao, and J. P. He. Multiferroic nanoparticulate $Bi_{3.15}Nd_{0.85}Ti_3O_{12}$-$CoFe_2O_4$ composite thin films prepared by a chemical solution deposition technique. *Applied Physics Letters*, 90(15):152903, 2007.

[238] Rong-Fen Zhang, Chao-Yong Deng, Li Ren, Zheng Li, and Jian-Ping Zhou. Ferroelectric, ferromagnetic, and magnetoelectric properties of multiferroic NiZnFeO-$BaTiO_3$ composite ceramics. *Journal of electronic materials*, 43(4), 2014.

[239] H. J. Van Hook. Oxygen stoichiometry in the compound bafeo3-x. *The Journal of Physical Chemistry*, 68(12):3786–3789, 1964.

[240] W. W. Malinofsky and H. Kedesdy. Barium iron oxide isomorphs of hexagonal and tetragonal batio3. *Journal of the American Chemical Society*, 76(11):3090–3091, 1954.

[241] Etienne du Tremolet de Lacheisserie, Damien Gignoux, and Michel Schlenker. *Magnetism: Fundamentals*. Springer-Verlag, New York, 1 edition, 2005.

[242] Morad Etier, Carolin Schmitz-Antoniak, Soma Salamon, Harsh Trivedi, Yanling Gao, Ahmadshah Nazrabi, Joachim Landers, Devendraprakash Gautam, Markus Winterer, Detlef Schmitz, Heiko Wende, Vladimir V. Shvartsman, and Doru C. Lupascu. Magnetoelectric coupling on multiferroic cobalt ferrite-barium titanate ceramic composites with different connectivity schemes. *Acta Materialia*, 90:1–9, 2015.

[243] G Srinivasan, ET Rasmussen, BJ Levin, and R Hayes. Magnetoelectric effects in bilayers and multilayers of magnetostrictive and piezoelectric perovskite oxides. *Physical Review B*, 65(13):134402, 2002.

[244] C.M. van der Burgt and A.L. Stuijts. Developments in ferrite ceramics with strong piezomagnetic coupling. *Ultrasonics*, 1(4):199 – 210, 1963.

[245] F. G. Brockman, P. W. Beck, and W. G. Steneck. Magnetostrictive Ferrites with Small Change in Coupling Coefficient from 0 ℃ to 20 ℃. *Journal of the American Ceramic Society*, 46(4):167–170, 1963.

[246] Standards Committee, Institute of Electrical, and Electronics Engineers. *IEEE Standard on Piezoelectricity.* ANSI/IEEE Std. American National Standards Institute and IEEE Ultrasonics, Ferroelectrics, and Frequency Control Society, 1988.

[247] F. Cordero, F. Craciun, M. Dinescu, N. Scarisoreanu, C. Galassi, W. Schranz, and V. Soprunyuk. Elastic response of (1-x)$Ba(Ti_{0.8}Zr_{0.2})O_3$-$x(Ba_{0.7}Ca_{0.3})TiO_3$ ($x = 0.45$-0.55) and the role of the intermediate orthorhombic phase in enhancing the piezoelectric coupling. *Applied Physics Letters*, 105(23):232904, 2014.

[248] O.E. Mattiat. *Ultrasonic Transducer Materials.* Ultrasonic Technology. Springer US, 2013.

[249] D. Bonnenberg and K. A. Hempel. Co spinels and Co spinels with substitutions: Datasheet from Landolt-Börnstein - Group III Condensed Matter · Volume 12B: "Part B: Spinels, Fe Oxides, and Fe-Me-O Compounds" in SpringerMaterials, 1980.

[250] Morad Etier, Vladimir V. Shvartsman, Soma Salamon, Yanling Gao, Heiko Wende, and Doru C. Lupascu. The direct and the converse magnetoelectric effect in multiferroic cobalt ferrite-barium titanate ceramic composites. *Journal of the American Ceramic Society*, 99(11):3623–3631, 2016.

[251] CM Van der Burgt. Ferrites for magnetic and piezomagnetic filter elements with temperature-independent permeability and elasticity. *Proceedings of the IEE-Part B: Radio and Electronic Engineering*, 104(7S):550–557, 1957.

[252] J. A. Osborn. Demagnetizing factors of the general ellipsoid. *Physical Review*, 67(11-12):351–357, 1945.

[253] R. Skomski, G. C. Hadjipanayis, and D. J. Sellmyer. Effective demagnetizing factors of complicated particle mixtures. *IEEE Transactions on Magnetics*, 43(6):2956–2958, 2007.

[254] Jean-Luc Mattei and Marcel Le Floc'h. Percolative behaviour and demagnetizing effects in disordered heterostructures. *Journal of Magnetism and Magnetic Materials*, 257(2):335 – 345, 2003.

[255] J.A. Stratton. *Electromagnetic Theory.* McGraw-Hill New York and London, 1941.

[256] M. Naveed Ul-Haq, Tayyaba Yunus, Arif Mumtaz, Vladimir V. Shvartsman, and Doru C. Lupascu. Magnetodielectric effect in relaxor/ferrimagnetic composites. *Journal of Alloys and Compounds*, 640:462 – 467, 2015.

[257] Muhammad Usman, Arif Mumtaz, Sobia Raoof, and S. K. Hasanain. Magnetic control of relaxor features in $BaZr_{0.5}Ti_{0.5}O_3$ and $CoFe_2O_4$ composite. *Applied Physics Letters*, 102(11):112911, 2013.

[258] M.P.K. Sahoo, Zhang Yajun, Jie Wang, and R.N.P. Choudhary. Composition control of magnetoelectric relaxor behavior in multiferroic $BaZr_{0.4}Ti_{0.6}O_3/CoFe_2O_4$ composites. *Journal of Alloys and Compounds*, 657:12 – 20, 2016.

[259] J. Lee, J. Heo, J. Lee, and Y. Han. Design of small antennas for mobile handsets using magneto-dielectric material. *IEEE Transactions on Antennas and Propagation*, 60(4):2080–2084, 2012.

[260] S. Kumar and D.K. Vishwakarma. Miniaturisation of microstrip patch antenna using an artificial planar magneto-dielectric meta-substrate. *IET Microwaves, Antennas and Propagation*, 10(11):1235–1241, 2016.

[261] ASM Alqadami and MF Jamlos. Effect of a flexible polymer dielectric and magneto-dielectric composite substrates in antenna array. In *Antennas and Propagation (ISAP), 2015 International Symposium*, pages 1–4. IEEE, 2015.

[262] S.-E. Lee, H.-J. Kim, J.-H. Lee, K.-S. Oh, H.T. Hahn, and J.-W. Choi. Magnetodielectric hexaferrite flake/polymer substrate for implantable antenna with an enhanced insensitivity to implant position. *Materials Letters*, 187:94–97, 2017.

[263] F. Farzami, K. Forooraghi, and M. Norooziarab. Miniaturization of a microstrip antenna using a compact and thin magneto-dielectric substrate. *IEEE Antennas and Wireless Propagation Letters*, 10:1540–1542, 2011.

[264] J. S. Kim, Y. H. Lee, B. Lee, J. C. Lee, J. J. Choi, and J. Y. Kim. Effects of magneto-dielectric ceramics for small antenna application. *Journal of Electrical Engineering and Technology*, 9(1):273–279, 2014.

[265] Xiaoyong Wei and Xi Yao. Preparation, structure and dielectric property of barium stannate titanate ceramics. *Materials Science and Engineering: B*, 137(1):184 – 188, 2007.

[266] Wei Xiaoyong, Feng Yujun, and Yao Xi. Dielectric relaxation behavior in barium stannate titanate ferroelectric ceramics with diffused phase transition. *Applied Physics Letters*, 83(10):2031–2033, 2003.

[267] Xiaoyong Wei, Yujun Feng, Lianmao Hang, and Xi Yao. Dielectric properties of barium stannate titanate ceramics under bias field. *Ceramics International*, 30(7):1401–1404, 2004.

[268] Xiaoyong Wei, Yujun Feng, Xing Wan, and Xi Yao. Evolvement of dielectric relaxation of barium stannate titanate ceramics. *Ceramics International*, 30(7):1397–1400, 2004.

[269] Xiaoyong Wei and Xi Yao. Preparation, structure and dielectric property of barium stannate titanate ceramics. *Materials Science and Engineering: B*, 137(1-3):184–188, 2007.

[270] I. A. Santos and J. A. Eiras. Phenomenological description of the diffuse phase transition in ferroelectrics. *Journal of Physics-Condensed Matter*, 13(50):11733–11740, 2001.

[271] Dwight Viehland, S. J. Jang, L. Eric Cross, and Manfred Wuttig. Freezing of the polarization fluctuations in lead magnesium niobate relaxors. *Journal of Applied Physics*, 68(6):2916–2921, 1990.

[272] Zong-Yang Cheng, Liang-Ying Zhang, and Xi Yao. Investigation of glassy behavior of lead magnesium niobate relaxors. *Journal of Applied Physics*, 79(11):8615–8619, 1996.

[273] L. Eric Cross. Relaxor ferroelectrics. *Ferroelectrics*, 76(1):241–267, 1987.

[274] L. Eric Cross. Relaxorferroelectrics: An overview. *Ferroelectrics*, 151(1):305–320, 1994.

[275] Z. Y. Cheng, R. S. Katiyar, X. Yao, and X. L. Wang. Dielectric properties and glassy behaviour in the solid-solution ceramics $Pb(Zn,Nb)O_3$-$PbTiO_3$-$BaTiO_3$. *Philosophical Magazine Part B*, 78(3):279–293, 1998.

[276] C. Lei, A. A. Bokov, and Z. G. Ye. Relaxor behavior in $Ba(Ti_{0.72}Sn_{0.28})O_3$ solid solution. *Ferroelectrics*, 339(1):129–136, 2006.

[277] D Viehland, M Wuttig, and LE Cross. The glassy behavior of relaxor ferroelectrics. *Ferroelectrics*, 120(1):71–77, 1991.

[278] R. Pirc and R. Blinc. Vogel-fulcher freezing in relaxor ferroelectrics. *Physical Review B*, 76(2):020101, 2007.

[279] Marian Stingaciu, PG Reuvekamp, C-W Tai, RK Kremer, and Mats Johnsson. The magnetodielectric effect in $BaTiO_3$–$SrFe_{12}O_{19}$ nanocomposites. *Journal of Materials Chemistry C*, 2(2):325–330, 2014.

[280] Nidhi Adhlakha, K. L. Yadav, and Ripandeep Singh. $BiFeO_3$-$CoFe_2O_4$-$PbTiO_3$ composites: structural, multiferroic, and optical characteristics. *Journal of Materials Science*, 50(5):2073–2084, 2015.

[281] Shilpi Banerjee, Partha Hajra, Anindya Datta, Asim Bhaumik, MykanthReddy Mada, Sri Bandyopadhyay, and Dipankar Chakravorty. Magnetodielectric effect in $Ni_{0.5}Zn_{0.5}Fe_2O_4$-$BaTiO_3$ nanocomposites. *Bulletin of Materials Science*, 37(3):497–504, 2014.

[282] S. M. Salunkhe, S. R. Jigajeni, A. N. Tarale, M. M. Sutar, and P. B. Joshi. Investigations on magnetoelectric and magnetodielectric properties of CMFO-PBT composites. *Journal of Electronic Materials*, 42(6):1122–1132, 2013.

[283] Martin Kriegisch, Weijun Ren, Reiko Sato-Turtelli, Herbert MÃijller, Roland GrÃűssinger, and Zhidong Zhang. Field-induced magnetic transition in cobalt-ferrite. *Journal of Applied Physics*, 111(7):07E308, 2012.

[284] Ludwig Geske, Horst Beige, Hans-Peter Abicht, and Volkmar Mueller. Electromechanical Resonance Study of the Diffuse Ferroelectric Phase Transition in $BaTi_{1-x}Sn_xO_3$ Ceramics. *Ferroelectrics*, 314(1):97–104, 2005.

[285] Vladimir. V. Shvartsman, W. Kleemann, J. Dec, Z. K. Xu, and S. G. Lu. Diffuse phase transition in $BaTi_{1-x}Sn_xO_3$ ceramics: An intermediate state between ferroelectric and relaxor behavior. *Journal of Applied Physics*, 99(12):124111, 2006.

[286] Vladimir V. Shvartsman and Doru C. Lupascu. Lead-free relaxor ferroelectrics. *Journal of the American Ceramic Society*, 95(1):1–26, 2012.

[287] George A. Samara. The relaxational properties of compositionally disordered abo3 perovskites. *Journal of Physics: Condensed Matter*, 15(9):R367, 2003.

[288] V. V. Shvartsman and A. L. Kholkin. Evolution of nanodomains in $0.9PbMg_{1/3}Nb_{2/3}O_3$-$0.1PbTiO_3$ single crystals. *Journal of Applied Physics*, 101(6):064108, 2007.

[289] Wenhui Ma and L. Eric Cross. Flexoelectricity of barium titanate. *Applied Physics Letters*, 88(23):232902, 2006.

[290] John Y. Fu, Wenyi Zhu, Nan Li, Nadine B. Smith, and L. Eric Cross. Gradient scaling phenomenon in microsize flexoelectric piezoelectric composites. *Applied Physics Letters*, 91(18):182910, 2007.

[291] Wenhui Ma and L. Eric Cross. Large flexoelectric polarization in ceramic lead magnesium niobate. *Applied Physics Letters*, 79(26):4420–4422, 2001.

[292] Casey Israel, ND Mathur, and JF Scott. A one-cent room-temperature magnetoelectric sensor. *Nature materials*, 7(2):93–94, 2008.

[293] Jun-Xian Ye, Jian-Nan Ma, Jing Ma, Jia-Mian Hu, Zheng Li, Ming Feng, Q. M. Zhang, and C. W. Nan. Temperature dependence of magnetoelectric coupling in FeBSiC/PZT/FeBSiC laminates. *Journal of Applied Physics*, 116(7):074103, 2014.

[294] Vasiliki Tileli, Martial Duchamp, Anna-Karin Axelsson, Matjaz Valant, Rafal E. Dunin-Borkowski, and Neil McN. Alford. On stoichiometry and intermixing at the spinel/perovskite interface in $CoFe_2O_4/BaTiO_3$ thin films. *Nanoscale*, 7:218–224, 2015.

[295] R. V. Chopdekar and Y. Suzuki. Magnetoelectric coupling in epitaxial $CoFe_2O_4$ on $BaTiO_3$. *Applied Physics Letters*, 89(18):182506, 2006.

[296] Ce-Wen Nan, M. I. Bichurin, Shuxiang Dong, D. Viehland, and G. Srinivasan. Multiferroic magnetoelectric composites: Historical perspective, status, and future directions. *Journal of Applied Physics*, 103(3):031101, 2008.

[297] M. I. Bichurin, V. M. Petrov, and G. Srinivasan. Theory of low-frequency magnetoelectric effects in ferromagnetic-ferroelectric layered composites. *Journal of Applied Physics*, 92(12):7681–7683, 2002.

[298] Antony Adair, Jose T. Elizalde Galindo, Cristian Botez, Verónica Corral Flores, Dario Bueno Baques, Luis Fuentes Cobas, and José A. Matutes-Aquino. AC-Susceptibility Measurements of the Superparamagnetic Relaxation in Systems of $Ni_{1-x}Zn_xFe_2O_4$ Nanoparticles. *MRS Proceedings*, 962, 2006.

[299] Y. D. Zhang, J. I. Budnick, W. A. Hines, C. L. Chien, and J. Q. Xiao. Effect of magnetic field on the superparamagnetic relaxation in granular Co-Ag samples. *Applied Physics Letters*, 72(16):2053–2055, 1998.

[300] J. Wan, G. Tang, and Y. Qian. Room temperature synthesis of single-crystal Fe_3O_4 nanoparticles with superparamagnetic property. *Applied Physics A*, 86(2):261–264, 2007.

[301] Gabriel Caruntu, Amin Yourdkhani, Marian Vopsaroiu, and Gopalan Srinivasan. Probing the local strain-mediated magnetoelectric coupling in multiferroic nanocomposites by magnetic field-assisted piezoresponse force microscopy. *Nanoscale*, 4:3218–3227, 2012.

[302] Harsh Trivedi, Vladimir V. Shvartsman, Doru C. Lupascu, Marco S. A. Medeiros, Robert C. Pullar, Andrei L. Kholkin, Pavel Zelenovskiy, Andrey Sosnovskikh, and Vladimir Ya. Shur. Local manifestations of a static magnetoelectric effect in nanostructured $BaTiO_3$-$BaFe_{12}O_9$ composite multiferroics. *Nanoscale*, 7:4489–4496, 2015.

[303] Harsh Trivedi. *Mapping Local Manifestations of the Strain Mediated Magnetoelectric Effect in Composites*. PhD thesis, Universität Duisburg-Essen, Germany, 2015.

[304] JW Matthews and AE Blakeslee. Defects in epitaxial multilayers: I. misfit dislocations. *Journal of Crystal Growth*, 27:118–125, 1974.

[305] R. M. Bozorth, Elizabeth F. Tilden, and Albert J. Williams. Anisotropy and magnetostriction of some ferrites. *Phys. Rev.*, 99:1788–1798, Sep 1955.

[306] C.G. Stefanita. *From Bulk to Nano: The Many Sides of Magnetism*, chapter 3 Combined Phenomena in Novel Materials, pages 41–70. Springer Series in Materials Science. Springer Berlin Heidelberg, 2008.